RATE-DEPENDENT LOCOMOTION AND INTRUSION PHENOMENA IN GRANULAR MEDIA

A Dissertation
Presented to
The Academic Faculty

By

Andras Karsai

In Partial Fulfillment
of the Requirements for the Degree
Doctor of Philosophy in the
School of Physics

Georgia Institute of Technology

May 2022

RATE-DEPENDENT LOCOMOTION AND INTRUSION PHENOMENA IN GRANULAR MEDIA

Thesis committee:

Prof. Daniel I. Goldman, Advisor
School of Physics
Georgia Institute of Technology

Prof. Ken Kamrin
Department of Mechanical Engineering
Massachusetts Institute of Technology

Prof. Elisabetta Matsumoto
School of Physics
Georgia Institute of Technology

Prof. Chloé Arson
School of Civil and Environmental Engineering
Georgia Institute of Technology

Prof. Michael F. Schatz
School of Physics
Georgia Institute of Technology

Date approved: April 21, 2022

Reflecting its potential fluidity and fickleness, sand, as the quintessential granular material, has become a symbol of instability and impermanence.

Michael Welland

What makes the desert beautiful is that it hides, somewhere, a well.

Antoine de Saint Exupéry

For my parents Istvan and Johanna,

and for those I hold dear.

ACKNOWLEDGMENTS

My graduate education would not have been possible without the support of many amazing and wonderful people over the years. First of all, I would like to thank my advisor, Professor Daniel I. Goldman, for his constant support and guidance. He showed me how to work, think, and succeed not just in scientific thinking, but in the entire domain of professional and social development. Without his mentorship, I would not have grown nearly as much as I have over these past seven years.

I would like to thank the members of my thesis committee: Prof. Ken Kamrin for his many years of great collaborative work in the theory/computation world; Prof. Chloé Arson for her leadership on the BRISS project; and Profs. Elisabetta Matsumoto and Michael E. Schatz for their guidance on this thesis over the years.

My gratitude goes out to my colleagues and professional collaborators: Shashank Agarwal (MIT) for his insightful energy, savoir faire, and years of scientific collaboration and support; Nicholas D. Naclerio (UCSB) for his ingenuity, experimental aptitude, and project ambition; Siddharth Shrivastava (Georgia Tech) for his precocious expertise and tenacity; and Prof. Yasemin Ozkan-Aydin (now University of Notre Dame) for her expertise and resolve.

My thanks to the support of my personal friends: Steven & Thomas Harrington, Benjamin Northrup, Ben McInroe, William Bailie, Shukiko Tanaka, Alex & Jordan & Sonny & Pamela Sellers, Matthew Johnson, Haluk Ergodan, Brendon Palowitch, and CJ Warner. Your companionship and encouragement has made the past seven years all the more worthwhile.

I would like to thank all of the current and past members of the CRAB Lab, chief among them Shengkai Li, my scientific complement synchronously initiated from the other side

of the world. Your support and friendship has been irreplaceable these past years, and you were my intellectual sounding board and mirror. Special thanks to Kelimar Diaz-Cruz for her prowess, Steven Tarr for his banter, Madison R. Hales for her spirit, Akash Vardhan for his resolution, Daniel Soto for his alacrity, Marine Maisonneuve for her sophistication, Baxi Chong for his expertise, Joseph Brunner for his positivity, Enes Aydin for his helping hands, and Dr. Deniz Kerimoglu for his geniality.

My gratitude goes out to my senior mentors and collaborators over the years: Dr. Sarah Sharpe, Dr. Daria Monaenkova, Prof. Yasemin Ozkan-Aydin, Dr. Jeffery Aguilar, Dr. Tingnan Zhang, Dr. Perrin Schiebel, Prof. Jennifer Reiser, Prof. Feifei Qian, Prof. Chen Li, Prof. Elliot Hawkes, and Prof. Paul B. Umbanhowar. All of your advice, support, and guidance over the years has been invaluable.

My heartfelt thanks to the funding organizations that have supported me and my projects over the years: the Godbold Scholarship, without which I never could have come to Georgia Tech to begin with; Georgia Tech's President's Fellowship; the Army Research Office (ARO); the National Science Foundation (NSF); the National Aeronautics and Space Administration (NASA); and the U.S. Army Tank Automotive Research, Development and Engineering Center (TARDEC).

Finally, I would like to thank my family members who have given much such wonderful encouragement over the years: Katalin Trogmayer, Tibor & Katalin Preiszner, and Márton & Katalin Buzsáki. My most heartfelt thanks to my parents, István Karsai and Johanna Preiszner for their unending love and support. Even at my lowest points, they never gave up on me, and raised me up to where I am today. I could never express enough gratitude to them for what they've done for me.

TABLE OF CONTENTS

LIST OF TABLES

LIST OF FIGURES

LIST OF ACRONYMS

ABS Acrylonitrile Butadiene Styrene

CSSM Critical State Soil Mechanics

DEM Discrete Element Method

DRFT Dynamic Resistive Force Theory

GM Granular Media

IM Intermediate Mound

InSIGHT Interior exploration using Seismic Investigations, Geodesy and Heat Transport

JSC Johnson Space Center

LCROSS Lunar Crater Observation and Sensing Satellite

LOLA Lunar Orbiter Laser Altimeter

MPM Material Point Method

NASA National Aeronautics and Space Administration

PIV Particle Image Velocimetry

PPR Pulses Per Rotation

PS Poppy Seeds

RFT Resistive Force Theory

RP15 Resource Prospector 15

RPM Rotations Per Minute

RRP Rear Rotator Pedaling

RS Rotary Sequence

SD Standard Deviation

UDP User Datagram Protocol

VFD Variable Frequency Drive

VIPER Volatiles Investigating Polar Exploration Rover

SUMMARY

In movement on solid terrains, animals, vehicles, and robots can make use of well-established contact dynamics for planning movement and locomotion gaits. However, when the terrain can be deformed significantly, effective traversal can be inhibited by terrain heterogeneities created before and/or during locomotion. Understanding the physical behavior of such deformations such complex forcings like locomotion can inform robotic navigation strategies and expand our physical intuition of soft matter substrates.

The objectives of this dissertation were to examine various rate-dependent phenomena for a specific class of flowable substrates abundant in the natural world: granular media. Granular substrates exhibit multiphase and hysteretic properties as a collective of many small rigid bodies. Their physics is dominated by a network of frictional contacts between simple particles, which nevertheless display a wealth of unexpected multiphase phenomena depending on their stresses and packings. In this dissertation we present a series of experimental studies on such media.

An anthropogenic mode of terrain traversal, wheeled locomotion, can locomote via the reaction force generated from actively shearing a granular substrate. We show using an automated wheel carriage testbed that this locomotion can induce rate-dependent weakening via the centripetal acceleration of the media under shear. By combining experiment and reduced-order modeling of granular resistive forces, we present a fundamental physics-based cause for why vehicular slippage occurs at high wheel rotation rates.

Terrain deformation can also be used to improve traversal if the terrain is remodeled in an advantageous manner. In a 'robophysical' study, we demonstrate how a small rover robot can effectively remodel steep granular slopes via strategic open-loop gait selection. By selectively avalanching frictional media towards itself, the robot could traverse loosely consolidated granular hills that otherwise would not be possible for it to climb.

Finally, we investigated how directional fluidization of granular media during intrusion

could modulate the resistive forces to allow a body to move efficiently within a substrate that constantly attempts frictionally hinder it. Our findings were used to inform local fluidization strategies in a soft burrowing robot built by collaborators. We further explored local fluidization by pinning aerated cavities within granular media with an automated air probe system. Upon forced overexpansion of the cavity, we discovered a strongly periodic grain transport structure, which we show as a creeping boundary oscillation sustained by the input flow.

This dissertation showcases not only the strength of experimental investigation in physics to discover new phenomena, but also how simple reduced-order models can be adapted to explain them. We show how new insights can come from understanding the experiment first, then using that intuition to synthesize our observations into a general model for application in robotics, terradynamics, and more.

CHAPTER 1
INTRODUCTION

1.1 Stories of Desert Environments

A blistering sun beats down on a golden expanse. Under a cloudless sky, undulating dunes stretch to every corner of the horizon. With the sun directly overhead, the scene appears strangely flat as shadows shrink to specks, offering no refuge from the heat. The air itself thirsts for moisture. High temperatures and zero humidity quickly evaporate any exposed liquid water. Uncountable grains of sun-baked sand rest in stillness, each one having journeyed untold distances across the planet by aeolian processes. This scene appears a landscape devoid of life, where no green plant takes root in the shifting sands, and no other creature's stirring disturbs the torrid air. Standing on a dune ridge, we struggle to keep our balance as the sands flow unpredictably beneath our feet, avalanching and collapsing under our weight. Each grain moves as a fickle unit of an immense collective, supported only by its fellows in an intractable cascade of motion.

We are currently in one of the many ergs of the Sahara, the hyperarid hot desert (Köppen classification BWh) that dominates the northern half of Africa. This spectacle is not unique to the Sahara, as such hot deserts cover approximately 14 percent of Earth's land area [1]. The Sahara, the Kalahari, the Mojave, the Arabian, the Danakil, the Great Victoria, all of these deserts' climates are dominated by high atmospheric pressure zones and stable descending air masses that create hot, calm, and arid conditions with intense sunshine (Figure 1.1). These conditions result from global convection cells where the planet's equatorial regions are heated by the sun, and hot air rises and diverges toward the northerly and southerly directions. As the air finally nears the 30° north and south parallels, the air once again sinks, completing a convection cycle known as a Hadley cell. The geographical

bands along which this occurs are colloquially known as the “horse latitudes”, and are the sites of the world’s largest hot deserts [2].

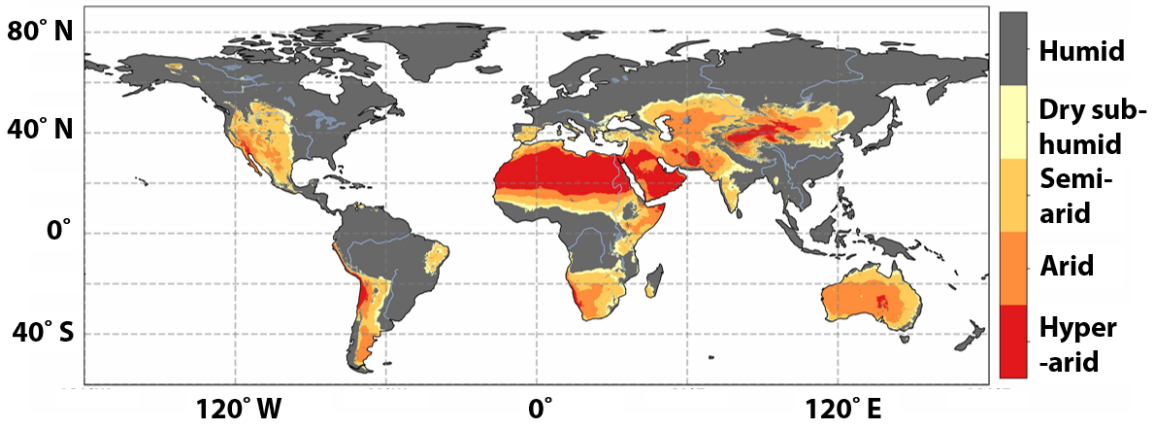

Figure 1.1: **Distribution of Arid Regions on Earth** Geographical distribution of drylands, delimited based on the aridity index (AI). The classification of AI is: Humid $AI > 0.65$, Dry sub-humid $0.50 < AI \leq 0.65$, Semi-arid $0.20 < AI \leq 0.50$, Arid $0.05 < AI \leq 0.20$, Hyper-arid $AI < 0.05$. Data: TerraClimate precipitation and potential evapotranspiration (1980–2015). Adapted from Abatzoglou et al. [3] and Mirzabaev et al. [4].

These conditions turn out to be ideal for the natural generation of sand. The large variation in temperatures between day and night in the arid air puts heat stress on exposed rock, which slowly break into smaller and smaller chunks. Whenever rainfall occasionally occurs, the raindrops striking hot rocks further stresses them and can break them into fragments, eventually grinding them down to granular sand [5]. Here the lack of consistent precipitation is a burden, as without a minimum of moisture, no plant species can thrive. The lack of abundant plants that typically anchor and fix the soil exposes granular particles to the desert winds. Aeolian processes are free to transport these unconsolidated sediments over time into dunes, creating the classical image of the barren, lifeless desert [6].

However, many hot deserts exist on Earth outside of this hyper-arid extreme (Figure 1.1). In semi-arid drylands, plant life adapted to low levels of moisture can take root and fixate the top layers of soil, preventing it from being blown away by wind. While smaller dust particles on the order of a few microns may still travel, the majority of sand particles are fixed in place. Now a thriving desert ecosystem can begin with photosynthetic,

aridity-adapted plants forming its basis. Stable soils can also lead to desert biocrust, a web of minuscule fungi, lichens, and cyanobacteria living within the upper few millimeters of sandy soil [7] which further stabilize the soil, benefit plants, and fix carbon, nitrogen, and moisture. Various desert-dwelling animals now have food sources and the ability to find shelter in stabilized soil, and the desert may thrive with life despite its arid conditions.

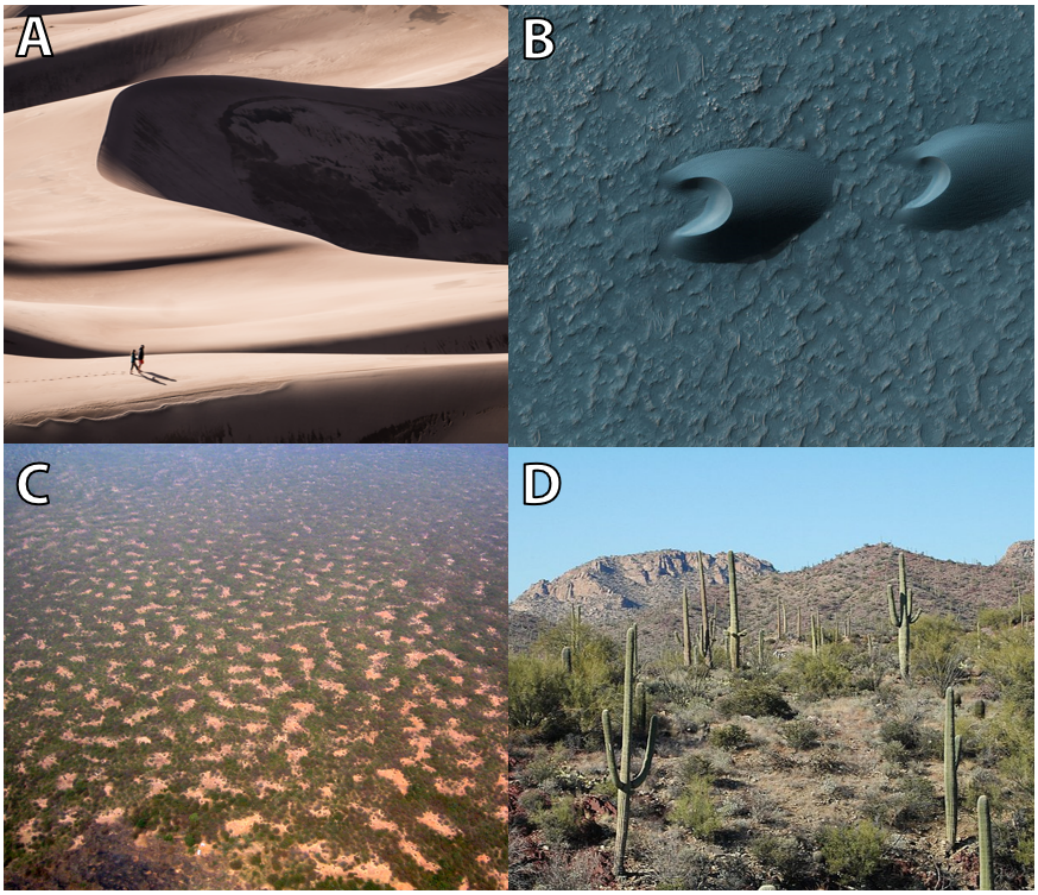

Figure 1.2: **Varieties of Desert Environments** (A) Great Sand Dunes National Park and Preserve, United States. Photo credit: Lionello DelPiccolo (B) Barchan dunes [6] on Mars' Hellespontus region as seen by HiRISE on the Mars Reconnaissance Orbiter. These dunes are formed into a saif, a linear formation parallel to the direction of the wind. Photo credit: NASA/JPL/UArizona (C) Aerial oblique view of a gapped bush plateau in W National Park, Niger. The mean distance between two consecutive gaps is 50 meters. Vegetation is dominated by *Combretum micranthum* and *Guiera senegalensis*. Photo credit: Nicolas Barbier (D) View of the Sonora Desert in Arizona. Photo credit: Felix Gottwald

Deserts can thus take on a multitude of forms, from great dunes of granular sand (Figure 1.2A, B) driven purely by physical climate processes of the planet, to thriving ecosystems where countless biological systems interact (Figure 1.2C, D). Both deserts and dry-

lands collectively cover 41 percent of Earth's land area (Figure 1.1) and are home to more than 38 percent of the global population. Human existence within drylands is a coupled, dynamic, and co-adapting balance, with no singular equilibrium point, being the co-evolved product of complex interactions between biophysical (e.g., climate, soil, biota) and human (e.g., demographic, economic, institutional) subsystems [8]. Both thriving and desolate drylands can be created or changed due to anthropogenic intervention. Some form of severe land degradation is present on between 10 to 20 percent of these lands: a threat which may grow in the face of human population growth and climate change.

A famous example of such ecological degradation was the Dust Bowl of the 1930s, where failure to apply dryland farming methods combined with drought led to unprecedented wind erosion and dust storms in the Oklahoma Panhandle [9]. The intense storms and desertification of the region led to mass emigration and left hundreds of thousands homeless and destitute. Further ecological intervention was needed, as President Franklin D. Roosevelt initiated the Great Plains Shelterbelt project to plant over 220 million trees along the 98th meridian west to fix the soil and reduce wind velocity [10]. This significantly reduced soil erosion and allowed the plains ecosystem to slowly recover once the drought ended.

Desertification can be indeed reversed by humans, but requires a concentrated effort in sustainable land management [4]. However, there is some cause for optimism. Evolving technologies and increased understanding of drylands conservation methods can avoid, reduce, and reverse desertification, simultaneously contributing to climate change mitigation and adaptation while providing long-term economic benefits [4, 3]. Recent examples of checkerboard barriers stabilizing sand dunes [11] and sand "soilization" via sodium carboxymethyl cellulose mixtures that modulate sand rheologies [12] showcase the variety of methods that can cause drylands to thrive.

These stories of the desert and humanity's coexistence with it serve as context and motivation for the rest of this thesis. Desertification poses an existential threat to large parts

of the planet's ecology, and without the proper understanding and perspective, we can not develop the tools to combat it in the coming years. In the public cognizance, arguably the most famous science-fiction story written is intertwined with this concept: Frank Herbert's famous 1965 science fiction work *Dune* was inspired by his 1959 visit to Florence, Oregon, where the USDA was planting European grasses to halt migrating sand dunes [13]. This planted the seed of a science fiction story where the desert planet Arrakis is caught between the external factions that wish to exploit it and its inhabitants that work to transform it into a thriving paradise. Herbert drew many ecological, political, and moral parallels between his fictional universe and our own, much of which are still just as relevant today.

Given this motivation, let us examine the unit, the grain which constitutes our oceans of sand. Let us investigate the world of granular frictional materials which form the basis of our drylands. Every plant that grows in the desert is worth treasuring, but we must also understand the basic unit of the barren desert: granular matter.

1.2 Granular Matter and its Properties

The natural world holds a vast array of environments of great complexity. Much of the abiotic solid phase of matter on Earth is rock, all types of which can constitute sand when broken to small sizes by natural processes [14], creating granular material. A granular material is most often defined as any collection of discrete rigid bodies between 100 microns and 3 mm in size [15]. For smaller particles, other interactions such as van der Waals forces, humidity, and air drag begin to play important roles, falling within the domain of powders [16]. When a collection of grains form a natural terrain, they function as a frictional and flowable volume, with inter-grain interactions dominated by elastic contact and dry friction (often Coulomb friction). While deserts are the most evocative and commonly associated environment of flowable terrain, many other environments contain flowable materials like leaf litter, snow, gravel, and silt. For scientific understanding of such environments, a quantitative understanding of their properties and interactions is necessary. To accomplish this,

descriptions of granular phenomena often involve solid, liquid, and gaseous-like behaviors, with support from physical arguments of elasticity, plasticity, statistical physics, fluid mechanics, and geomorphology [16].

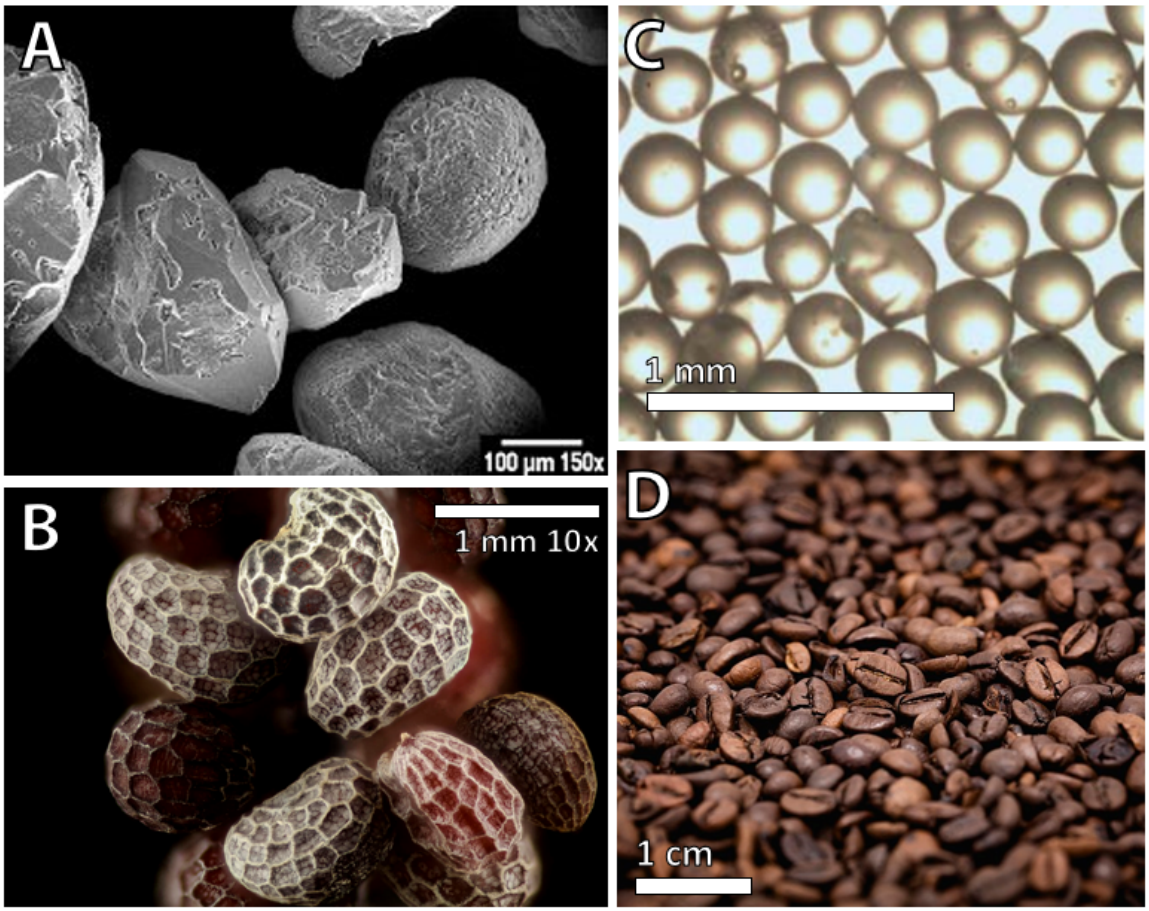

Figure 1.3: **Examples of Granular Media (GM)** (A) Grains of "Ottawa Silica Sand" under a scanning electron microscope. "Ottawa Sand" is a by-product of hydraulic mining of Ordovician orthoquartzites. Image credit: NASA. (B) Seeds of the opium poppy (*Papaver somniferum*). Image Credit: United States Geological Survey. (C) Microscopic image of 300 micron glass beads. Image credit: Li et al. 2013 [17]. (D) Roasted coffee beans (*Coffea arabica*). Image credit: Popo le Chien.

Quantitative understanding of Granular Media (GM) is difficult due to many factors, such as the large number of particles, lack of thermal fluctuations creating equilibrium, complex inter-grain interactions, multiphase phenomena [18], and energy dissipation [16]. Indeed, unlike the Navier-Stokes equations for fluid mechanics, there are no fundamental equations of state for granular systems. Describing GM is further complicated by the large amount of its potential properties, such as cohesion, particle size(s), particle shape(s), com-

paction, and stress/strain history. As detailed later in this chapter, we may approach this challenge to modeling GM behavior by applying various techniques.

Throughout this dissertation, we will be focusing on flowable, frictional GM as our primary substrate of physical interest. Natural granular materials such as sand, glass beads, biological grains like poppy seeds (Figure 1.3) serve as a representative model for flowable terrains. These substances fulfill the simple requirements of elastic contact and Coulomb friction being the primary mechanisms of interaction between particles [16]. In a GM volume under external stress, this dissipative repulsive contact is inhomogenously carried by force chains along only a small fraction of the total grains [19]. In studies of dry GM, the lack of moisture between grains eliminates cohesion, meaning dry GM cannot support any tensile loads.

GM at rest without external perturbation can primarily be considered a solid, as the material can support external loads without flowing [16]. In other words, a sand pile can stand up against gravity without avalanching, since each sand grain's contact and frictional forces hold its neighbors in place. This is again in contrast to simple Newtonian model of viscous fluids, which follow the well-known equation:

$$\tau_{ij} = \mu \left(\frac{\partial v_i}{\partial x_j} + \frac{\partial v_j}{\partial x_i} \right) \tag{1.1}$$

where x_j is the jth spatial coordinate, v_i is the fluid's velocity in the direction i, τ_{ij} is the jth component of the stress tensor perpendicular to axis i, and μ is the fluid's shear viscosity. This tensor equation is not applicable to GM, which we will see later may behave as a *frictional* fluid rather than a viscous one. However, GM will begin to flow if an applied stress overcomes the material's critical yield stress, as detailed in Section 1.4.

Two more important properties generic to granular matter are the coefficient of restitution and volume fraction. As a simple example, when grain A in GM collides with the stationary grain B at some nonzero velocity v, they undergo an inelastic collision, as some

kinetic energy is always lost to various mechanisms (plastic deformation, viscoelasticity loss, local heating, etc.) and grain A now has velocity after the collision:

$$v' = -ev \tag{1.2}$$

where $0 \leq e < 1$ is the (normal) coefficient of restitution. For dry GM and low grain speeds, e approaches close to 1 as dissipative effects vanish in this limit (e.g. for steel balls $e \approx 0.9$). However, as v increases, more energy goes into the plastic deformation of the GM volume, and energy balance and experiments find that:

$$e \propto v^{-1/4} \tag{1.3}$$

showing that GM becomes more dissipative especially at high impact speeds [20]. We will see in later chapters how this increased dissipation can also manifest as additional resistive forces on an intruding body.

The volume fraction of a granular volume characterizes the density of a granular packing, defined as the ratio of the volume occupied by the grains to the total volume occupied by the packing:

$$\phi = \frac{V_{grains}}{V_{total}} \tag{1.4}$$

which cannot exceed the value $\phi = 1$. Stable packings of frictional GM exist in a finite range of ϕ, with random loose packing of spheres corresponding to $\phi \approx 0.55$, and random close packing to $\phi \approx 0.64$. Applied stresses that induce flow, vibrations, and other disturbances can cause ϕ to change as the grains rearrange into a new packing, which in turn affects the effective yield stress (among other properties) of the granular volume [16].

Much of the later chapters of this dissertation deal with how rate-dependent effects emerge in various locomotion and intrusion scenarios in GM. If we are to understand ef-

fective means of traversal in GM, we must understand both the mechanisms of both the substrate and the locomoting body. After a discussion on various locomotion methods, we will examine various approaches available to understanding complex granular terrains.

1.3 Locomotion in Frictional Substrates

A specific type of body interaction with granular materials is locomotion, whether legged, wheeled, undulatory, or otherwise. Locomotion occurs when an object uses some kind of motion to actively propel itself across/through a granular environment. Discovering principles of locomotion for organisms in natural environments requires integrating several approaches to generate and test hypotheses of interaction between a locomotor and its surroundings [21]. For terrestrial locomotors, substrate properties and responses greatly influence locomotor performance and strategy [22]. Examples include the how a sandfish (*Scincus scincus*) modulates its undulatory wave as it swims under sand (Figure 1.4A) [21], the hopping of a Lesser Egyptian jerboa (*Jaculus jaculus*) across a sandy surface (Figure 1.4B) [23, 24], and even why running across sand feels easier than walking for humans (Figure 1.4C) [25, 26].

For tracked and wheeled vehicles locomoting through granular substrates (Figure 1.4D-F), the engineering field of terramechanics was developed to model soil vs. track/wheel interactions [28, 29, 30]. In terramechanics, quasi-static loading and theories of soil mechanics are used to generate empirical models that can predict vehicular performance off-road. This *a priori* knowledge of the terrain's characteristics and interaction with the locomoting surfaces allows vehicles to maintain appropriate speed and traction through proper control algorithms [31]. The field of terramechanics has seen success in predicting vehicular performance, especially for large, heavy vehicles moving at slow speeds [32]. However, it is not fully established whether these models can be scaled and applied to modeling the locomotion scenarios of faster, smaller vehicles. At high speeds, the granular terrain's inertial mechanics could affect locomotion through emergent rate-dependent effects [26, 17]. The

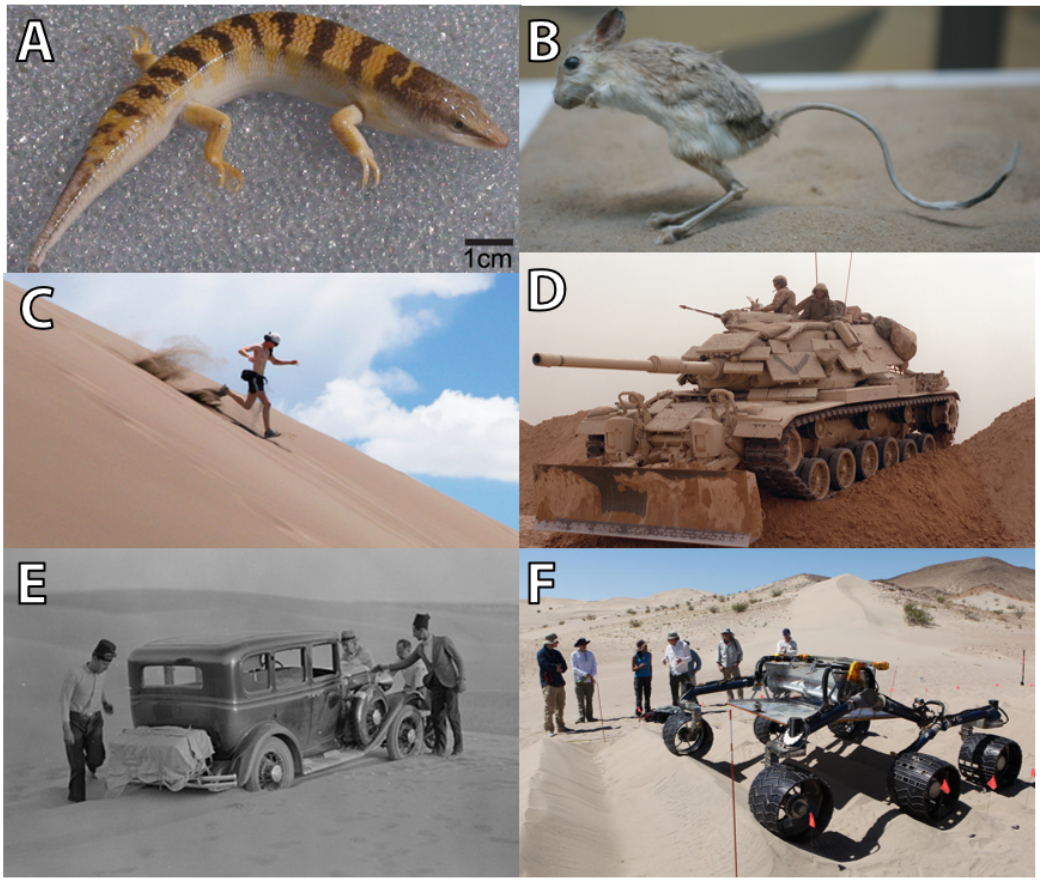

Figure 1.4: **Natural and Artificial Locomotion Methods in GM** (A) A sandfish (*Scincus scincus*) resting on glass beads, which can bury itself and use body undulation to propel itself through dry GM (Photo from Ding et al. [27]). (B) A lesser Egyptian jerboa (*Jaculus jaculus*) Photo credit: Cliff (C) Human (*Homo sapiens*) running down a dune in Great Sand Dunes National Park, Colorado. Photo credit: Daniel Schwen (D) A tracked M-60A1 battle tank driving over a sand berm. Photo Credit: Staff Sgt. M.D. Masters. (E) Car stuck in the midst of a sand dune en route to Sinai, ca. 1920. Photo credit: Matson Collection, Library of Congress. (F) *Scarecrow*, a copy of the National Aeronautics and Space Administration (NASA) *Curiosity* rover's locomotion systems, performs a test drive at the Dumont Dunes in California's Mojave Desert. Photo Credit: NASA/JPL-Caltech

empirical methods and measurements used to predict performance of large, heavy vehicles may not be applicable to small, lightweight ones, such as interplanetary rovers [33].

Our lab has done studies of snakes [34], legged robots [17], and sand-swimming lizards [35] (see Figure 1.4A) in the past. For my dissertation, wheeled locomotion in GM stood out as an interesting problem open to physics-based approaches, in the same vein as those previous studies. We will show in Chapter 2 and Chapter 3 how both constitutive models for GM can be applied to great effect, and how reduced-order models can be effective

in understanding such complex locomotion scenarios under conditions that properly re-homogenize GM. We will now introduce the some of the tools used to understand and characterize GM behavior.

1.4 Models of Granular Media Interaction

Granular substrates' macroscopic properties like yield stress, local density, and coefficient of friction are dependent on the microscopic shape, hardness, packing, and moisture content of the various grains comprising the substrate [36]. Different moisture and grain sizes give rise to materials commonly known as sands, clays, soils, silts, and other terrain classifications. When a rigid body intrudes into terrain comprised of granular material, many thousands of contact interactions occur among the grains themselves and the time-varying intruding surfaces. To successfully predict the role that granular terrain plays in these kinds of intrusions, it is necessary to simplify the behavior of the granular media into tractable models for intrusion forces. This is needed since there are no fundamental physical equations that describe these interactions, unlike stresses and flows in fluids, which are described by the Navier-Stokes equations solving various constitutive fluid models. Some possible approaches to this problem include simulating the motion of individual grains (via Discrete Element Method (DEM)), applying reduced-order empirical models (like Resistive Force Theory (RFT)), applying continuum mechanics treating GM as a deformable body with a yield stress to obtain analytical solutions of stress and strain, or applying these yield criteria via various numerical methods (like Material Point Method (MPM)).

1.4.1 Discrete Element Modeling

Discrete numerical simulations where the motion of each grain is computed are powerful tools with which to study GM [16]. Variables that are difficult to access experimentally, such as the forces between grains pairs and the contact distributions can be easily measured in simulation. DEM also help calibrate other approaches and descriptions by averaging

contact forces to compute stress and strain tensors [37]. However, these methods remain computationally expensive, as one to one simulations of common real-world scenarios, involving billions of grains of sand, have just begun to be feasible on large computing clusters [38].

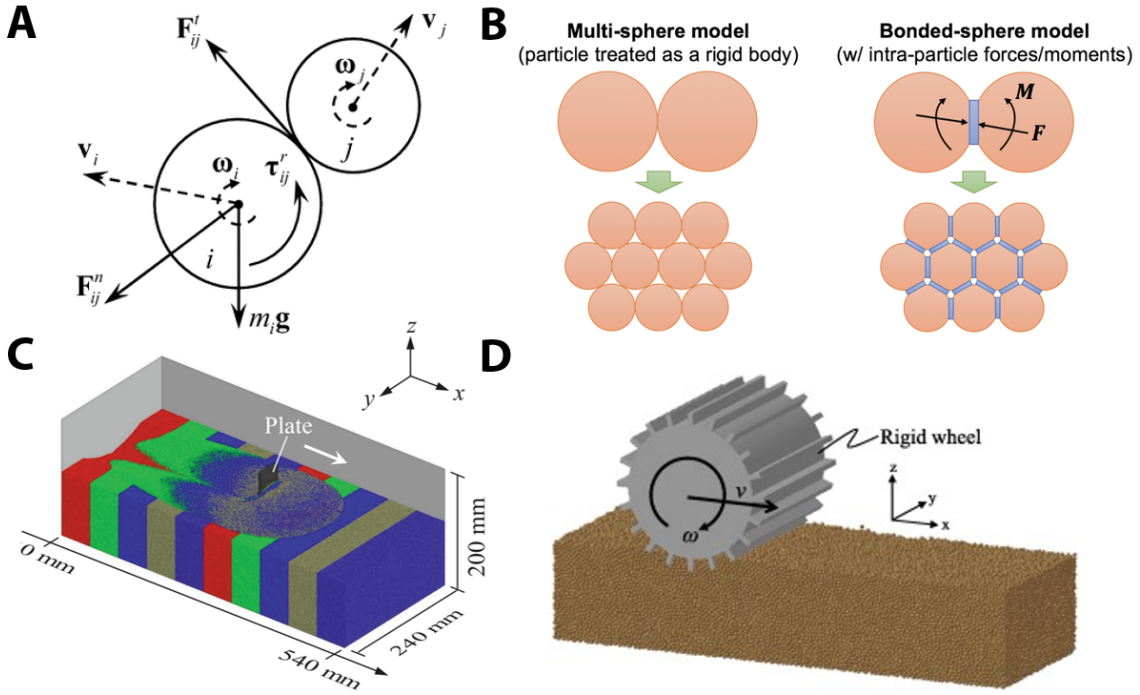

Figure 1.5: **Discrete Element Methods for Simulating Intrusions in GM** (A) A schematic representation of two spherical particles i, j contacting. DEM modeling approaches use various contact models to define generated forces and torques to solve equations of motion for each particle. Subfigure adapted from Yan et al. [39]. (B) Groups of particles are often assigned additional spatial constraints or properties to model rigid intruding bodies in GM. Subfigure adapted from Xia et al. [40] (C) Oblique view of a large-scale DEM simulation of plate drag in GM. Subfigure adapted from Kobayakawa et al. [38], based on a study by Gravish et al. [41]. (D) A DEM simulation of grousered wheel locomotion in GM. Subfigure adapted from Suzuki et al. [42].

DEM approaches are nevertheless well-established and useful for understanding GM phenomena on the grain scale [43]. The most popular DEM approach, the soft-particle method, computes the motion of each grain from Newton's laws and from the contact forces between grains, where the grains are non-deformable but are allowed to slightly interpenetrate. The grains mutually apply forces based on their degree of interpenetration, often via Hertzian contact models for spheres [44]. In simulation these grains are often softened from their real-world Young's moduli to lengthen typical collision times, allowing

for longer simulation timesteps and computational feasibility. For such methods, the DEM grain parameters tuned to match the experimental bulk response of the tested material [39]. Another approach is the contact-dynamics method, where particles cannot interpenetrate and tangential forces are strictly set by the sliding and/or rolling coefficients of friction: $F_T = \mu F_N$ (Figure 1.5A). These must be solved implicitly to calculate the grains' equations of motion, where simulations iterate to find an appropriate contact force network for all contacting grains, and only then updating the grain velocities [16].

For testing GM response to an intruding rigid body, particles may be constrained into a collective shape (Figure 1.5B) and intruded into a loose GM substrate. Resistive forces on the intruder can then be obtained by properly summing the contact forces on the rigid collective from its loose GM neighbors. In addition to extracting force response, knowledge of the GM state in simulation is for the corresponding experiment, as in the plate drag simulations of Kobayakawa et al. [38] (Figure 1.5C). Granular DEM can also be effective at capturing more complex intrusion scenarios like wheeled locomotion (Suzuki et al. [42] Figure 1.5D), which will be relevant in Chapter 2. However, all DEM methods are necessarily computationally expensive despite their power and ability to give physical insight. For a rapid iterative and possible real-time onboard calculation for locomotors like robots, a reduced-order model for GM force response will be useful.

1.4.2 Granular Resistive Force Theory

When a rigid body intrudes into terrain comprised of granular material, many thousands of contact interactions occur among the grains themselves and the time-varying intruding surfaces. To successfully predict the role that GM plays in these kinds of intrusions, it is necessary to simplify the behavior of the GM into a tractable model for intrusion forces. There is evidence that calculations of quasi-static interactions between deformable, heterogeneous granular materials and the bodies intruding or submerged in them can be made tractable through an empirical theory called Resistive Force Theory (RFT). RFT was orig-

inally a theory introduced in fluid mechanics used to simplify the Navier-Stokes equations describing fluid motion in order to model undulatory and flagellar propulsion in fluids at very low Reynolds numbers, for motions where inertial forces are small relative to viscous forces [35]. However, RFT has had success in many relevant granular locomotion scenarios that are relatively slow, such as horizontal planar sand swimming, wheeled locomotion, legged locomotion in the quasistatic locomotor regime, and jumping on granular media [45, 46, 47, 48, 49, 26]. Interestingly, RFT has demonstrated repeatedly to be more effective in modeling the forces in granular interactions between solids, rather than the viscous fluids which it was initially used to model.

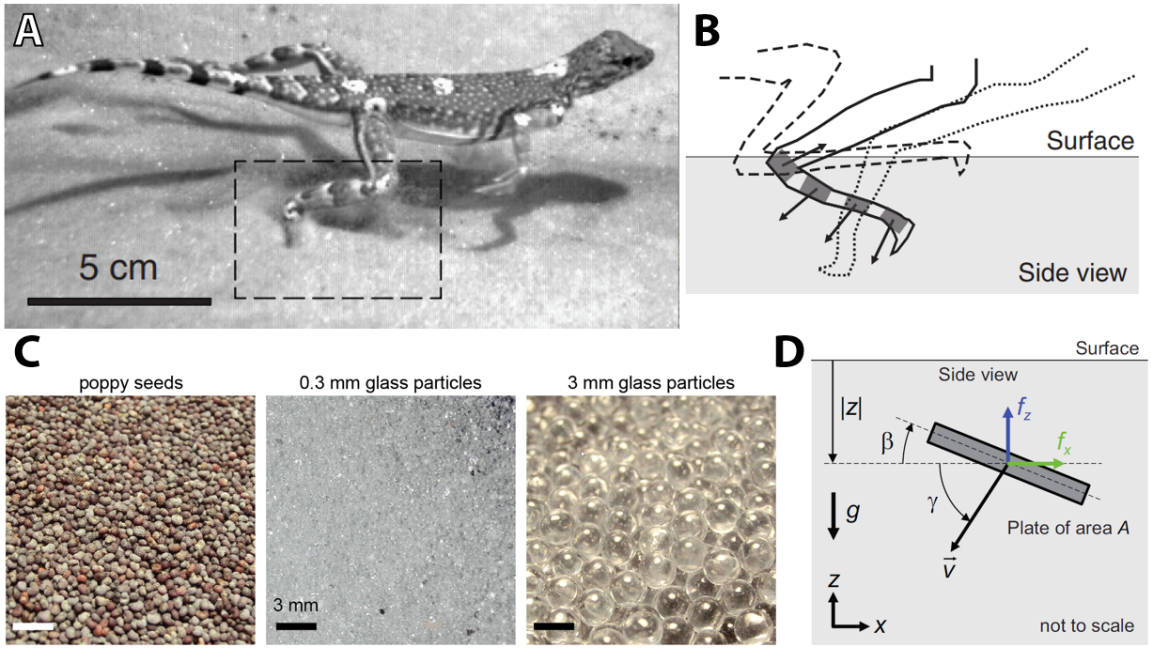

Figure 1.6: **Overview of Granular Resistive Force Theory (RFT)** (A) A zebra-tailed lizard (*Callisaurus draconoides*) runs across flowable ground, intruding its foot rapidly into GM. (B) Schematic sketch of the lizard's intruding appendage. The leg can be decomposed into multiple plate-like elements. (C) Samples of GM particles of various size, shape, and roughness tested in Li et al. [17]. Photo credit: Sarah Sharpe (D) A single plate element within a GM volume at depth $|z|$, with angle of attack β and angle of intrusion γ. These variable plate elements form the basis of granular RFT, which empirically predicts GM force response $[f_x, f_z]$. All subfigures adapted from Li et al. [17].

A significant portion of this thesis is due to the excellent work done by Li, Zhang, and Goldman on establishing a terradynamic description of legged locomotion on GM [17]. RFT application to sand swimming of the sandfish [45] (Figure 1.4A) and calculation of

lift and drag forces on simple objects moving through GM [50] found that linear superposition was valid for intruders moving at fixed depths and low speeds. This success led to the hypothesis that the net forces on an intruding leg or body (Figure 1.6A) moving in GM could be approximated by the linear superposition of resistive forces on infinitesimal leg or body elements (Figure 1.6B), now in the vertical plane [17]. Li et al. found that during intrusion, the resistive forces for a variety of GM (Figure 1.6C) was highly localized since the substrates' pressure responses were friction-dominated, and thus linear superposition is valid. These pressures were also linear in depth, proportional to the hydrostatic-like pressure present in GM. Therefore, if a simple test plate geometry (Figure 1.6D) can provide pressure per unit depth equations in the form of N/m^3 for surfaces of arbitrary orientation (β) and intrusion (γ) angles, then RFT can use these pressure response functions for any intruding geometry.

RFT works best for convex-shaped solids slowly intruding into granular material, as intruding surfaces may 'shadow' other body elements from the frictional substrate. The intruding surfaces can be decomposed into arbitrarily small leading surfaces due to the high degree of locality in GM strain fields, a phenomenon which has been observed experimentally [51]. If the force for each subsegment can be found as a function of the intruder's orientation angle β and the intrusion's velocity vector angle γ, then the forces experienced by the small leading surfaces can simply be summed to calculate the resistive force on the whole intruder. Assuming surface superposition and linearity in depth, the resistive force vector $\vec{F}$ in two dimensions can be calculated as:

$$\vec{F} = \int_S \vec{\alpha}(\beta, \gamma) H(-z)|z| dA \tag{1.5}$$

where $H(-z)$ is the Heaviside function, z is the intrusion depth, and dA is a leading surface plate element. This equation integrates over the surface each infinitesimal element dA under the GM surface (set by $H(-z)$) scaled by depth z by its corresponding stress per unit

depth $\vec{\alpha}$. The stress upon these intruding surfaces are defined by the empirical functions $\vec{\alpha}(\beta, \gamma)$ which have dimension N/m^3.

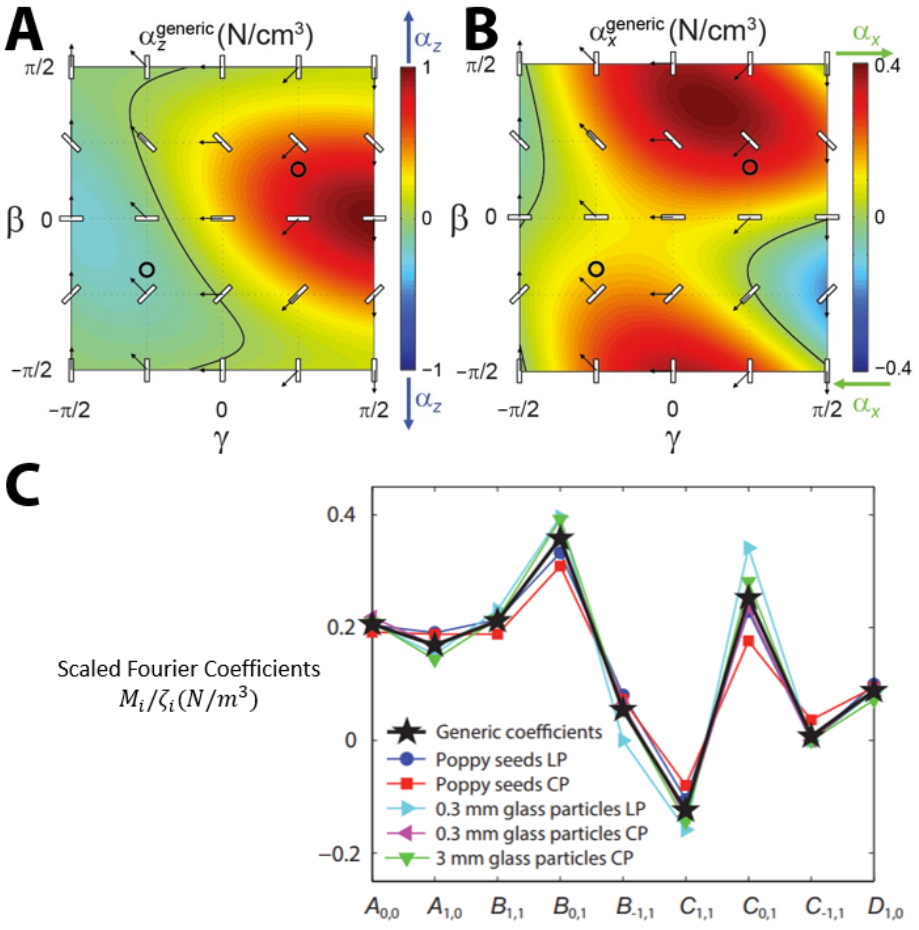

Figure 1.7: **Alpha Functions and Fourier Coefficients of Granular RFT** Generic stress (per unit depth) profiles of the RFT alpha functions in the z direction of Figure 1.6(D) in subfigure (A), and in the x direction in subfigure (B) for all tested media in Li et al. [17]. Plate schematics with arrows denote the representative orientation and movement directions for each angle pair (β, γ). (C) Scaled alpha function Fourier coefficients M_i/ξ_i for all media tested in Li et al. that can be approximated by the generic coefficient curve M_0 in black. All subfigures adapted from Li et al. [17].

RFT takes an empirical approach by determining these functions through repeated slow experimental intrusions of a small flat plate in the tested media at various values of β and γ, creating a pressure diagram from force measurements for these angled surface elements. Figure 1.7A & B show the 2D Fourier series which best approximates $\vec{\alpha}(\beta, \gamma)$ for multiple types of tested GM. The mappings for $\vec{\alpha}$ were also found to be extremely similar between various types of dry granular media [17] once divided by a single scaling constant ξ (Fig-

ure 1.7C). All dry GM tested in Li et al. exhibited resistive forces in a similar pattern, just at scaled magnitudes. These advantages makes RFT a useful tool for estimating the forces on both submerged and intruding bodies in granular media, and we will show in Chapter 2 and Chapter 3 how RFT can be further modified to capture rate-dependent scenarios as well.

1.4.3 Continuum Mechanics Applied to Frictional GM

It is convenient in many cases to treat a granular material as a continuum and to measure its bulk properties without enquiring in detail about their causation [15]. For example, both density and internal friction angle are often measured rather than predicted in practice, and in this way do not differ from the conventional approach for fluids [36]. Continuum mechanics approaches supply convenient conservation laws (e.g. mass, linear & angular momentum) given constitutive relationships for an object's physical properties [52]. However, since GM often exhibits both solid-like and fluid-like phenomena depending on its local state, rheological models for GM must consider their multiphase nature. Even for a simple granular material, a constitutive framework encapsulating all granular phenomena would have to merge many different approaches together [53], such dissipative kinetic theory [54] in dilute regimes; strengthening based on packing fraction [55] and internal state variable evolution; rate-dependence of the strength (such as $\mu(I)$ rheology [56]); and particle size effects [57] in the dense flow regime. Despite these difficulties, some situations (like quasistatic simple intrusion into GM) can closely align with similar problems of plastic deformation in solid mechanics. Understanding these requires knowledge of the substrate's yield surface, as once the stress state at a point passes the yield surface, plastic deformation of the GM continuum begins.

A yield surface is an (often convex) surface in a 3D principal stress space $(\sigma_1, \sigma_2, \sigma_3)$, where material response is *elastic* inside the surface, and *plastic* outside of it [52]. There are a few yield criteria that are useful for describing GM stress/strain response, as GM usually

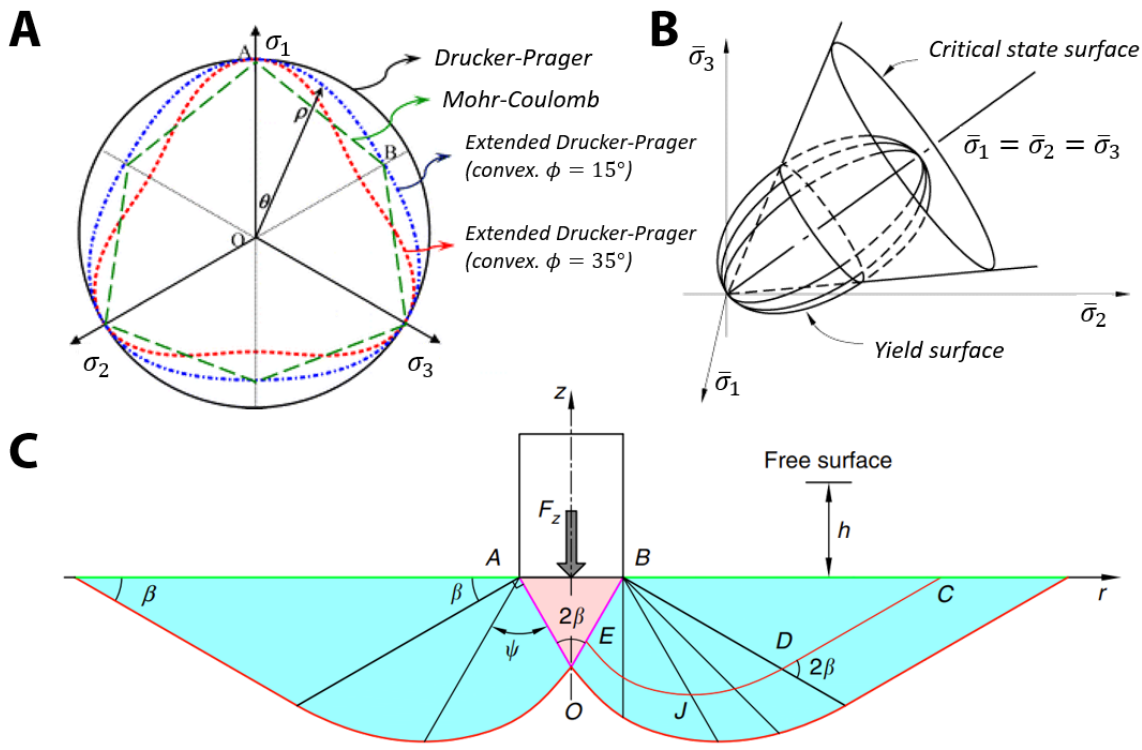

Figure 1.8: **Continuum Mechanics Interpretations of GM** (A) Diagram of the Mohr-Coulomb and Drucker-Prager (which smooths the Mohr-Coulomb yield surface) yield criterions in principal stress coordinates, along with Extended Drucker-Prager models with different internal friction angles. Subfigure adapted from Zhang et al. [58]. (B) The yield surface of the Modified Cam-Clay model and the critical state surface used in critical state soil mechanics in the principal stress space. Subfigure adapted from Kuznecova et al. [59]. (C) Application of the Mohr-Coulomb yield criterion to solve the characteristic curves of slip (blue region), along with the stagnation zone (violet region) during intrusion of a cylinder into GM. The angles β are equivalent to the ϕ internal friction angle described in Equation 1.6. Subfigure adapted from Kang et al. [60].

has high compressive strength and very low tensile strength. A well established theory for such a yield surface is Mohr-Coulomb theory [61], which proposes a failure criterion of the form:

$$\tau = \sigma \tan(\phi) + c \tag{1.6}$$

where τ is the shear strength, σ is normal stress, c is the material's effective cohesion, and ϕ is the angle of internal friction. This formulation is very simple yet provides a good predictor of the shear failure domains for many practical materials, such as concrete. The Mohr-Coulomb yield criterion creates a conical prism yield surface in principal stress space

with sharp corners (Figure 1.8A), which may be difficult to resolve when calculating plastic flows. To alleviate this, a smoothed, approximate version of Mohr-Coulomb theory known as the Drucker-Prager yield criterion [62] provides an smooth conical yield surface. In the process of approximating Mohr-Coulomb, the Drucker-Prager yield surface can be drawn inscribing, circumscribing, or on the midpoints of the Mohr-Coulomb surface (Figure 1.8A). For example, the circumscribing equation for Drucker-Prager yield criterion can be written as:

$$\sqrt{J_2} = A + BI_1 \tag{1.7}$$

where $I_1 = \sigma_1 + \sigma_2 + \sigma_3$. is the first Cauchy stress invariant in principal stress coordinates, and

$$J_2 = \frac{1}{6}\left[(\sigma_1 - \sigma_2)^2 + (\sigma_2 - \sigma_3)^2 + (\sigma_3 - \sigma_1)^2\right] \tag{1.8}$$

is the second invariant of the deviatoric Cauchy stress in principal stress coordinates. The constants A, B are determined from experiments and are related to the cohesion and internal friction angle via:

$$A = \frac{6c\cos\phi}{\sqrt{3}\,(3 - \sin\phi)} \tag{1.9}$$

$$B = \frac{2\sin\phi}{\sqrt{3}\,(3 - \sin\phi)} \tag{1.10}$$

where c is the material's effective cohesion, and ϕ is the angle of internal friction. These yield criteria are frictional constitutive approaches to modeling GM as a continuum.

Various other constitutive relations for GM as a continuum have been proposed, such as the Cam-Clay model (Figure 1.8B) used in the domain of Critical State Soil Mechanics (CSSM). CSSM asserts that GM evolves towards a critical state if continually sheared as a frictional fluid, whereupon further shear can occur without any changes to deviatoric stress,

yield stress, or volume [55]. These models are less relevant overall to the problem of locomotion and related rate-dependent phenomena, as frictional models can still hold a degree of power and generality in describing frictional substrates, from modelings intrusions (Figure 1.8C), to complex wheeled locomotion as we will show in Chapter 2. For the purposes of this thesis, we will be pursuing frictional models, their relationship with reduced-order models like RFT, and their practical use for examining locomotion scenarios.

1.4.4 Frictional Plasticity

The functions of dry GM stress response per unit depth (Figure 1.7) are useful for various situations, but with some knowledge of continuum descriptions of GM, it is worth asking why RFT takes such a form from a more fundamental physical perspective. RFT is an empirical theory that happens to work very well for dry GM intrusions, but it required many experimental trials to calibrate and validate. A deeper theoretical understanding would make granular RFT more powerful.

In 2016, Askari and Kamrin published a paper [63] which validated the RFT work by Goldman's lab [64, 17] by showing how the results of empirical RFT could arise out of a model implementing the Drucker-Prager yield criterion introduced above, and provided the impetus for Chapter 2 and various other parts of this thesis. They showed that "granular RFT arises as a consequence of two of the most salient mechanical features of dry granular media: a frictional yield criterion and no cohesion". RFT's predictive results could also be re-derived without any parameter fitting from a more fundamental Drucker-Prager frictional-plastic continuum model. With the aim of matching the results of Equation 1.5 via a more fundamental model, Askari and Kamrin created a frictional plasticity continuum model with three basic assumptions:

1. The GM has a constant internal friction coefficient μ_c
2. The GM rapidly evolves toward the critical state of volume conserving flow at some close-packed density ρ_c.

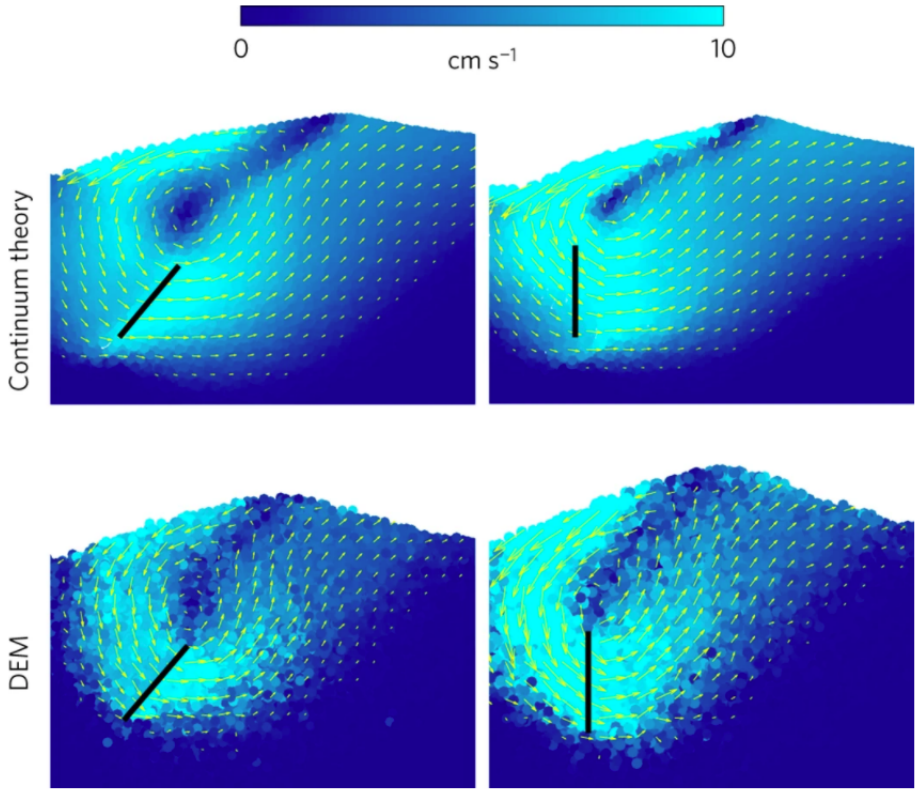

Figure 1.9: **Finite Element Methods Implementing Frictional Plasticity** Speed distribution (contours) and velocity directions (arrows) created by motion of a submerged flat intruder moving rightward at 10 cm/s at two sample orientations. Results from a frictional plasticity continuum theory in [63] (top) and DEM simulations from Ding et al. [64] (bottom) for the same geometry. Figure reproduced from Askari & Kamrin 2016 [63].

3. The GM can volumetrically expand (i.e. $\rho < \rho_c$) to model the cohesionless granular disconnection response.

The strain rate tensor of a continuum can be derived from its spatial velocity field v_i as $D_{ij} = (\partial v_i/\partial x_j + \partial v_j/\partial x_i)/2$, which has a deviatoric component $D'_{ij} = D_{ij} - \delta_{ij}D_{kk}/3$ and an associated scalar shear rate $\dot{\gamma} = \sqrt{2D'_{ij}D'_{ij}}$. Along with a Drucker-Prager yield surface and momentum balance

$$\rho \dot{v}_i = \frac{\partial \sigma_{ij}}{\partial x_j} + \rho g_i \tag{1.11}$$

from continuum mechanics, we can write a closed form equation for the Cauchy stress:

$$\sigma_{ij} = -P\delta_{ij} + \frac{2\mu_c P D'_{ij}}{\dot{\gamma}} \quad \text{if} \quad \dot{\gamma}, P > 0 \tag{1.12}$$

where $P = -\sigma_{kk}/3$ is the isotropic pressure. Askari and Kamrin implemented this in a continuum finite element solver (Abaqus/Explicit) and found the continuum theory to match well with the corresponding DEM simulation for submerged flat intruders (Figure 1.9). This was done without fitting parameters and only with the substrates' bulk properties of internal friction μ_c and density ρ [63].

When recreating the RFT test plate intrusions detailed previously [17], Askari and Kamrin found that the frictional plasticity model also matched well to the corresponding experimental results (Figure 1.10). Both RFT and the continuum model created the same geometry independent local force formula, creating a link between the empirical but experimentally proven RFT and a more general plastic flow rheology. When applied to more complex geometries, the frictional plasticity model also produced the same superposition behavior as RFT. This property may be related to the hyperbolic nature of GM's governing equations [15], as stress characteristic curves extend from intruder boundaries along slip-lines (Figure 1.8C). The stress distribution in surcharge zones of GM are independently attributed to tractions on specific surfaces of an intruder. This fundamentally differs from force response in a viscous fluid, where the equations are elliptic, and surface stress is globally influenced by the motion and shape of an intruder's entire boundary [63].

Viscous fluids follow Stokes' flow equations at low Reynold's numbers, with the form:

$$\eta \frac{\partial^2 v_i}{\partial x_j^2} - \frac{\partial P}{\partial x_i} + \rho g_i = 0 \tag{1.13}$$

$$\frac{\partial v_i}{\partial x_i} = 0 \tag{1.14}$$

for dynamic viscosity η. For an arbitrary intruding plate-like geometry of characteristic

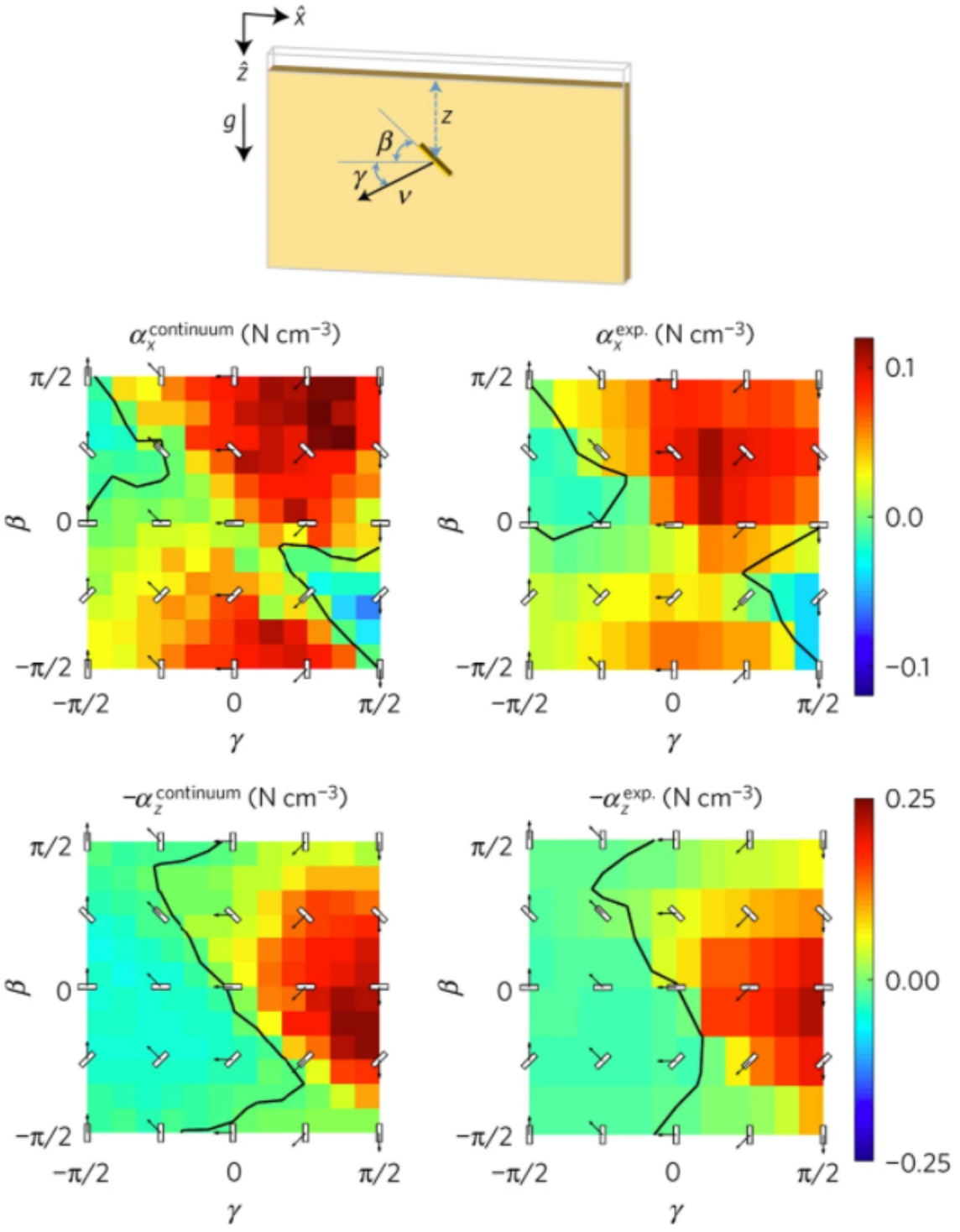

Figure 1.10: **Continuum GM Models Match a Reduced-Order RFT** Generic stress (per unit depth) profiles of the RFT alpha functions in the x, z directions of the top inset, for the frictional plasticity simulations in the left column, and the published experimental measurements in the right column [17]. Solid black lines show the zero values. Figure reproduced from Askari & Kamrin 2016 [63]

length L, Askari and Kamrin show via Buckingham analysis that drag force must scale as

$$\vec{F}_{\text{visc}} = Lv\vec{\Psi}_{\text{visc}}(\beta, \gamma) \tag{1.15}$$

similarly to other Stokesian drag formulae. Now suppose an isolated are of small characteristic width λ experiences this local drag formula. Applying superposition of this local Stokesian drag rule to a macroscopic geometry would result in:

$$\vec{F}^{\text{RFT}}_{\text{visc}} = \frac{L^2}{\lambda} v\vec{\Psi}_{\text{visc}}(\beta, \gamma) \tag{1.16}$$

Equation 1.16 scales as L^2, but this contradicts Equation 1.15 where the actual force scales with L, so superposition is not precise for viscous fluids. The factor λ, the selected micro-size common in slender body applications of RFT will cause an increasing error term in viscous fluids which is not present in GM (see Askari and Kamrin [63] supplemental sections for more detail). Under a similar analysis analysis for frictional media, Askari and Kamrin show that resistive force scales as L^3 for *both* the local and superpositioned force response formulations. This shows that RFT may be more suited to frictional GM than the viscous fluids for which it was originally formulated.

We will revisit applications of frictional plasticity for modeling wheeled locomotion scenarios in Chapter 2. Locomotion on GM, which can cause modeling difficulties by over-deforming meshes in finite element methods. For large deformations, mesh-free approaches such as MPM can combine advantages of DEM, finite element, and continuum methods, as we will show in Chapter 2.

1.5 Organization of this Dissertation

During my years of PhD work from 2015 to 2022, I have had the opportunity to work with some fantastic colleagues and scientists (see the Acknowledgements section for more detail). I have done a large amount of collaborative work, and it would not have been

possible without the efforts and expertise of all involved. For this thesis, I will be detailing the most significant of these projects in an order that will ideally tell a coherent story: beginning with granular intrusion studies that exhibit surprising results, to more complex dynamic locomotion in GM, to locomotion that exploits GM deformation itself, to a pair of studies investigating multiphase locomotion in GM via local aeration. Each chapter was the result of a different collaboration, and I credit my collaborators in the 'Contributions' section closing each chapter, as well as in the footnotes of each chapter's opening page. Given the framework introduced in this chapter, the rest of the thesis is organized as such:

- Chapter 2 describes a class of complex, rate-dependent intrusion scenarios: rapid wheeled locomotion, adapted from a publication in *Science Advances* [65].
- Chapter 3 describes how the locomotive gaits of a robophysical rover can climb loose GM slopes via local terrain remodeling, adapted from a publication in *Science Robotics* [66].
- Chapter 4 details the construction and performance of a growing, everting soft robot that uses local aeration to tunnel through GM, adapted from a publication in *Science Robotics* [67].
- Chapter 5 covers currently unpublished studies of stability and transport of locally aerated cavities in GM, extending the local aeration capabilities introduced in Chapter 4.
- Chapter 6 investigates unusual granular intrusion scenarios and features content from a publication in *Soft Matter* [53], along with additional unpublished studies on the thermodynamics of impact.
- Chapter 7 features concluding remarks and various projects currently in progress.

CHAPTER 2

DYNAMIC WHEELED LOCOMOTION IN GRANULAR SUBSTRATES

2.1 Preface and Summary

Granular intrusions, such as dynamic impact or wheel locomotion, are complex multiphase phenomena where the grains exhibit solid-like and fluid-like characteristics together with an ejected gas-like phase. Despite decades of modeling efforts, a unified description of the physics in such intrusions is as yet unknown. Here, we show that a continuum model based on the simple notions of frictional flow and tension-free separation describes complex granular intrusions near free surfaces. This model captures dynamics in a variety of experiments including wheel locomotion, plate intrusions, and running legged robots. The model reveals that one static and two dynamic effects primarily give rise to intrusion forces in such scenarios. We merge these effects into a further reduced-order technique called Dynamic Resistive Force Theory (DRFT) for rapid modeling of granular locomotion of arbitrarily shaped intruders. The continuum-motivated strategy we propose for identifying physical mechanisms and corresponding reduced-order relations has potential use for a variety of other materials.

2.2 Introduction

Intrusions into GM can create complex flow and force responses, where the media can exhibit both solid-like and fluid-like characteristics. GM deforms elastically under stress like a solid, but begins to flow like a fluid once a friction-based yield criterion is met. Large variations in the GM's stress, momentum, and volume fraction in different regions often result in complicated system dynamics exhibiting multiphase characteristics [68, 69].

The majority of this chapter's contents are adapted from a co-first authored paper published 2021 in *Science Advances* [65], by Shashank Agarwal*, Andras Karsai*, Daniel I. Goldman, and Ken Kamrin.

The flow complexity also makes interpreting resistive forces non-trivial if the intruder re-interacts with the deformed region [70, 71], as the GM now has a new inhomogeneous state near the surface. The coupled system of intruder and media becomes challenging to model, as the media's inhomogeneous flow and multiphase nature often restricts modeling to discrete particle methods that track the individual grains, unlike fluids that can be solved with the Navier-Stokes equations.

Figure 2.1: **Examples of Locomotion on Granular Surfaces at Various Speeds** (A) Wheel of the Curiosity Mars rover (Diameter ~ 50 cm) [72] (B) A running human [73], (C) RHex C-legged robot (C-leg limb length ~ 18 cm) [74], and *(D)* A dirt bike racing through loose terrain (Diameter ~ 50 cm) [75]. [Photo credits: (A) MAHLI Imager on *Curiosity*, NASA; (B) A. Singh, Pexels; (C) G. C. Haynes, A. M. Johnson, and D. E. Koditschek, University of Pennsylvania; (D) Daniel, Pexels].

A common granular intrusion scenario involves a rigid or flexible solid penetrating into GM and using the resistive force to propel itself into a state of locomotion (see Figure 2.1). If a body slowly intrudes into GM, granular stress arises independent of the intrusion rate, and the resistive force on the intruding body remains in the quasistatic limit [56, 76, 77]. However, various intrusion scenarios can arise which deform the media rapidly enough

that the net force response, and hence the locomotive behavior, is affected. Examples of such intrusions include ballistics, meteor impacts, rapid locomotion, and many industrial processes [78, 79, 80, 81, 82].

Rigid wheel locomotion is an exemplar of a system that combines these effects, exhibiting multiphase granular behavior, complex grain-surface interactions, and reinteraction with deformed media. Rigid wheels like those found in planetary rovers [66] continuously shear and sometimes rapidly deform the local GM [29] to locomote in loosely consolidated terrain. These intrusions, particularly in high-angular-velocity cases, cause the substrate material to behavior to deviate substantially from its quasi-static response, driven by potentially nontrivial surface interactions with the wheel. Thus, we first focus on rigid wheel locomotion as a diagnostic scenario of complex intrusion, which includes a wide array of nontrivial effects.

Wheeled locomotion can be an energy-efficient means of traversing ground, but when applied to soft granular terrain, excessive wheel slippage and sinkage due to incorrect wheel actuations can entrap vehicles. We examine the scenarios that occur in dry granular media with a rapidly turning wheel using our lab's "robophysics" principles of systematic, accurate, and repeatable experiments. To capture the phenomena that occur, we use both models of RFT and granular plasticity which emulate the locomotions we perform in experiment. The similarities and differences between experimental and model outputs give insight what physics are being captured by each model, and also what emergent physical effects occur.

2.3 Constructing a Dynamic Wheeled Locomotion Testbed

To perform systematic experiments of free-wheel locomotion, we built a automated "terramechanics testbed". A powerful gearmotor is mounted in a carriage (Figure 2.2), which moves freely along vertical and horizontal linear bearings. We control the effective vertical loading of the wheels through a combination of weights and pulleys. The system runs trials in a fluidizing bed of Poppy Seeds (PS) (a dry noncohesive GM) across a bed length of 1

m, allowing for controlled resets of terrain via air fluidization of the GM in the bed.

In constructing this testbed, our objective was to create a system that could consistently reset both its position in space and the terrain in which it locomotes. For resetting the carriage's position, a combination of an externally mounted electric hoist (Figure 2.3A and Figure 2.5A) and a lifting assembly made from a Firgelli linear actuator (Figure 2.2) allowed control of the wheel carriage's horizontal and vertical positioning, respectively. During experimental trials, both of these systems were 'slack' to allow the wheel carriage to be in a freely kinematic state, as detailed later. For controlling the locomotion terrain, the PS we used were fluidized from the bed's bottom via a ducting system blowing air through a porous base of material. This repeatably reset the GM to a loosely-packed state of volume fraction $\phi \approx 0.58$ after each experimental trial. We now go into detail of the construction and operation of the automated testbed.

2.3.1 Construction Details of the Wheel Carriage

The wheel carriage's main base of support are two large aluminium plates, each of which has a number of holes waterjet in them for mounting various parts. We will refer to these as the top plate and bottom plate (Figure 2.2). These plates are linked together by a set of four igus® R pillow block FJUM-02 linear bearings hugging a pair of vertical shafts. These rails constrain the relative position of the two plates while allowing the bottom plate to freely move up and down, providing kinematic freedom in the vertical direction as long as the bearings do not reach their end of travel. At its lowest point, the bottom plate rests on a pair of shaft collars attached to each shaft's end. The other end of each vertical rail is rigidly fastened to the top plate by feeding the shafts through holes in the top plate, then sandwiching the top plate between shaft collars and tightening down. The screws and nuts fastening the vertical shaft bearings to the bottom plate are deliberately left as loose as possible, tightened just enough to pin the bearings through the holes in the bottom plate. This is done to take advantage of the double rail system's self-aligning properties

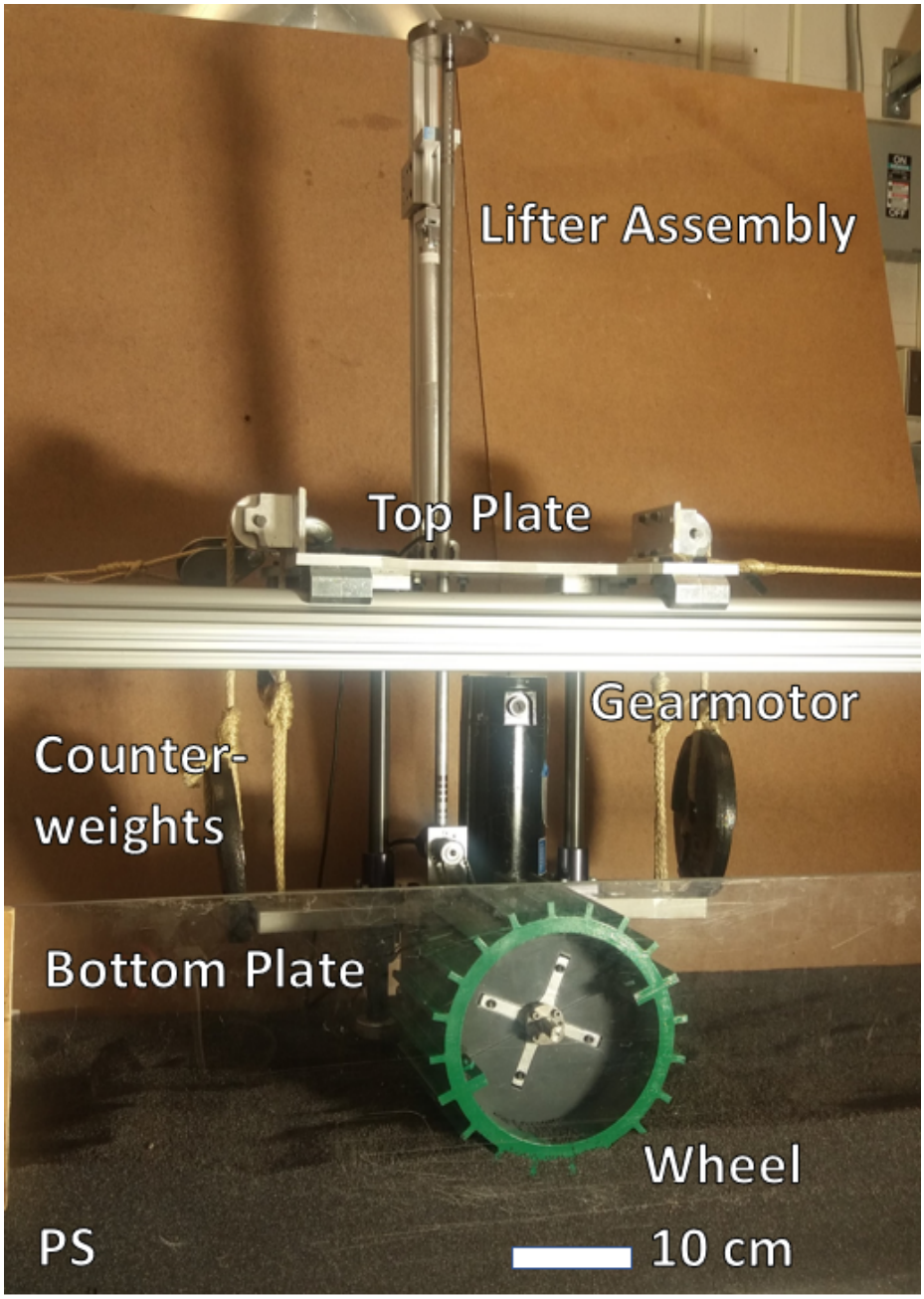

Figure 2.2: **Photo of the Wheel Testbed Apparatus** (A) Photo of the completed wheel carriage assembly, with a 20 cm diameter grousered wheel mounted and hugging the front wall.

by intentionally allowing some play in the bearing's movement. We found that tightening the bearings fully would tend to seize up any vertical motion once external torques were applied to the carriage. This 'looseness to allow self alignment' under torque was a key element in achieving proper carriage kinematics.

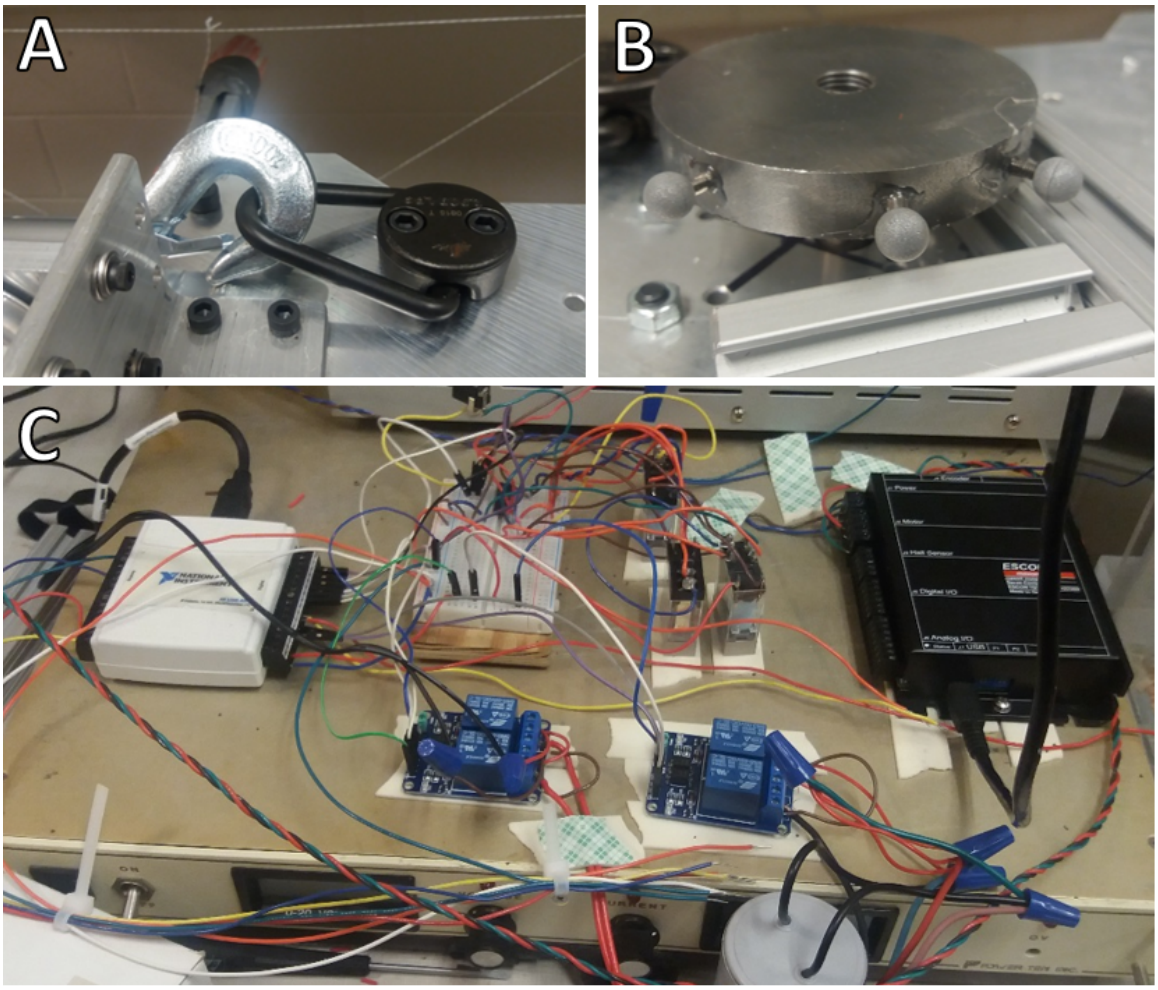

Figure 2.3: **Hoist, Lifter, and Electric Subsystems of the Wheel Testbed** (A) Close-up of the top plate's hoist ring and hook. An externally mounted hoist dragged the carriage back to a set starting position after each trial. (B) Close-up of the top plate of the lifter assembly. Reflective markers embedded in the top plate define the X-Y position of the carriage via Optitrack. (C) Photo of the system control wiring. An NI USB-6009 DAQ controls the system logic and drives an ESCON Maxon Motor 70/10 Motor controller, as well as mechanical relays controlling the hoist and lifter assembly.

The bottom plate houses the primary driver of our experiments: a permanent magnet DC gearmotor (LEESON Model CM34D25NZ11C) capable of providing up to 70 Rotations Per Minute (RPM) at 14.1 N*m. We mounted this motor rigidly to the bottom plate

by feeding it through a pre-cut square hole (Figure 2.5C) and attaching to another plate which was bolted perpendicular to the bottom plate, which then had the appropriate mounting holes to fix the gearmotor's base via screws. This resulted in the gearmotor standing vertically in the carriage with its output shaft pointing outwards (towards the viewer in Figure 2.2). Two additional plates were bolted to either side of the bottom plate, each of which serves as a connection point for the vertical counterweight rope and pulley system. Rope is looped through these smaller plates and threaded through a pair of pulleys mounted to the top plate (Figure 2.4), then terminate with counterweights of various weights hanging from them. This serves as a controlled 'gravity offload', effectively reducing the weight of the bottom plate and the wheel pressure exerted on the GM.

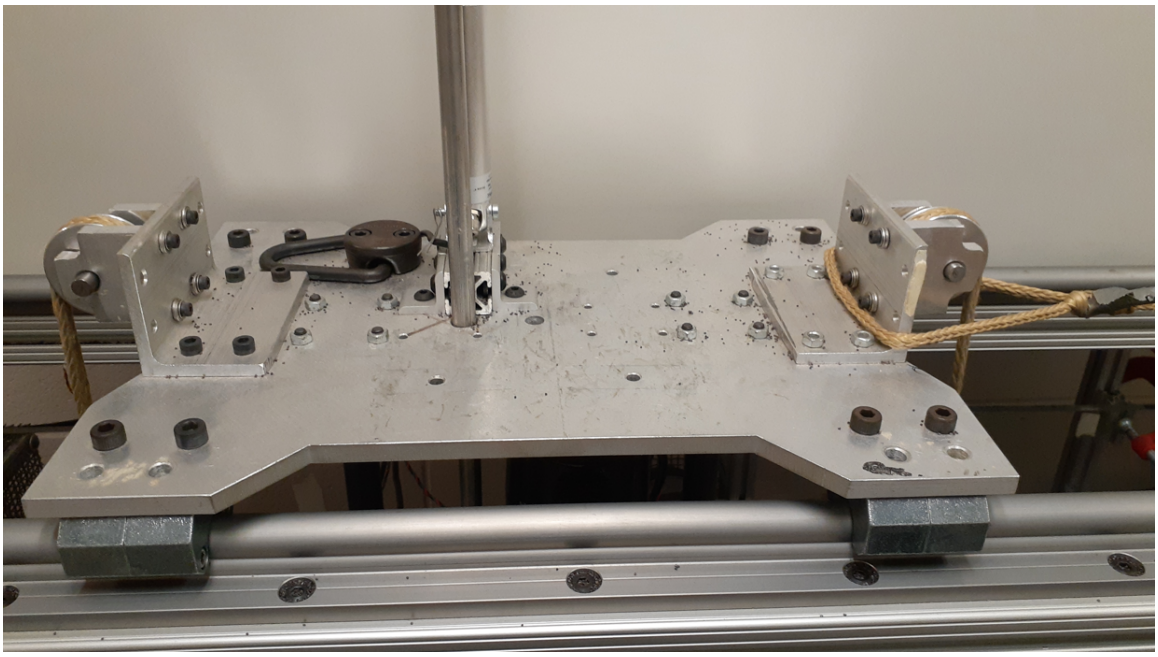

Figure 2.4: **Top Plate Carriage of the Wheel Testbed Apparatus** Top plate of the wheel testbed A water-jetted aluminum sheet serves as the base mounting points for an igus® linear motion system, counterweight pulley system, and the hoist ring.

Based on consultations and conversations with collaborators that built a similar setup [47], we used a 1/4" inch set screw solid shaft coupler to connect the gearmotor's output shaft to another shaft which used a crossbar mounting piece to attach to our tested wheel. A shaft tightening bushing held the crossbar in place, which interlocked into recesses in the

3D printed wheels. There was unfortunately no encoder built into our chosen gearmotor, so we affixed/hacked on a 600 Pulses Per Rotation (PPR) optical rotary encoder to the solid shaft coupler via a timing belt and pulley system (Figure 2.5B). By counting pulses with a DAQ (detailed later) and knowing the timing belt/pulley ratios, we could accurately extract out the resultant ω (RPM) from our open loop control commands to the gearmotor.

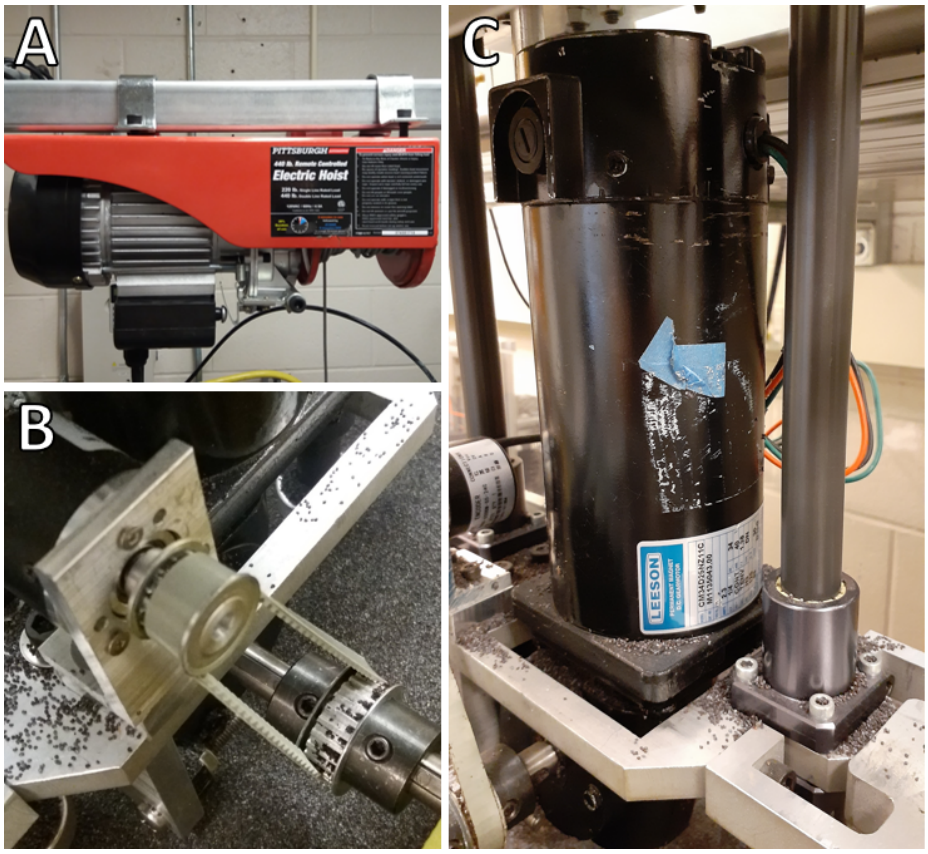

Figure 2.5: **Additional Subsystems of the Wheel Testbed Apparatus** (A) A Pittsburgh Automotive 440 lb. electric hoist mounted above the bed dragged the wheel carriage back to the starting position after each trial. (B) A 600 PPR optical rotary encoder coupled to the main shaft with a timing belt recorded the RPM for each runs. (C) Close-up of the lower plate holding the gearmotor. Four igus® flanged plastic bearings mounted to a lower plate support the motor and allow free vertical movement.

We chose to test wheels with overall simple, smooth geometries for ease of interpretation in theory and modeling, but we also added small protrusions known as "grousers" to the geometry to ensure the wheel fully engages and shears the GM. Otherwise, we found that smooth printed wheels would only slip in the PS without locomoting, as their low friction could not shear sufficient volumes of GM to push the wheel carriage forward.

Examining the top of the carriage (Figure 2.4), the top plate acts as the main load-bearing structural element for our system. The top plate is bolted to a set of four igus® WJRM-21 hybrid rolling/sliding bearings, which ride on a pair of parallel igus® drylin W rails. These rails are screwed into structural T-slot aluminum framing mounted to the bed containing the GM. The screws fastening the pair of WJRM-21 pillow blocks to our top plate on the side nearest the driving wheel were set to be tightened as much as possible. Conversely, the screws were left relatively loose on the side farthest from the wheel. The corresponding aluminum framing rails farthest from the wheel were also left loosened. We found that this was essential for proper free kinematics of the dual rail system, as allowing play in one side of the dual bearing system would allow for the bearings to self-correct any misalignments without seizing up the carriage.

Mounted on either side of the top plates are the pulleys which couple a portion of the bottom plate's vertical loading to the top drylin W rails. The top plate also houses a hoist ring (Figure 2.3A) for an external electric hoist (Pittsburgh Automotive, Figure 2.5A) that pulls the wheel carriage back to its original position after each trial. The WJRM-21 hybrid rolling/sliding bearings supply a low effective friction to the horizontal motion of the system ($\mu \approx 0.05$), but we nevertheless want a horizontal net force balance of zero for ease of interpretation. This equates to an effective 0 Newton "drawbar force" in the terramechanics vernacular. To achieve this, we tie a horizontal assist weight, consisting of a cloth bag filled with steel BBs, to the top plate and drape it over a pulley on the end of the bed. This weight is set to have a mass equal to $\mu m_{carriage}$. The pulley allows this assist weight to pull the top plate in the direction of travel and offset any frictional forces created by the rails during trials.

Finally, the top plate features a 'lifter assembly' for lifting the wheel out of the GM after each trial. This is essential for ensuring a repeatable free surface of the GM after each fluidization, as any intruded bodies in the bed will create heterogeneity in the GM both during and after fluidization. Also, having the sunken wheel being dragged back by the

hoist was a violent process and would damage the bed and the more fragile elements of the carriage. To build the lifter assembly, we first screw a very long steel shaft (approx. 84 cm) with died threads on either end into a corresponding tapped hole in the bottom plate. This rod goes through a corresponding aligned through hole in the top plate without touching the sides, ensuring the bottom plate remains free to move vertically in any direction during a locomotion trial. Whenever the lifter is not engaged, the bottom plate is still vertically 'free' so we can capture the free-running kinematics.

We next mount a small linear actuator (Firgelli Automations FA-B-110-12V-4"), along with an adjacent vertical structural framing rail, to the top plate. The linear actuator is linearized to move purely vertically by bolting its moving end to a plastic sliding bearing which encloses the vertical framing rail. We screwed on a round steel disk with a tapped hole onto the top of the long shaft screwed into the bottom plate (Figure 2.3B). A fork-like aluminum appendage is attached to the top of the plastic sliding bearing, which can only contact the steel disk during lifting when the Firgelli actuator was extended sufficiently, but otherwise can not contact the long shaft. When the Firgelli actuator extends, it pushes upward on the topmost steel disk, pulling the bottom plate and wheel upward. This action completely offloads the bottom plate's weight onto the top plate and its rail bearings (from the reaction force of the lifter assembly) such that the entire weight of the wheel carriage rests on the top plate, which can be safely dragged back to its starting position.

2.3.2 Operating and Tracking the Wheel Carriage

To show how the testbed operates, we now describe the electronics setup needed to run the wheel carriage. For successful automated locomotion tests, a series of events has to occur: the wheel must start from rest and traverse the length of our bed at the desired rotation rate without crashing into the bed's far wall, the GM must be fluidized to reset its state after each trial, and then the wheel carriage must be set down at its starting point on the now settled GM. To execute these experiments, we use an NI USB-6009 DAQ to send timed

digital output control signals to a bank of relays (Figure 2.3C, Songle SRD-05VDC-SL-C Electromechanical Relays), which are wired in an H-bridge configuration and switch 12V DC to control the extension/retraction of the Firgelli linear actuator in the lifter assembly. Another pair of relays in the same bank switch 12V DC to a pair of more powerful relays (Songle SLA-12VDC-SL-C Electromechanical Relays) which then switch a 120V AC circuit wired to replicate the directional switch of the external hoist, allowing it to spool wire in to pull the carriage back to its initial position, or out to provide slack during experiments. The DAQ also sends analog voltage outputs as commands to a DC motor controller (an ESCON 70/10 Maxon Motor Controller). This controller sends the proper PID control signals to our main gearmotor, and is powered by a Volteq HY7530EX DC Power Supply. To get feedback on the rotation rates generated by our motor controller, we powered the mounted 600 PPR optical encoder with another DC power supply and connected its two-phase digital output to the DAQ as well. We used National Instruments' LabVIEW software to program our DAQ to step through a sequence of timed output commands to the relays and controller, while also recording rotary encoder pulses during wheel rotation. However, tracking the vertical and horizontal position of the carriage without interfering with its kinematics proved more challenging.

Many existing terramechanics testbeds enforce a "forced-slip condition" in which the wheel carriage's translational motion is set to a constant speed by an external driving element. This is often done by fastening a timing belt/pulley system to the top plate and controlling its horizontal motion via another external motor. By enforcing the desired kinematics, these testbeds test for force response in the terramechanical system via a variety of embedded force and torque sensors. Our experiments examine the opposite case, where we leave the forces unresolved and free as possible, and deduce the physics at play by observing the resultant kinematics. To observe such free-running kinematics, we had to make some creative compromises deviating from standard testbeds' construction. Determining position in space precisely in forced-slip testbeds often uses draw-wire encoders, which

are high-precision rotary encoders with wires extending from them under constant-force spring tension. While robust for their intended purpose, these devices could have affected the kinematics of or caused damage to our setup, especially for fast-running experiments. To track the carriage position in real-time without interference, we had to come up with some method that would not touch our carriage. From a practical perspective, we also encountered this problem: LabVIEW runs our experiments and has to know where the wheel is during each trial. If the wheel did not stop in time (as in some early attempts) via some external command, the carriage would violently crash into the end of the bed. We could stop the carriage with soft foam buffers at the rail terminus or via limit switches that cut wheel power, but our carriage with a mass of 20kg could move up to a meter per second for our fastest trials, still causing violent crashes into the buffer or limit switches. We wanted a more elegant and contactless method for a permanent solution, so we hacked together an optical tracking and streaming pipeline which would both reliably stop the wheel in time, precisely track its position at 120 Hz, and allow automated resets to the same position in space.

To track the wheel carriage's kinematics, we setup an OptiTrack motion capture system to track a trio of infrared reflective markers screwed into the top plate of the lifter assembly (Figure 2.3B). OptiTrack is ubiquitous in our lab and proved immensely useful for this project. We set up four FLEX-13 OptiTrack cameras (Figure 2.8A) such that they could continuously track the trio of points as a rigid body in 3D space, and since the top plate was mechanically coupled to the bottom plate of the carriage, these markers served as the indicator for the carriage's kinematics. The OptiTrack software Motive would solve for the 3D position based on the cameras' infrared feeds, which could be visualized through a position viewer within Motive. However, for seamless automated experiments, we needed a method to communicate this kinematic data back into the LabVIEW code running the experimental timings, electronics, and motor commands.

To accomplish this, we constructed a data streaming pipeline for this experiment using

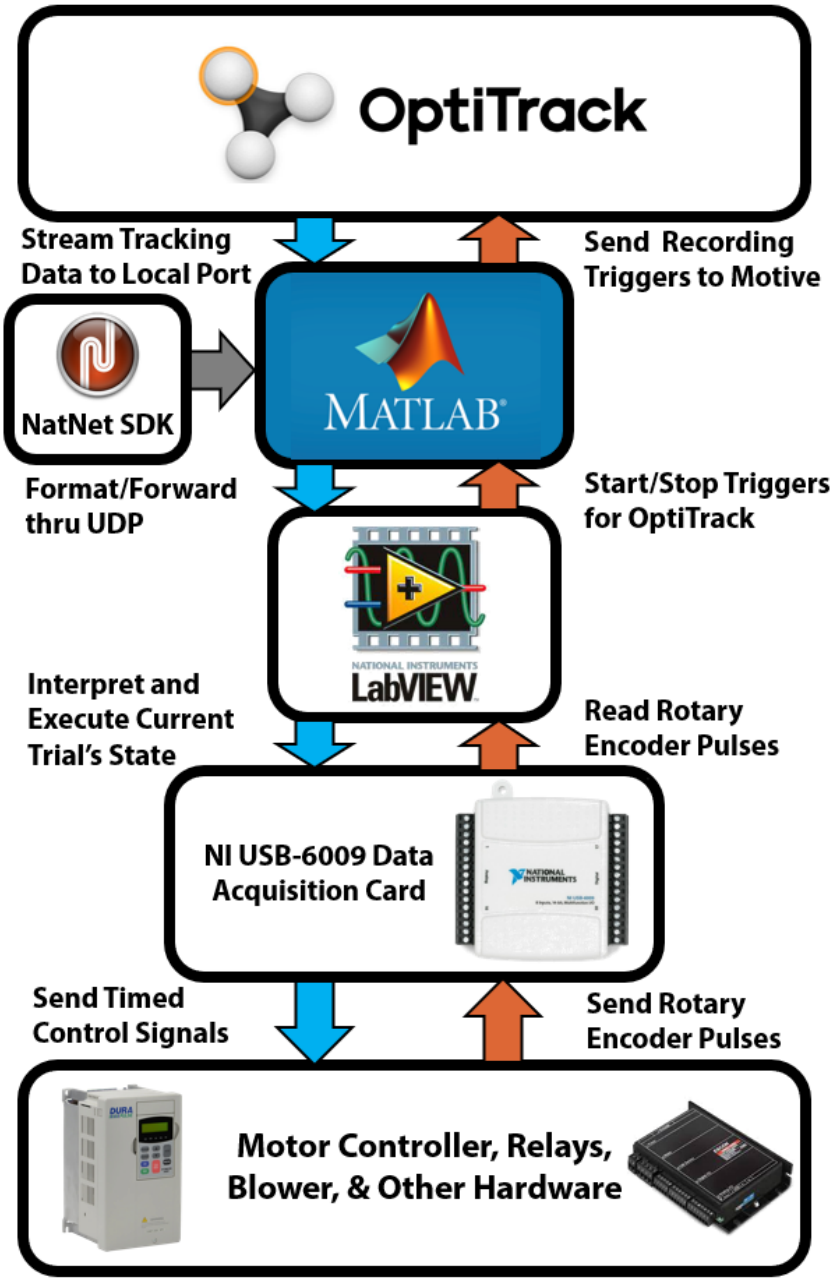

Figure 2.6: **Diagram of Software Stack Running the Automated Wheel Testbed** LabVIEW serves as the central "brain" of the experiment's runtime code, with OptiTrack providing kinematic data of the testbed (Figure 2.8A) as LabVIEW manages and sends control signals to the necessary experimental hardware.

NatNet SDK provided by OptiTrack. With a simple MATLAB script that implemented NatNet commands, we set up a local data stream via a User Datagram Protocol (UDP) channel that received packets from OptiTrack Motive, formatted them, then forwarded those packets to a UDP listener function within our LabVIEW program. LabVIEW could thus receive lagless real-time kinematic data of the wheel carriage at 120 Hz by running Motive and our MATLAB script as parallel programs (see Figure 2.6). This proved immensely valuable for coding our experimental logic, as the kinematic data stream provided immediate position feedback for generating our experimental timings. Specifically:

- The horizontal position at which to stop the wheel before colliding with the testbed during forward locomotion,
- The horizontal position to target by the hoist when resetting the wheel to a starting position,
- The vertical position to target by the lifter assembly where the wheel is fully disengaged from the GM to allow resetting,
- The vertical position at equilibrium when the wheel is set down at rest on the GM, which served as the zero for each measurement of wheel sinkage.

The kinematic data of horizontal velocity and vertical sinkage, combined with the rotational speed feedback provided by the optical rotary encoder connected to the main wheel shaft, would now give us sufficient data to characterize the behavior and trends of rapid wheeled locomotion in GM.

For our automated experiments, we wanted to vary wheel rotation speed ω over many trials at constant horizontal and vertical effect inertias for the wheel carriage (Table 2.1), with the PS terrain being in a loosely packed state for each trial. The measured variables would be the horizontal velocity v_x, and the wheel sinkage z recorded over time. Our LabVIEW code thus ran the following sequence of events, with each trial taking approximately 2 minutes to execute:

Table 2.1: Wheel Dimensions and Material Properties of Locomotion Experiments

Grousered Wheel Properties †

1. Inner Diameter, D	188 mm	2. Wheel width, W	140 mm
3. Grouser height, h_g	12 mm	4. Grouser width, w_g	6 mm
5. Gravity, g	9.8 kg/m^2	6. Number of grousers, N	20
7. Effective horiz. inertia	23.0 kg	8. Effective vert. inertia	6.3 kg

Four-Flap Wheel Properties

1. Inner Diameter, D	50 mm	2. Wheel width, W	1 m
3. Flap length, h_{flap}	70 mm	4. Flap width, w_{flap}	14 mm
5. Gravity, g	9.8 kg/m^2	6. Mass of wheel, m	10.5 kg

Material (PS) Properties

1. Density, ρ_{grain}	1100 kg/m^3
2. Critical packing fraction, ϕ_c	0.58
3. Internal friction, μ (2D, MPM)*	0.56
4. Wheel-PS surface friction (2D, MPM)	0.35
5. RFT scaling coefficient, ξ	0.35

† A constant forward force of 4 N was also applied on the grousered wheel MPM simulations to calibrate them with the friction-compensating mechanism used in the experiments.

* The internal friction (μ) for the PS was obtained by calibrating the sinkage of the grousered wheel between MPM simulations and experiments, at low angular velocity (10 RPM) where system is in the quasistatic state.

1. Initialize the kinematic tracking pipeline.

2. Spool out sufficient cable from the hoist such that the wheel carriage has enough slack to run the length of the bed.

3. With the wheel at rest, send a command to the ESCON motor controller to begin ramping up wheel rotation speed. The ramp rate was set such that the wheel would reach its target ω for the trial within 0.5 sec. We also begin recording kinematic data once this command is sent and send a trigger to OptiTrack to save the capture locally.

4. Once OptiTrack detects that the carriage is at the bed's terminus, set $\omega = 0$ and stop recording kinematic data.

5. Engage the lifter assembly to lift the carriage upwards and disengage the wheel from the GM.

6. Retract hoist cable to pull the wheel carriage horizontally back to its starting position. Also, send a command to blower controller (detailed later) to begin fluidizing the bed to reset the PS to a loosely packed state.

7. Wait 15 seconds until fluidization finished, then turn off the blower, then wait 10 more seconds to allow grains to settle.

8. Lower the lifter assembly completely such that the wheel rests on the PS surface.

9. Save out the recorded kinematic data of v_x, z, and ω into a data file.

With this experimental protocol, we could repeatedly execute many trials collecting kinematic data, all while automatically resetting the terrain and wheel carriage position. By nesting the above sequence into a parent function caller in LabVIEW, I as the experiment operator could simply leave the experiment room while the trials executed. This was in fact preferred, as the terrain's air fluidization was quite loud and human movement could interfere with the motion tracking. We will next briefly describe the method of terrain resets and some additional visualization methods for characterizing grain flow.

2.3.3 Controlling the Consistency of Granular Media

As the wheel rolls across the PS exerting stress and shearing forces, it would deform the terrain in increasingly unpredictable states as ω increases. To reset the GM to a repeatable, loosely packed state, we use an industrial air blower to fluidize the bed for at least 15 seconds after each trial. We connected a 230V three phase power input to an Automation Direct DuraPulse Variable Frequency Drive (VFD) (Model GS3-25P0) and programmed it start/stop upon detecting a trigger voltage from the NI USB-6009 DAQ. The VFD runs a Dayton 5HP High Pressure Blower (Item number 7D771) which blows air through solid

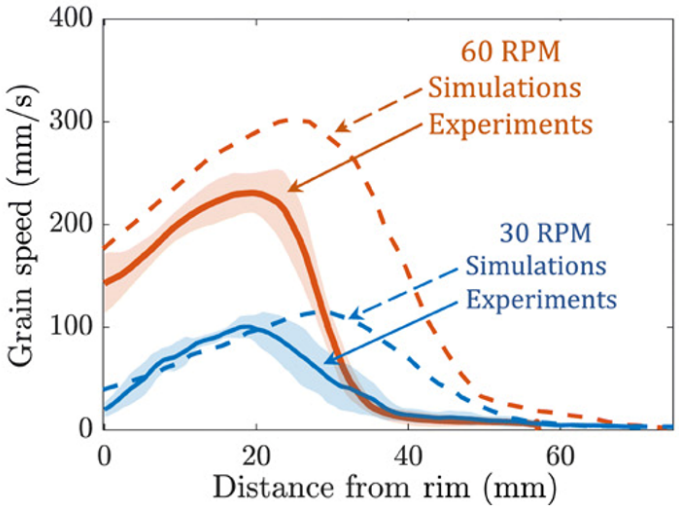

Figure 2.7: **Mean Sheared Grain Speeds During Wheeled Locomotion** Mean grain speeds from continuum simulations and Particle Image Velocimetry (PIV) experiments along the radial direction directly below the center of the wheel. Some wall friction from the frontal plexiglass plate slows the grains in the experiment but not in the continuum solution. Key structural features of the flow under the wheel agree between the experiments and model in Figure 2.9 and Figure 2.7. Continuum simulations courtesy of Shashank Agarwal [65].

ducting into the bottom of our fluidizing bed, previously constructed and used by Chen Li [83]. The bed is filled with PS to a depth of approx. 15 cm, has a length of 205 cm and width of 52 cm, and is retrofitted to allow a single duct input into its bottom chamber. In this bottom chamber, the moving air expands to fill the cavity and passes through a porous membrane with enough remaining velocity to fluidize the PS successfully. The PS act as the representative material for the class of noncohesive granular materials in our study. We specifically choose them due to the ease of running wheel locomotion experiments within them and previous experience using RFT. This fluidization redistributes the grains evenly into a homogeneous medium after each experiment, giving nearly identical terrain for each test [83].

For experimental visualization of the granular flow around the wheels (Figure 2.9), we also performed PIV analysis of the wheel locomotion at different ω values using the MATLAB package PIVLab [84]. We placed the wheel adjacent to the transparent side wall of the PS bed and perform the locomotion trials. Images of the flow field are captured with a high-speed camera (an AOS Technologies S-PRI) mounted on a tripod at a resolution of

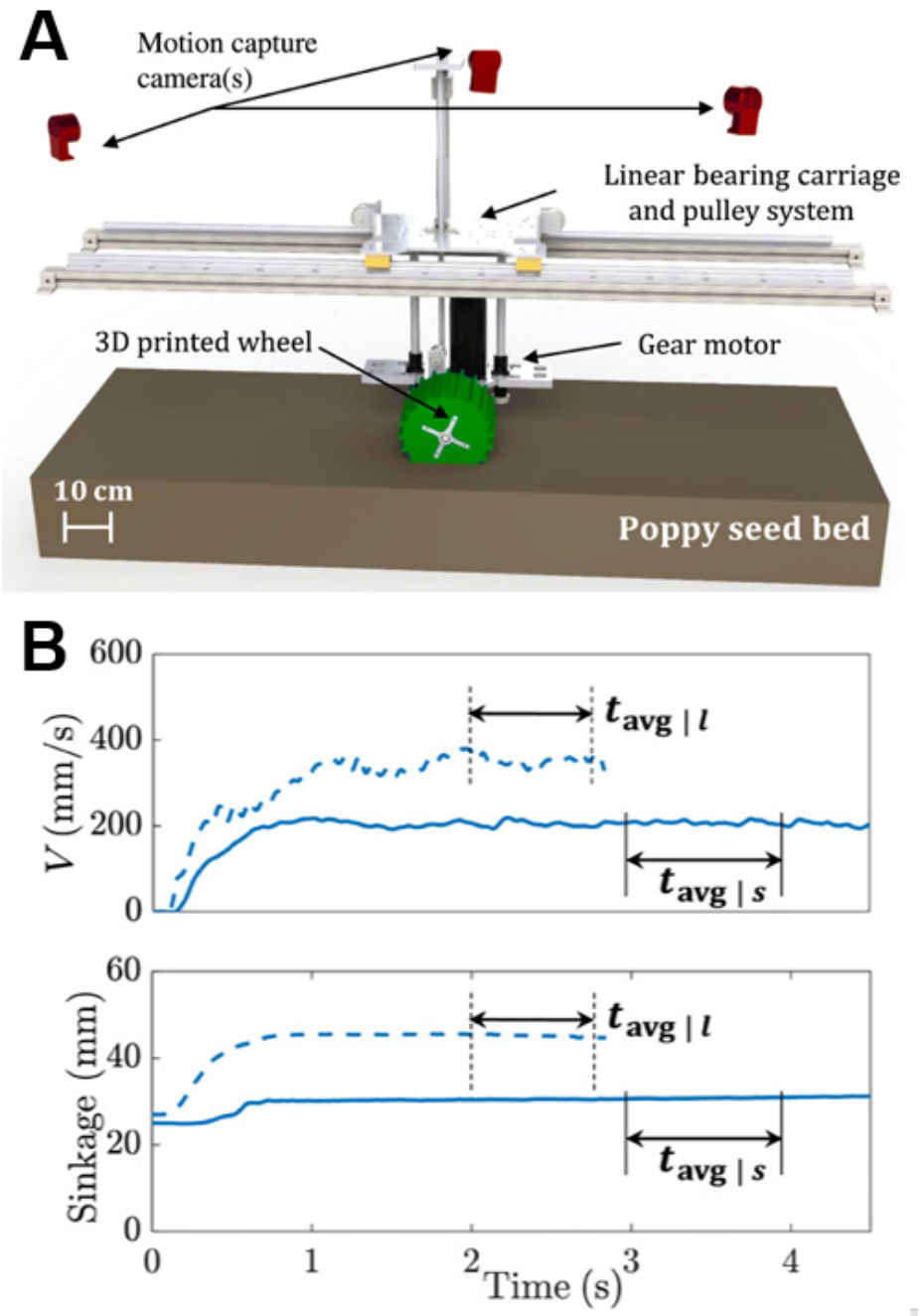

Figure 2.8: **Wheel Testbed Apparatus and Primary Kinematic Data** (A) 3D model of experimental setup. (B) Sample experimental time series data for translation velocity (top) and sinkage (bottom) at low ω (20 RPM, solid lines) and high ω (50 RPM, dotted lines), respectively. $t_{avg}|s$ and $t_{avg}|l$ show the time windows used for averaging low- and high-ω data, respectively.

1280 × 1024 and a frame-rate of 500 frames per second. We expect minor variations in the flow fields due to the friction experienced by the material flowing next to the sidewall.

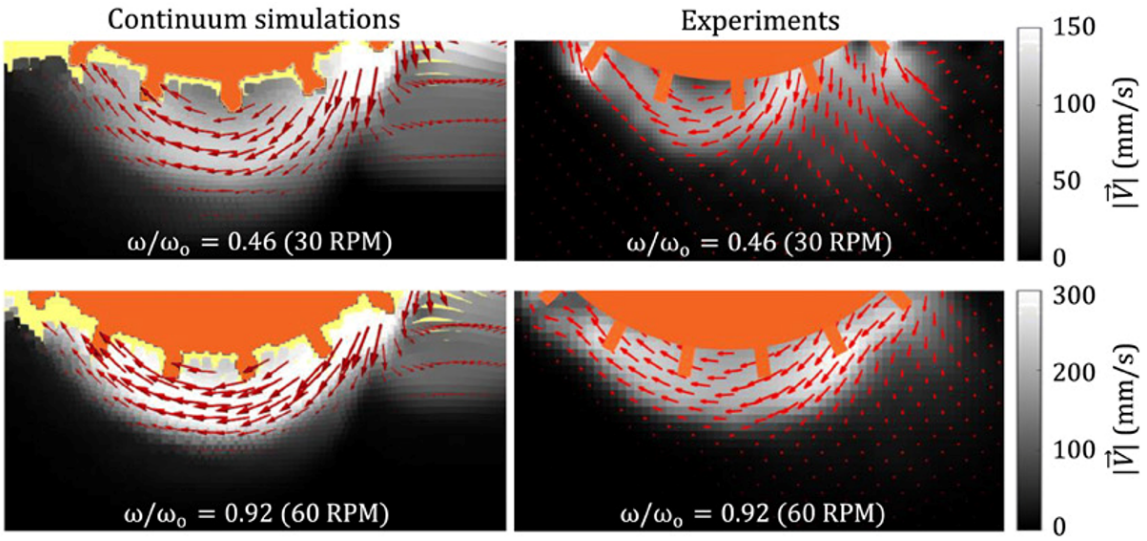

Figure 2.9: **Granular Flow Fields of Wheeled Locomotion** Granular flow field velocities obtained from continuum modeling and experiments via PIV for slow (30 RPM, top) and fast (60 RPM, bottom) wheel locomotion. Data are averaged over an effective rotation of 0.1 rad (for PIV), with the orange regions representing the mean position of the wheel. Continuum simulations courtesy of Shashank Agarwal [65].

Now that we have described the construction and operation details of the testbed, we can discuss the results of our kinematic measuring trials and their interpretation. Figure 2.8A shows a Computer Aided Design (CAD) model of the laboratory setup used for performing wheeled locomotion experiments in this study [65], and Figure 2.8B indicates our data collection methodology. Each run's measured kinematics are not constant in time, as the wheel has to ramp up to its steady state speed, so we use a time-averaging window that targets from 60% to 90% of total time for each completed trial. This extracts the characteristic translation velocity and the sinkage of each trial while the wheel carriage is still far enough from the bed walls, avoiding boundary effects.

Figure 2.10 shows the trends of steady-state translation velocity and sinkage (respectively) with increasing angular velocity for a grousered wheel's free locomotion ($N = 274$ trials). Experiments indicate the emergence of a rate-dependent effect in wheel locomotion. An increase in slipping, accompanied by an increase in the sinkage of the wheels,

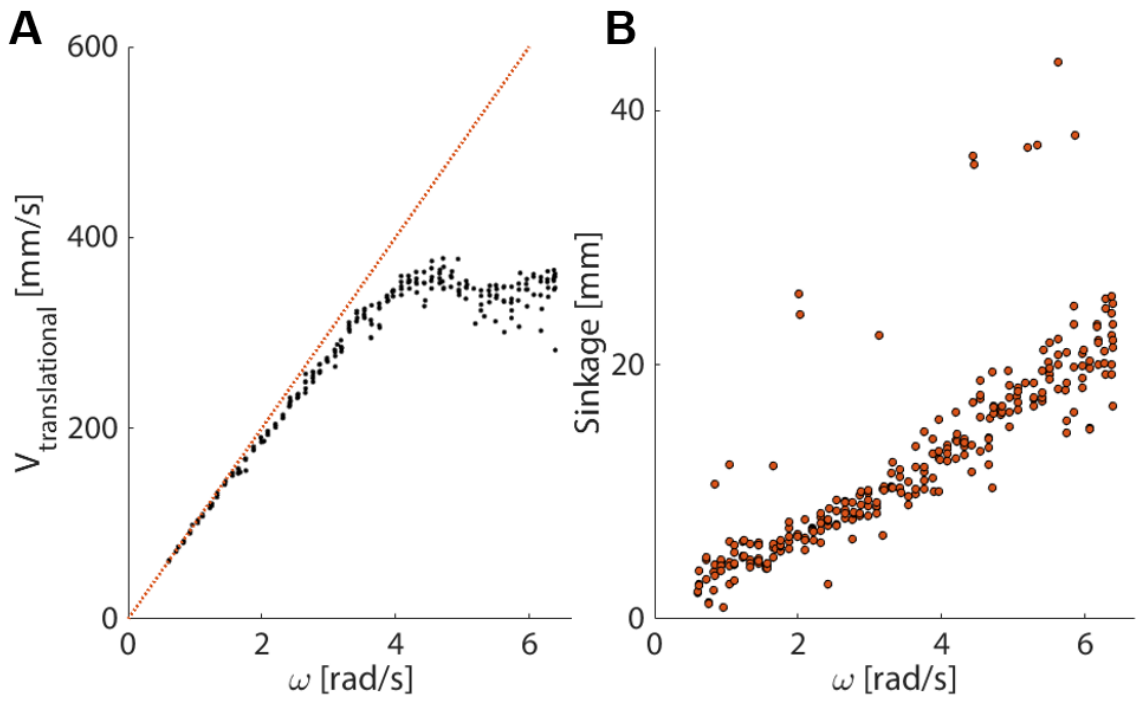

Figure 2.10: **Experimental Data Batch from Wheel Testbed Apparatus** (A) Resultant translation velocity and (B) sinkage from the initial equilibrium position vs. wheel rotation rate ω in wheeled locomotion experiments using the methods & constants outlined in Figure 2.8 and Table 2.1. $N = 274$ trials. The orange dotted line in (A) represents the zero slip line of $v = r\omega$. Outlier sinkage points in (B) are likely experimental errors where the wheel carriage rail had an irregular sticking point during that trial which caused excessive sinkage.

breaks the linear trend in velocity versus ω seen in the quasi-static domain of $\omega < 3$ rad/s (corresponding to $\omega/\omega_0 < 0.46$ in Figure 2.12). This break from linearity is unexpected according to previously established scaling relations [47], so we collaborated with experts in continuum modeling to discover this mechanism.

2.4 Continuum Modeling Analysis for Granular Intrusion

In collaboration with Shashank Agarwal (MIT) and Ken Kamrin (MIT), they used a simple granular continuum model created by Kamrin's group, which had captured intruder dynamics in previous studies in the slow, quasi-static regimes [46, 63]. Poppy seeds (PS), a model GM, are modeled as a granular continuum with a Drucker-Prager (rate-independent friction-based) yield criterion, incompressible plastic shear behavior, and a criterion that

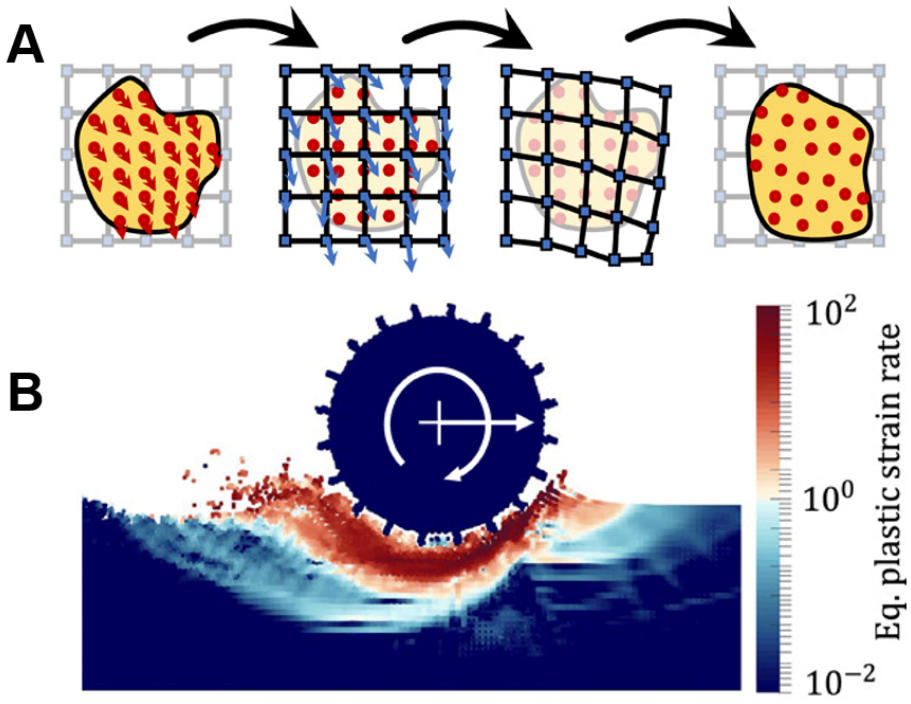

Figure 2.11: **Continuum Simulations via the Material Point Method** (A) Schematic representation of explicit time integration in a MPM step, whereby a background grid assists in integrating the motion on a set of continuum material points. Solid circles (red) are material points (Lagrangian tracers) and squares (blue) are the nodes of the background mesh. (B) A sample continuum simulation using MPM, logarithmically plotting the equivalent plastic strain rate. (Figures courtesy of Shashank Agarwal [65]).

the material separates into a stress-free media when brought below a critical density. This rheology can be defined by two simultaneous constraints shown below, describing the material's separation behavior and shear yield condition:

$$\text{Free separation:} \qquad (\rho - \rho_c)P = 0 \quad \text{and} \quad P \geq 0 \quad \text{and} \quad \rho \leq \rho_c \tag{2.1}$$

$$\text{Frictional yielding:} \qquad \dot{\gamma}(\tau - \mu_s P) = 0 \quad \text{and} \quad \dot{\gamma} \geq 0 \quad \text{and} \quad \tau \leq \mu_s P \tag{2.2}$$

for $i, j = 1, 2, 3$. We define $\sigma'_{ij} = \sigma_{ij} + P\delta_{ij}$ as the deviatoric part of the Cauchy stress tensor, $P = -\sigma_{ii}/3$ as the hydrostatic pressure, $\tau = \sqrt{\sigma'_{ij}\sigma'_{ij}/2}$ as the equivalent shear stress, μ_s as the bulk friction coefficient, and ρ_c as the critical close-packed granular density. The (plastic) flow rate tensor is $D_{ij} = (\partial_i v_j + \partial_j v_i)/2$ and $\dot{\gamma} = \sqrt{2D_{ij}D_{ij}}$ is the equivalent shear rate. When shearing plastically, the stress and flow-rate are presumed to align (e.g.

$\sigma'_{ij}/2\tau = D_{ij}/\dot{\gamma}$). The model evolves the flow by solving the momentum balance equations, $\partial_j \sigma_{ij} + \rho g_i = \rho \dot{v}_i$. Below the yield criterion, the grains act like a linear-elastic solid, so that our model is in fact elastic-plastic in the dense regime. We assume a constant surface friction coefficient describes the interaction of the granular continuum with solid-body surfaces, and use the input material properties in Table 2.1.

Agarwal and Kamrin used the MPM algorithm described in Dunatunga and Kamrin [85, 86] to implement these constitutive equations assuming two-dimensional plane-strain motion. A schematic representation of an explicit time integration MPM step is shown in Figure 2.11A. The material points carry the continuum data and are moved each step with the help of a background grid (more details in Materials and Methods). Figure 2.11B shows a sample wheel locomotion using MPM, plotting the variation of equivalent plastic shear rate in the system.

The trends of steady-state translation velocity and sinkage with varying ω obtained using continuum modeling are plotted in Figure 2.12(A and B). Continuum modeling successfully captures the experimental trends for wheel locomotion. In particular, the model captures the plateau in the normalized v_x vs. ω curve at the correct rotation speed and correctly predicts increased sinkage with rotation rate. To verify robustness of the results, we also applied small changes to the initial state of the experimental and simulated systems, including variations in initial wheel depth, initial wheel velocity, and ramp rate of the wheel, and observed that the steady-state results were insensitive to these variations.

2.4.1 Toward Reduced Order Models

A major benefit in identifying an accurate continuum model for a system is the possibility of using it to extract global-scale simplifications of the system's dynamics that can be used to develop further-reduced models. For example, in previous work on slow quasi-static intrusion, Askari and Kamrin [63] found a connection between frictional yielding and a reduced-order intrusion force model called granular RFT [17]. The success of the

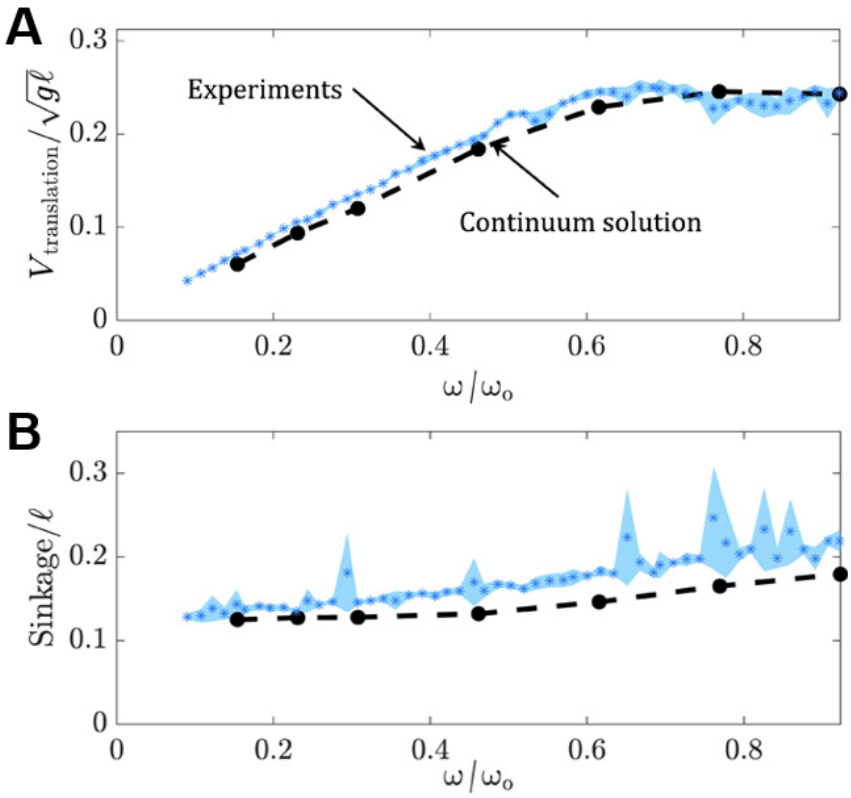

Figure 2.12: **Kinematic Results of Wheel Locomotion Experiments and Continuum Simulations** (A) Translation velocity and (B) sinkage from experiments (blue) compared with continuum modeling solutions (black). The results are nondimensionalized using a characteristic system velocity $(g\ell)^{0.5} = 1440$ mm/s for translation velocity, a characteristic system length $\ell = 212$ mm for sinkage, and a characteristic angular velocity, $\omega_0 = (g/\ell)^{0.5} = 65$ RPM for angular velocity, where g represents acceleration due to gravity and ℓ represents the wheel's outer diameter. Wheel dimensions are provided in Table 2.1. Continuum solutions courtesy of Shashank Agarwal [65].

present continuum model for slow and rapid locomotion in wheels (and the other intrusion scenarios in this study) motivates us to ask whether an RFT-like reduced-order model for complex, rapid intrusions exists and if it might be derivable based on phenomena observed within the continuum model. We begin by first defining the quasi-static form of RFT and evaluating its predictions for wheeled locomotion dynamics.

RFT is an empirical methodology that has been successful in estimating the force response for arbitrarily shaped intruding geometries in the quasi-static limit, permitting direct simulation of locomotion in granular volumes [46, 17, 49]. RFT assumes the stress on a small surface element of an intruder follows a localized formula in which depends only on the motion, location, and orientation of that element [45]. This local formula decouples

the stress response among the surface elements of an intruder, thereby permitting RFT to predict intrusion forces with near real time numerical calculations.

In a coordinate system where z points positive upward with granular free surface at $z = 0$, and x is a chosen horizontal axis perpendicular to z, RFT presumes the force-per-area vector (or traction) $\vec{t}$, on each surface element can be written as $\vec{t} = \vec{\alpha}(\beta, \gamma)H(-z)|z|$, dependent on the element's orientation angle (β), velocity angle (γ), and vertical depth from the free surface $(|z|)$, with H being the Heaviside function. The empirical traction-per-depth vector $\vec{\alpha}(\beta, \gamma) = (\vec{\alpha}x(\beta, \gamma), \vec{\alpha}z(\beta, \gamma))$ is measured with small plate intrusion experiments which vary β and γ. By summing these locally defined tractions, RFT predicts the net resistive force and moment on the entire intruder surface S. For example, RFT gives the following intrusion force formula:

$$\vec{F} = \int_S \vec{\alpha}(\beta, \gamma)H(-z)|z|dA \tag{2.3}$$

Figure 2.13 shows the results of applying quasi-static RFT (solid blue line in Figure 2.13) in modeling grousered wheel locomotion. In implementing the RFT model of locomotion, we also used a "leading edge condition" to ensure that resistive forces experienced by the wheel consist of contributions only from surface elements that move "into" the sand, i.e., surfaces whose outward normal $(\vec{n})$ and velocity $(\vec{v})$ make a positive inner product:

$$\text{For all elements in surface :} \quad \vec{v} \cdot \vec{n} > 0 \tag{2.4}$$

We use the established RFT functions α_x and α_z, for the GM used in our experiments [17]. Figure 2.13B shows that while RFT captures the speed versus ω trends at low ω, at higher ω it does not predict the wheel locomotion kinematics. RFT predicts a linear relation between the angular and translation velocities, which matches the experiments' dynamics at low speeds, but diverges as ω increases. The fact that quasi-static RFT predicts the steady

speed of a round wheel to always be a constant multiple of the wheel spin can be shown as a consequence of the rate independence of the RFT traction relation in Equation 2.3.

2.4.2 Exploiting the Continuum Treatment for Physical Insight

We also obtain a global-level physical understanding of intrusion dynamics by analyzing plasticity solutions, which guide the development of a reduced-order model for intrusion that we call dynamic resistive force theory (DRFT). We show that DRFT accurately models all considered granular intrusion cases. By combining existing literature, continuum modeling, and experimental verification, we identify the relevant physics that go into DRFT and its interpretation as corrections to an existing quasi-static RFT model [46, 17, 49] for slow intrusion. Key effects that generate rate-dependent behaviors are identified, and, once incorporated, DRFT allows rapid calculation of the expected resistive forces in GM.

An important step in developing a general reduced-order model for high-speed granular intrusion scenarios is to identify the key underlying physics. In granular intrusions, rate effects could arise due to a variety of physical causes. Increased vibrations in the media could fluidize the material at high speeds and reduce its strength [87]. Increasing velocities could decrease the friction on the wheel/media interface (per a dynamic friction drop), which, in turn, could decrease the traction on the wheels. Rapid flows may also have substantial micro-inertia, which makes the rheology rate dependent by causing the stress ratio $\mu = \tau/P$ to depend on shear rate through the "inertial number" I, where $I = \dot{\gamma}\sqrt{d^2\rho_s/P}$, where $\dot{\gamma}$ is the shear rate, d the mean grain diameter, ρ_s the solid particle density, and P the local pressure [88]. Moreover, conventional macro-inertia (i.e., the $\rho\dot{v}_i$ term in the momentum balance equation) adds inertial body forces that could alter the flow of the media and its resistance against the intruder.

Predicting the dominating rate effect(s) is difficult using experiments alone. In this regard, our continuum modeling approach greatly aids in eliminating candidates from the possible rate effects above. The key is to recall that our model implements a rate-insensitive

frictional surface interaction with no dynamic friction drop on the wheel-sand interface and a rate-insensitive constitutive model with no dependence on the inertial number nor any accounting of material thermalization or fluidization. The model does, however, include macro-inertia in the momentum balance equations. The fact that the continuum model is successful in capturing the wheel dynamics along with many other granular intrusion scenarios (discussed later) indicates that the observed rate effects should be reconcilable solely from macro-inertia ($\rho \dot{v}_i$). At the same time, the global consequences of local macro-inertial forces may be subtle and depend on the particular system and its dynamics.

On the basis of this insight, along with analysis of the continuum solutions to wheel locomotion and other granular intrusion scenarios from the literature, we now propose and test a more general RFT that encompasses the domain of slow to rapid intrusions in GM, which we refer to as DRFT.

2.5 Dynamic Resistive Force Theory

DRFT modifies the quasi-static RFT in two ways to account for macro-inertial effects. First, we add a momentum flux contribution, which we term the dynamic inertial correction. This term is required for the transfer of momentum to the granular material surrounding the intruder. This term is also in accord with many previous studies on high-speed granular intrusions [89, 90, 91, 92, 93, 48, 94], and has the form of an additional rate-dependent force proportional to velocity squared.

The second modification, which turns out to be critical for more complex intrusions, describes the way in which increased bulk inertia can change the free-surface geometry. A change to the free-surface geometry then feeds back into the resultant resistive forces through the depth dependence of RFT. We'll refer to this modification as the dynamic structural correction. Together, DRFT imposes the following formula for the traction on a

surface element:

$$\vec{t} = \vec{\alpha}(\beta, \gamma) H(-\tilde{z}) |\tilde{z}| - \vec{n} \lambda \rho v_n^2 \tag{2.5}$$

where $|\tilde{z}|$ indicates the effective depth of the surface element. That is, $\tilde{z} = z + \delta h$ where δh represents the height decrease of the free surface in the zone affecting the traction at (x, z). Recall $\vec{n}$ represents the outward normal to the surface element (and $-\vec{n}$ the inward), and we define v_n as the normal component of the surface velocity. To use DRFT properly, one must determine the appropriate δh for each surface element of the intruder as a function of the intruder motion and an appropriate λ, an $O(1)$ scalar fitting constant. Similar to RFT, DRFT asserts a localized formula for the calculation of stresses on intruder subsurfaces and thus allows for near real-time modeling of intruder motion.

2.5.1 The Dynamic Inertial Correction

We discuss the two dynamic corrections included in DRFT, beginning with the dynamic inertial correction. Analysis of the momentum balance equations under certain simplifying circumstances (see section S1) allows one to deduce that the transition from a quasistatic flow to a faster flow comes with a resistive force increases as $\rho A v_n^2$, similar to dynamic pressure in a fluid, where A is the intruder area. Physically, this term represents the reaction force that comes from transferring momentum to the GM.

A number of previous studies [89, 90, 91, 92, 93, 48, 94] have modeled the rate dependence of intrusion force similarly, by adding a term proportional to normal speed squared to a depth-dependent "static" term. Examination of experimental data in [91, 71] agrees with a rate-dependent force addition of the form $\lambda \rho A v_n^2$ in simple vertical and horizontal intrusions, where λ is a $O(1)$ scalar fitting constant that accounts for certain approximations in the analysis.

This velocity-squared additive pressure contribution for macro-inertial forces is valid

due to the momentum balance equations for a continuum. In a reference frame co-moving with an intruder, the steady-state momentum balance (from the Cauchy momentum equation) is:

$$0 = \rho g_i + \sum_{j=1}^{3} \frac{\partial}{\partial x_j} \left(\sigma_{ij} \vec{x} - \rho v_i(\vec{x}) v_j(\vec{x}) \right) \tag{2.6}$$

Consider a reference case in the quasistatic limit with a slow intruder velocity V_i^R in the lab frame. Let $\sigma_{ij}^R(\vec{x})$ and $v_i^R(\vec{x})$ represent the corresponding quasistatic stress and flow solutions in the intruder frame. Thus,

$$0 = \rho g_i + \sum_{j=1}^{3} \frac{\partial}{\partial x_j} \sigma_{ij}^R(\vec{x}) \tag{2.7}$$

Let us suppose the velocity of the intruder is scaled up to a non-negligible value $V_i = CV_i^R$ beyond the quasistatic limit. Consider the candidate intruder frame flow field $v_i(\vec{x}) = Cv_i^R(\vec{x})$ and stress field $\sigma_{ij}(\vec{x}) = \sigma_{ij}^R(\vec{x}) + \rho(v_i(\vec{x})v_j(\vec{x}) - V_iV_j)$. The proposed flow field assumes similarity of flow between slow and high speed cases, and the stress field reduces to the quasistatic solution when C is small. If we suppose the far-field flow vanishes in the lab frame, these candidate fields comprise a valid solution by satisfying Equation (2.6) while preserving the far-field stress condition from σ_{ij}^R. We assume kinematic constraints such as incompressibility transfer between the quasistatic and high-speed solutions. In the intruder frame, the velocity field vanishes at the leading intruder-grain interface, so the stress at a point $\vec{x}^I$ on the intruder interface gives $\sigma_{ij}(\vec{x}^I) = \sigma_{ij}^R(\vec{x}^I) - \rho V_iV_j$. The presence of macro-inertia provides an additional pressure at the intruder-grain interface that scales as ρV^2. This solution is approximate, as even if $[\sigma_{ij}^R, v_i^R]$ satisfies the frictional-plastic constitutive relation, the proposed solution $[\sigma_{ij}, v_i]$ may not.

It is natural to ask whether the addition of a velocity-squared term to the quasi-static RFT relation is enough alone to explain the rate dependence observed in general intrusion scenarios, including wheeled locomotion. We suppose the surface traction is modeled to

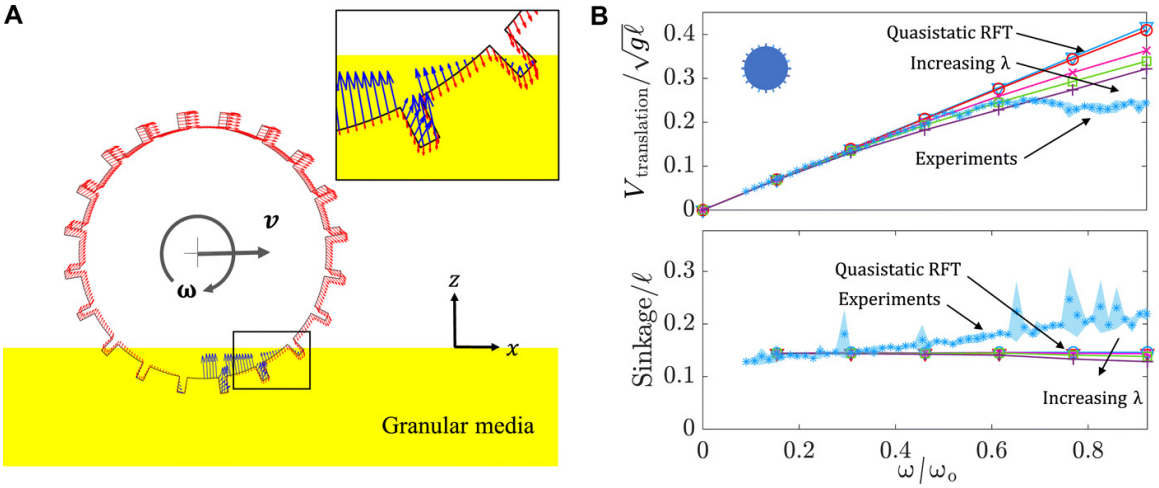

Figure 2.13: **Wheel Locomotion Experiments vs. RFT Simulations** (A) Snapshot of a quasistatic RFT simulation, used for studying grousered wheel locomotion. Direction and magnitude (normalized) of the velocity and resistive stress are indicated by red and blue arrows, respectively, along surface elements of the wheel boundary. (B) Translational velocity (top) and sinkage (bottom) of the wheel, experimental mean and 1σ SD (light blue data) and RFT results with local $\lambda\rho v^2$ modification (solid lines) as in Equation 2.8. The results in (B) are nondimensionalized in the same manner as Figure 3.6. The direction of increasing λ is indicated (λ = 0, 1, 25, 50, and 100). Red solid lines with $\lambda = 0$ [in (B)] correspond to quasistatic RFT results.

obey the relation in Equation 2.8 below and use this relation to re-evaluate the grousered wheeled locomotion problem

$$\vec{t} = \vec{\alpha}(\beta, \gamma)H(-z)|z| - \vec{n}\lambda\rho v_n^2 \tag{2.8}$$

Figure 2.13 shows the results for various values of λ. The case of $\lambda = 0$ represents the previously discussed quasi-static RFT in these graphs. The introduction of the inertial force term $(\lambda > 0)$ adds a new force contribution having net force components upward and opposite to the horizontal direction of wheel translation. This upward force results in a decrease in wheel sinkage, opposite to the experimental observation. The magnitude of these extra forces is very small. The prefactor λ was varied from 1 to 100 in an attempt to match the experiments, but this has little effect on the outcome and the trends for both velocity and sinkage cannot be matched (Figure 2.13B). It is clear that the dynamic inertial correction alone is not sufficient to describe this set of tests.

2.5.2 The Dynamic Structural Correction

To understand the rationale behind the dynamic structural correction in DRFT, we start by considering the spatial variation of plastic strain rate magnitudes from continuum modeling simulations for low and high ω cases shown in Figure 2.14B. The plots make it possible to visualize how different portions of the wheel derive their resistive forces from different zones of the GM. While the strain rate profiles change as angular velocities increase, the basic patterns of shearing remain similar. The sheared material reaches the free surface of the granular volume in two zones. Approximately half of the flow originating from the leading edge of the wheel reaches the free surface on the trailing rear face of the wheel. The remaining flow lines extend to the free surface on the leading front face of the wheel. The height of the free surface on the rear side of the wheel decreases with increasing ω. Qualitatively, as ω grows, the wheel expels material on the rear side. The reduction in rear free-surface height suggests a reduction in the pressure head and consequent weakening of the material in the rear shear zone. This is the key observation which motivates the form of the dynamic structural correction.

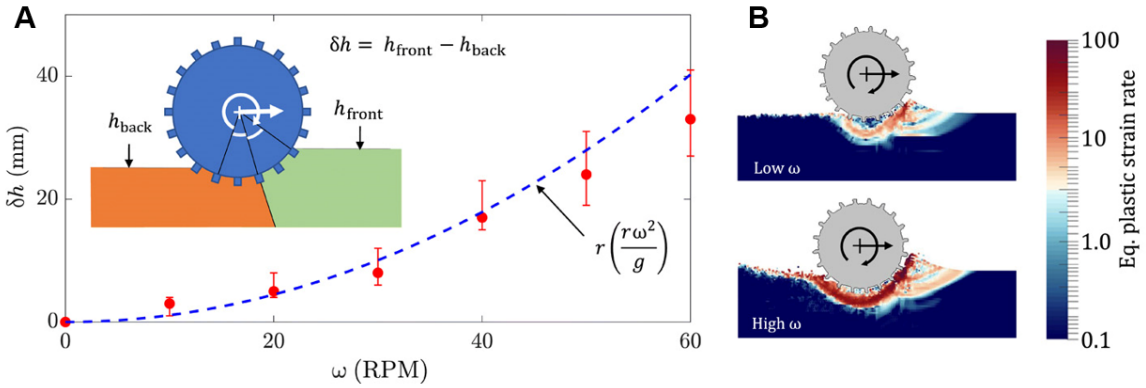

Figure 2.14: **Mechanism of Dynamic RFT Free-surface Height Reduction** (A) Presumed zones of influence and effective free-surface modification for constructing the dynamic structural correction. δh represents the gap between the effective front and back free-surface positions. MPM simulation data (red circles) and an empirical fit (blue dotted line) for δh. (B) Equivalent plastic strain rate magnitude obtained using MPM continuum modeling for slow-speed (30 RPM) and high-speed (90 RPM) wheel locomotion. Continuum and DRFT simulations courtesy of Shashank Agarwal [65].

Figure 2.14A shows the free-surface height reduction, δh, as measured from continuum

model simulations by identifying the lowest point making rear contact with the wheel for which hydrostatic pressure $\rightarrow 0$. We observed in continuum simulations that the more rapidly the wheel spins, the deeper this point descends. Given the paucity of parameters in the continuum model, dimensional analysis is useful. For a given substrate material, it suggests the form:

$$\delta h = r \cdot \psi \left(\frac{r\omega^2}{g} \right) \tag{2.9}$$

for some function ψ. Unexpectedly, we found that ψ is well approximated by the identity function. The fit of $\delta h = r \cdot (r\omega^2/g)$ and the continuum modeling results in Figure 2.14A agree with each other. Combined with the experimental observations from Figure 2.9 and Figure 2.7 and our understanding of the continuum model's flow patterns, the form of the effective free surface is approximated using a simple partition as shown in the inset of Figure 2.14A, with the rear zone of the wheel set to have a constant free-surface height reduction h_{back} reduced from the initial free-surface height (height of the undisturbed GM) by a magnitude of:

$$\delta h = r \left(\frac{r\omega^2}{g} \right) \tag{2.10}$$

To define the dividing angle delineating the front- and rear-affected zones of flow, we chose to equally divide the driven wheel's contact zone with the GM. This choice of division is motivated by both its simplicity, and by observing a similar division of contact zones for representing traction on wheels by Hambleton and Drescher [95]. This model thus modifies the effective free-surface heights only for the surface elements near the rear of the contacting wheel surface.

By including this effective free-surface height formulation, we now arrive at DRFT,

shown in Equation 2.5. The term $\delta h = r \cdot (r\omega^2/g)$ thus modifies $\tilde{z}$ as:

$$\tilde{z} = z + r\left(\frac{r\omega^2}{g}\right) \tag{2.11}$$

This term reduces the free surface height and effectively weakens the GM by a ratio between the wheel's centripetal and gravitational accelerations. We implement this DRFT model using the same implicit RFT code framework discussed previously, using $\lambda = 1$ and $\rho \approx \rho_c = 638\ kg/m^3$. The trends of translation velocity and sinkage with respect to ω now show good agreement between experiment and DRFT (Figure 2.15). We also include, for comparison, the solution when solely the dynamic inertial correction is used. While the formulation for DRFT combines both dynamic corrections, it is clear that the dynamic structural correction dominates the dynamic inertial correction in the case of wheeled locomotion.

For simplicity, we previously stated that the division point between the two contact zones takes place halfway through the wheel-sand interface (Figure 2.14A, inset). From the visualizations in Figure 2.9 and Figure 2.14B, we observe that the division between zones may be closer to the front of the wheel in actuality. This could explain the slight over-prediction of translational speed for high ω (Figure 2.15A).

The agreement with DRFT suggests that the low-to-high slip transition in wheeled locomotion (where slip $S = 1 - (v/r\omega)$ for v is the translational velocity, r is the nominal radius, and ω is the angular velocity of the wheel) occurs largely because more rapidly spinning wheels remove material from behind the wheel, which reduces the pressure in the rear zone, thereby weakening the base of material that would otherwise provide supporting ground. Updating RFT by accounting for this effect appropriately captured the dynamics of the complex wheel locomotion scenario in a reduced-order modeling framework.

To further verify the robustness of DRFT, we simulate a smaller version of the grousered wheel geometry via continuum modeling as well as DRFT. This also demonstrates the use

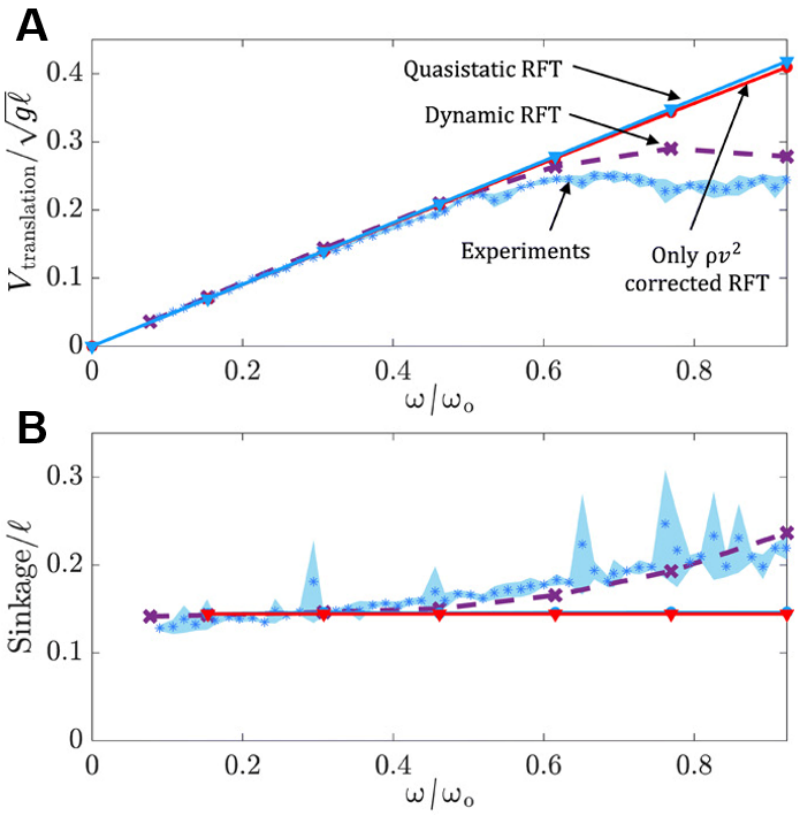

Figure 2.15: **Dynamic RFT Captures Experiments and Continuum Modeling** (A) Wheel translation velocity and (B) sinkage from experiments compared to quasi-static RFT, DRFT, and DRFT without any dynamic structural correction (i.e., having only a ρv^2 correction). Continuum and DRFT simulations courtesy of Shashank Agarwal [65].

of scaling analyses in characterizing the free surface profiles for any given class of intruders, using grousered wheels as a test case. The new wheel is similar in shape and composition to the one used in the experimental study (Table 2.1), but halved in spatial dimensions. The GM properties remain the same as before. Wheel shape and other dimensionless variables $[\rho_{wheel}/\rho_c, \mu_s, h_g/D, N]$ are maintained between the two wheels, so we can assume that the free surface function remains $\psi = r\omega^2/g$. We can thus perform DRFT to predict the dynamics of the smaller wheel, comparing vs. the continuum model results for the same scenario. The results are plotted in Figure 2.16 with the larger wheel data set in blue and the smaller wheel data set in black. Both the larger and smaller wheel DRFT calculations overall match the trend of the reference continuum solution, verifying the robustness of DRFT.

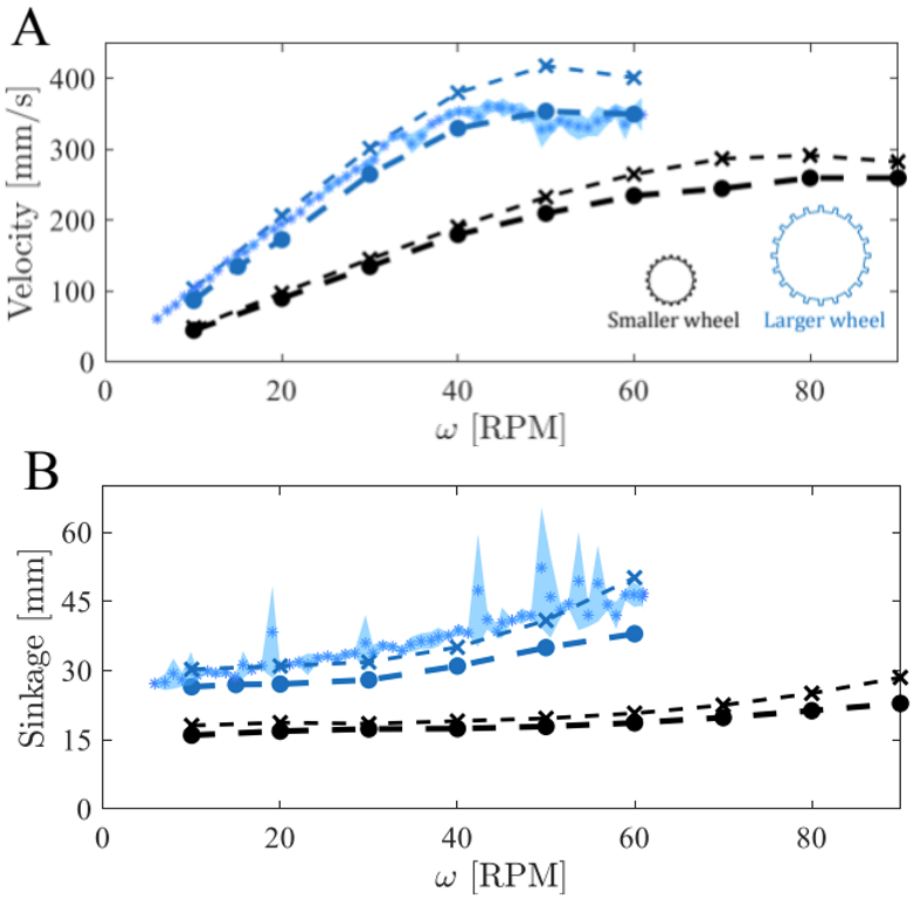

Figure 2.16: **DRFT Verification for Wheels of Various Dimensions** (A) Wheel translation velocity and (B) sinkage from experiments (blue data with asterisk markers), continuum modeling (thin dashed lines with filled circular markers) and DRFT modeling (thick dashed lines with x markers) with respect to angular velocity ω for two wheels of varying dimensions. The blue data set represents the wheel used in the experimental study above (Table 2.1), and the black data set corresponds to a scaled-down, smaller wheel. Continuum and DRFT simulations courtesy of Shashank Agarwal [65].

2.6 An Expanded DRFT Formulation of Wheeled Locomotion Performance

Now that we've established a convincing agreement between DRFT, experiment, and the continuum model results, it is worth investigating the potential of DRFT in giving closed-form predictive solutions of wheeled locomotion performance. Since we've shown that DRFT exhibits linearity in force superposition its application to wheels, we can extend the single-element description of traction (Equation 2.5) into a description of the net force on the full locomoting wheel scenario.

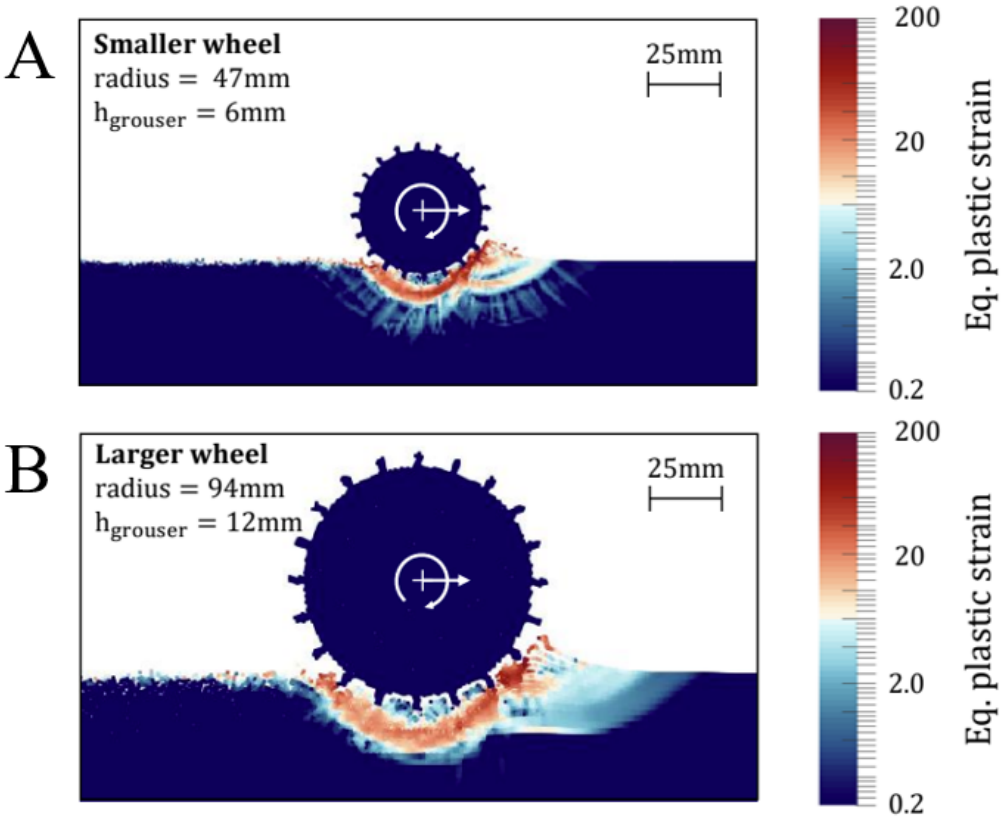

Figure 2.17: **Continuum Modeling for Wheels of Various Dimensions** (A) and (B) show the equivalent plastic strain rate for the smaller and larger wheels at 90 RPM and 60 RPM, respectively. Continuum and DRFT simulations courtesy of Shashank Agarwal [65].

2.6.1 Quasistatic Wheel RFT

We first examine the equilibrium round wheel geometry: Assume we have a circular wheel with radius (r) and out-of-plane width (W) spinning in GM of a fixed free surface at a constant rotational velocity (ω) at a non-negative slip. The force response from shearing the GM balances any frictional losses such that the wheel has an unchanging horizontal velocity ($v_x \leq r\omega$), a zero vertical velocity ($v_y = 0$), and some positive sinkage ($0 < h \leq r$). The angle from the horizontal of front contact that the wheel makes with the GM surface is given by:

$$\theta_1 = -\sin^{-1}\left(\frac{r-h}{r}\right) \tag{2.12}$$

Introducing the change of variables for the reduced sinkage: $l = 1 - (h/r)$ gives $\theta_1 = -\sin^{-1}(l)$. Also, recalling the definition of slip as $S = 1 - (v_x/r\omega)$ allows us to have a pair of reduced variables (l, S) that concisely describe all possible wheel states. We also define the angle from the vertical of rear contact, where the wheel disengages with the GM, as θ_2. We will leave this undefined for now and return to it later. Returning first to the quasistatic RFT of Equation 2.3, the direct integral for the net forces on our wheel can be rewritten as:

$$\vec{F}(l, S) = \int_S \vec{\alpha}(\beta, \gamma) H(-z)|z| dA \tag{2.13}$$

$$= \int_{\theta_1}^{\theta_2} \vec{\alpha}(\beta, \gamma)|z| dA \tag{2.14}$$

$$\vec{F}(l, S) = rW \int_{-\sin^{-1}(l)}^{\theta_2} \vec{\alpha}(\beta, \gamma)|z| d\theta \tag{2.15}$$

where the Heaviside function has been absorbed into the definitions of θ_1 and θ_2, and we can integrate purely across the coordinate θ by pulling out rW. (Note that our θ coordinates are between π and 2π as we are working with Quadrants III and IV of the unit circle.) Now let us also rewrite each sub-element's sinkage ($|z|$) in terms of the wheel state via the coordinate transform: $z = -h + r(1 + \sin\theta)$:

$$\vec{F}(l, S) = rW \int_{-\sin^{-1}(l)}^{\theta_2} \vec{\alpha}(\beta, \gamma)|r - h + r\sin\theta| d\theta \tag{2.16}$$

$$\vec{F}(l, S) = r^2 W \int_{-\sin^{-1}(l)}^{\theta_2} \vec{\alpha}(\beta, \gamma)(l + \sin\theta) d\theta \tag{2.17}$$

where pull out a radius term (r) and we can discard the absolute value restriction since we asserted $h \leq r$. The final step to fully define this integral is to create a mapping of the RFT alpha functions from the "plate space" defined in Li et al. [17] as functions of the orientation and velocity angles (β, γ) to an equivalent "wheel space" of the variable pair (θ, S). The alpha functions in wheel space will be independent of the reduced sinkage l since that

dependence is contained within other terms of the RFT integral. As defined in Li et al. [17], the plate orientation angles β of the outward normal are an offset $(-\theta + 3\pi/2)$ from the standard angular coordinate θ. Similarly, the velocities with respect to the laboratory frame of each i^{th} wheel subsegment (v_x^i, v_y^i) can be mapped to Li's γ angle:

$$\theta = -\beta + \frac{3\pi}{2} \tag{2.18}$$

$$\gamma = \arctan 2(v_y^i, v_x^i) \tag{2.19}$$

$$\gamma = \arctan 2(v_y + \frac{d}{dt}(r\sin\theta), v_x + \frac{d}{dt}(r\cos\theta)) \tag{2.20}$$

$$\gamma = \arctan 2(v_y + r\omega\cos\theta, v_x - r\omega\sin\theta) \tag{2.21}$$

Since we assumed $v_y = 0$ and $S = 1 - (v_x/r\omega)$, we observe that both γ and S can be fully defined with the same set of variables (r, ω, v_x):

$$\gamma = \arctan 2\left(r\omega\cos\theta, r\omega(1 - S - \sin\theta)\right) \tag{2.22}$$

$$= \arctan 2(\cos\theta, 1 - S - \sin\theta) \tag{2.23}$$

The required transform of alpha functions $\vec{\alpha}(\beta, \gamma) \rightarrow \vec{\alpha}(\theta, S)$ is thus:

$$\vec{\alpha}(\beta, \gamma) = \vec{\alpha}(-\theta + \frac{3\pi}{2}, \arctan 2(\cos\theta, 1 - S - \sin\theta)) \tag{2.24}$$

With these angle transforms, we can numerically generate sweeps of (β, γ) that input into Li et al's. granular RFT for any wheel position and slip pair (θ, S), then map those back into wheel space to create our alpha functions $\vec{\alpha}(\theta, S)$. Like Li et al's. granular RFT, these can be well approximated as Fourier series of less than five terms. Let us also introduce Li's granular scaling factor ξ from the study [17] to generalize the alpha functions, and

rewrite the RFT integral as:

$$\vec{F}(l,S) = \xi r^2 W \int_{-\sin^{-1}(l)}^{\theta_2} \vec{\alpha}_{gen}(\theta,S)(l+\sin\theta)d\theta \tag{2.25}$$

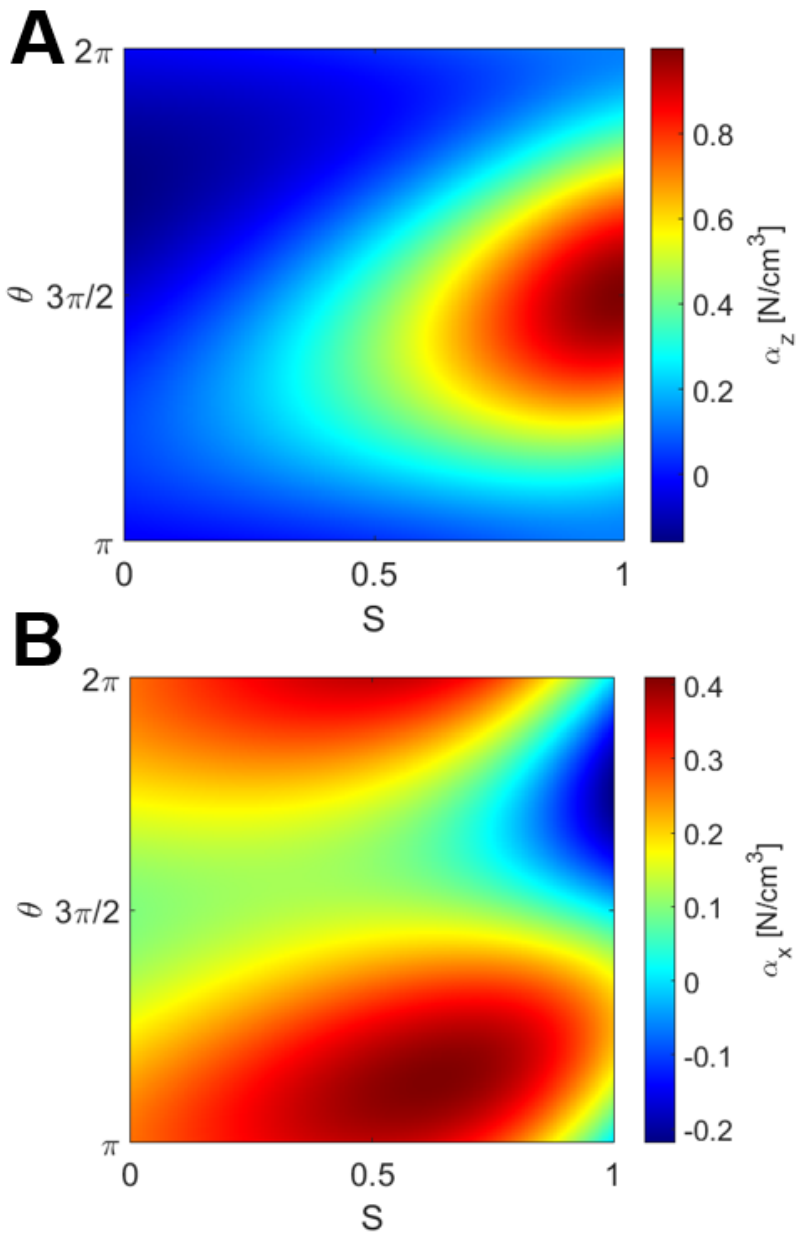

Figure 2.18: **Alpha Functions for RFT in Wheel Angle/Slip Parameters** Colormaps of the transformed Fourier series of Li et al's. [17] RFT alpha functions using Equation (2.24) and Equation (2.25) in the z (subfigure A) and x (subfigure B) directions. Alpha functions follow the generic scaled form of Figure 1.7.

We've successfully rewritten quasistatic RFT into wheel space with some angle trans-

forms, but there remains an undefined θ_2 as the upper bound of integration. We will address and define this angle in the following section, then show how properly selecting this angle will allow us to integrate the dynamic structural correction of Equation 2.11 as a single term addendum to Equation 2.25 that captures both experimental and continuum results.

2.6.2 An Alternative Leading Edge Condition

The leading edge condition defined in Equation 2.4 states that we require $\vec{v} \cdot \vec{n} > 0$ for all wheel surface elements. This condition enforces that the GM can only exhibit compressive resistive forces, as dry GM cannot support tensile loads. In wheel space for a round wheel, this condition can be used to set the upper bound of θ_2 in Equation 2.25, as was done in Agarwal & Karsai et al. [65]. However, for a round wheel geometry such that $S > 0$, this means the upper bound would be fixed at $\theta_2 = 3\pi/2 = -\pi/2$. In the terramechanics literature, the normal pressure distribution on the wheel surface during locomotion is observed to extend beyond $\theta = 3\pi/2$ for real-world locomotion scenarios on GM [96, 95, 42]. To reconcile this discrepancy, we suggest an alternative, implicit leading edge condition for θ_2 such that:

$$\text{For all elements in surface :} \quad \vec{F}_{RFT} \cdot \vec{n} > 0 \tag{2.26}$$

Rather than enforcing a $\vec{v} \cdot \vec{n} > 0$ relation, we can attempt to loosen this constraint by observing that the wheel still actively shears GM past $\theta = 3\pi/2$ in both experimental PIV and the continuum model (Figure 2.9). If we loosen our condition to Equation (2.26), RFT will still preserve the essential feature that GM will generate only compressive and not tensile loads on a contacting surface. This will lead to an implicit calculation of θ_2 such that θ_2 becomes the angle at which RFT transitions from compressive to tensile pressures on the wheel surface. We can apply this condition and see if the RFT alpha functions in wheel space can match the observed pressure patterns in terramechanics. If we plot the resultant

force vectors for both tested leading edge conditions (Figure 2.20), we can see that indeed Equation (2.26) more closely matches the traditional terramechanics locomotion pressure pattern (Figure 2.21A).

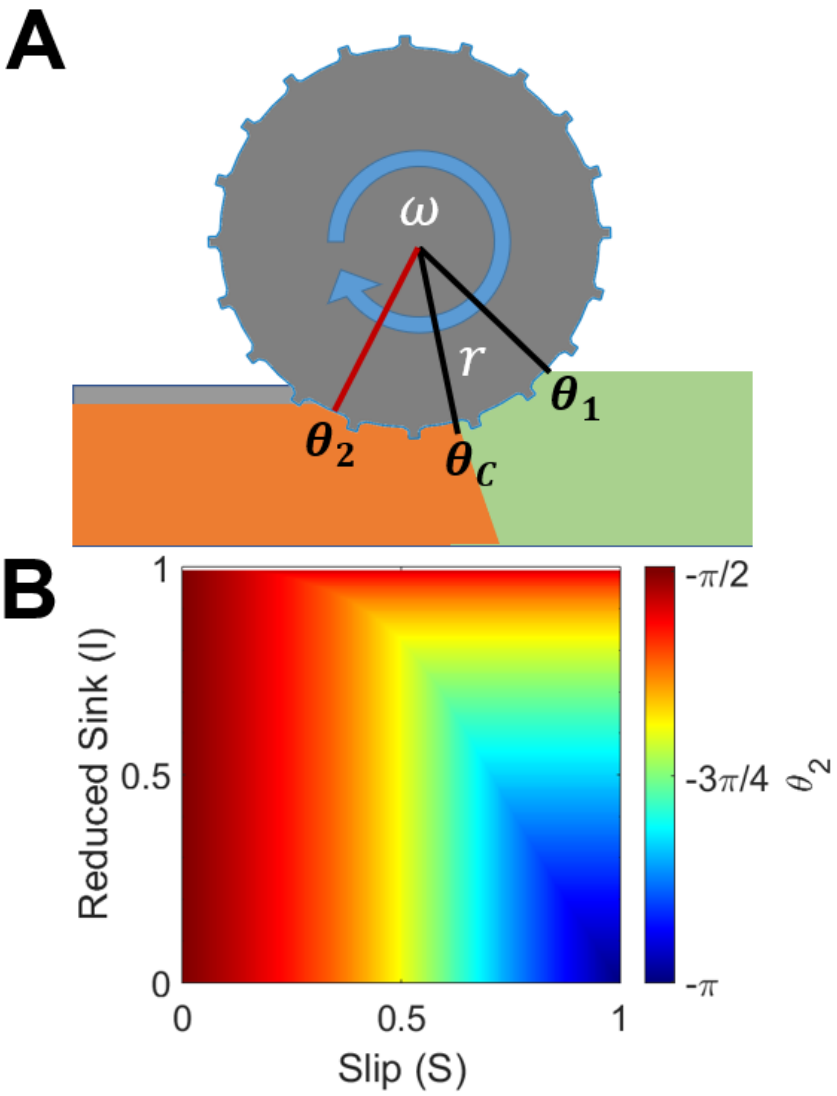

Figure 2.19: **An Alternate Leading Edge Condition** (A) Diagram of an possible zone splitting schematic for Figure 2.14. (B) Colormap of θ_2 in reduced sink ($l = 1 - (h/r)$) and slip ($S = 1 - (v/r\omega)$) parameters using eq. (2.26) for a round wheel in quasistatic RFT.

Equation (2.26) appears to create a feasible wheel pressure pattern [95, 29] (Figure 2.20) and a similar condition to Equation (2.26) was used for RFT wheel locomotion simulations in Suzuki et al. [42]. This allows us to create a map of the value θ_2 for quasistatic RFT as a function of reduced sinkage and slip: $\theta_2(l, S)$ (see Figure 2.19B).

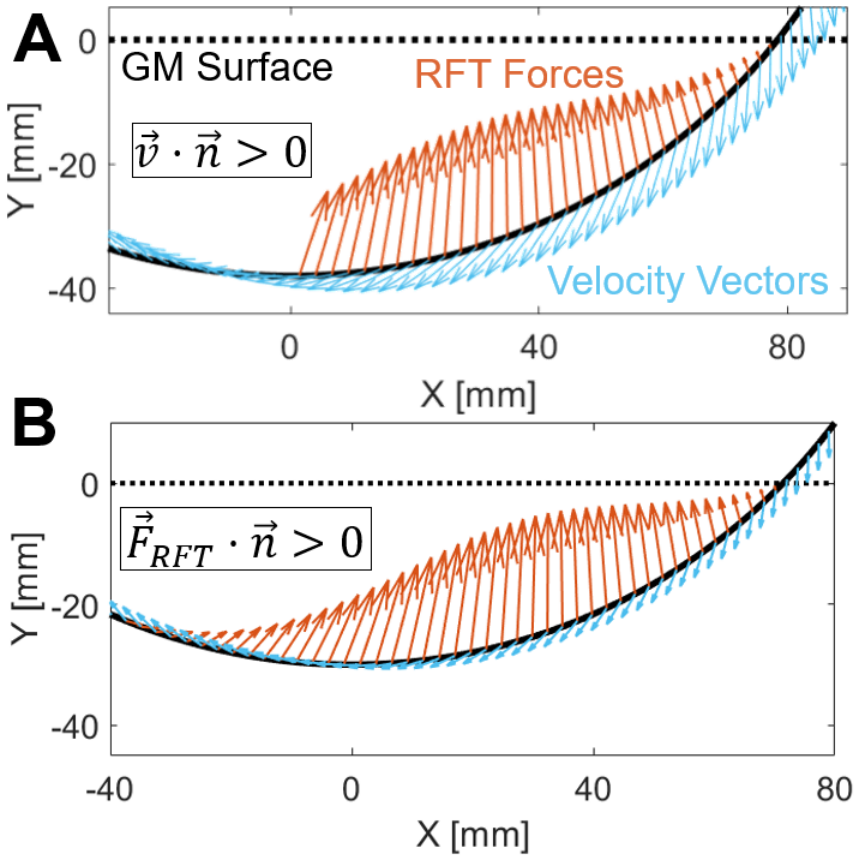

Figure 2.20: **Differences in Force Patterns of Leading Edge Conditions** (A) Snapshot of a round wheel at slip $S = 0.38$ in a quasistatic RFT simulation using Equation (2.4) for the leading edge condition. (B) Snapshot of a round wheel at slip $S = 0.38$ in a quasistatic RFT simulation using Equation (2.26) for the leading edge condition.

With definite values of θ_2 now in hand, we make one final heuristic angle definition for the splitting of the front zone (FZ) and rear zone (RZ) relevant from Figure 2.14. We can use Hambleton et al's. [95] definition of a critical angle θ_C where the normal pressure is maximized (Figure 2.21A), and split the zones into FZ and RZ along that angle. Thus we arrive at the angle definitions:

$$\theta_1 = -\arcsin l \tag{2.27}$$

$$\vec{F}_{RFT}(\theta_2) \cdot \vec{n}(\theta_2) \to 0 \tag{2.28}$$

$$\theta_C = \frac{\theta_1 + \theta_2}{2} \tag{2.29}$$

and can calculate θ_C in reduced sink/slip parameter space (Figure 2.21B).

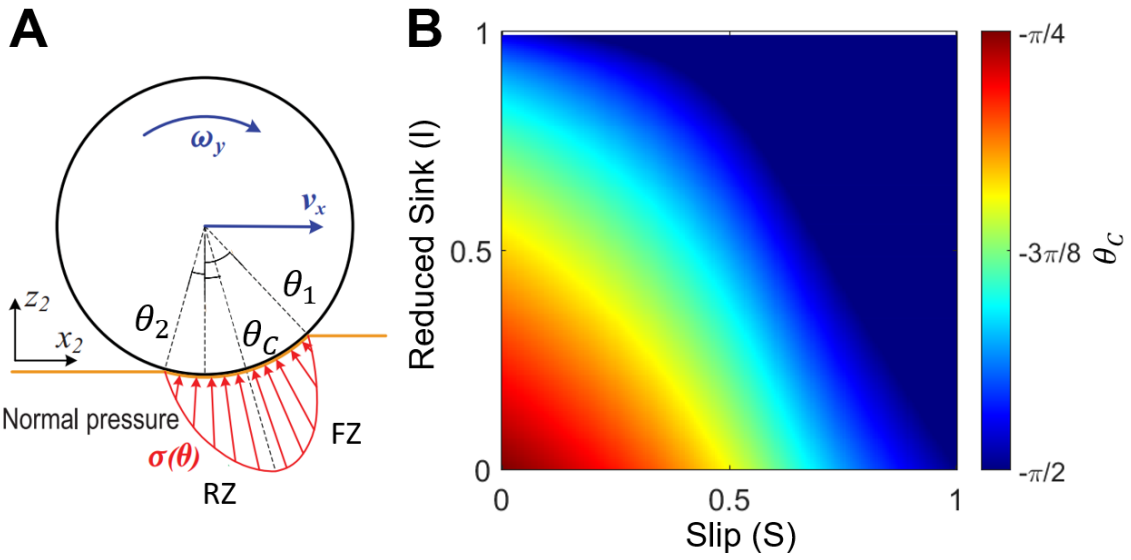

Figure 2.21: **Splitting Angle Hypothesis** (A) Diagram of round wheel locomotion adapted from Hambleton et al. [95] showing the normal pressure distribution from Bekker-Wong terramechanics [96] and how θ_C can act as the splitting angle between the front zone (FZ) and rear zone (RZ) for DRFT. (B) Colormap for the values of θ_C in full reduced sink/slip parameter space calculated using Equation (2.29).

Now that θ_C and θ_2 are defined, we can return to Equation (2.25) and write it as:

$$\vec{F}(l,S) = \xi r^2 W \left(\int_{-\arcsin l}^{\theta_2} \vec{\alpha}_{gen}(\theta,S)\,(l+\sin\theta)\,d\theta \right) \tag{2.30}$$

where θ_2 is calculated via the method in Figure 2.19. This finally gives a closed-form expression for the force balance in quasistatic wheel locomotion. However, we wish to apply this equation to the dynamic scenarios detailed previously such that the force balance also has a dependence on ω. Fortunately, thanks to our angle definitions in Equation (2.29), we can easily unify the quasistatic equation with the dynamic structural correction term of Equation (2.11) for DRFT and obtain:

$$\vec{F}(l,S,\omega) = \xi r^2 W \left(\int_{-\arcsin l}^{\theta_2} \vec{\alpha}_{gen}(\theta,S) \left(l+\sin\theta + H(\theta_C)\frac{r\omega^2}{g} \right) d\theta \right) \tag{2.31}$$

where ω is the wheel rotation rate, and $H(\theta_C)$ is the Heaviside function acting on the critical splitting angle that splits FZ and RZ. Thus the dynamic structural correction term $r\omega^2/g$

only affects the range of θ within RZ.

One last modification to this DRFT force balance equation considers the grousers that protrude from most wheel designs that allow the wheel to engage fully with the GM substrate under shear. For integration into Equation (2.31), we can consider grousers as small protuberances that periodically modulate the radius r of the wheel by some grouser length δr for some interval $\delta\theta$. For the function $r(\theta)$, this would be a pulse wave of low duty factor with baseline r, pulse duration $\delta\theta$, and amplitude δr. Since r now depends on θ, we must bring it inside the integral and we obtain:

$$\vec{F}(l, S, \omega) = \xi W \left(\int_{-\arcsin l}^{\theta_2'} r^2(\theta) \vec{\alpha}_{gen}(\theta, S) \left(l + \sin\theta + H(\theta_C') \frac{r(\theta)\omega^2}{g} \right) d\theta \right) \quad (2.32)$$

In addition to the protuberances in the radial direction, the plate-like elements of each grouser must be accounted for. Each grouser has an intruding face of length δr and width W that moves into the GM with a leading edge in the direction of ω in the wheel frame. Since the grousers are rigidly attached to the parent wheel, their alpha functions can easily be calculated simply by rotating θ by $-\pi/2$. Thus each grouser within the GM represents a small plate-like element along the angular coordinate in the wheel frame, rather than the radial coordinate as in Equation (2.32). If we consider the set G to be the set of grousers within the GM between θ_1 and θ_2, then the net resistive force due to the angular grouser shearing can be calculated as:

$$\vec{F}(l, S, \omega) = \xi r W(\delta r) \left(\sum_G \vec{\alpha}_{gen}(\theta - \frac{\pi}{2}, S) \left(l + \sin\theta + H(\theta_C) \frac{(r + \delta r)\omega^2}{g} \right) \right) \quad (2.33)$$

By summing together Equation (2.32) and Equation (2.33) for a grousered wheel, we can thus get the net force balance for an input state (l, S, ω). To test these functions' validity, we used a MATLAB script to solve these equations using the fminsearch() function and input RFT coefficients of PS, the wheel geometry and inertia balance of Table 2.1, and the tested ω values of our experiments. We want to find an equilibrium state (l, S) for each

input ω such that the DRFT equations satisfy a net zero force balance against the wheel carriage's inertia. Each calculation per ω value rotated the wheel geometry randomly so that the grouser set G was tested at various positions to smooth out any grouser induced asymmetries induced by Equation (2.33). The minimum search function successfully returned a set of (l, S) solutions for each tested ω, which we then transform back into translational velocity and sinkage to compare with our previous methods in Figure 2.22.

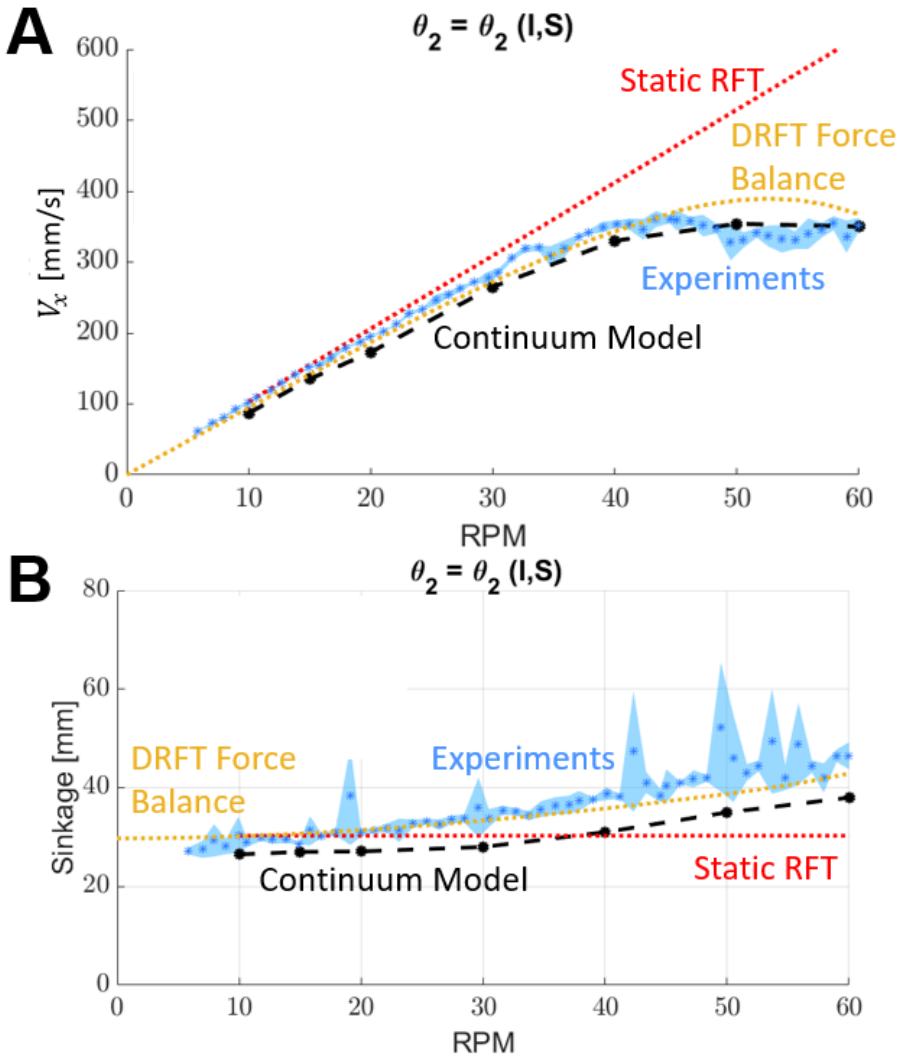

Figure 2.22: **Closed Form DRFT Equation Kinematic Results** (A) Translational velocity and (B) sinkage for using the force balance equations for DRFT (Equation (2.32) and Equation (2.33)) in the yellow dotted line. θ_2 is defined via the colormap of Figure 2.19B. The force balance matches the trends observed in the experiments and the continuum model results.

There is good agreement between experiment, continuum model, and the closed-form

DRFT equation for our tested scenarios. Due to the success of DRFT characterizing wheels of different dimensions (Figure 2.16) and previous understanding of wheeled locomotion scaling relations [97, 46], we suspect this formulation can be applied as a reduced-order model for grousered wheels on GM of many inertias and geometries, all within a simple single-line equation. Additionally, the complete DRFT equation can show the relevant geometrical scaling relations in the force response at a glance, which is useful for physical intuition.

2.7 Additional Verification Studies for DRFT

The grousered wheel tests we performed provide a complex intrusion scenario while having a dynamic structural correction that is much larger than the inertial correction. To check the robustness of the continuum modeling approach and of Equation 2.5 for DRFT, Agarwal and Kamrin examined the converse situation with two additional sets of simulations: rapid submerged plate intruders, and locomoting runners. They evaluated these cases with data from continuum solutions, validations against existing literature, and the arguments presented in the previous section. In these cases, we expect the dynamic structural correction to be small and the dynamic inertial correction to dominate.

Visually, these cases represent two separate classes of intruders. While the dragged plates represent forced motion, the runners represent a class of self-propelling locomotors that appear similar to the wheels. However, the force responses in both these cases are dominated by the dynamic inertial correction and do not follow the observed trends of the grousered wheel trials. Thus, these distinct cases test the breadth of the modeling capability of DRFT.

Submerged horizontal intrusion: Thin plates submerged in a GM at various fixed depths (20 to 40 mm) are dragged horizontally at different speeds within the continuum model. The continuum model runs in plane strain, where the plate has a length of $16mm$ and the effective medium density is $900\ kg/m^2$. The chosen density is similar to that of ground

coal or marble. The filled circles in Figure 2.23 show the observed drag force variations with respect to drag speed. Experimental studies by Schiebel et al. [71] found that the variation of drag forces in such a scenario to follow the trend:

$$F = K|z| + \lambda \rho A v^2 \tag{2.34}$$

where κ and λ are constants, $|z|$ is the depth of the plate below the free surface, ρ is the effective granular density, A is the plate area, and v is the horizontal plate velocity.

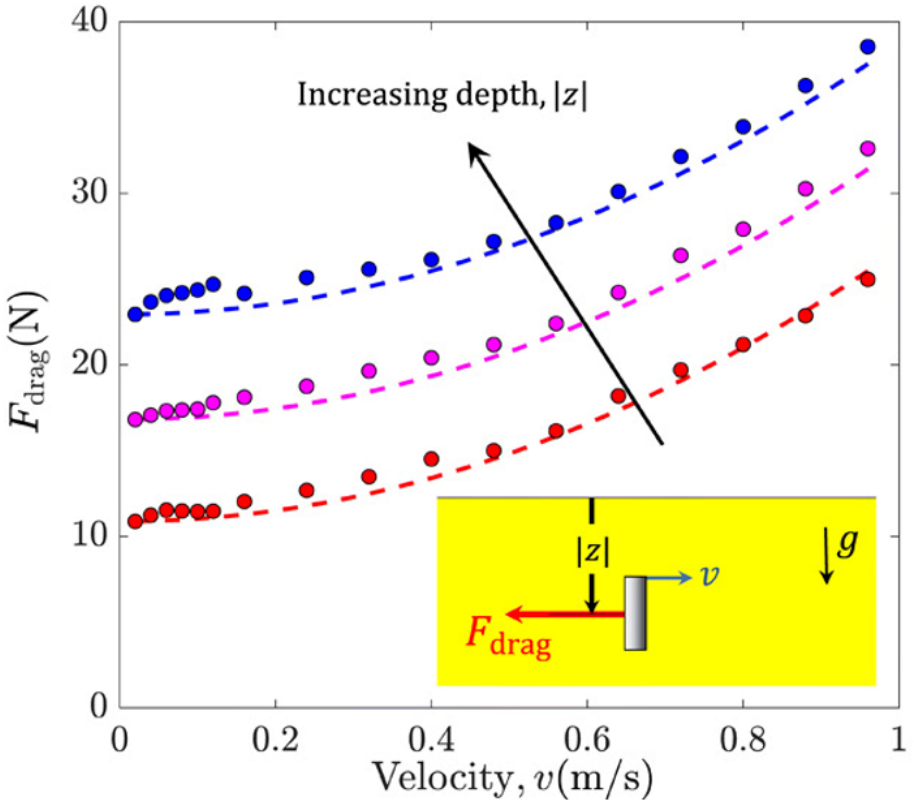

Figure 2.23: **Modeling Slow-to-Rapid Plate Intrusion** Continuum MPM data (colored circles) and $K|z| + \lambda \rho A v^2$ fits (dotted lines) for horizontal intrusions at various depths ($|z|$) ([20,30,40] mm), where $K = 580$ N/m and $\lambda = 1.1$. Simulations are plane strain. Figure courtesy of Shashank Agarwal [65].

The continuum modeling results also show the same trend (Figure 2.23). In the slowest cases ($v \approx 0$), Agarwal and Kamrin obtain a linear force versus depth relation, $F_{drag} = K|z|$ for $K = 580\ N/m$. As speed increases, they find that continuum predictions match the data well at three different depths, for $\lambda = 1.1$. Incidentally, the same value of λ

also matches the rate dependence observed in the Schiebel et al. [71] experiments for horizontally driven intruders at the free surface.

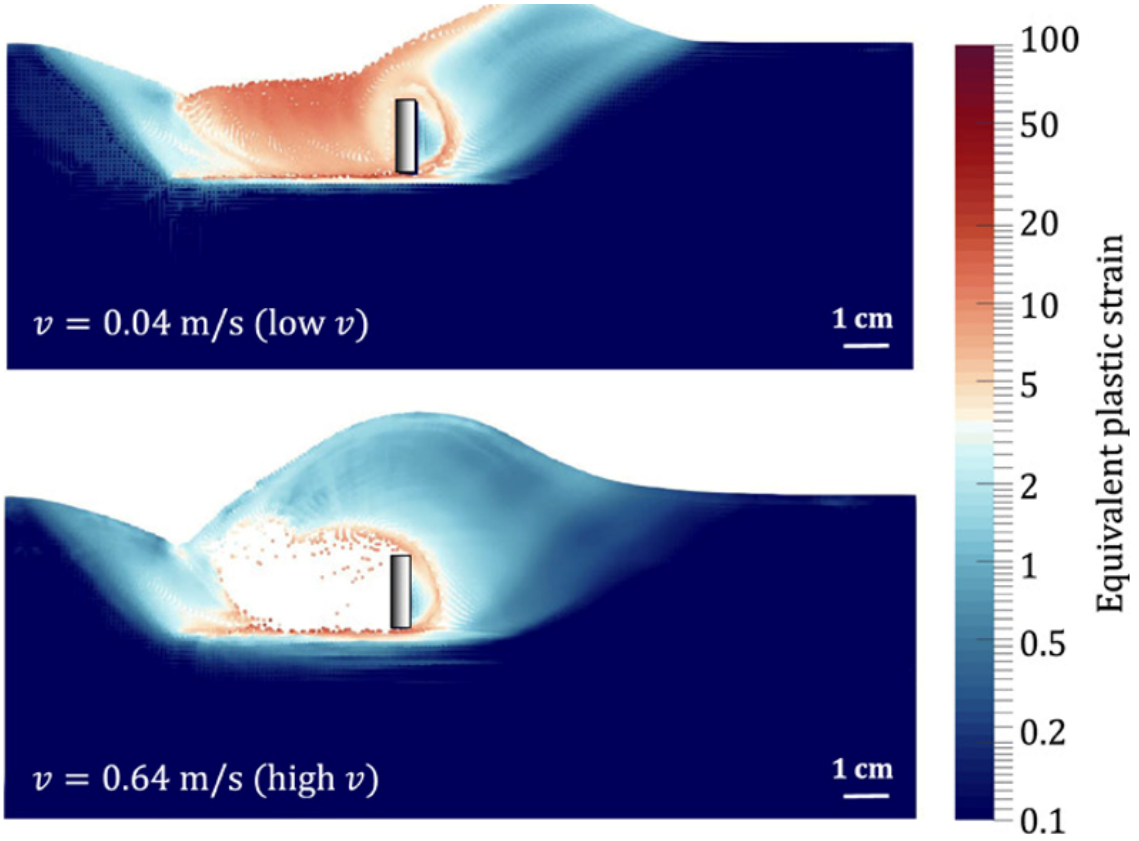

Figure 2.24: **Continuum Sim Visualization of Slow-to-Rapid Plate Intrusion** Variation of equivalent plastic strain rate for (top) low-velocity (0.04 m/s) and (bottom) high velocity (0.64 m/s) intrusion cases (at 30 mm depth). Simulations are plane strain. Figure courtesy of Shashank Agarwal [65].

A comprehensive understanding of the drag force trends can be obtained by observing continuum modeling results in the context of DRFT. Figure 2.24 shows the deformation profiles around the plate at two select speeds (which differ by about an order of magnitude). The profiles in Figure 2.24 of high- and low-speed intrusion suggest that the traction on the intruders arises from pressing the granular material in front of the plate upward and rightward, toward a common free-surface height, h_{front}. The rear flow zone, which changes form in low- versus high-speed intrusion, is either in the fully separated phase (Equation 2.1) or newly consolidated as it falls and fills in the gap behind the moving plate. Likewise, the rear GM makes a negligible contribution to the resistive plate force. No part

of the of the rear face of the plate is a "leading edge" satisfying $\vec{v} \cdot \vec{n} > 0$ (Equation 2.4), so forces locally go to zero. This is heavily in contrast to the grousered wheel case, where due to rotation, a substantial portion of the rear half of the wheel is a leading edge that can interact non-trivially with GM behind the wheel. We thus expect a negligible dynamic structural correction for horizontal plate drag, due to both the lack of a leading edge on the rear face of the plate, and an approximately speed-independent h_{front}.

Indeed, the force relation $F_{drag} = K|z| + \lambda\rho A v^2$ (Equation 2.34) obtained from experiments as well as continuum modeling, displays only the dynamic inertial correction of DRFT as expected. These results are in accord with the previous hypothesis and confirm the DRFT prediction for submerged horizontal intrusion. We also expect the symmetric vertical intrusion of plates to also invoke a negligible structural correction. In our plate drag studies, we have restricted our intrusion depths to within an $O(1)$ factor of the plate width. This depth range indicates the approximate limits of RFT, since beyond this depth range, the key assumptions of RFT (such as linear dependence of granular resistance with depth) begin to degrade [98].

Four-flap runner: While the dragged plates are forced to move at set speeds, we also study a self-propelling locomotor: a four-flap runner. The runner's locomotion speed is determined via the interactions of the locomotor's self-actuated limbs (spinning motion of the flaps) and the substrate dynamics (geometric details are in Table 2.1). The low number of flaps, along with the large ratio of flap length to inner radius, minimizes the interaction between consecutive flap intrusions of the runner's resultant deformations of the GM.

In Figure 2.26A, we show an experimental build attempt of a four-flap runner. We use many of the same build approaches as the previously described terramechanics testbed. We construct a top carriage plate out of aluminium that holds a set of four OpenBuilds® Delrin® Mini V-Slot wheels designed to smoothly run on OpenBuilds® 20mm V-Slot Linear Rail. A pair of 6.35mm steel shafts rigidly attach to the top plate via shaft collars, and a bottom plate that can move vertically is attached to these shafts with a pair of flanged

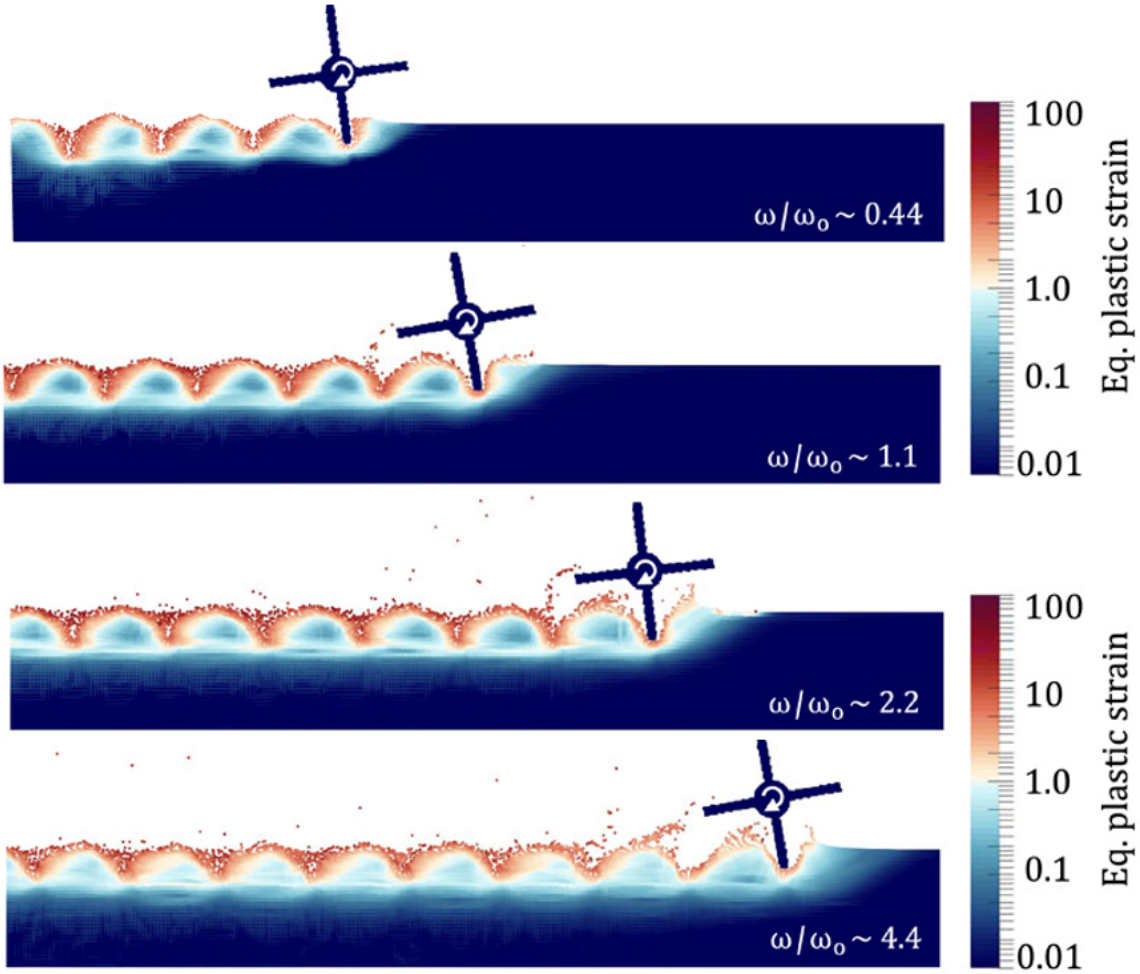

Figure 2.25: **Four-flap Running on GM** Continuum model solutions for the equivalent plastic strain at increasing angular velocities ω for four-flap runner locomotion ($\omega_0 = 65RPM$). Continuum simulation and figure courtesy of Shashank Agarwal [65].

linear roller bearings. Shaft collars and springs near the bottom of the vertical shafts prevent the bottom carriage from coming off of the rails. A 1kg capacity bar-type load cell (uxcell) is then rigidly screwed into the top plate, and a pair of 3D printed Acrylonitrile Butadiene Styrene (ABS) rings are screwed into the top load cell and bottom plate, and an extension spring with hooks (spring constant $k = 0.11$ N/mm) connects the two hooks so that vertical position and force could be extracted from the reactive motion of the bottom plate during locomotion. A Pololu 37D metal gearmotor with an encoder was then attached to the bottom plate, and a 3D-printed ABS paddle wheel, representing the four-flap runner, attached to the gearmotor's output shaft. The entire carriage has a mass of 840 grams, and

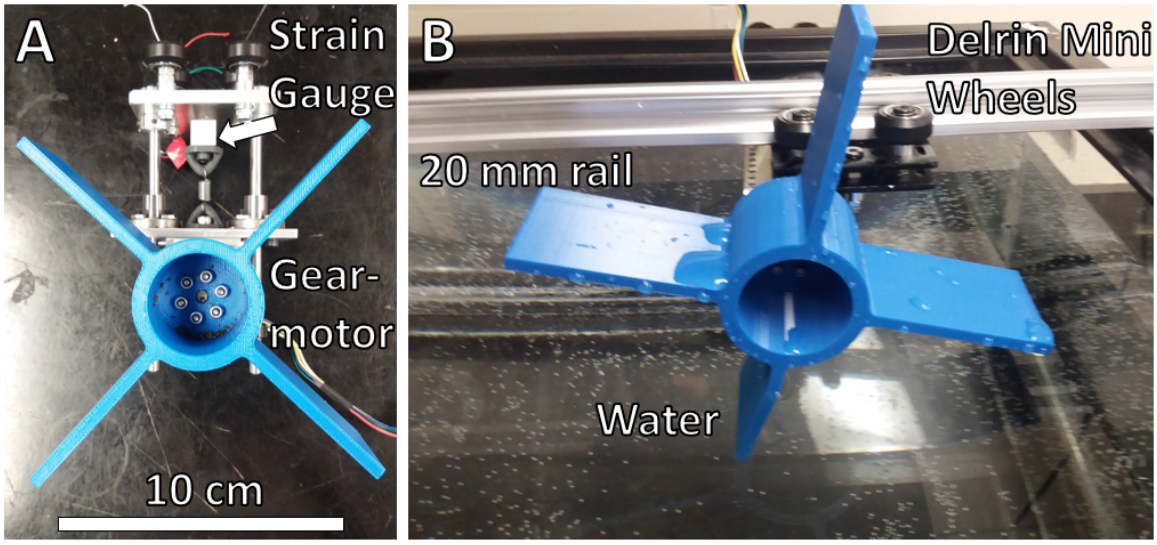

Figure 2.26: **Experimental Build of the Four-flap Runner** (A) Front view photo of the four-flap runner paddle wheel carriage. Like the terramechanics testbed in Figure 2.2, it can freely move horizontally and vertically. (B) The four-flap runner carriage mounted on a 20mm OpenBuilds rail mounted on top of a water tank such that the bottom flap is almost completely submerged underwater.

each paddle has dimensions of 68 x 50 x 5 mm, attached to an interior cylinder component with an outer diameter of 52 mm. In locmotion, the carriage is qualitatively similar to the idealized four-flap runner in GM shown in Figure 2.25.

Unfortunately, some preliminary calculations and simulations showed that these physical experiments would be difficult to perform due to the very high speeds required before inertial force effects become significant in frictional GM. No convenient gearmotor could provide the required speed and torque combination (up to 31 rad/s), and these experiments would have needed a new, very long GM testbed. Unlike the wheeled locomotion experiments, the four-flap runner on GM experiments were also not the primary focus of the original study [65] and were not performed. Preliminary tests in a water tank (Figure 2.26B) showed a near-quadratic relation of v_x vs ω in water, but that was expected since viscous drag in Newtonian fluids is dominated by its v^2 term unlike frictional GM. The apparatus remains in Goldman's lab if a future researcher wishes to investigate these phenomena experimentally.

This runner takes inspiration from the experiments of Li et al. [17] and Zhang et al.

[99] with running C-legged robots (similar to Figure 2.1C). Li et al. [17] drove their robots with dimensionless spin ratios (ω/ω_0) ranging from 0 to 1.25 ($(\omega_{max}, \omega_0) = (240, 190)$ RPM) and observed a decreasing slip with increasing angular velocity in their experiments. Similarly, Zhang et al. [99] tested locomotion over a larger ω/ω_0 range of 0 to 3.8 ($(\omega_{max}, \omega_0) = (720, 190)$ RPM) and observed that in this higher range of spins, the sinkage in their experiments broke away from the trends observed by Li et al. [17], i.e. the robots would gain height relative to their resting depth during locomotion. Their running robots displayed qualitatively opposing behaviors to those of grousered wheels: As rotation rates increase, runners sink less and move faster, whereas wheels sink more and travel slower.

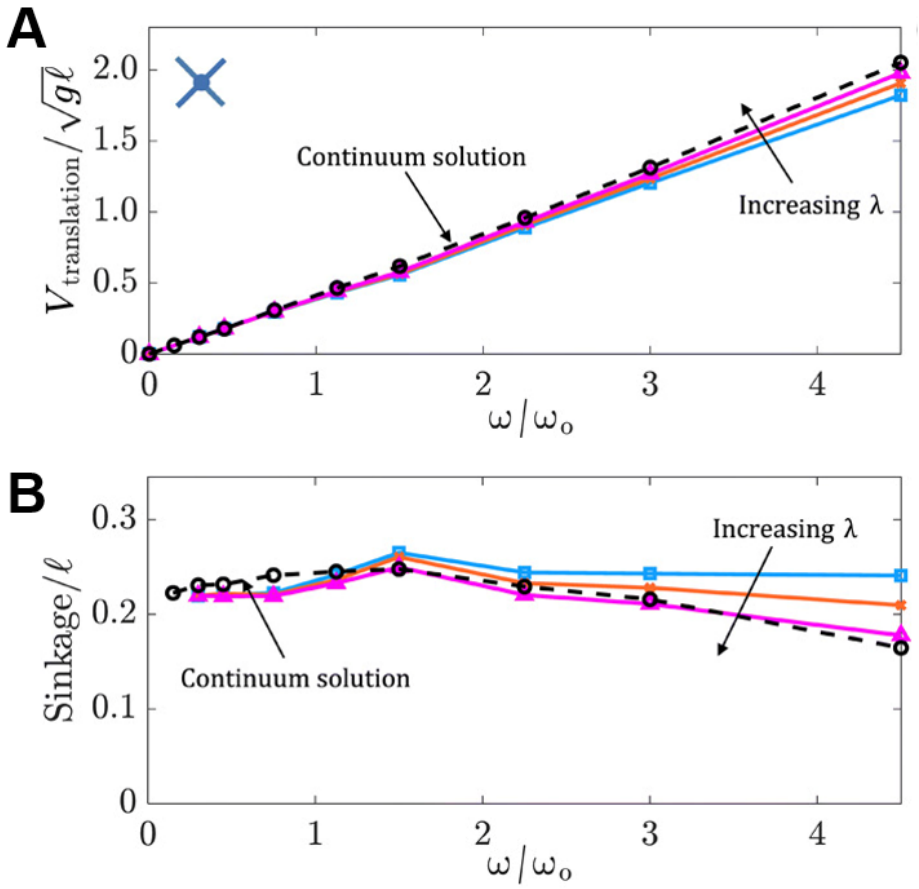

Figure 2.27: **Continuum Simulation vs. DRFT Results for Four-flap Running** Continuum solutions from MPM (black dotted line with "o" markers) and DRFT solutions (solid lines) for translation velocity (A) and sinkage (B) versus angular velocity ω in four-flap runner locomotion. Pictured are DRFT solutions for $\lambda = 0, 2, 4$. The results in (A) and (B) are nondimensionalized as detailed in Figure 2.12 with $\ell = 190$ mm (the runner's outer diameter). Continuum simulation and figure courtesy of Shashank Agarwal [65].

We explore whether the fundamental physics of such qualitatively reversed behavior is already embedded in our continuum modeling and consequent DRFT framework. Because Agarwal and Kamrin's continuum modeling capabilities were limited to plane strain (2D) problems, we cannot implement a full C-legged robot running in 3D. Agarwal and Kamrin took the four-flap runner as a representative of the family of runners and explored their 2D continuum model's capability in modeling such behaviors.

In the continuum model trials, the dimensionless mass ratio of the runner, given by $m/\rho_c \ell^2 W$ for W being the out of plane width, is set in the same range (≈ 6) as the corresponding wheels with 20 grousers shown previously. This is done to keep the runners and grousered wheels comparable. For similar reasons, we keep the four-flap runner's diameter similar to that of the grousered wheel (190 mm versus 212 mm). We vary the angular velocity of the runner over a range of 10 to 300 RPM, which corresponds to a dimensionless spin ratio ranging from $\omega/\omega_0 = 0$ to 4.5 ($\omega_0 = 65$ RPM). The continuum results show qualitative agreement with the findings of Li et al. [17] and Zhang et al. [99], as increasing spin rate results in decreases in effective slip and sinkage. Incidentally, the turning point of locomotion height vs. spin rate for our runners was at a spin ratio ~ 1.4, similar to the result obtained by Zhang et al. [99].

Agarwal and Kamrin then use the continuum model as a baseline reference to evaluate the DRFT performance for runners. Figure 2.25 shows the equivalent plastic strain for runners at four different angular velocities in the continuum model. Because of the relatively large separation between intruding flaps, there is no visible self-interaction of the granular material between intrusions, as expected. The free surface height directly behind the intruding flaps thus remains unchanged, which suggests a minimal role of the dynamic structural correction Equation 2.10. This observation guides us to model these scenarios using DRFT with typical $O(1)$ λ values ($\lambda = 0, 2, 4$) with no dynamic structural correction Equation 2.8. Figure 2.27 (A and B) shows the resultant steady-state sinkage and translation velocity at various angular velocities from DRFT calculations (solid lines). DRFT appears to capture

the kinematic trends of the reference solution, approaching quantitative accuracy for $\lambda \approx 4$. DRFT thus can capture the dependence on ω in both runners and grousered wheels, despite these locomotors following opposing kinematic trends as rotation rate ω increases.

The four-flap runner study also explains the observations of the above-mentioned C-legged robot studies. We believe that the quasistatic RFT modeling in Li et al. [17] was sufficient because the dynamic inertial correction was still small in their tested range (in our continuum model trials, the dynamic inertial correction becomes noticeable only above a ω/ω_0 ratio of ~ 1.2). The study of Zhang et al. [99] examined higher rotation rates, revealing the nontrivial elevation and slip trends due to rate that we see in both the continuum and DRFT solutions.

2.8 Discussion and Conclusions

In this chapter, we showed the construction of a high-speed terramechanics testbed which could probe the kinematics of a free-running wheel carriage. We discovered an unusual effect in wheeled locomotion on GM, as the linear scaling relations between rotation and translation speed were broken at higher ω values. We then turned to a continuum modeling approach by Agarwal and Kamrin to gain understanding of this phenomenon. We focused on evaluating the effectiveness and implications of a continuum model for problems of granular intrusion up to high speeds, which allows for detailed modeling of complex multiphase inhomogeneous granular systems. We observed two unexpected results. First, a continuum model based only on a constant friction coefficient and tension-free separation is able to quantitatively model complex granular intrusions in a variety of scenarios. Second, we found that just two macro-inertial corrections to RFT allows successful modeling of granular intrusions across speed regimes.

By analyzing the continuum model's solutions, we gained insight into the key physics involved in such complex intrusion scenarios, which in turn motivated the ingredients of DRFT. Dynamic RFT allows for robust, near real-time modeling of granular intrusion in

a large variety of cases, including self-propulsion. Our study of rigid intrusion into GM indicates that the force response upon intrusion consists of two primary rate-dependent modifications: (i) a dynamic inertial correction and (ii) a dynamic structural correction. The dynamic inertial correction accounts for the momentum transfer to the surrounding material, whereas the dynamic structural correction describes how a rapidly moving intruder can change the pressure head by modifying the free surface. Both effects are related to the macro-inertia of the media (stemming from the $\rho\dot{v}_i$ term in the momentum balance partial differential equation). For the scenarios considered here, micro-inertial effects (per a $\mu(I)$ rheology) are not significant. Even though the motion appears "fast", previous studies on rapid projectile penetration [86] indicate that the high pressures that develop around rapid intruders tend to keep I relatively small. This implies the observed rate-dependent dynamics are reconcilable with a rheology that is rate-independent. In terms of limitations, it is known that quasi-static RFT loses accuracy when intruders are too deep, as the linear force versus depth dependence eventually plateaus in the lift direction [98] for slow intruders. We expect the same constraints on depth to apply to DRFT as well.

Dynamic RFT has enough generality to explain two opposing scenarios: weakening of the GM during grousered wheel locomotion, as well as strengthening of the GM during rapid running. We have shown that DRFT accurately predicts the GM system behaviors in the limiting cases, i.e., when one of the two dynamic effects is dominant. Further studies are required to fully test the model for mixed cases where both dynamic corrections are significant. We have assumed additivity, in line with previous notions of a static component and an inertial component of the intrusion force [77, 87, 90, 94]. However, it is possible that a more complicated functional combination may arise.

Although our study has mainly focused on dry noncohesive GM, the formulation of DRFT in granular flows suggests the existence of other similar reduced-order models in other materials. A combination of experiments and continuum modeling proved vital in this study for verifying the underlying physics. The proposed continuum framework can

easily be modified to encompass a large variety of materials once their constitutive equations are known. Future work may explore faster methods of predicting flows, along with various complex intruders to systematically determine the form of the dynamic structural correction. Further studies could also explore the existence of similar reduced-order models for related classes of materials like noncritical state GM, cohesive sands/muds, and fluid-saturated sands.

2.9 Contributions

Andras Karsai built the wheeled locomotion testbed and four-flap runner, performed its experiments, analyzed and processed the data, and assisted in DRFT conceptualization and simulations. Shashank Agarwal performed the numerical analysis, continuum model and DRFT simulations, and interpreted the experimental results. Shashank Agarwal, Andras Karsai, Daniel I. Goldman and Ken Kamrin all conceived the study, interpreted the data, discussed the results, and came up with the theory. Shashank Agarwal and Andras Karsai co-wrote the original manuscript [65]. Ken Kamrin and Daniel I. Goldman supervised the project, provided comments on and modified the original manuscript [65].

CHAPTER 3

ROBOPHYSICAL ROVER LOCOMOTION OVER GRANULAR TERRAIN

3.1 Preface and Summary

Autonomous robots and vehicles must occasionally recover from locomotion failure in loosely consolidated granular terrain. Recent mobility challenges led the NASA's Johnson Space Center (JSC) to develop a prototype robotic lunar rover called Resource Prospector 15 (RP15) capable of wheeled, legged, and crawling behavior. To systematically understand performance of such a device, we developed a scaled-down rover robot and studied its locomotion on slopes of dry granular media. Addition of a cyclic legged gait to the robot's wheel spinning action changes the robot dynamics from that of a wheeled vehicle to a locomotor paddling through frictional fluid. Granular drag force measurements and modified RFT facilitate modeling of such dynamics. A peculiar gait strategy that agitates and cyclically reflows grains under the robot allows it to 'swim' up loosely consolidated hills. Whereas substrate disturbance typically hinders locomotion in granular media, the multi-mode design of RP15 and a diversity of possible gaits facilitate formation of self-organized localized frictional fluids that enable effective robust transport.

3.2 Introduction

3.2.1 Locomotion Challenges faced by Planetary Rovers

Planetary rovers face difficulties in soft soil during extraterrestrial exploration [100]. NASA's Mars Exploration Rover *Spirit* became entrapped in the low-cohesion sulfate sands of Troy near the Gusev crater, ending its mobility [101, 102]. Modern Mars rovers like *Spirit* use

This chapter's contents are adapted from a co-first authored paper published 2020 in *Science Robotics* [66], by Siddharth Shrivastava*, Andras Karsai*, Yasemin Ozkan Aydin, Ross Pettinger, William Bluethmann, Robert O. Ambrose, and Daniel I. Goldman.

six wheeled rocker-bogie suspensions which provide significant ability to climb large solid obstacles [103, 104]. Even so, these suspension systems cannot actively apply forces to the ground as their design passively enforces equal pressure among their wheels [105]. Given the capability to individually apply active loads for each wheel, legged locomotion strategies like those in in terrestrial robots [48, 17, 106] could be a viable method for successful rover extraction from loosely consolidated substrates.

Soft, loose soil known as regolith covers large expanses of both lunar and Martian terrain [107]. NASA's Lunar Crater Observation and Sensing Satellite (LCROSS) mission revealed that regolith at the lunar poles is far less consolidated than in the regions explored during the Apollo missions [108, 109]. Data from the Lunar Orbiter Laser Altimeter (LOLA) project show polar slopes up to a maximum of 35° [110, 111], near the angle of repose for the dry lunar regolith [112]. In this dry granular regime, such steep slopes are sensitive to disturbance, are weak to stress and shear, and can readily avalanche [113, 114]. These findings illustrate a genuine risk of entrapment for future rovers exploring the lunar poles. To avoid this, active suspension and independent steering systems that can apply loads and lifts to individual wheels could enable the rover to execute various crawling behaviors to free itself and resume normal locomotion. Planetary rovers could thus navigate soft soil and traverse steep granular inclines, enabling them to access sites previously out of reach.

GM, like regolith, poses a challenge for crawling locomotion as such substrates act like solids but flow when a yield stress is exceeded. The complex interactions between the media and an intruding body exerting stress can create a strongly coupled relation between the intruder's motion, the resistive force on it, and the terrain's state during and after intrusion [115, 17]. Under locomotive shear, media may even be distributed into piles which act as obstacles for the locomotor. Disturbed GM presents challenges to locomotion by asymmetric piling or changing consolidation such that the GM is no longer homogeneous and predictable. Legged robots in previous studies met with significant locomotive fail-

ure when re-intruding into disturbed GM [83, 70], an effect exacerbated in granular slopes where grains weaken and avalanching can deform supporting structures [34]. These systems demonstrate a feedback effect of speed reduction coupled to greater GM disturbance. To break this feedback, a locomotion method's dynamics must be insensitive to or even assisted by GM disturbance created by the locomotion.

3.2.2 A Prototype Lunar Rover for Prospecting

As part of an early study for exploring for volatiles at the lunar poles, NASA's JSC participated in a mission study to provide mobility for carrying prospecting and processing instruments at the lunar poles, with the goal to verify orbital data with direct measurements of the volatiles. This project was called Resource Prospector. In 2015, the NASA Resource Propector team built a prototype terrestrial robotic lunar rover called RP15, a 300 kg rover which coupled conventional rotational wheel spin motion with a lifting and sweeping motion on each of its four appendages (Figure 3.1A). This drive-train allows the rover to use crawling strategies with its active suspension to traverse hills and escape entrapment (i.e. the state of no forward motion due to excessive sinkage) where wheel spinning alone would fail [116]. However, Resource Prospector was cancelled as a mission concept in 2018, hence little progress has been made on developing capabilities for RP15.

3.3 Mini Rover Robot Experiments in Dry Granular Media

To discover the locomotion principles for effective RP15 mobility and for more novel rover designs, Georgia Tech and NASA JSC collaborated to create a scaled rover robot (Figure 3.1B) called the Mini Rover that acts as a counterpart to RP15. Like RP15, the Mini Rover's locomotion combines aspects from both legged and wheeled robots, with appendages that intrude to provide propulsion (leg-like) while also spinning to disturb the local terrain through shear (spin-like). Experiments in a controlled tilting bed of loosely packed granular media (e.g. poppy seeds, used for their low polydispersity, low cohesion,

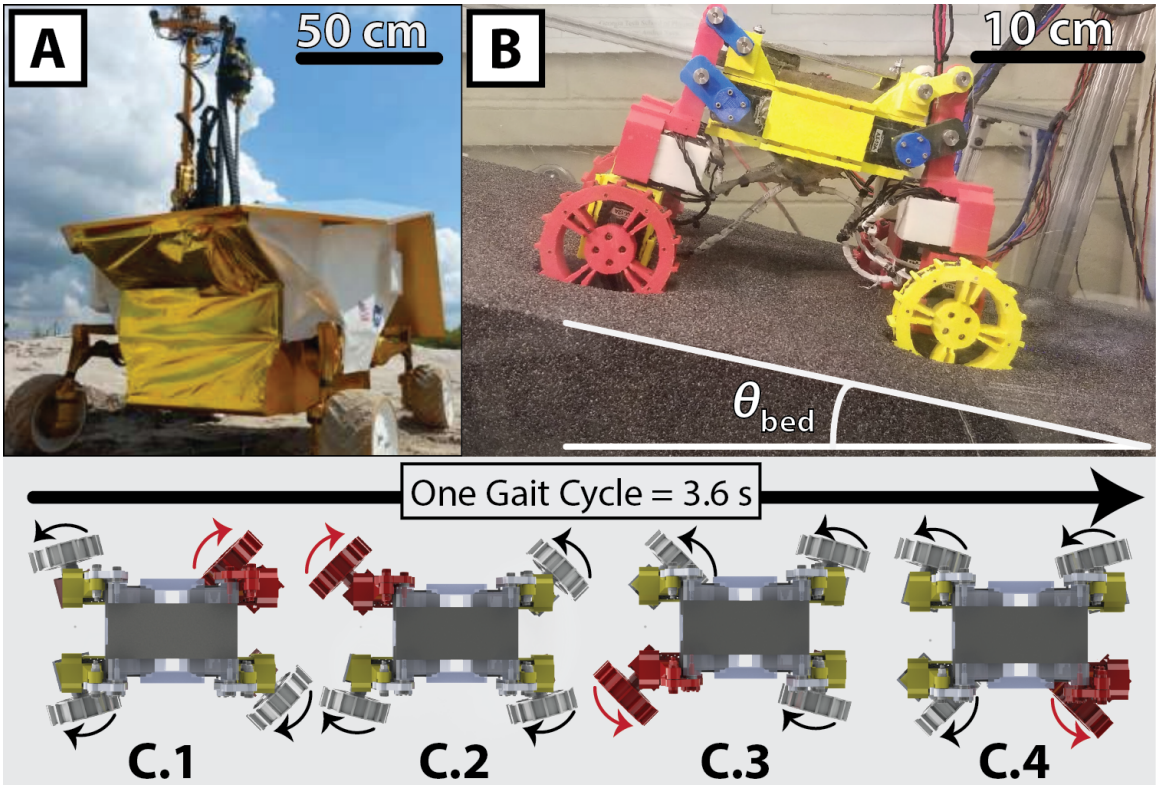

Figure 3.1: **Prototype Rovers with Legged Gait Capabilities** (A) NASA's RP15 prototype. (B) The Mini Rover resting on a bed of loosely packed poppy seeds on an incline of $\theta_{bed} \approx 20°$ (C) Four top-view rendered snapshots of the Mini Rover executing a quadrupedal gait: a Rotary Sequence (RS) gait with no modulation. In the RS gait, all wheels except the one colored in red sweep toward the rear of the rover for 2.7 sec. The sweep direction for each wheel in each snapshot is shown with the black arrows. Once the sweep is complete, the wheel begins the reset phase, where the wheel is colored in red. The Mini Rover lifts the resetting wheel with its four-bar linkage and rotates it 90° toward the front of the rover in 0.9 sec. The reset direction for each wheel is shown in red arrows.

and inability to damage robotic components) allow us to study its locomotion on slopes of GM with various open loop gait patterns and strategies. Open loop gaits have no feedback in their control logic, as each servomotor only receives position commands over time. These strategies are effective at greatly extended timescales for a much lower power draw in the robot, as the media has negligible rate-dependence in its force response in the quasistatic regime we tested [16]. Since these gaits mostly depend on geometrical shape changes of the rover rather than time-dependent dynamics, they are only force-limited and remain viable for low-power robots and rovers. The core mechanism in these gaits is movement and reconfiguration of the local terrain.

3.3.1 Mini Rover Construction and Experimental Methods

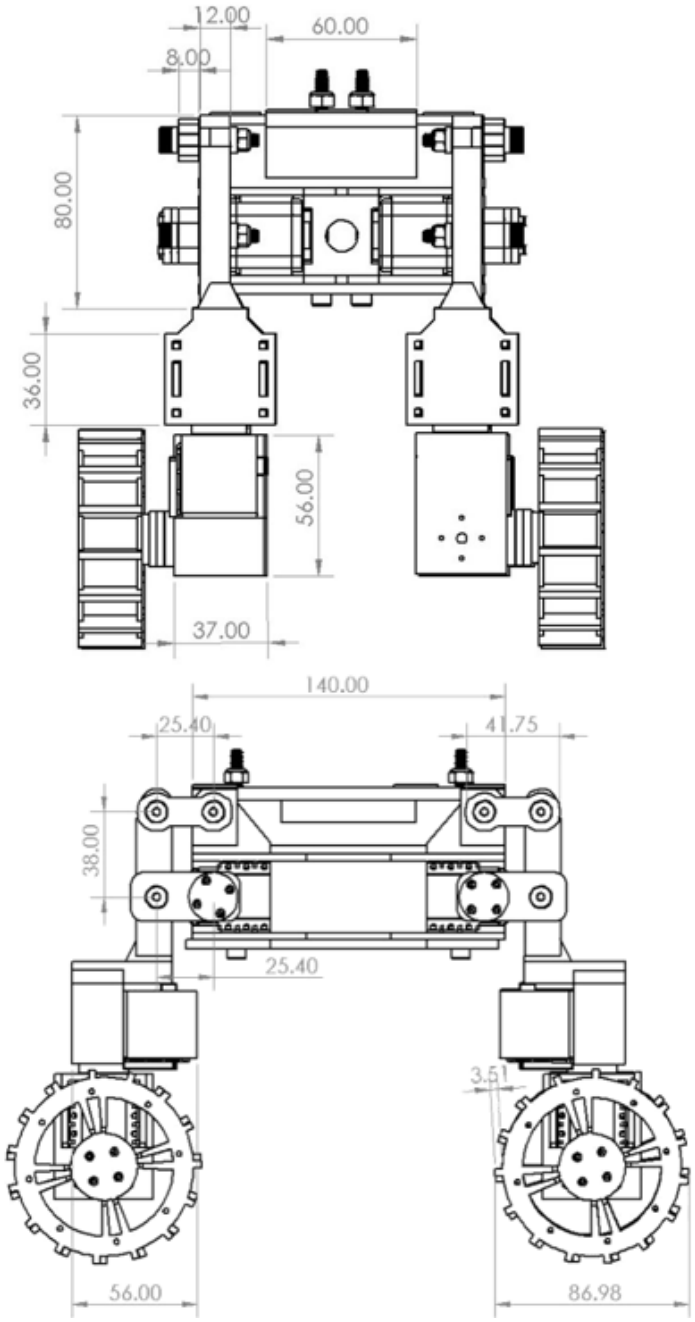

Figure 3.2: **Engineering Sketches of the Mini Rover** Front view and side view engineering sketches of the Mini Rover. Dimensions are in millimeters. Rover design by Siddharth Shrivastava [66].

To systematically evaluate the performance impact of varying the gait and to understand the dynamics of rover performance, a robophysical model rover (the Mini Rover) was de-

veloped by Shrivastava, inspired by RP15's morphology and movement. This model rover is 30 cm in length, 23 cm in height, and 20 cm in width. All rover body and appendage components were made of 3D printed ABS plastic. The rover has four appendages (an appendage is a term used to classify a rover subassembly containing the lifting, sweeping, and wheel spinning motors) which achieve lifting motion through a four-bar linkage, and the sweeping and spinning motions through direct motor connections. Each appendage is operated by three separate Dynamixel AX-12 servo actuators that are controlled with a Robotis USB2Dynamixel board. The appendages were assembled using various screws to fasten the four-bar linkages and servos, and a series of radial and ball bearings to minimize frictional forces. 3D printed hollow-body grouser-spoked wheels (8.7 cm diameter) were attached to wheel spinning motors. All assembly components were rigid and had negligible elastic deformation. Reflective markers were placed on the body to enable an Optitrack motion capture system to capture rover kinematic data. A steel bar attached to the top of the rover enabled an electromagnet on the automated gantry to lift and reset the rover for each experiment.

All Mini Rover experiments was conducted in an automated test bed (Figure 3.1B) full of our selected granular media (dry poppy seeds, $\sim$1 mm diameter) capable of tilting to change the bed incline (up to 30^o), air fluidization of granular media, capture of rigid body kinematic data, and precise resets of the robot through an Arduino controlled 3-axis OpenBuild gantry system. The gantry has a custom-made gripper that includes a DC-powered electromagnet (McMaster Carr,12V DC, 1.4W). Bed tilt was adjusted via two Firgelli heavy duty rod linear actuators (Firgelli Automations, Model FA-200-L-12-3). The granular fluidization mechanism (consisting of four RIDGID 16 gallon leaf blowers) blows air to fluidize the poppy seeds and reset the granular state as discussed in reference [117]. Four Optitrack motion capture cameras (NaturalPoint, Flex13, 120 FPS) were mounted on the tilting frame (the same frame of reference as the Mini Rover) above the granular bed and captured kinematic data of the IR reflective markers attached to the Mini Rover. All

the components of the automated setup were controlled via NI Labview.

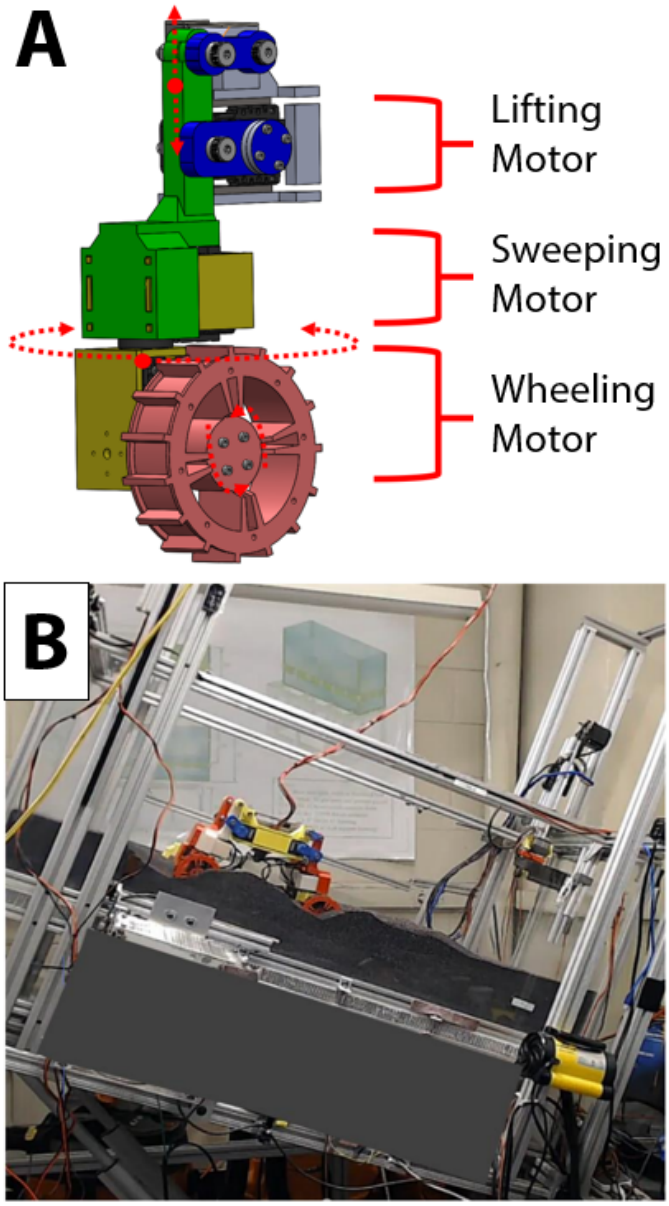

Figure 3.3: **Rover Appendage Actuation and Experimental Gantry Bed** (A) Diagram of the lifting, sweeping, and wheeling motions of a single rover appendage. (B) Photograph of the complete granular experimentation bed with terrain fluidization, motion capture, and an automatic robot-reset gantry.

Any usage of the term "gait" implies either RS or RRP gaits. In a traditional experimental cycle, the testbed angle (θ_{bed} between 0° and 30°), gait cycle quantity (≥ 0 cycles), and the duration of wheel spinning prior to gait execution (≥ 0 seconds) is set prior to trial initiation. The parameters of step frequency and wheel speed are constant for all trials

shown. Once these experimental parameters for the gait have been set, the trial is initiated and the rover wheels spin for a set time interval of 30 seconds. After this time interval, the wheels are sufficiently buried to be at the full slip condition and the rover is fully entrapped within the granular substrate. The rover then executes the gait, enabling positive locomotion from the embedded state. After the rover has stopped executing gait cycles, the trial concludes, the kinematic data from OptiTrack is imported to MATLAB and analyzed. The rover and granular terrain are then reset to their initial state through the automated gantry and bed fluidization respectively.

3.3.2 Rotary Sequence (RS) Gait Locomotion Results

The quadrupedal gait used for small θ_{bed} is the RS Gait with No Modulation. A series of four Solidworks renders viewed from the top of the Mini Rover looking downwards illustrate this gait in Figure 3.1C. At the figure's top is the arrow of time/sequence order, showing that one gait cycle takes a total 3.6 seconds to execute. The Mini Rover is drawn moving rightward. When executing its RS gait, the Mini Rover performs the same sequence of two-phase ('sweep' and 'reset') motions to each of its four wheels in a counterclockwise order, beginning with the front left wheel in the C.1 frame being in the 'reset' phase. In the RS gait, all wheels except the one colored in red 'sweep' towards the rear of the rover for 2.7 seconds. The sweep direction for each wheel in each snapshot is shown with the black arrows. Once the 'sweep' is complete, the wheel begins the 'reset' phase, where the wheel is colored in red. The Mini Rover lifts the resetting wheel with its four-bar linkage and rotates it 90 degrees towards the front of the rover in 0.9 seconds. The reset direction for each wheel is shown in red arrows. The Mini Rover then sets the wheel down to its original position, the 'reset' phase completes, and that wheel returns to the 'sweep' phase. The entire gait cycle is cyclic, so the motion repeats from C.1 after C.4 is complete. Each wheel is always offset in time and position from the others. During an RS Gait, each wheel is also spinning at 2.1 rad/s.

Shrivastava first investigated an open loop gait derived from tests of RP15's crawling capabilities at JSC. Previous studies showed that various open loop strategies for granular slope climbing were sufficient if the locomotor's dynamics allowed it to repeatedly intrude into undisturbed media [34, 118]. He implemented this gait on the Mini Rover (Figure 3.1C), by cyclically sweeping rearwards with three appendages while one appendage lifts upward to disengage from the medium, while also spinning all four wheels at a constant rate of 2.1 rad/s. This gait is classified as a quadrupedal RS gait with regards to its foot placement [119], which cycles around the rover's locomotion appendages. In Figure 3.1C, the RS gait has a time interval between each snapshot of 0.9 seconds. The wheels each have a radius of $R = 4.2$ cm and 15 grousers evenly spaced along the rim, so at a rotational speed of 2.1 rad/s each wheel intrudes approximately 5 grousers per second into the GM. We chose this wheel spin speed to agitate the local terrain multiple times per RS gait sweep, but when compared to a effect of gravity, the wheel spin is relatively slow. A comparable rate effect from gravitational acceleration of $\sqrt{g/R} \approx 15.3[1/s]$ is larger than the grouser intrusion rate. Since gravity is the larger rate effect in the GM, grains do not enter freefall and grain-grain contact is overall maintained. The wheel spins are considered 'fast enough' for repeatedly disturbing the GM, but not so rapidly that they dominate the terrain's acceleration over gravity.

Shrivastava tested the RS gait's dynamics against wheel spinning alone by placing the Mini Rover in the granular testbed, having it spin its wheels for 30 seconds, then it executed the cyclic RS gait for 60 seconds. Figure 3.4A shows the displacement vs. time for these trials at $\theta_{bed} = 0^\circ$. In the initial spin-only phase, the wheels increasingly slip and sink, which leads to eventual entrapment. For the Mini Rover in loose PS, 'wheel spin only' strategies resulted in entrapment for all tested $\theta_{bed} \geq 0^\circ$, as the Mini Rover's deep sinkage creates too much granular drag for effective wheel traction. However, once the RS gait began, the rover restarted locomotion at a speed comparable to that prior to entrapment. The speed attained with the RS gait was insensitive to the depth of the rover wheels in

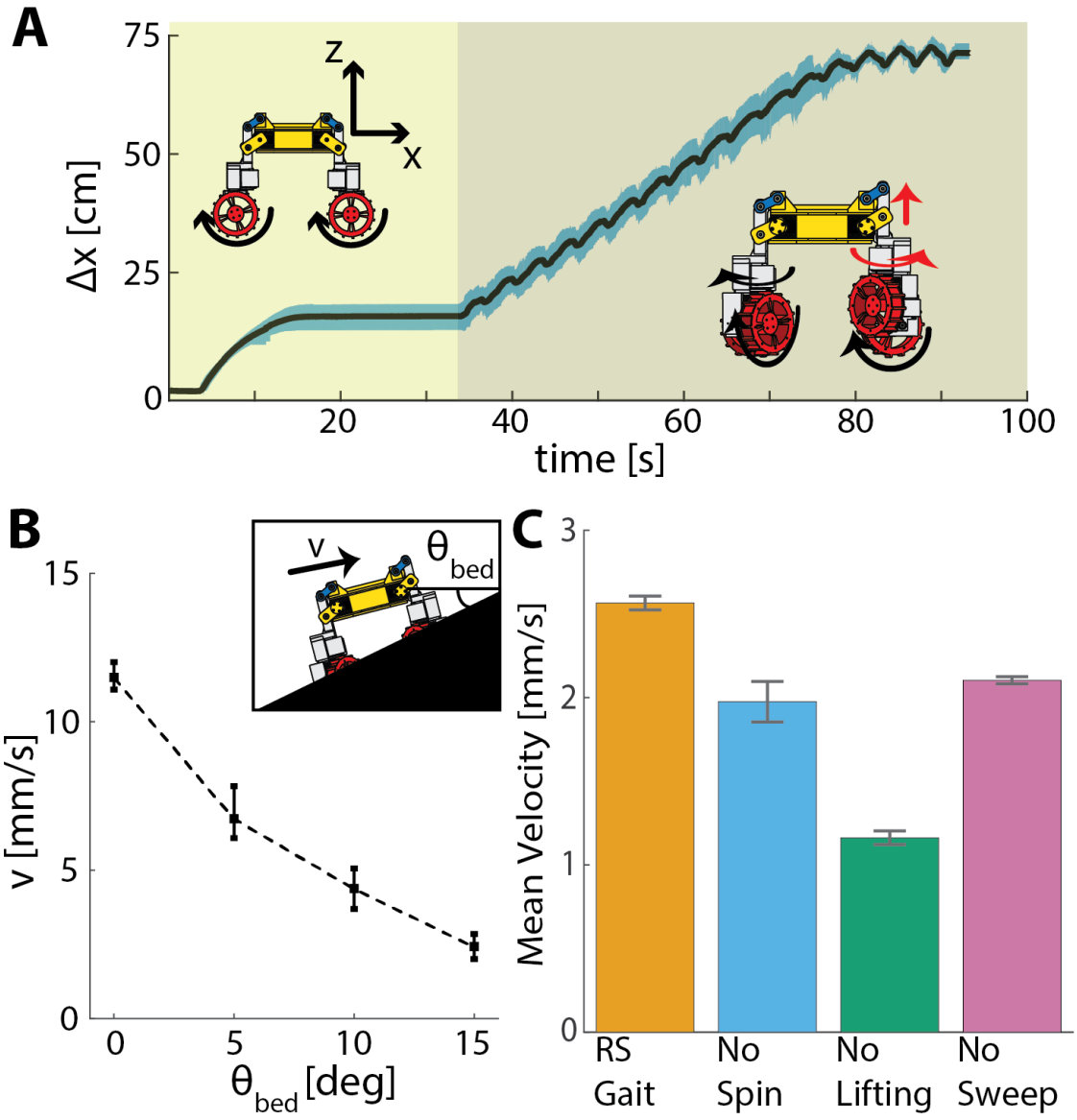

Figure 3.4: **Robustness and Performance of the RS Gait** (A) Horizontal displacement over time of the Mini Rover at rest for 5 sec. using wheel spin only on a 0° slope of loose poppy seeds for 30 sec. and then executing the RS gait described in Figure 3.1(C) for 60 sec. Data shown are means ± SD for seven runs. The time interval shaded yellow from 0 to 35 sec. is the "wheel spin phase," and shaded orange from 35 to 95 sec. is the "RS gait" phase. The Mini Rover reaches the end of the test bed near the 80-sec mark. (B) Mean ± SD velocities going uphill of the RS gait shown in Figure 3.1(C) for different granular slope angles, varying the θ_{bed} in Figure 3.1(B), with seven trials for each bed angle. (C) Mean ± SD average velocity over seven trials each in the steady state of the RS gait on a $\theta_{bed} = 15°$ poppy slope, with various subsystems of the gait disabled.

the granular medium (see Supplemental Fig. S4), as the Mini Rover will sweep against the terrain to generate motive force. Since the rover's sinkage oscillates over time during the RS gait, the rover also generates a lift force from its sweeping to push itself out of entrapment, an effect observed in granular media locomotion by previous studies [50]. This locomotion paradigm contrasts with the traditional relationship between slip & sinkage for wheeled vehicles [120], and instead behaves more like a locomotor paddling through a self-organized rate-independent frictional fluid [118, 45].

The Mini Rover's locomotion ability is not limited to flat terrains. The RS gait enables motion after entrapment on granular slopes θ_{bed} of up to 15° (Figure 3.4B). For each tested bed angle θ_{bed}, the rover achieves a different equilibrium speed for the RS gait when climbing hills with differing slopes. As slope increases, gravity gains a force component equal to $mg\sin(\theta_{bed})$ pulling the rover rearward, along with the grains losing resistive strength and avalanching more easily [113, 34, 121]. The robustness of the RS gait in climbing loosely consolidated slopes motivated investigation of the individual dynamics of the RS gait's different subsystems: wheel spinning, lifting, and sweeping. Shrivastava performed locomotion trials at $\theta_{bed} = 15^\circ$ with different subsystems disabled, along with the regular RS gait described before as the control (Figure 3.4C). Disabling any one of the three subsystems produced a lower mean velocity for the slope climbing. Disabling the lifting motion was the most detrimental to the forward velocity. By not lifting the wheels during the reset sweeps of the RS gait, the wheels did not disengage with the granular media and pushed the rover rearwards, decreasing its mean velocity. Disabling the sweeping subsystem reduced the granular volumes encountered and transported by each locomotor appendage. The wheels oscillate purely vertically, which temporarily escapes entrapment and avalanches small amounts of media rearward during intrusion due to wheel spin. Finally, disabling the wheel spin subsystem resulted in an $\approx 20\%$ speed decrease. Compared to the sweeping subsystem, the wheel spin requires less power.

3.4 Single-Wheel Gantry Experiments and RFT Modeling

To develop an understanding of these phenomena, we next isolated the multi-appendage Mini Rover locomotion system to a single locomotor appendage. We mounted a replica of a Mini Rover appendage which has both wheel spinning and sweeping capabilities to a six-axis force transducer (Figure 3.6A and Figure 3.5B). The entire system was mounted to a 2D gantry driven by stepper motors in a tilting, fluidizing bed of poppy seeds (Figure 3.5A). By approximately replicating the dynamics of the sweeping motion for a single locomotor appendage, we estimate the reaction forces felt by each appendage during the Mini Rover's gaits.

3.4.1 Recreating the RS Gait Trajectories

The appendage is forced at different fixed velocities v_x at set bed tilts θ_{bed} chosen to match the RS gait results from Figure 3.4B. To interpret the single wheel system, the forcing speed v_x is set as a constant value matching the average gait speeds of Figure 3.4B, whereas in the real Mini Rover system v_x varies with time as the gait executes. The variable θ_{sweep} in Figure 3.6A represents the degree of sweeping rotation of the wheel (i.e. a -90° offset from the wheel's steering angle), which varies over time as position commands are sent to the sweeping servomotor. We set the limits of this angle as $\theta_{sweep} \in [-\frac{\pi}{4}, \frac{\pi}{4}]$ to match the RS gait's sweeping motion, and this produces approximate motion paths which replicate the Mini Rover appendage's trajectory through the bed of poppy seeds. Figure 3.6B shows a shaded rectangle as a top down projection of a single wheel, with a crosshair in its center that moves along the trajectory paths. As θ_{bed} increases and its coupled v_x decreases, the Mini Rover wheel tends to sweep a greater percentage of the same granular area for each gait cycle.

In Figure 3.6A a diagram details the single wheel gantry testbed for testing granular force responses in the Mini Rover's locomotion. Two perpendicular rail systems (Fig-

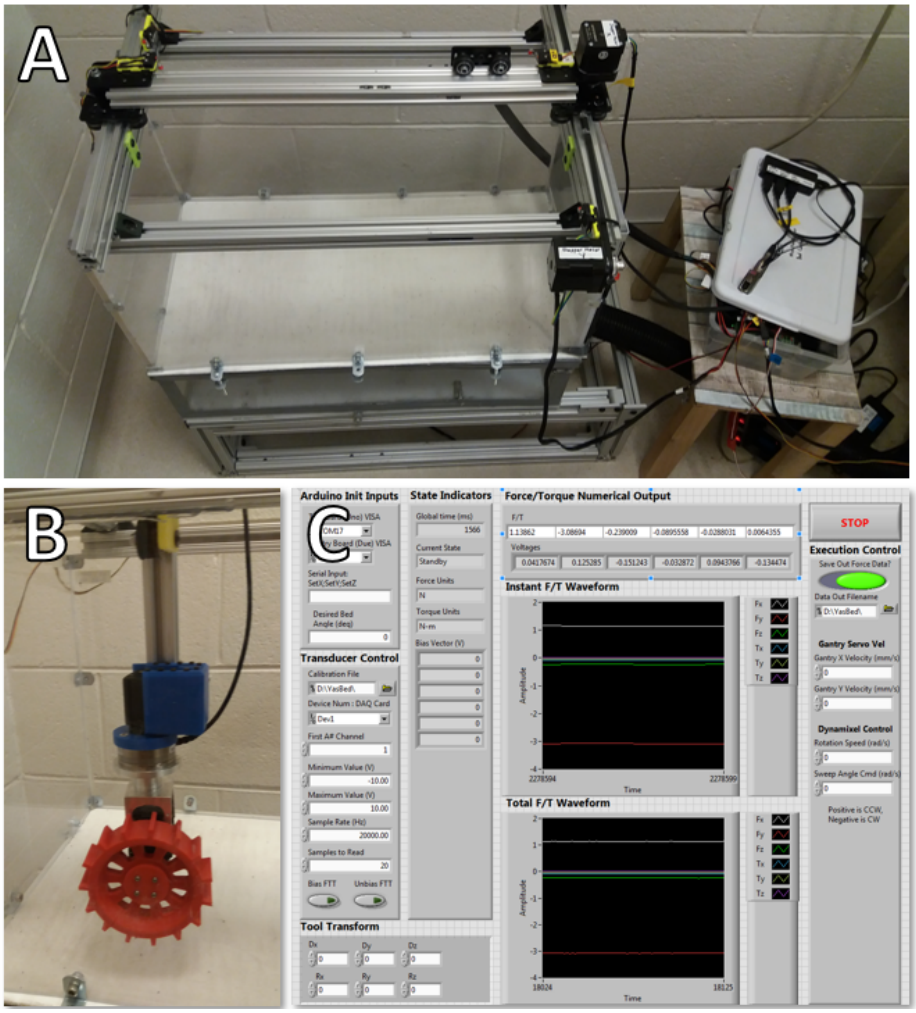

Figure 3.5: **Isolation Studies of the Single Mini Rover Wheel** (A) Single-wheel gantry test bed used for isolation studies, without poppy seeds. Stepper motors control the wheel's placement and forced velocity within the bed, and a leaf blower controlled by a proportional relay fluidizes the bed between trials. (B) Close-up of the wheel, Dynamixel servo, and force transducer assembly. (C) NI Labview front-end for running trials. An NI-DAQ commands the gantry steppers and servos via an Arduino microcontroller, and records reaction forces from the force transducer.

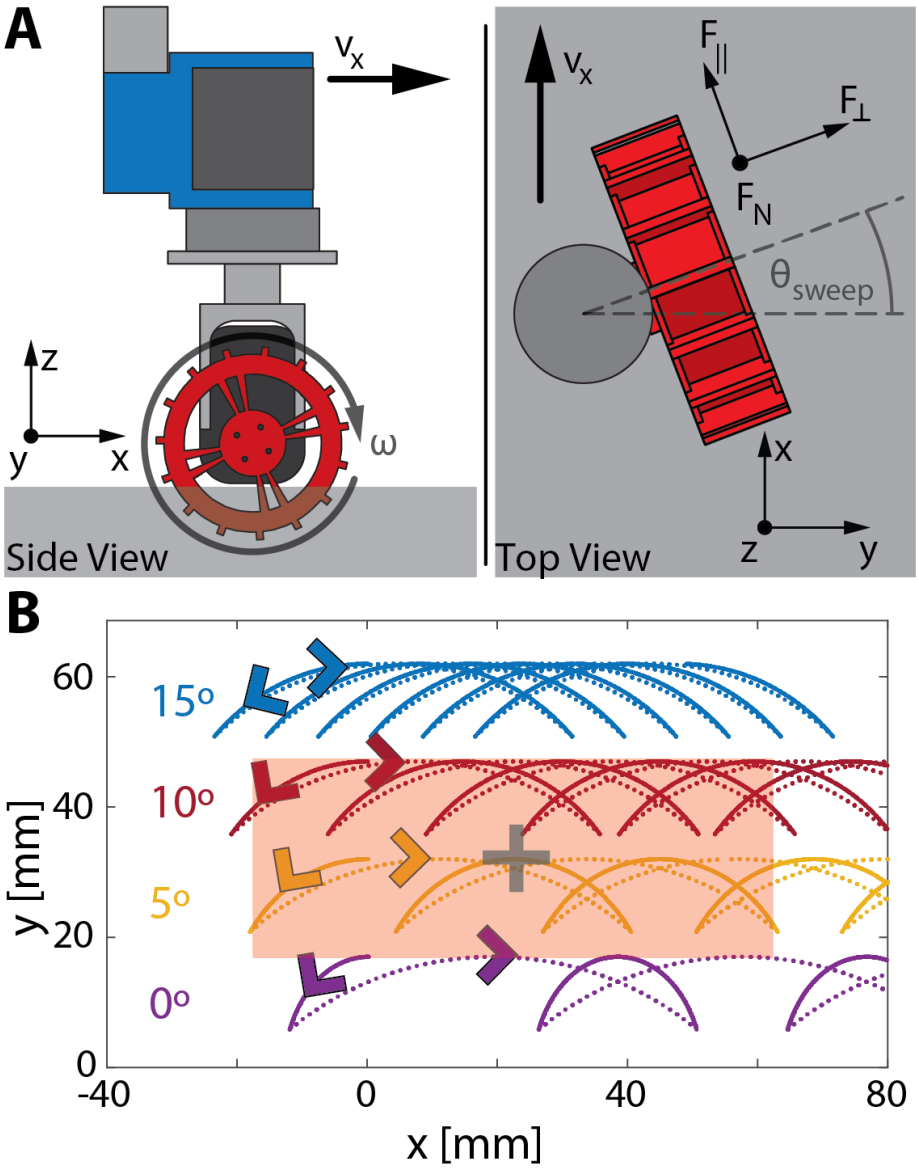

Figure 3.6: **Isolation Studies of Single-Wheel Force Response** (A) Side view and top view schematics of the single-wheel gantry test bed. The Cartesian coordinate system (x, y, z) describes the world frame aligned with the test bed, whereas a local Wheel coordinate system $(F_{\parallel}, F_{\perp}, F_N)$, which rotates about z by θ_{sweep}, defines the force responses parallel, perpendicular, and normal to the wheel at each sampled θ_{sweep}. The wheel coordinate system rotates over time as the appendage executes its gait. (B) Top-down sketch of the sweeping wheel path input into the system in (A) at different θ_{bed} values. The shaded rectangle is a projection of the top-down view of a single wheel for scale.

ure 3.5A) hold a sweeping Dynamixel servomotor connected to a six-axis Force/Torque transducer (ATI Mini40), with its tool side connected to a wheel spinning Dynamixel servo, which spins a wheel design copied from the Mini Rover (Figure 3.5B). The system locomotes in a granular bed of poppy seeds which fluidizes to a loose-packed state after every trial and can tilt up to 30° from horizontal like the granular bed described previously.

The left panel of Figure 3.6A is a side view with the y-axis of a Cartesian coordinate system out of the page. The gantry system is forced in the $+x$ direction by a stepper motor coupled to a timing belt at a speed v_x at various granular bed tilts θ_{bed}. v_x is chosen for each bed angle to approximate the actual Mini Rover speeds measured in Figure 3.4B. The gantry is free to fall under its own weight during locomotion, simulating the normal force on the Mini Rover. Measurements with a scale gave 3.4 Newtons (350 grams) of normal force when the wheel rests on a solid surface. For all trials where wheel spinning is enabled, the wheel spins at $\omega = 2.1$ rads/second.

To match a single wheel's RS gait period, θ_{sweep} sweeps back from $+45^\circ$ to -45° in 2.7 seconds, then sweeps forward to reset from -45° to $+45^\circ$s in 0.9 seconds, as shown in Figure 3.6B. All of the paths are represented by dots evenly spaced in time by 30 ms. The different colors represent different tilt angles and thus different commanded v_x. For bed tilt angles of [0,5,10,15] degrees, v_x was matched as [11.5, 6.7, 4.4, 2.4] mm/s respectively. These correspond to path colors [violet, yellow, crimson, blue] respectively. Each path is drawn for a total of 6 gait cycles. The different v_x values are the only parameters that influence these, as the sweeping period and amplitude is identical among all these paths. This motion command creates an arcing motion in space that has the wheel sweep the same granular area multiple times in its locomotion.

3.4.2 Single-Wheel Force Results and RFT Approximations

In the absence of a fully validated continuum model of complex granular interactions, a reduced-order empirical model called granular RFT can approximate the resistive forces

on arbitrary intruders like our Mini Rover wheel by modeling the GM as a non-deforming isotropic medium and modeling the intruder as a rigid body composed of small plate elements [17]. Due to the locality of granular force responses, it is possible to linearly add each small plate element's respective resistance (calibrated via simple intrusion experiments) as a function of depth, orientation, and velocity. This sum of plate elements acts as a good approximation for the whole intruder for most intrusion states [49]. Although RFT does not account for local terrain deformations in its force calculation, we will show how external agitations that reflow media to be locally homogeneous allow RFT to accurately predict force response as though the medium was fixed in place. This reflow of the GM allows us to accurately calculate the force responses of the Mini Rover's RS gait.

In Figure 3.7, we observe that the resultant PS surface varies significantly after the single wheel is forced through the substrate at $v_x = 11$ mm/sec with various additional motions. With spin only, we dig a narrow trench of width approximately that of the wheel as GM is agitated and forced laterally (Figure 3.7A). With sweeping only, the wheel forms an asymmetric mound biased towards the $\theta_{sweep} > 0^\circ$ direction as it collects and pushes GM with its intruding face (Figure 3.7B). However, when both spinning and sweeping motions are applied, the agitation of the local GM from spinning redistributes the uneven mound into a loosely packed, yet overall smooth surface (Figure 3.7C). We will show that this action of constantly reflowing grains to maintain a local frictional fluid makes such complex locomotion more tractable in the RFT interpretation.

An entrapped Mini Rover in flat GM has an RS gait of $v_x = 0$ mm/s and $\theta_{bed} = 0^\circ$, where the appendage is repeatedly sweeping through the same granular volume. The force transducer is mounted to the sweeping actuator, so its orthogonal coordinate system measures forces parallel, perpendicular, and normal $\{F_{||}, F_{\perp}, F_N\}$ to the wheel's orientation which depends on the current θ_{sweep}. With $v_x = 0$, a stationary rotational axis of symmetry about z lets us interpret the force components with only the single variable θ_{sweep}. This allows a 2D calculation of the expected forces on the sweeping intrusion geometry. We use

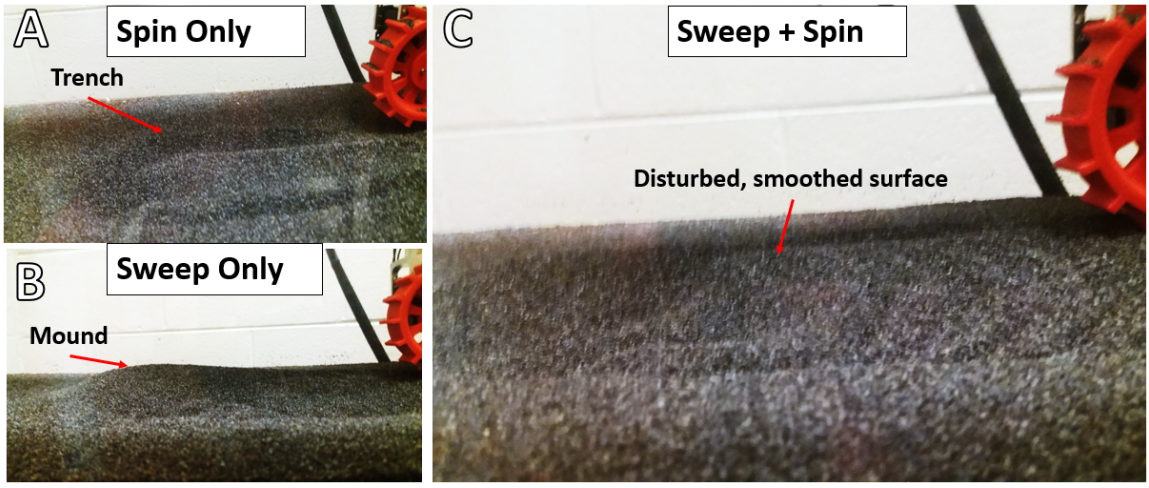

Figure 3.7: **Granular Surface Profiles from Mini Rover Single-Wheel Studies** (A) View of the poppy seed surface after a test with only wheel spin at 2.1 rad/sec and $v_x = 11$ mm/sec. The test leaves a shallow trench of disturbed poppies with small piles to either side. (B) View of the poppy seed surface after a test with only an RS gait sweep and $v_x = 11$ mm/sec. The test leaves a deep trench with large mounds of poppies on the sweep-ending side. (C) View of the poppy seed surface after a test with both an RS gait sweep, wheel spin at 2.1 rad/sec, and $v_x = 11$ mm/sec. This test both sweeps and agitates a large swathe of poppies to create a relatively smooth surface with a wavy pattern.

RFT to calculate the expected values of the three force components for the sweeping wheel geometry. Figure 3.8 shows the RFT predictions along with the experimental mean and SD of these force components over 20 rearward gait sweeps each (i.e. from $\theta_{sweep} = \pi/4$ to $\theta_{sweep} = -\pi/4$) in a steady state with the wheel not spinning vs. the wheel spinning at 2.1 rad/s. These trials investigate why wheel spinning might create the significant speed improvement seen in Figure 3.4C. Force data show that spinning the wheel during the sweep produces flatter force responses which are more predictable from RFT, as the wheel spinning reflows local grains and homogenizes the local medium by actively avalanching local mounds (Figure 3.7). Unlike traditional wheeled locomotors which gain motive force by shearing terrain under pressure rearward with their wheels [120], the Mini Rover in the RS gait uses its wheels chiefly as agitators, while gaining the majority of its motive force from the sweeping motion. By adding agitation to the local terrain, the granular mound interactions which cause deviations from simple RFT-like force response are smoothed out.

For Figure 3.8, the commanded sweeping motion describes a simple path through space that is symmetric about the z-axis with $v_x = 0$ mm/s. This cylindrical symmetry about the

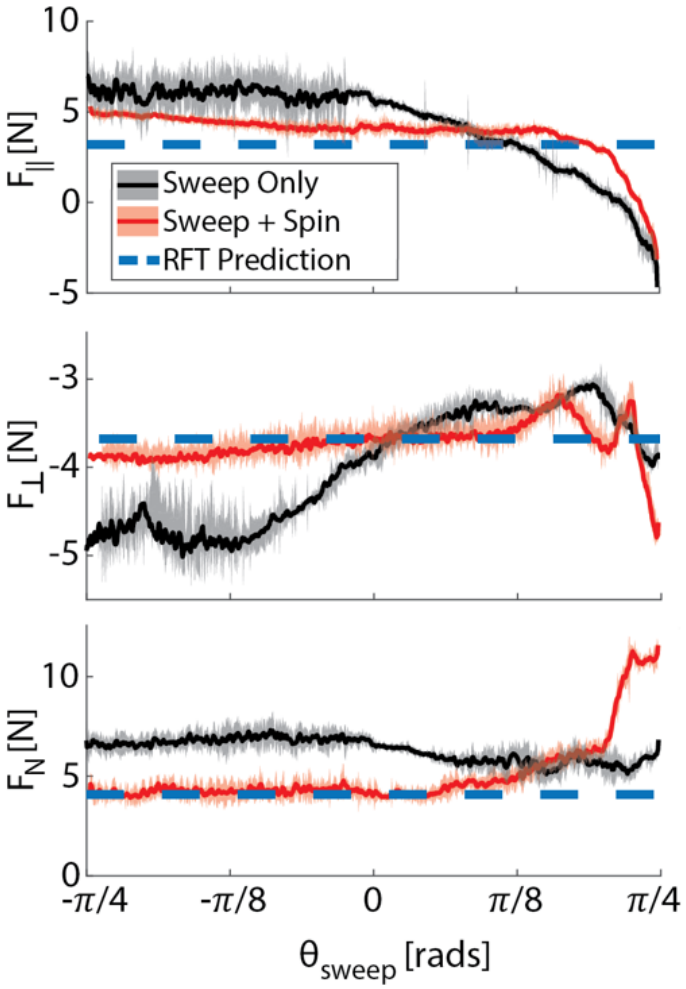

Figure 3.8: **Single-Wheel Force Response in the Stationary Frame vs RFT Predictions** For $v_x = 0$ mm/sec and $\theta_{bed} = 0°$, force components for a stationary RS gait sweep rearward with wheel spin off versus wheels spinning at 2.1 rad/sec. RFT calculation of the resistive forces for this trajectory gives flat force response curves with respect to θ_{sweep}, because of cylindrical symmetry about the z axis.

z-axis of the force response allows a simple calculation through RFT which is independent of θ_{sweep}, giving a flat force response for all three force component plots, shown in the blue dashed lines in Figure 3.8. The RFT calculation approximates the single wheel geometry as a narrow cylinder then projects to two dimensions. Once in 2D, we calculate the forces for a partially intruded cylinder with the dimensions of the Mini Rover wheel sweeping about the z-axis using the techniques described by Li, Zhang, and Goldman [17]. The depth was calibrated by matching the RFT wheel depth to the experimentally observed depth of the single wheel in video recordings of gantry experiments. We use in the established RFT

coefficients of loosely packed poppy seeds from the Li et al. paper for all of our RFT calculations.

When $v_x \neq 0$ mm/s, the cylindrical symmetry breaks and a more complete three-dimensional RFT calculation is needed. For each set of experiments in Figure 3.9, we perform a quasi-3-D RFT simulation which recreates the single wheel gantry experiment geometry. This calculation decomposes the top view of Figure 3.6A into a geometry of many adjacent small rectangles at depths dictated by the wheel sinkage. The wheel is still approximated as a narrow cylinder, but now each subsegment has a more complex motion through space dictated by the test trajectories of Figure 3.6B. The RFT calculation is then performed on this set of subsegments and summed to give the net resistive force. Also, only subsegments which had both leading edges in their normals (i.e. $\hat{v} \cdot \hat{N} > 0$) and were sunk below the surface were included in the force calculation. For the 3D RFT calculation, the wheel was modeled as a non-grousered solid cylinder with caps, with the sides of the wheel approximated as the flat faces of a cylinder. The force per plate calculation is performed by projecting the 3D problem into in the xz-plane as shown in the side view of Figure 3.6A (left) and calculating the resistive forces in the intruding 2D cylinder. We then approximate 3D RFT as being cylindrically symmetric, such that the resistive force vectors of the xy-plane in Figure 3.6A (plane parallel to granular surface) are exactly opposite to each subsegments' velocity vector (i.e. $\hat{F} = -\hat{v}$ in Figure 3.6A right). In this way, we neglect drag anisotropy by observing that most subsegments have velocity vectors mostly pointing toward the normal (i.e. overall $\hat{v} \cdot \hat{N} > 0.5$) in their commanded motions. This is not trure 3D RFT as there exist additional symmetries beyond cylindrical in the 3D case, but this was appropriate for our scenario as long as we obeyed the leading edge condition. The forces in the xy-plane are thus approximated by projecting the horizontal forces of each subsegment calculated from the diagram in Figure 3.6A (left) into the proper xy velocity frame. The same method calculates the resistive forces to the two flat sides of the wheel, just with the normal vectors rotated 90 degrees.

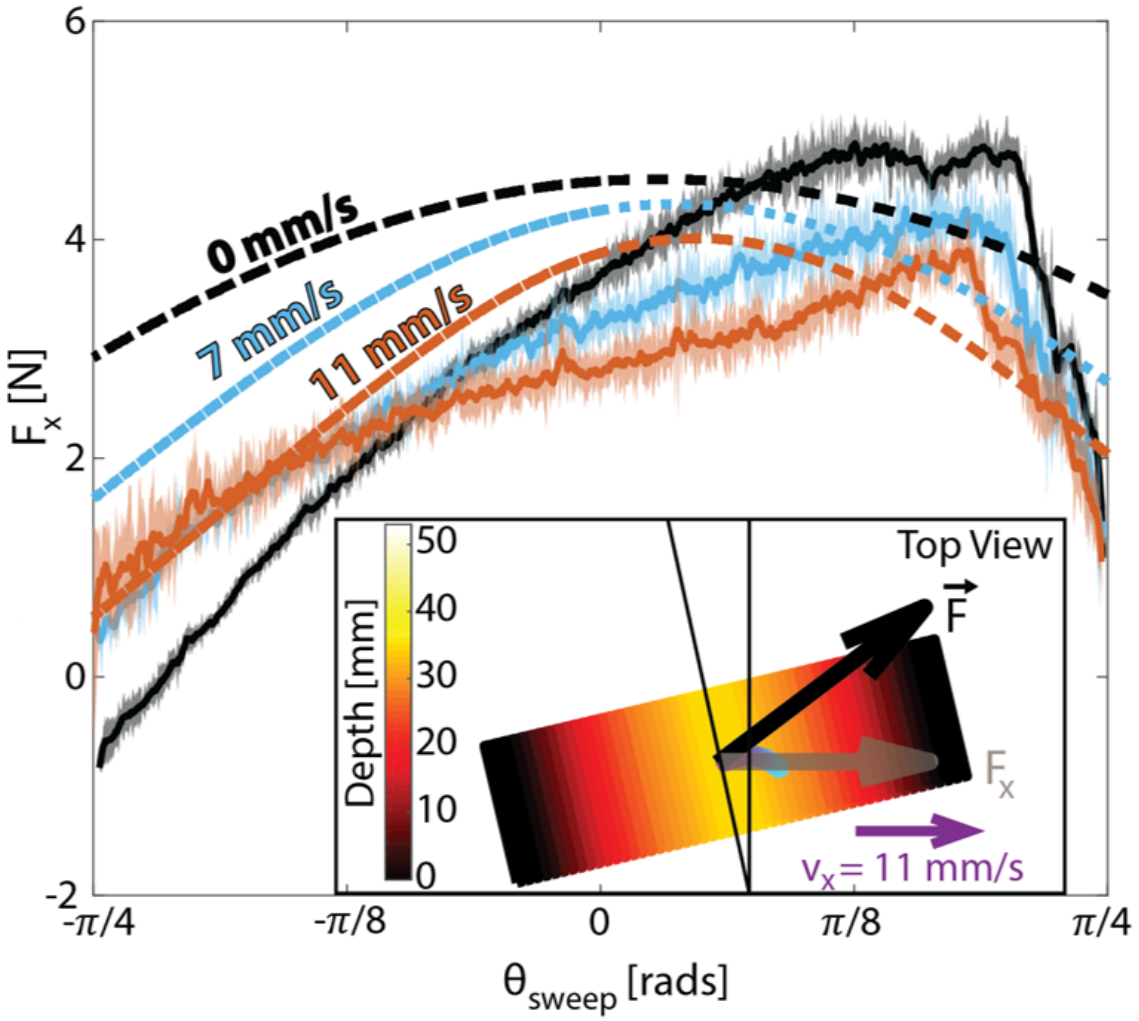

Figure 3.9: **Single-Wheel Net Drawbar Force Response in the Moving Frame vs. RFT Predictions** For $\theta_{bed} = 0°$, varying v_x in the gantry system Figure 3.4(A) varies the drawbar force curves with respect to sweep angles. Experiments in solid lines, mean $\pm$ SD across 20 sweeps in the steady state, and wheel spinning at 2.1 rad/sec. Inset: 3D RFT simulation diagram for $v_x = 11$ mm/sec.

The inset for Figure 3.9 shows a simulation snapshot for $v_x = 11$ mm/s, with a net force response vector which we then project onto the x-axis to obtain the drawbar force at each θ_{sweep} value. From experimental video, we estimate the single wheel to be buried about 35 mm deep at its deepest point, from which we can infer the depths for each wheel segment in the RFT calculation. The wheel's subsegments are colored by depth, with the hotter colors indicating deeper burial (up to 35 mm). A trailing series of dots near the wheel center also show the last 0.3 seconds of trajectory. These RFT simulations create the force curves represented by the dashed line curves in Figure 3.9.

A primary force of interest in Figure 3.9 is F_X (the 'drawbar' force in the vehicle mechanics literature [122]), as this represents the motive force the Mini Rover generates with one appendage during its RS gait. For nonzero v_x, there is no stationary axis of symmetry about z, so we transform the force components into the gantry coordinates (x, y, z) with a rotation matrix about z by the time-dependent θ_{sweep}. We can also approximately extend the RFT calculation to three dimensions via a similar set of transforms (described above) for each tested v_x. Figure 3.9 shows the RFT predictions for three chosen v_x as dashed lines along with the corresponding experimental force data. RFT predicts higher net F_X as v_x decreases due to more segments of the wheel having net rearwards motion due to θ_{sweep}. However, the experimental forces match best at the highest tested v_x and then diverge from the RFT calculation at lower v_x. Since RFT approximates the granular media as a fixed volume in space, its predictive power is best for undisturbed, homogeneous regions of terrain. As v_x increases, the sweeping wheel encounters more undisturbed terrain per gait cycle (see Figure 3.6B), so RFT gives a more accurate estimate. The data also suggest significant decreases for drawbar force for $\theta_{sweep} < 0$ for all tested v_x, whereas RFT predicts a mostly symmetric response response about $\theta_{sweep} = 0$. This is due to the wheel re-encountering previously disturbed terrain that was swept away by previous gait cycles, suggesting that gait strategies should seek to both sweep through undisturbed terrain if possible as well as actively reflowing the local terrain to eliminate its 'memory' from previous gait cycles (as shown in Figure 3.7C).

3.5 Rovers' Motive Forces and Robustness to Appendage Disability

3.5.1 Measurement and RFT Prediction of Mini Rover Motive Force

To further explore the Mini Rover's motive forces, Shrivastava performed experiments measuring the net drawbar force for different slopes using the RS gait (Figure 3.10A). After 30 seconds of wheel spin, the Mini Rover executes the RS gait for 215 seconds while we measure its drawbar force with a strain gauge. The saturated force values near the end of

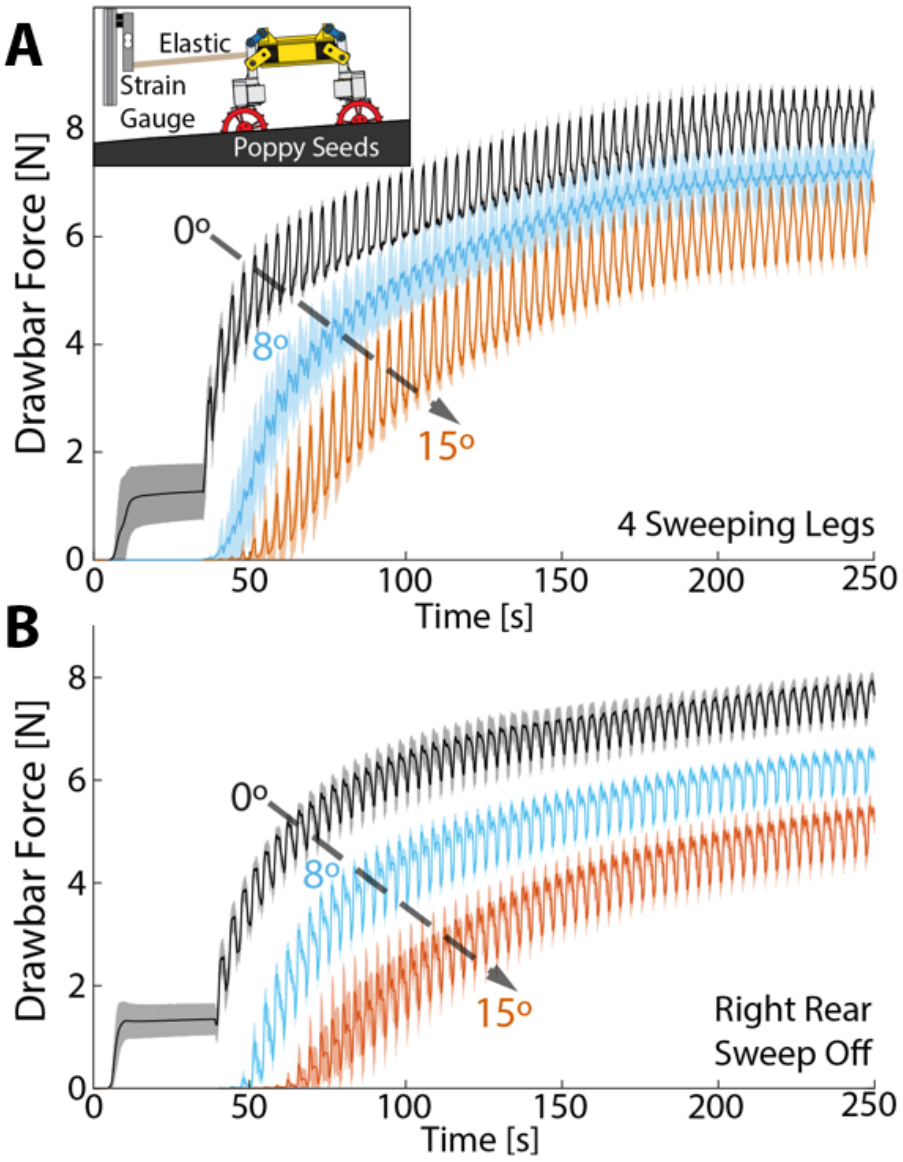

Figure 3.10: **Propulsive Forces in the Mini Rover's RS Gait** (A) Drawbar forces exerted over time by the Mini Rover using the RS gait with four sweeping legs up a bed of loosely packed PS at $\theta_{bed} = [0°, 8°, 15°]$ (inset shows experiment setup). Data shown are means $\pm$ Standard Deviation (SD) over seven trials for each value of θ_{bed}. (B) Drawbar forces exerted over time by the Mini Rover using the RS gait with three sweeping legs (with rear left leg sweeping disabled) up a bed of loosely packed PS at $\theta_{bed} = [0°, 8°, 15°]$. Data shown are means $\pm$ SD over seven trials for each value of θ_{bed}.

each trial approximate the maximum possible drawbar force the Mini Rover can exert at a given θ_{bed}, which we can then compare to the sum of four gait appendages in the previous RFT calculation. Figure 3.11A shows each saturated experimental drawbar force from Figure 3.10A compared with the corresponding potential drawbar from RFT. In this subfigure, the rover has periodicity in its force profile over a gait cycle which cycles through the reset phase for all four wheels. Meanwhile, the RFT is expected to have a quarter of the periodicity of one gait cycle, as it simply involves summing drawbar forces over four offset 'isolated' wheels with no wheel-wheel interaction on unchanging flat terrain force at a constant v_x. In experiment, the rover also experienced oscillations over its gait cycle (see Figure 3.4A) which add variation to the drawbar measurement due to its spring-like attachment to the sensor. For increasing θ_{bed}, gravity increasingly pulls the Mini Rover rearwards, so its sink and slip increases. Yet due to the active reflowing of the Mini Rover's wheel spin, local terrain was homogenized enough for RFT to predict net drawbar reasonably well based on v_x alone assuming a singular sinkage. Despite all the kinematic differences, this simple RFT calculation estimates the mean drawbar for a range of bed angles.

To capture the drawbar experiment data, a Uxcell bar-type load cell was fastened to the bed frame. One end of an elastic tube was attached to the load cell and the other end to the rover. A HX711 Load Cell Signal Amplifier was used to process and feed the signal into a microcontroller. The microcontroller printed drawbar values at 11 Hz to a connected computer.

For Figure 3.11A, the RFT calculation results for each set of [θ_{bed}, v_x] parameters from Figure 3.9 were interpolated as functions of θ_{sweep}. We then created four 'virtual' wheels which had the gait sequence, timing, and trajectory of the RS gait to represent the four wheels of the Mini Rover, calculated the forces on each wheel with our interpolated RFT functions, then summed the drawbar forces created by each virtual wheel to estimate the net drawbar force over time.

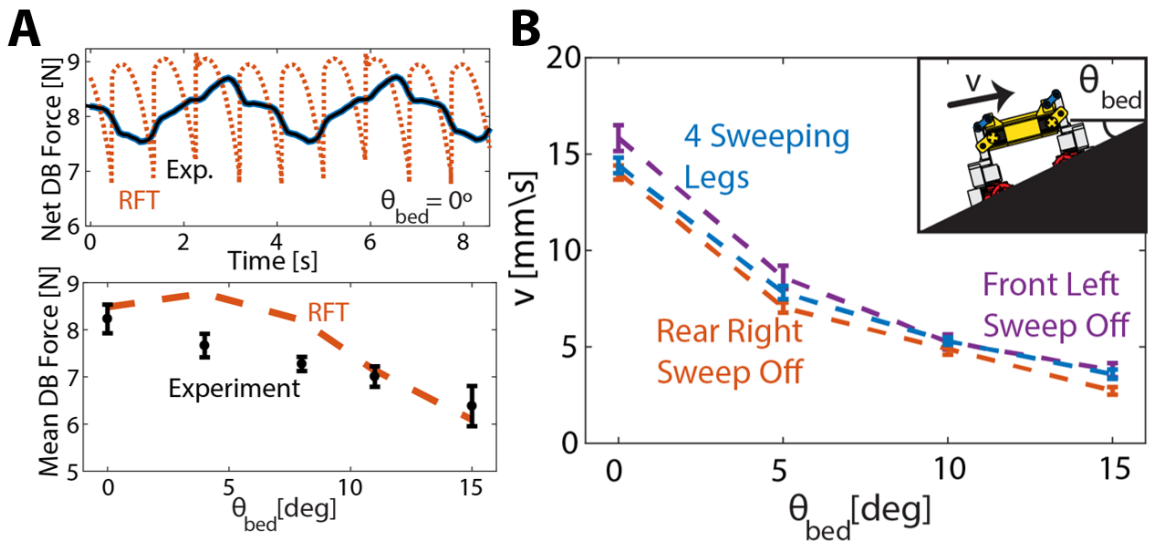

Figure 3.11: **Mean Drawbar Forces and Locomotion Speeds of the Mini Rover's RS Gait** (A) Mini Rover saturated drawbar forces with the RS gait (top) experimental (solid) versus RFT-based calculation (dashed) over time for two gaits cycles of the RS gait, summed over all four locomoting appendages. Bottom: Mean saturated drawbar pull with respect to θ_{bed} for experiment (error bars) versus RFT calculation (dashed). (B) Mean $\pm$ SD velocities going uphill of the RS gait with four sweeping wheels versus selectively disabled sweeping wheels for different granular slope angles, varying the θ_{bed} with seven trials performed for each bed angle.

3.5.2 Robustness to Appendage Failure

We also investigate the robustness of the RS gait by selectively disabling the sweeping motion of a single locomotor appendage. For Figure 3.10B, we disabled the sweeping capability of the rear right appendage and measured the Mini Rover's drawbar pull for different granular slopes. The rear right wheel still executed its spinning motions during these trials, so it effectively acted as a passive agitator of contacted grains, rather than an active sweeping component that exerts locomotive force. Compared to Figure 3.10A, the rover exerted lower net drawbar force over time for all tested slopes. Since each appendages' sweeping motion is the primary generator of drawbar force, we expect such a force reduction. The Mini Rover made progress with one of its rear wheel's sweeping disabled and exerted an increasing drawbar force through the RS gait with only three sweeping legs. We then removed the drawbar apparatus and tested the unburdened rover's performance on various slopes as in Figure 3.4, again with the rear left appendage's sweeping disabled.

Surprisingly, our results in Figure 3.11B show that the RS gait's velocity was only slightly reduced by this handicap. Even on the steeper slopes, the 3 legged trials maintained similar displacement profiles to the 4 legged trials, albeit at a lower speed. Since the disabled sweeping wheel still spins to fluidize local grains, we hypothesize that the other appendages were still able to function normally in the locally agitated medium. Another set of trials disabled the front left appendage's sweeping motion, and the translational velocities of the unburdened rover even surpassed that of the 4 trials on some slopes. Along with Figure 3.4C, this result showcases the robustness of the RS gait's locomotion mechanism to component failure, along with potential for future optimizations for the gait performance.

3.5.3 Rovers' Motive Forces in Wet GM

To validate our laboratory tests of the Mini Rover, Shrivastava & Pettinger also performed drawbar tests with the RP15 rover (Figure 3.1A) at NASA JSC to compare the RS gait vs. wheel spinning alone (Figure 3.12A). RP15's dimensions are 140 cm in length, 200 cm in height, and 140 cm in width, with a mass of 300 kg. A mechanical scale captures the drawbar force exerted by RP15. One end of the scale was fastened to the ground and the other to an elastic which was attached to the rear of RP15 (Figure 3.12A). A Phoenix motion capture system captured the kinematic data of the rover via reflective markers placed on RP15.

Due to technical issues with the NASA rover, they conducted RP15 tests with only three operational sweeping leg actuators. As a result, only 3 appendages were able to fully execute the RS gait. They were also only able to conduct tests of RP15 on a flat, moist, sand bed due to constraints in the testbed environment. The moist terrain led to accumulation of compacted sand between the grouser spokes, changing the wheels' effective geometries to cylinders over time. RP15 would begin its experiment with only wheel spinning, and then initiate the RS gait. A trial was concluded once RP15 could no longer locomote due to the saturation of drawbar force once it was at 100% slip. To reset the rover, the grousered

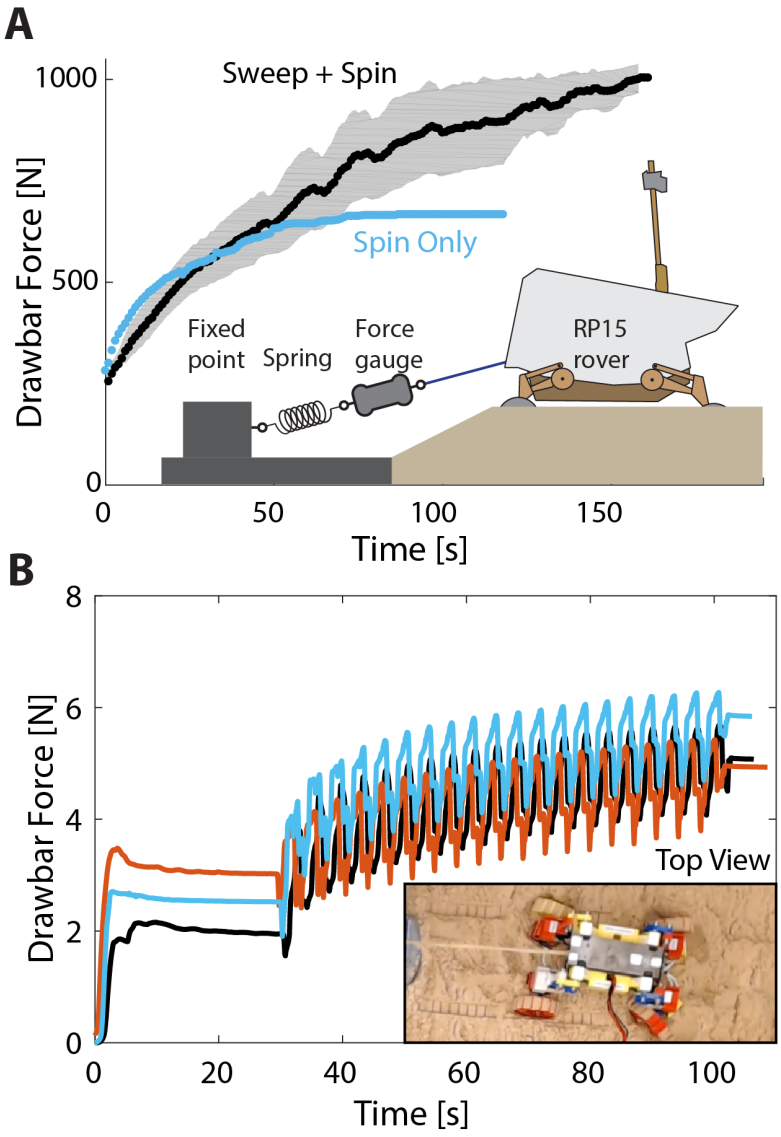

Figure 3.12: **Propulsive Forces of RP15 and Mini Rover in Wet GM** (A) Drawbar forces exerted over time by RP15 during tests in a bed of moist sand at JSC (diagram shows experimental setup). Blue data points show one trial of RP15 executing a wheel spin motion for 120 sec, and black data show the means $\pm$ SD for three trials of RP15 executing an RS gait for 170 sec. (B) Drawbar force versus time for three moist sand RS gait drawbar trials of the Mini Rover. Each different colored line represents a different trial. The Mini Rover generates increasing drawbar force with the RS gait even with one appendage sweeping mechanism disabled and in a much more cohesive substrate than the dry GM trials with three active wheels. Inset: Mini Rover in a bed of moist sand exerting drawbar forces with the RS gait in a bed of moist sand (top view). Qualitatively, the grouser-sand interaction appears to closely mirror the RP15 experiments (e.g., the grousers became smooth as the wheels spin and sand aggregates between the grousers.)

wheels were excavated from entrapment, and the rover reversed its motion back to the initial starting position. They then pushed a device which aerated the wet sand to restore terrain homogeneity between experiments. Only the flat incline angle (0°) had experiments performed. An experiment with only wheel spinning motion was also conducted without any transition to the RS gait for comparison.

Despite these differences from previous laboratory tests of the Mini Rover, we observed an increase in motive force in the RS gait as opposed to wheel spinning only (Figure 3.12A), same as the lab results. Like the Mini Rover it inspired, RP15 creates a significant drawbar advantage using its active suspension via crawling gaits over traditional wheeled locomotion. This strategy can increase drawbar pull without large decreases in rover velocity [123]. Shrivastava also performed drawbar experiments on the Mini Rover which imitated the constrains of the RP15 tests, including disabling the sweeping mechanism of one Mini Rover appendage. Drawbar tests for the Mini Rover using the RS gait in moist sand (with a 1.8% water mass to dry GM mass ratio) yielded similar results to the wet sand trials with RP15 (Figure 3.12B). This wet sand has a very different rheology from dry GM due to its high cohesion, force saturation length scales, and high critical angle, making it inaccurate to model with dry substrate RFT [124]. However, the RS gait still increased the Mini Rover's drawbar pull in this differing rheology. The legged RS gait with wheel spin is thus robust to varying terrain types and even component failure.

3.6 Rear Rotator Pedaling (RRP) and Slope Reconfiguration

The RS gait developed for RP15 is robust for many scenarios, but cannot successfully climb granular slopes near the critical angle of avalanching. For $\theta_{bed} > 20^\circ$, the RS gait generates unpredictable behavior - from roll over to significant yaw. To climb these steeper slopes in the laboratory, Shrivastava developed a specialized hill climbing gait which we refer to as "Rear Rotator Pedaling" (RRP, see Figure 3.13). Like the RS gait, the Mini Rover lifts and resets the wheel colored red at each snapshot of Figure 3.13, now alternating between

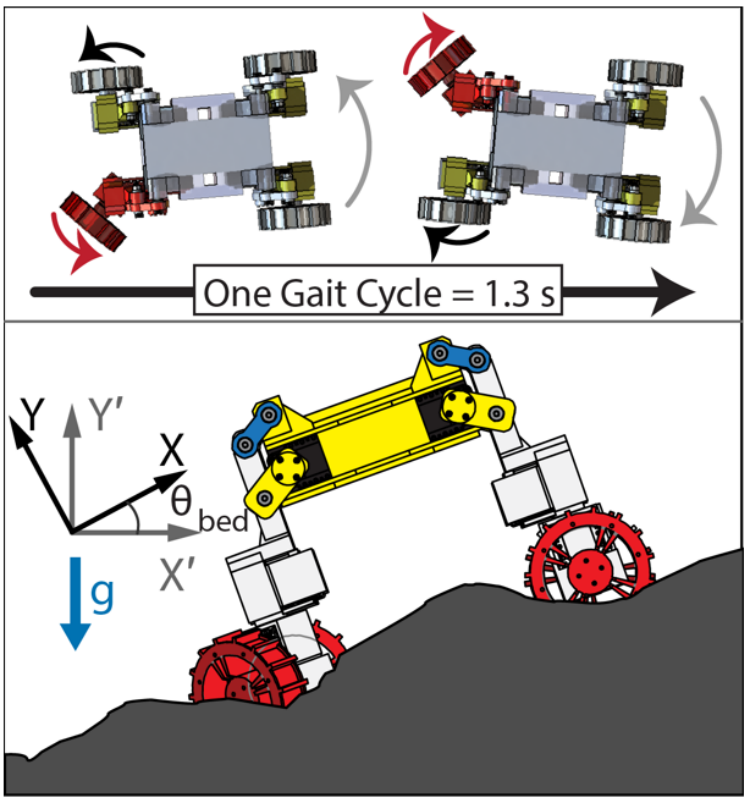

Figure 3.13: **Steep Granular Slope Climbing via Dynamic Remodeling with an RRP Gait** Top: Two top-down snapshots showing a RRP gait with no modulation, with a time interval between each snapshot of 0.65 sec. In the RRP gait, the rear wheel colored in white sweeps toward the rear of the rover up to $45°$. The sweep direction for each wheel in each snapshot is shown in black arrows. Once the sweep is complete, the wheel begins the reset phase, where the wheel is colored in red. The Mini Rover lifts the resetting wheel with its four-bar linkage and rotates it $45°$ toward the front of the rover. Bottom: Side-view illustration of the Mini Rover climbing a hill of GM using the RRP gait.

only the rear wheels. Each wheel spins at 2.1 rad/s during the RRP gait, including the front wheels. These motions generate a periodic yaw oscillation of the rover. After spinning wheels for 30 seconds to embed the Mini Rover in the media, once the RRP gait initiates (node 1 in Figure 3.16A), if $\theta_{bed} > 20°$, the rover will initially slide backwards until a large enough mound develops behind its rear wheels, which prevents further rearward sliding (node 2) and acts as a buffer the rear wheels can push on to move forward. After this initial mound is generated, the rover climbs the slope at constant speed (Figure 3.16A). Even though RRP locomotes more slowly than the RS gait at $\theta_{bed} = 0$, the RRP gait outpaces the RS gait for all other tested slopes, managing to climb hills of θ_{bed} that the RS gait could not (Figure 3.14).

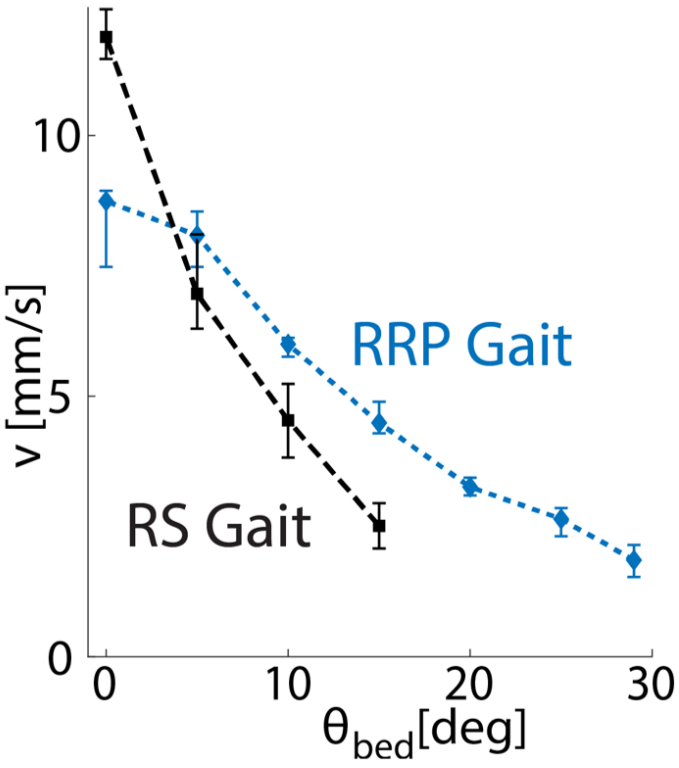

Figure 3.14: **RRP Gait Mean Velocities Climbing Granular Slopes** Mean velocities going uphill of the RS and RRP gaits shown in Figure 3.1(C) and Figure 3.13, respectively, for different granular slope angles (θ_{bed}). Data shown are means $\pm$ SD over seven trials for each angle. There is overall less variance in the RRP gait's mean velocity over multiple trials than the RS gait's, because RRP exhibits a more predictable and stable speed at steep θ_{bed}.

3.6.1 Granular Transport Mechanisms of RRP

The RRP gait's performance arises from a stable granular conveyance action which develops along the Mini Rover's long axis. As the front wheels spin and shear the steep granular slope at the rover's front, the material avalanches downhill [121] and is transported between the rover's front and rear wheels to an "IM" closer to the rear wheels' reach (see Figure 3.15 inset). The yaw oscillation of the rover body pushes media in the IM rearward where the RRP gait's sweeping reaches and pushes it into a rear mound to apply a net propulsive force. On steep slopes of $\theta_{bed} > 20°$, over time the gait will dynamically reconfigure an insurmountable slope through avalanching and granular conveyance to create a terrain profile it can climb (Figure 3.15). The rover needs a large enough rear mound to provide propulsive force, and the IM arises from the granular conveyance action. This

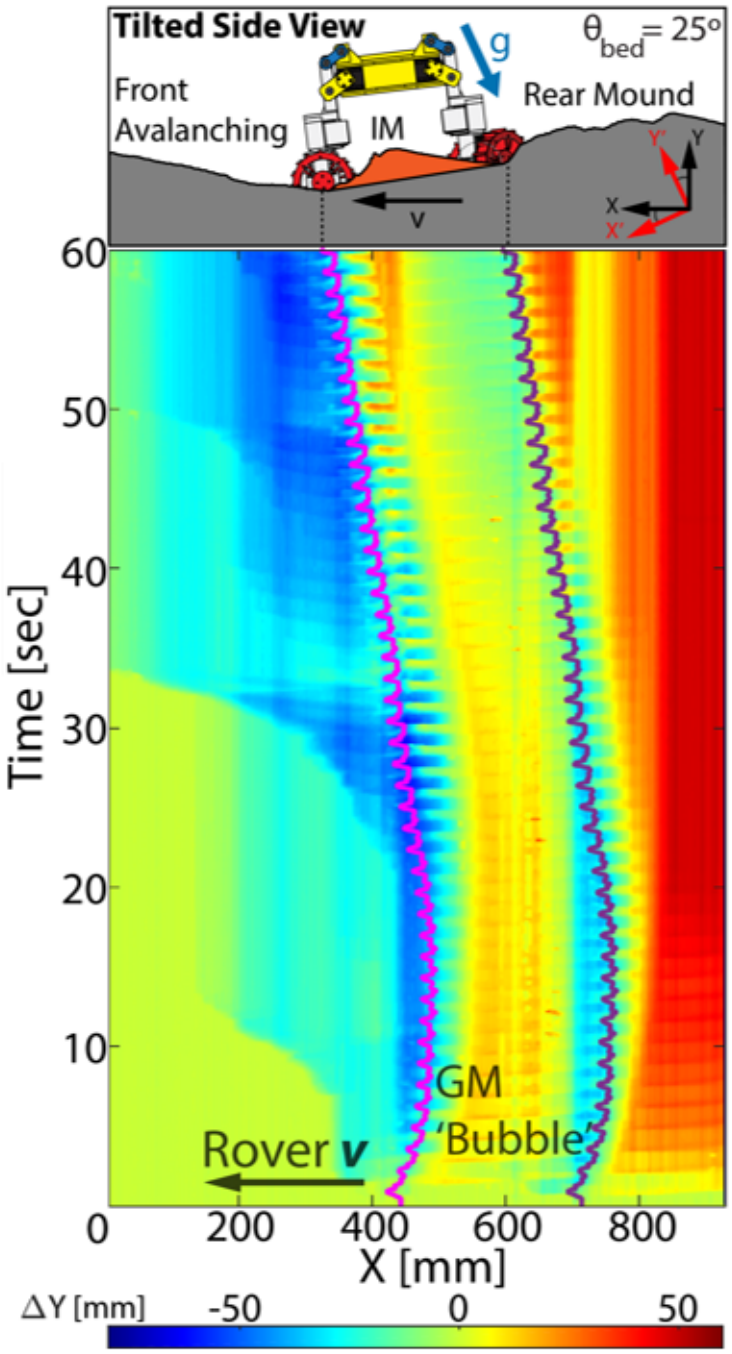

Figure 3.15: **Terrain Remodeling Profile of the RRP Gait** Height difference color map of the GM profiles over time as the Mini Rover executes the RRP gait on a 25° granular slope, with the spatial components in the tilted bed coordinate system (x, y) shown in Figure 3.13. A pink line indicates the rover's front wheel's position over time, and a violet line indicates the rear wheel's position over time. The rover carries the Intermediate Mound (IM) as a bubble of GM between these dots as it locomotes forward, maintaining a net flux of GM from the rover's front wheels to the rear mound.

dynamic reconfiguration allows the Mini Rover to "swim" uphill in the agitated frictional fluid created by its wheel spin. If the front wheel spin is disabled in the RRP gait (Figure 3.16A, node 1), the rover will continue to slide backward until it encounters the rear test bed wall (node 2'), and then push off that boundary to slowly climb up the slope (node 3'). Disabling the granular conveyance mechanism causes failure in the RRP gait for steep slopes, showing that avalanching through local agitation is necessary to climb.

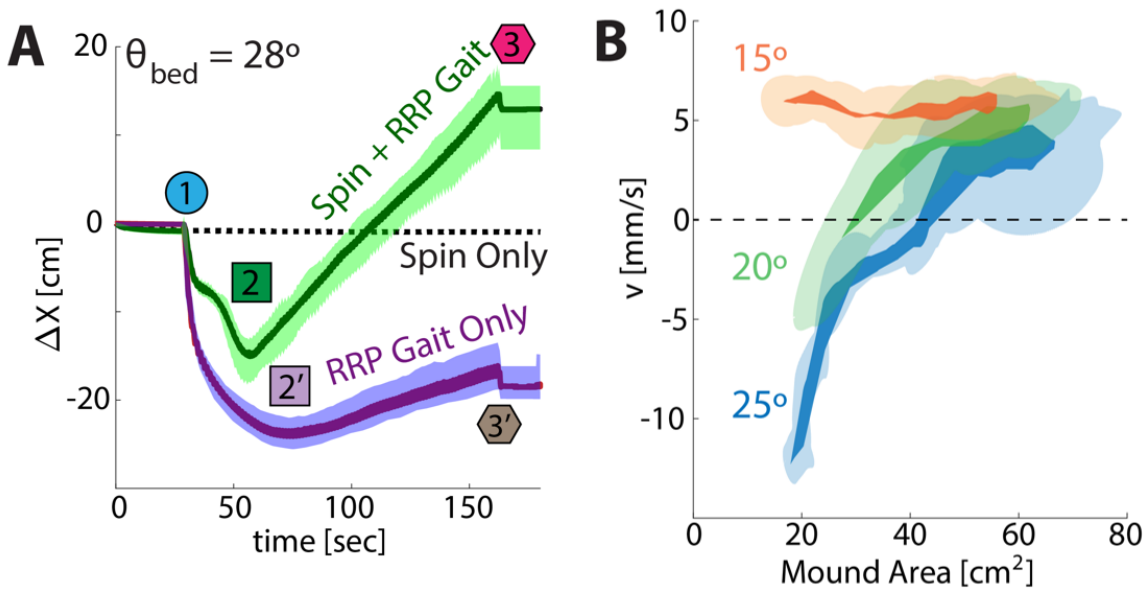

Figure 3.16: **Performance and Granular Transport Mechanisms for the RRP gait]** (A) Uphill displacement over time of Mini Rover using the RRP gait to climb a 28° granular incline. Turning off the wheel spinning or sweeping components of the RRP gait causes failure to climb. Data represent means ± SD for seven trials for each condition. The numbered nodes represent key events in the rover's climbing dynamics, where the rover initiates the RRP gait at node 1, ends sliding back and begins forward progress once the rear mound has formed at node 2, and ends the RRP gait at node 3. (B) Bivariate boxplot of the 2D-projected area of the IM that forms between the two wheels of the Mini Rover as it climbs with RRP (see diagram in Figure 3.15 and complete granular media profiles in Figure 3.18) with respect to the Mini Rover's uphill velocity, with 13 total trials of 50 sec each over three values of θ_{bed}. The solid colors are the boundary of mean trajectories over time for these two variables. At each mean trajectory point, the covariance matrix of velocity and mound area at that time stamp creates an error ellipse centered at μ (mean) with dimensions $\pm 1\sigma$ (SD). The union of the set of error ellipses for each mean trajectory point gives the shaded regions, representing the variance between trials for each group of θ_{bed}.

For trials where $\theta_{bed} > 20°$, the rover carries the IM as a 'bubble' of granular volume as it locomotes forward, showing how the granular conveyance mechanism maintains a net flux of media across the rover's length. These steep slopes require this IM to increase in volume before the rover will gain any net forward locomotion, whereas rover speed

is mostly insensitive to the IM size at shallower slopes (Figure 3.16B). Insufficient IM volume causes the rover to slide backward until the granular conveyance process saturates to a steady state, at which point the rover maintains a steady speed and IM volume over time (Figure 3.16).

3.6.2 Characterizing Granular Transport and the Intermediate Mound

In Figure 3.15, a colormap shows the granular media profiles over time as the Mini Rover executes its RRP gait. This colormap was generated by analyzing video taken at the side view of the granular testbed over an entire RRP trial, with the Mini Rover hugging the side wall (as shown in Figure 3.17). The granular bed is tilted to some angle θ_{bed}, and the camera is tilted as well such that the granular media initially lies horizontal in the camera frame. The mound profiles at each moment in time were found by edge detection along with various post-processing techniques to get accurate mound profiles. The mound changes over time were then subtracted from the grain level at $t = 0$ to obtain the height differences of the grain surface. In Figure 3.15, we have restricted the time dimension shown to between the start of the RRP gait and the end of RRP for clarity. Figure 3.18 shows the granular media profiles over time for RRP trials of $\theta_{bed} = [15°, 20°, 25°]$. We also show the overall slope and slope change magnitudes pre- and post-RRP execution for each RRP trial in Figure 3.17. These overall slopes were calculated by a best-fit linear regression to the spatial mound data extracted from edge detection.

The plots in Figure 3.16 show three groups of data at different bed tilt angles (the independent variable): 15 degrees (orange), consisting of 5 RRP trials; 20 degrees (green), consisting of 5 RRP trials; and 25 degrees (blue), consisting of 3 RRP trials. Each trial is synced in time with the other trials in its group. The time interval that each trial examines begins at marker 1 in Figure 3.16A (when RRP begins) to 60 seconds after marker 1. This is so that the Mini Rover can reach a steady limit cycle but is far away in space from reaching the end of the granular bed. Since the trials for each data groups are synced in time,

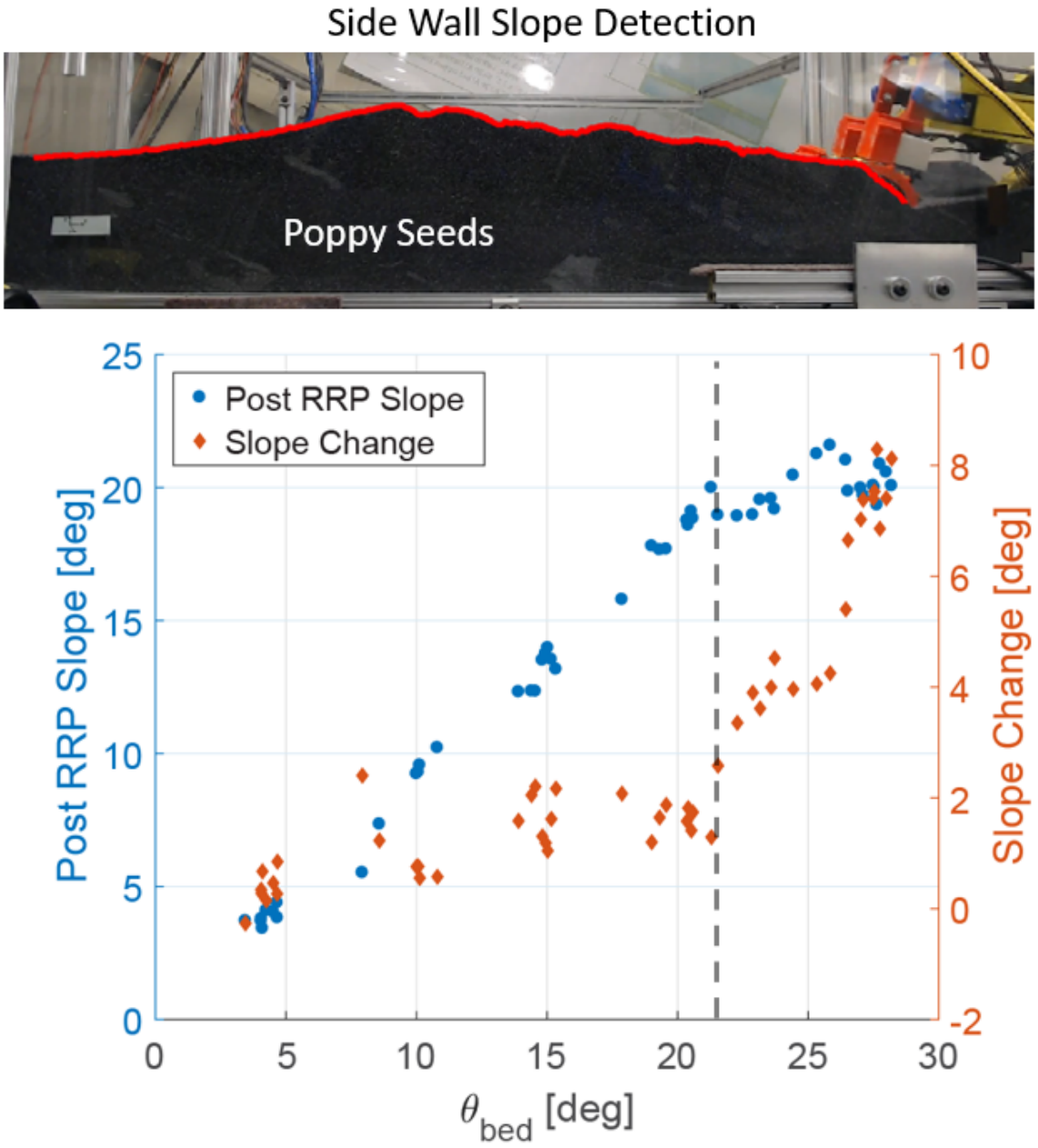

Figure 3.17: **Granular Slope Shifts via the RRP Gait's Remodeling and Transport** (Top) Side view snapshot of the image processing output of the post RRP gait slope detection, with the mound boundary outlined in red. The PS mound at the side wall is detected for the full duration of each run. (Bottom) Scatter plot of the side wall slopes (blue) and slope changes (orange) generated by RRP gait trials as functions of θ_{bed}. The dashed line at $\theta_{bed} = 22°$ shows a sudden increase in the slope change magnitude as the post RRP slope plateaus to approx. $20°$ to the right of the dashed line.

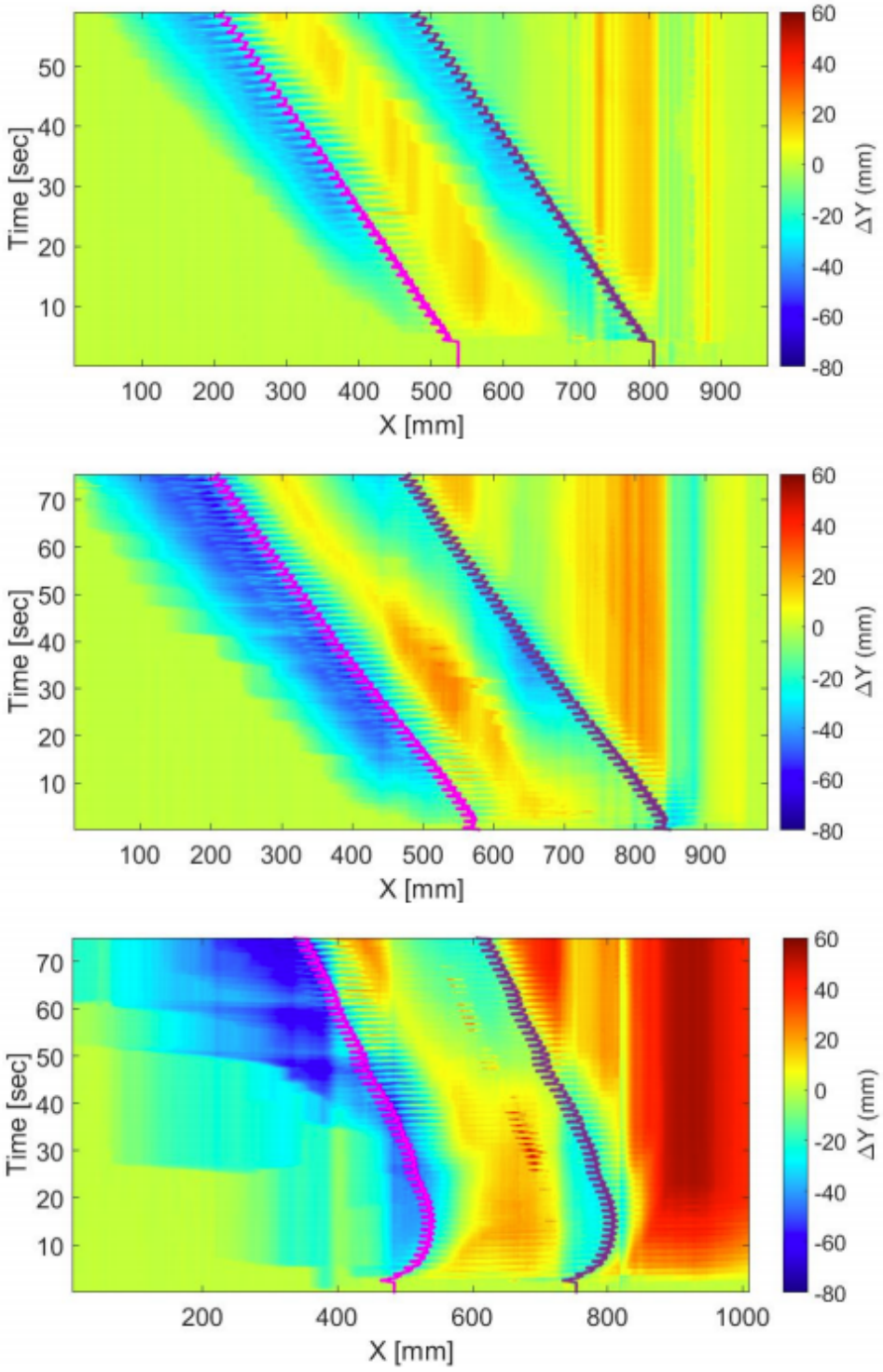

Figure 3.18: **Granular Media Profiles of Various Slopes for the RRP Gait** Additional height difference colormaps of the granular media profiles over time as the Mini Rover executes the RRP gait for trials of $\theta_{bed} = 15°$ (top), $20°$ (middle), $25°$ (bottom), with the spatial components in the tilted bed coordinate system. Magenta dots indicate the rover's front wheel's position over time, and purple dots indicate the rear wheel's position over time.

each trial's data can be compared to the other trials' data in the same group. This allows us to calculate the mean and covariance of each trial group and condense the parametric trajectories of each trial into an area plot. We calculate the means between all the trials for each group, which creates a mean "trajectory" for each bed angle through the mound area plus velocity variable space. We take the boundary of this mean trajectory for each group and represent it as the solid colored area for each bed tilt group. At each mean trajectory point, we also calculate the covariance matrix for that observed timestamp, then create an error ellipse about that mean trajectory point (confidence interval is 0.68, the first standard deviation). This gives us a representation of the variance between trials. We then take the union of the entire set of error ellipses for each group and plot the error area as a lightly shaded region for each groups' color.

Figure 3.16B shows a bivariate boxplot of the emergent IM volume that forms between the two wheels of the Mini Rover as it climbs with RRP. This plot was generated by examining multiple videos of the type described for Figure 3.15, edge detecting the granular profile along with tracking the Mini Rover itself, then calculating the area of granular media that lay between the two wheels' lowest points (see the inset of Figure 3.15). This mound area is a projection onto two dimensions of the approximate volume of the IM the Mini Rover carries with itself while climbing. In the mound area calculation, the mound profiles were median filtered across a time window of 0.3 seconds to help resolve false detections.

3.7 Discussion and Conclusions

Our results demonstrate that robots with novel legged gaits and appropriate local fluidization via wheel spinning can use the loose consolidation of granular media to their advantage by creating self-organized localized frictional fluids. This loose consolidation in GM traditionally causes entrapment for wheeled and legged robots [83]. Both RP15 and the Mini Rover increased their drawbar pulls when they switched from wheeled locomotion to open loop gaits which agitate the local media. Creating a homogeneous terrain profile

through this agitation erases terrain memory effects that hinder locomotion, creates force uniformity, perturbs material to avalanche into more advantageous terrain, and allows force calculation via RFT.

While terrain reconfiguration with legged gaits appears effective for non-cohesive media, future studies must consider that planetary regolith is often very cohesive and polydisperse. Cohesive regolith will likely not avalanche and flow as easily as the non-cohesive poppy seeds in this study. The drawbar experiments for both RP15 and the Mini Rover in wet sand (Figure 3.12) exhibit some visible terrain reconfiguration due to the rovers' high slip, as mounds of granular material form behind the spinning wheels. However, these mounds appeared to be more loosely packed than the dry poppies due to their high cohesion. The grain-grain cohesion in flat terrain hinders the desired advantageous avalanching and reconfiguration that is key to the gait. We hypothesize sloped terrain may actually assist by introducing a gravity component downhill. Gravity could then avalanche the grains to help the rear mounds form and consolidate, rather than the rover scooping out a hole around the wheels that ensures entrapment. Future studies and experiments could examine how these gaits perform on sloped cohesive terrain. Investigating these gaits on more inhomogeneous granular media would also be interesting, as the rate of terrain reconfigurations may change according to the local media's constitutive particles.

Certain modern rover designs such as the ESA and Roscosmos' *Rosalind Franklin* already incorporate up to three degrees of freedom in active actuation per wheel [125], allowing the rover's locomotion subsystem to adjust its stance for crawling over obstacles. More traditional control [126] and wheel design [127] approaches are still effective, but the capability to perform active legged behaviors as well could enable future exploration of steep terrains [128] inaccessible to other planetary rovers. Fluidized granular beds and other improved substrate creation systems on Earth will be critical for evaluating the physical principles of legged climbing in these larger robots. RP15 and future rovers can use these principles to guide both robot and motion design. With different appendages, sensors,

actuation schemes, perhaps such dynamical terrain modification can be applied to more diverse substrates. In future studies, closing the control loop with additional local terrain sensing could further capabilities in rover exploration.

Shortly before the *Science Robotics* paper [66] on this project was published, a NASA team including one of our co-authors published reports [129, 130] on a new rover mission called the Volatiles Investigating Polar Exploration Rover (VIPER). This new rover reuses locomotion concepts such as the RS gait that were developed in RP15 and is scheduled to launch to explore near the southern lunar pole in 2023.

3.8 Contributions

Andras Karsai performed single-wheel experiments, data analysis and interpretation, RFT model calculations, and guided the study's experimental design. Siddharth Shrivastava designed and programmed the Mini Rover, performed its locomotion and drawbar experiments, and collected data on the Mini Rover and RP15. Yasemin Ozkan-Aydin and Enes Aydin constructed the fluidizing granular bed and gantry system shown in Figure 3.5A. Yasemin also aided greatly in experimental design. Ross Pettinger, William Bluethmann (JSC-ER411), and Robert O. Ambrose (JSC-ER111) facilitated on site RP15 experiments at JSC. Andras Karsai and Daniel I. Goldman wrote the paper on which this chapter is based [66].

CHAPTER 4

CONTROLLING SUBTERRANEAN FORCES IN A BURROWING SOFT ROBOT

4.1 Preface and Summary

The physics of intruding solid bodies within yielding substrates is important for characterizing many natural phenomena, from the locomotion of lizards on flowable terrains to studying celestial bodies via impact collisions. We have found that dry GM offer excellent examples of friction dominated yielding substrates that can self-organize and showcase unique multiphase physics, yet are unaffected by thermal fluctuations. The multibody physics of moving bodies within a granular substrate has traditionally focused on singular rigid bodies intruding into GM and characterizing the stress/shear responses of the substrate under various loads and global forcings. However, most GM interactions in the natural world consist of underexplored complex multibody deformable structures which interact via local stress, flow, and adjacency effects.

In previous chapters, we explored the methods and mechanisms of traversing across the surface of loosely consolidated granular volumes. There will be occasions where we wish to explore within these volumes, so now we turn our attention to possible locomotion strategies below the surface using a growing deformable structure, in a collaborative project done with Nicholas Naclerio and Prof. Elliot Hawkes of UCSB.

Robotic navigation on land, through air, and in water is well researched; numerous robots have successfully demonstrated motion in these environments. However, one frontier for robotic locomotion remains largely unexplored – below ground. Subterranean navigation is simply difficult to do, in part because the interaction forces of underground motion

The majority of this chapter's contents are adapted from a co-authored paper published 2021 in *Science Robotics* [67], by Nicholas D. Naclerio*, Andras Karsai, Mason Murray-Cooper, Yasemin Ozkan-Aydin, Enes Aydin, Daniel I. Goldman, and Elliot W. Hawkes

are higher than in air or water by orders of magnitude, and because we lack for these interactions a robust fundamental physics understanding. In this chapter, we present and test three hypotheses, derived from biological observation and the physics of granular intrusion, and use the results to inform the design of a burrowing robot designed by Nicholas Naclerio and Prof. Elliot Hawkes of UCSB in a collaborative study. Our results reveal that (i) tip extension reduces total drag by an amount equal to the skin drag of the body, (ii) granular aeration via tip-based airflow reduces drag with a nonlinear dependence on depth and flow angle, and (iii) variation of the angle of the tip-based flow has a nonmonotonic effect on lift in GM. Informed by these results, we realize a steerable, root-like soft robot that controls subterranean lift and drag forces to burrow faster than previous approaches by over an order of magnitude and does so through real sand. We also demonstrate that the robot can modulate its pullout force by an order of magnitude and control its direction of motion in both the horizontal and vertical planes to navigate around subterranean obstacles. Our results advance the understanding and capabilities of robotic subterranean locomotion.

4.2 Introduction

Robots are well suited for navigating extreme environments such as outer space, ocean floors, or disaster scenes where it is dangerous or expensive for humans to enter. Robots such as NASA's Mars Curiosity rover [131], Jason Jr. – the remotely operated vehicle that helped find the Titanic [132] – and TEPCO's series of robots for accessing the reactors of Fukushima [133] have contributed to scientific discovery, helped probe inaccessible locations, and captured the attention of the general public. Although many robots have been designed and built for these challenging environments, one under-examined extreme environment is the subterranean world. The focus of this chapter is locomotion through such an environment, in particular, directly through GM where no paths or tunnels exist.

Our understanding of subterranean locomotion is relatively limited when compared with the study of movement through gas and liquid, which established formalized prin-

ciples enabling effective airplanes and submarines more than 100 years ago. Theories from aerodynamics and hydrodynamics can help inform terradynamic locomotion [17], but the physics of locomotion through the ground are fundamentally different from those of movement in air or water. Not only are the resistive drag forces in soil and granular media orders of magnitude greater than in air or water [21], but also a different type of lift force is present that diverts a symmetric burrower from following a straight course (Figure 4.1A). We study these two challenges to advance the field of terradynamics and inform the design of a robot that can overcome them.

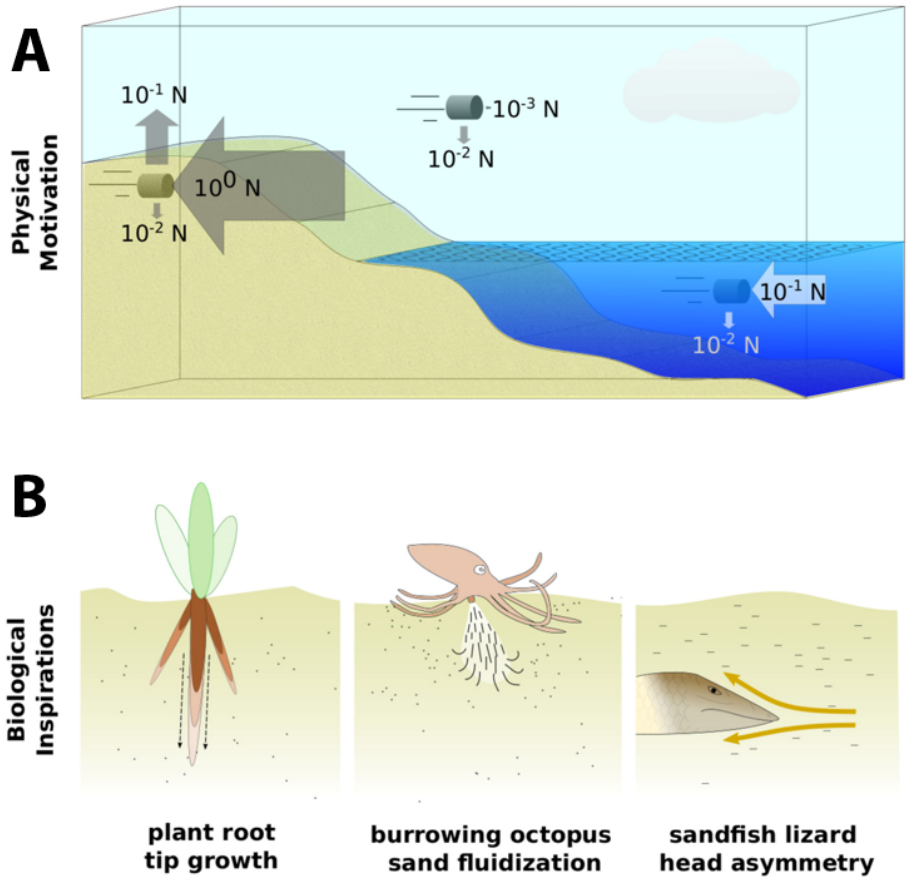

Figure 4.1: **Physical and Biological Motivations for a Soft Burrowing Robot** (A) The drag, lift, and net buoyancy forces on a 1 cm diameter steel cylinder moving at 4 m/s though granular media are qualitatively different than in a gas or liquid. Its drag is orders of magnitude higher, and a symmetric object experiences lift. Air and water drag forces calculated via fluid dynamics drag equation, and sand forces interpolated from Figure 4.8B and Figure 4.6. (B) The mechanisms of this robot are inspired by plant roots, various aquatic organisms, and burrowing reptiles. Figure prepared by Nicholas D. Naclerio [67].

The first challenge of subterranean locomotion is the drag force that directly resists

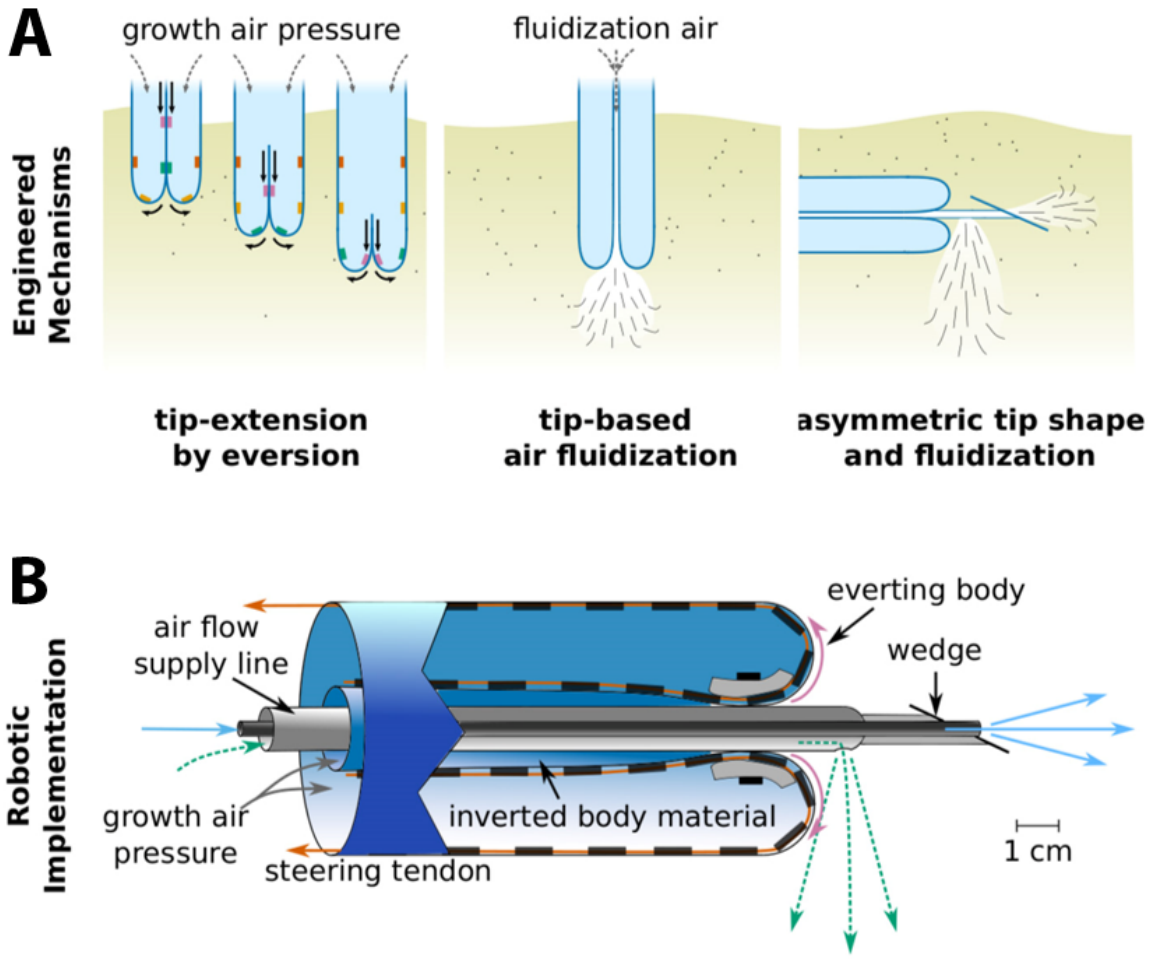

Figure 4.2: **Overview of the Mechanisms and Design of a Soft Burrowing Robot** (A) The robot features three engineered mechanisms to improve burrowing: tip extension by eversion to reduce skin drag, tip-based aeration and fluidization to reduce resistive forces, and asymmetric tip shape and airflow direction to overcome lift. (B) The robot features an everting body (blue) with a constrictor ring to seal it against the tip-flow air supply line (gray) that delivers both forward and downward airflow to the tip, with steering tendons (orange) for tip-localized steering. Figure prepared by Nicholas D. Naclerio [67].

movement (Figure 4.1A). We focus specifically on dry GM, i.e. collections of solid particles whose strength and normal resistive forces are created by frictional interactions without substantial cohesion, such as sand [134]. The total drag force on a body in GM can be computed via RFT as the integral of normal and tangential forces caused by friction and pressure acting on it ([17, 49], see also earlier chapters). Due to the combined action of gravity and friction, lithostatic pressure and yield strength increase linearly with depth in homogeneous GM [135, 98].

The second challenge is the interaction force that can divert a burrower from its intended

course (Figure 4.1A). This granular lift force is analogous to the lift force in fluids but differs in nature. The difference arises from the component of granular lift force that is caused by the gradient in lithostatic pressure, resulting in a yield strength gradient in the media. Because of this strength gradient, it is easier to push GM up than it is to compact it down. Thus, the magnitude of the normal force acting on a deeper part of a moving object is higher than that acting on a shallower part, causing lift opposite to gravity (see Equation 2.3). Therefore, symmetric objects moving horizontally through granular media experience a vertical lift force [98, 50, 136], causing some projectiles to "j-hook" upward after entering GM at an oblique angle [137] and burrowing robots to surface [138]. At the same time, for objects moving vertically downward (i.e. intrusion), this component of lift still opposes gravity, aligning with the drag force.

To overcome these two challenges of granular drag and lift forces, most current burrowing methods rely on mechanisms enabled by large machines with large and stiff excavating components. Conventional methods such as auger drilling, hydraulic rotary drilling, and tunnel boring [139, 140, 141, 142] effectively overcome these force constraints, but they are not ideal for small, minimally invasive, exploratory robots due to the heavy equipment required. Other mechanical burrowing methods have been proposed that would be more suitable for robots, including screw [143], reciprocating drill [144, 145], and hammer [146] mechanisms. A recent example robot application is NASA's Interior exploration using Seismic Investigations, Geodesy and Heat Transport (InSIGHT) mission, which used a hammering mechanism to drive a temperature probe into the Martian regolith. In laboratory testing, the device was able to burrow up to 5 m deep in 12 hours [147], but after 2 years on Mars, it was ineffective [148], illustrating the challenges of robotic burrowing. Instead of trying to combat lift and drag forces directly, examples in living systems suggest an alternative: reducing and controlling the otherwise large subterranean interaction forces via another mechanism (Figure 4.1B).

The first set of examples from nature uses tip extension, an effective method used by

plant roots to burrow through soil (Figure 4.1B, left). The mature, proximal region of a root can remain stationary relative to its surrounding while its apical tip extends, exerting more than 1 MPa of pressure [149, 150, 151], sloughing cells, and excreting mucus [152, 153, 154]. Tip extension allows the roots of a wild fig tree *Ficus natalensis* to extend as deep as 120 m [155] and those of a single American aspen (*Populus tremuloides*) clone to cover 0.433 km^2 [156]. Sadeghi, Mazzolai, and collaborators have pioneered tip-extending burrowing robots that "grow" by adding new material to their tips, realized either via additive manufacturing [157, 158, 159] or mechanically driven everting skins [160]. The UCSB group pursued a pneumatically driven everting skin design [161, 162].

Granular fluidization via the flow of fluid is another method found in effective burrowing organisms. Flow-based fluidization uses the pressure of an interstitial fluid passing through granular media to balance the gravitational force on the grains, suspending them in the fluid medium and allowing the particles to flow in shear [163]. This reduces the medium's yield strength and therefore the resistive force that it can exert on an object [164]. Some burrowing organisms and their respective fluidization methods include the Pacific sandfish (*Trichodon trichodon*), which expels water from its gills [165], the mole crab (*Emerita*), which quickly rows its legs [166, 163]; the southern sand octopus (*Octopus kaurna*), which expels a jet of water from its body (Figure 4.1B, center) [167]; and several clams (*Ensis*) that use the motion of their bodies and eject water from their shells [168, 169]. The clams inspired two burrowing robots [170, 171], whereas a proposed lunar excavation method used a gas jet to excavate regolith in a manner similar to the octopus [172]. Fluidization is also used to reduce forces in the construction industry, such as in pile jetting [173] and sonic drilling [174].

Lastly, asymmetries are used by burrowing animals to control lift, helping them maintain their course underground. Studies hypothesize that some desert-dwelling reptiles [175], such as the sandfish lizard (*Scincus scincus*) (Figure 4.1B, right) [45, 21] and the Western shovel-nosed snake (*Chionactis occipitalis*) [176], use the posture of their wedge-

shaped heads to modulate lift while burrowing in sand. A downward-pointing nose may create negative lift to help diving, and an upward-pointing nose may create positive lift to aid in resurfacing. The effect of wedged-shaped tips has been demonstrated to affect both lift [21] and horizontal steering [177] for robots burrowing in dry GM.

Given the observed biological mechanisms of tip extension, granular fluidization, and tip asymmetries, as well as an understanding of RFT, we form three hypotheses from these inspirations (Figure 4.1B) about the control of interaction forces on objects moving in GM.

1. A tip-extending body will experience less drag force than an equally sized intruding body by an amount equal to its skin drag. Tip extension should reduce tangential forces along an object's body because it eliminates relative motion with respect to the granular media; thus, only normal forces at the tip will contribute to drag in this case.

2. When tip-based airflow aerates or fluidizes the local media in front of a moving object, the drag force on the object will reduce by an amount proportional to the magnitude of the component of flow in the direction of the object's motion. Aeration should induce fluidization to reduce the strength of the surrounding medium.

3. An asymmetric tip-based flow of air will control lift in GM, reducing it by an amount proportional to the downward component of the airflow. Downward aeration should reduce the strength of the granular media below an object, thereby reducing the yield stress gradient that causes lift. Note that this is the opposite effect of what would occur in a gas or liquid, where the reaction force of a downward fluid jet would cause lift via Newton's third law.

Here we present (i) the results of experimental testing of our above hypotheses; (ii) the design, informed by these results, of a soft, steerable, burrowing robot made by Naclerio and Hawkes with tip extension and directional fluidization and aeration; and (iii) the characterization and demonstration of the robot. The robot (Figure 4.2B) builds upon pre-

liminary work on a vertical-burrowing device [161] to achieve the much more challenging tasks of controlled horizontal motion and steering. The robot realizes tip extension with a thin-walled tubular body of inelastic airtight fabric, inverted back inside itself. When pressurized, the tube everts, passing new material out of the tip to extend (Figure 4.2A, left). Local, directional airflow at the tip of the robot is achieved by passing air through the core of the robot and out of the tip (Figure 4.2A, center). Two nozzles at the robot's tip provide separate air supplies, one in line with the robot body for drag reduction, and the other perpendicular to it for asymmetric flow and lift reduction (Figure 4.2A, right). The robot is steered by tendons along the outside of its body that, when shortened, turn its tip. Although various other designs have been proposed for burrowing robots [178, 179, 180, 181], few have demonstrated subterranean streering capabilities. Those that have demonstrated steering [158, 177] have only done so in glass or plastic beads at speeds over an order of magnitude slower than Naclerio and Hawkes' device. The most well-known subterranean steering technology remains directional drilling [182]; however, it requires heavy machinery and cannot create sharp turns. Naclerio and Hawkes' robot provides a next step toward a practical burrowing robot – a tool for a wide range of shallow burrowing applications in sandy environments, noninvasive irrigation installation, pipe inspection, and extraterrestrial anchoring and soil sampling.

4.3 Results & Experimental Testing

This section includes experimental testing of the three hypotheses, the design of the robot based on our experimental findings, and tests to characterize the performance and capabilities of the burrowing robot.

4.3.1 Testing Three Hypothesis of Local Aeration During Intrusion

To test Hypothesis 1, in which tip extension reduces drag force compared with intrusion by an amount equal to the skin drag, Naclerio compared the drag force exerted on a tip-

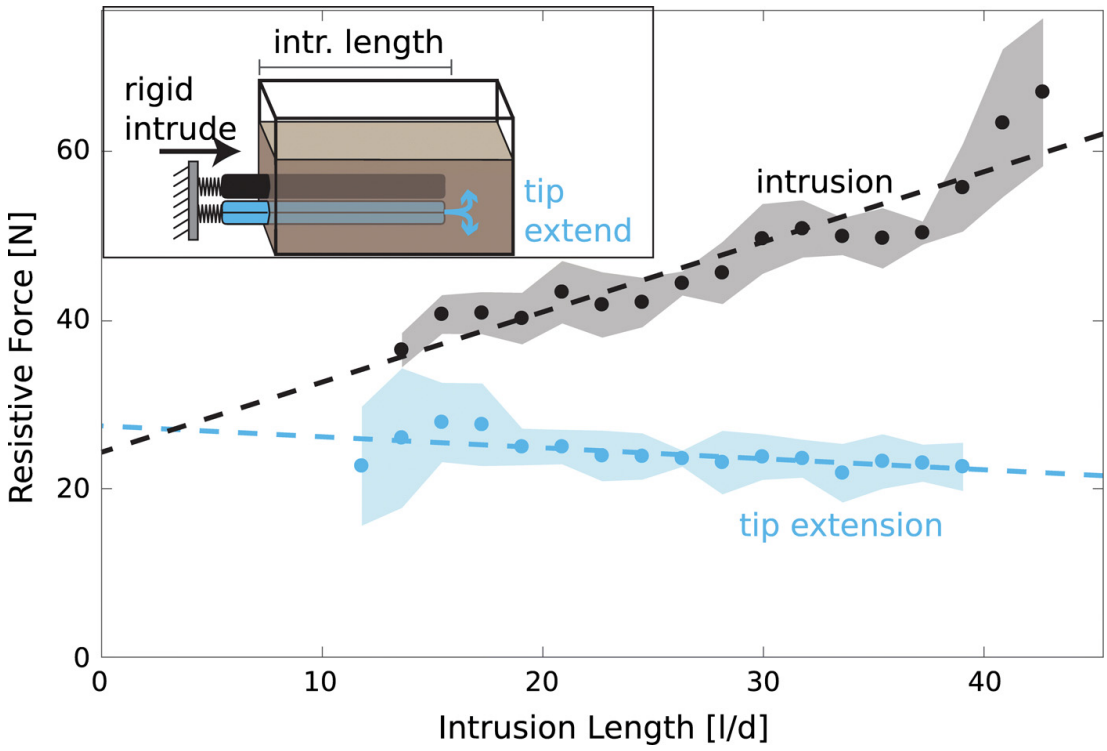

Figure 4.3: **Drag Reduction via Tip Extension** Plot of the measured force required to advance both a rigid intruder (black) and a tip-extending robot (blue) horizontally in loose, dry sand. Linear fit lines (dashed) intersect at 26.8 N. Diameter = 22 mm, N = 4 trials; shaded error bars represent ± 1 SD. Experiments performed by Nicholas D. Naclerio [67].

extending robot with that on a rigid intruder in loose, dry sand (polydisperse silica particles 300-850 microns in diameter). The results (Figure 4.3) show that drag force during tip extension remained nearly constant, whereas during intrusion, it increased approximately linearly with length. Further, extrapolation of the two datasets suggests that they intersect near zero length. Together, these data suggest that, in support of the hypothesis, both the extending robot and rigid intruder experience the same frontal drag ($\approx$ 25 N), and the higher total drag on the intruder is indeed equal to the length-dependent skin drag.

Hypothesis 2 predicts that local aeration and granular fluidization reduces drag by an amount proportional to the component of the airflow in the direction of motion. To test this hypothesis, we conducted experiments in both the vertical and horizontal directions of motion with tip-localized airflow and found that the relationships between flow rate and drag were more complicated than predicted. In the first test, we measured the drag force on an

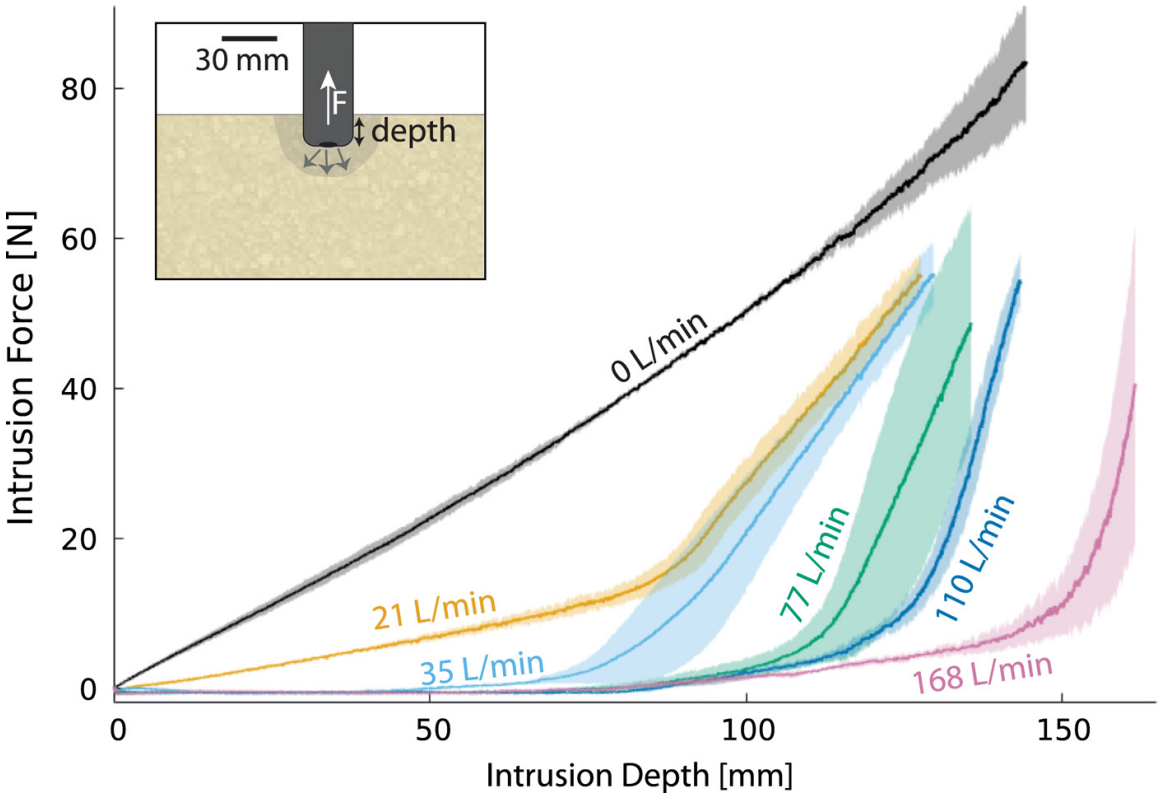

Figure 4.4: **Resistive Force Reduction in Intrusion via Tip-Based Aeration** Tip-based airflow reduces resistive force in vertical penetration in sand with a nonlinear dependence on depth. Resistive force versus depth for various tip flow rates plotted. Tip flow decreases resistive force to near zero until a critical depth beyond which it is less effective. N = 3 trials; shaded error bars represent ± 1 SD.

intruder plunged vertically into a bed of loose, dry sand while we varied airflow rates (see Materials and Methods). As shown in Figure 4.4, without airflow, force increases approximately linearly with depth; however, for higher flow rates, the relationship is nonlinear, with the force reduction becoming less substantial after a critical depth. This critical depth increases approximately linearly with flow rates above 21 liters/min, whereas power (fluidization air pressure times flow rate) increases exponentially (Figure 4.5). Although the force reduction was hypothesized, we did not expect this nonlinear behavior.

In the second test, we measured the resistive force on a horizontally oriented cylindrical intruder dragged horizontally through the sand. We varied both tip-localized airflow rate and angle from in line to perpendicular to the direction of movement (see Materials and Methods). The measured drag forces at a depth of 43 and 80 mm are shown in Figure 4.6(B

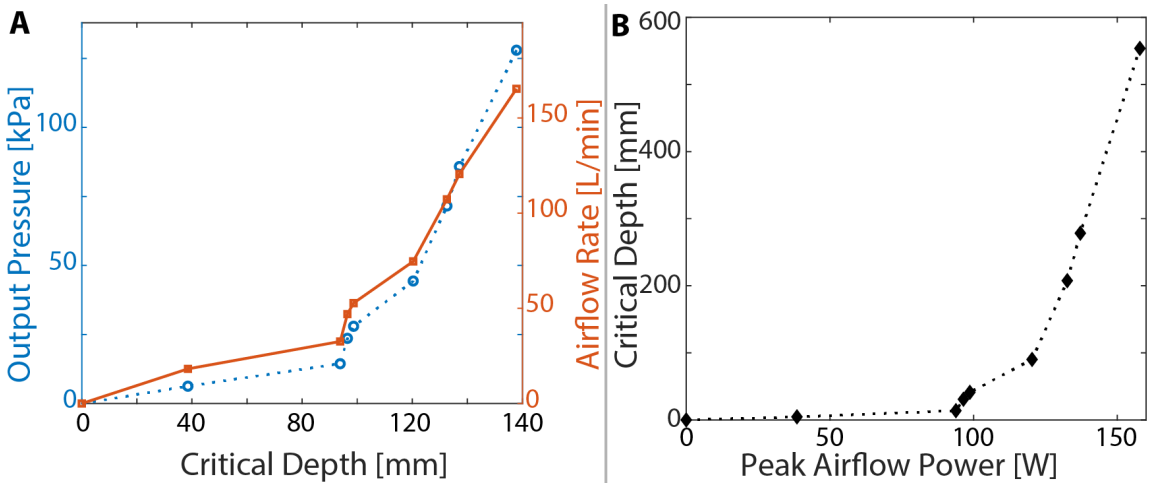

Figure 4.5: **Tip-based Air Pressure, Flow Rate, and Power as a Function of Critical Depth** Critical depth is defined as when the force during intrusion with air flow reaches 30% of the force required without air flow (see Figure 4.4). Power is approximated as pressure times volumetric flow rate. N = 3 trials.

& C), respectively. The data show that drag decreased roughly proportionally with increasing flow rates, as expected by our hypothesis. However, in contrast to our hypothesis, the drag reduction was not proportional to the component of airflow in the direction of motion: Perpendicular airflow also resulted in substantial drag reduction. Thus, our data show that nonaligned flows are less effective than aligned flows, but the magnitude of reduction is not as simple as a proportional term equal to the vector component of the airflow in the movement direction.

We next tested our third and final hypothesis that asymmetric, directed airflow reduces lift by an amount proportional to the vertical component of the flow. Using the same setup as in the previous experiment, we measured lift forces on the intruder as it was dragged horizontally at two depths through a bed of loose, dry sand with various airflow rates and angles. Tests at depths of 43 and 80 mm are presented in Figure 4.6(D and E), respectively. At a depth of 43 mm without airflow, the symmetric intruder experienced a roughly constant positive lift of 1.4 ± 0.2 N in all tests. Increasing the flow rate decreased lift at most airflow angles. However, in contrast to our hypothesis, the airflow angle exhibited a nonmonotonic influence on lift. For shallow airflow angles between $0°$ and $30°$, an increase in airflow angle meant an increase in lift to a maximum at $30°$ for all flow rates. Yet, as the angle increased

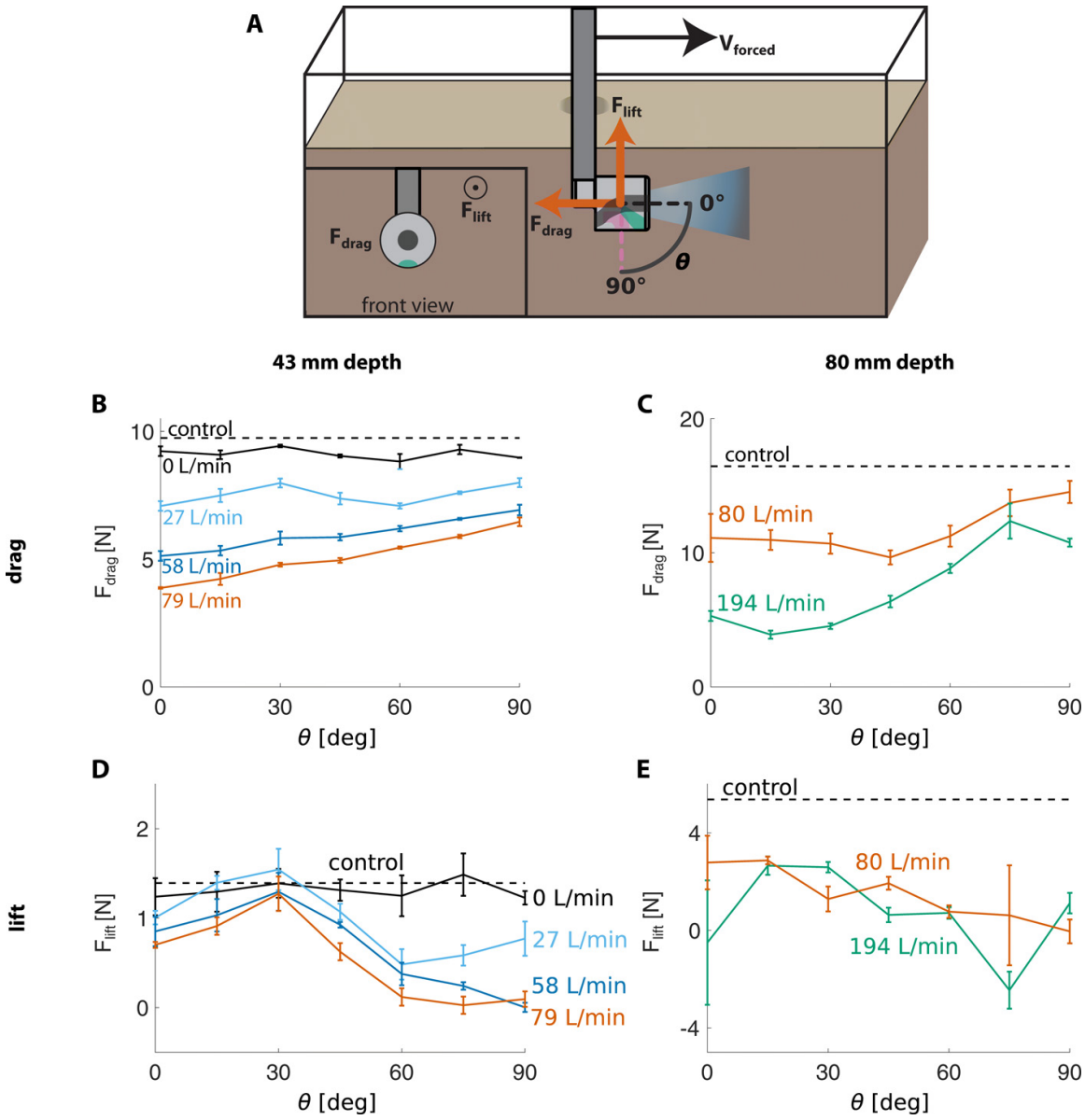

Figure 4.6: **Asymmetric Tip-based Airflow Reduces Drag and Lift in Horizontal Drag** (A) Experimental setup. Intruder was dragged horizontally at two depths, with varying tip flow angles. N = 4 trials for tests at 43-mm depth. N = 1 trial for tests at 80-mm depth with mean and SD of steady-state forces plotted (see raw data in Figure 4.14 and Figure 4.15). Error bars represent ±1 SD. (B) Drag forces as a function of flow angle at a depth of 43 mm. (C) Drag forces as a function of flow angle at a depth of 80 mm. (D) Lift forces as a function of flow angle at a depth of 43 mm. (E) Lift forces as a function of flow angle at a depth of 80 mm.

from 30° to 60°, lift decreased to a minimum of nearly zero at the maximum flow rate, which remained roughly constant for angles between 60° and $906\circ$. The results at a depth of 80 mm show a similar trend, with lower angles being less effective and higher angles being more effective at lift reduction. The local maximum is less pronounced, however. Although the lift reduction at high angles and flow rates was predicted by our hypothesis, the nonmonotonic behavior and local maximum at 30° were unexpected.

4.3.2 Everting Soft Robot Design

On the basis of the experimental findings of the previous section, Naclerio and Hawkes designed a soft burrowing robot that uses tip extension to eliminate skin drag, tip-based flow to reduce form drag, and directional tip flow combined with an asymmetric tip shape to control lift. This combination of tip extension and tip-based flow enables the robot to steer in curved shapes in dry sand (similar to that found in beach or desert dunes). First, we describe the design of the tip-extending robot body, then of the tip-based flow device, and lastly of the tendon steering mechanism, as shown in Figure 4.2B.

The tip-extending robot body is based on the principle that an inverted thin-walled tube everts when pressurized, as previously demonstrated for above-ground vine-like robots [183]. Because the interaction forces and internal pressures are higher than in these previous everting robots, there are more stringent requirements on the mechanical properties of the "skin" material. The skin must be circumferentially strong to resist the high hoop stress from internal pressure, torsionally stiff to resist twisting while turning, yet flexible to allow eversion. Their solution to this set of requirements is a custom bilayer composite airtight fabric, comprising a first layer with threads oriented axially and circumferentially and a second layer with threads oriented at 45° to these for torsional stiffness (see Materials and Methods).

Naclerio and Hawkes chose an intermediate scale for the diameter of the body (roughly 6 cm) based on trade-offs in scaling effects that make small and large diameters less de-

sirable. In the first scaling effect, the maximum internal pressure of a robot decreases linearly with increasing diameter because of the linearly increasing hoop stress. Second, the pressure required to overcome the internal resistance during eversion decreases quadratically with increasing diameter [184]. Lastly, both the force and the robot can apply to the medium at its tip and form drag scale proportionally with cross-sectional area balancing each other, regardless of diameter. With these three scaling trends in hand, there is an intermediate diameter where the difference between the maximum internal pressure and the pressure to overcome internal resistance is largest.

4.3.3 Tip-Based Flowing and Steering in the Everting Robot

To add airflow to the tip-extending body, Naclerio and Hawkes designed a tip-based flow device. To vary the tip flow direction, they used a two-nozzle system, each with its own air supply line; one nozzle is in line with the long axis of the body, whereas the other is oriented at 90° from this axis. Varying the flow between the two nozzles allows an approximate control over the flow direction. The two-channel air supply line runs through the core of the inverted body and is pushed forward as the robot grows.

The results of testing Hypothesis 3 (Figure 4.6) show that tip-based airflow can reduce lift to nearly zero, but it is inconclusive whether it can produce negative lift, so they added a small asymmetric wedge at the tip that generates negative lift. The wedge projects out in front of the tip of the robot, so that its effects are not negated by localized aeration or fluidization. The combination of airflow and a wedge is synergistic. Airflow alone cannot cause the robot to dive, and a wedge alone would need to be very large to mitigate the full lift force, thus creating high drag. However, in combination, aeration can reduce drag and mostly eliminate lift, meaning only a small wedge (low drag) is required to have net negative lift. By modulating the amount of airflow in such a setup, we can control the lift experienced by the moving robot.

They steer the robot with pull tendons that run the length of the body, which each applies

a moment to the entire body but only turns the tip of the robot. Tip extension allows only the tip of the robot to move with respect to the sand while the body is frictionally pinned in place by the non-flowing sand. This tip-localized steering allows dynamic curvature shapes to be created with pull-tendons that run the length of the body. Although three tendons would allow three-dimensional motion, four tendons are used to allow simplified control with left-right and up-down steering. In this work, they used visual feedback to locate the robot via a mast that protrudes from the sand. However, localization of the buried robot tip could be achieved by existing methods including magnetic tracking [185, 186], inertial measurement units coupled with length sensing [187], or optical fiber sensing [188].

Whereas simply pulling the "left" or "right" tendon is sufficient for steering in the horizontal plane, moving outside of this plane is more complicated due to the effects of lift and aeration or fluidization. To transition from horizontal burrowing to vertical diving, the robot requires negative lift. Simply pulling the "down" tendon is ineffective, because instead of the tip moving down, the proximal part of the body lifts up into the lower strength sand above it. We therefore require an additional downward airflow to dive. Transitioning from horizontal burrowing to vertical rising is easier and can be done either by pulling the "up" tendon or by reducing downward airflow. Turning from vertical diving to horizontal burrowing is also relatively easy because lift can again be used. The final transition from vertical rising to horizontal burrowing is not tested in this work but could be achieved with directed airflow and tendon steering.

4.3.4 Burrowing Robot Characterization and Performance

Naclerio and Hawkes conducted a series of tests to characterize the effects of tip extension on anchoring, tip flow on drag, growth rate on drag, and tip flow on lift. We also conducted demonstrations of robot performance.

Tip extension by eversion is reversible and allows the robot to retract by inverting its body without the concern of buckling, as can occur in air [189], because the surrounding

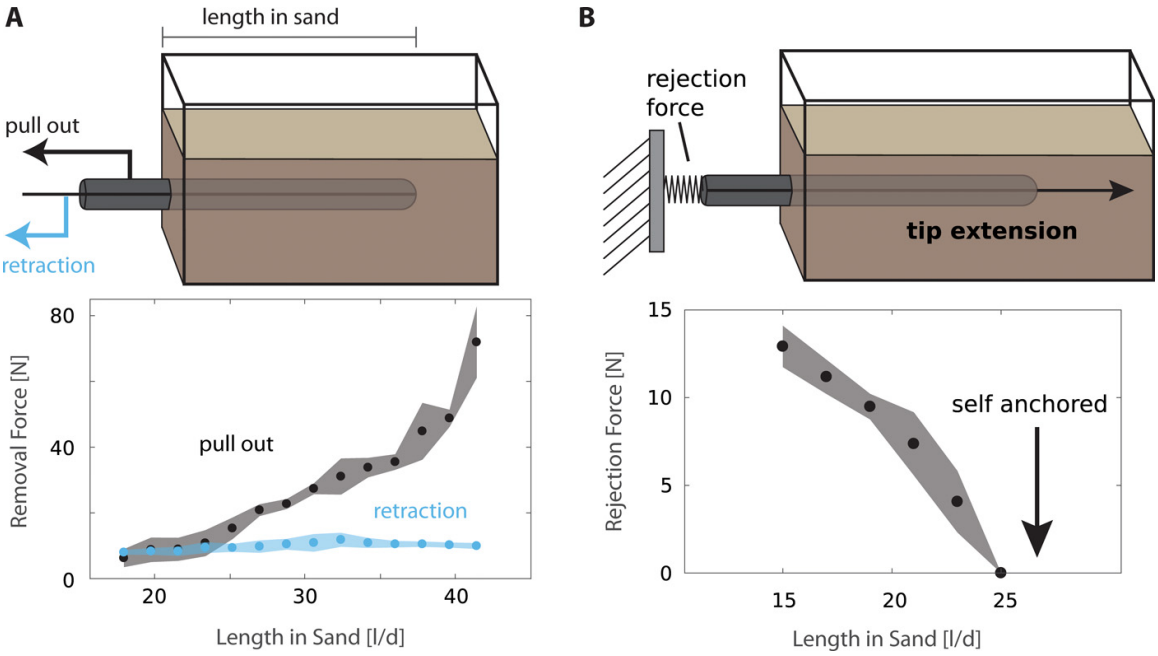

Figure 4.7: **Tip Extension Enables the Robot to Anchor in Loose, Dry Sand** (A) Plot of measured force to remove a buried robot from sand by pulling out its body (black) and retracting it by reinversion (blue). Diameter = 22 mm, N = 3 trials; error bars represent ± 1 SD. (B) Plot of rejection force as a robot extends into sand as a function of length. As the robot extends more than 25 diameters in length, the reaction force is reduced to zero and the robot is self-anchored. Diameter = 22 mm, N = 3 trials; error bars represent ± 1 SD. Experiments performed by Nicholas D. Naclerio [67].

sand supports the body. Inverting eliminates skin drag during removal from the ground and offers a method to control anchoring force. They measured the force required to pull a robot body out of the sand from the base and compared it with the force required to reinvert the robot (Figure 4.7A); during reinversion, the force is much smaller and nearly constant with length.

Next, Naclerio and Hawkes explored how tip extension enables self-anchoring. Self-anchoring occurs when the tip reaction force that rejects the robot from the sand is less than the skin friction that holds the robot in place. The reaction force is roughly constant at a given depth, whereas skin friction increases with robot length. Thus, at a critical length, the reaction and friction forces balance each other. To test self-anchoring, we measured the reaction force on the base of the horizontally growing robot as a function of length, showing that after a critical length, the force drops to zero and self-anchoring occurs (Figure 4.7B).

According to the results for the small, rigid test device shown in Figure 4.6(B and C),

we expect the soft robot to require less pressure to grow as tip flow rate is increased (for a given angle of flow). To test this, Naclerio recorded the pressure required to start growing the robot as a function of tip flow rates. The results in Figure 4.8A show that with increasing airflow, the pressure required to extend the robot decreases.

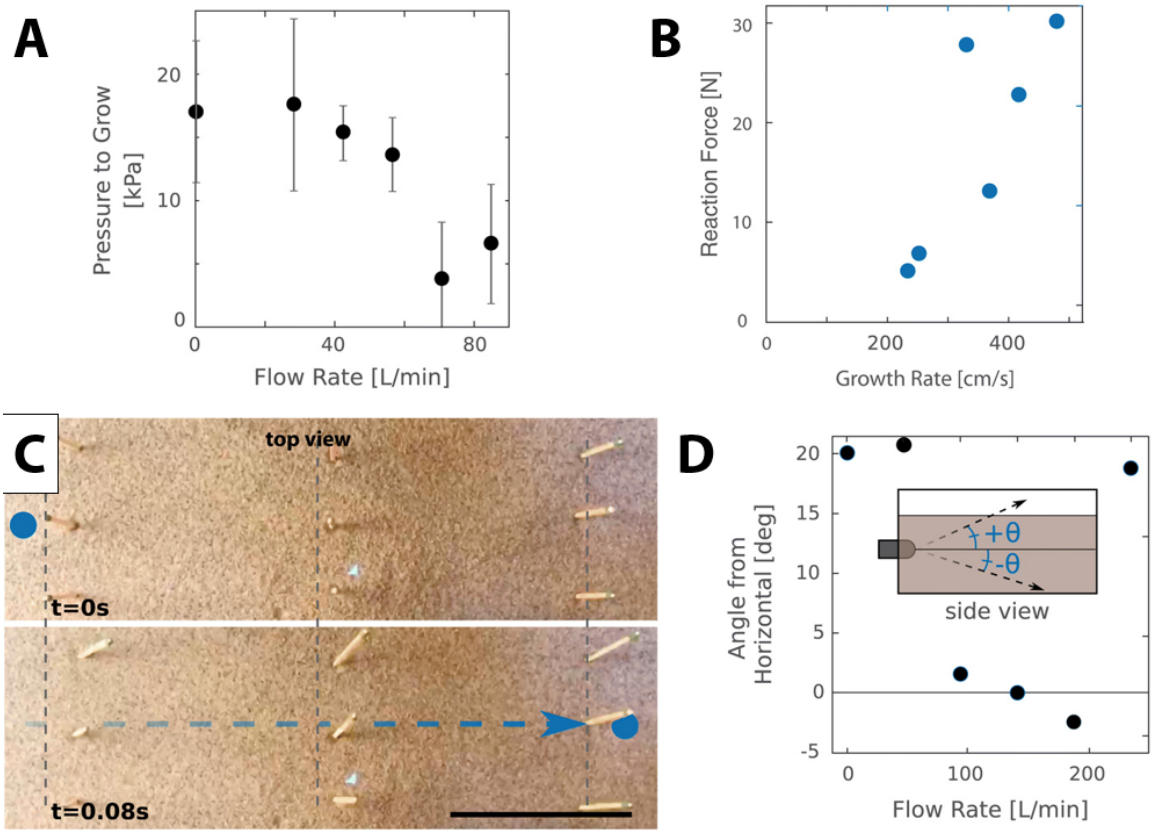

Figure 4.8: **Characterization of the Effects of Tip Flow and Growth Rate on Burrowing** (A) Plot of internal pressure of full-sized robot (see Materials and Methods) required to grow through sand as a function of tip airflow rate. The pressure to grow in the absence of sand has been zeroed out. N = 5 trials; error bars represent one SD. (B) Plot of reaction force as a function of horizontal tip extension rate in sand. N = 1 trial. (C) Overhead images of high-speed horizontal burrowing. A blue dot marks the tip of the robot, and vertical matchsticks help visualize its passage underneath. Vertical dashed lines mark the initial position of the tips of the matchsticks, which are disturbed (bottom image) after the robot passes beneath. (D) Effect of airflow rate on horizontal burrowing trajectory angle. N = 1 trial. Experiments performed and figure prepared by Nicholas D. Naclerio [67].

On the basis of previous tests with rigid intruders, drag in GM is rate independent at slow speeds [190, 191] but increases roughly quadratically at high speeds as inertial forces become non-negligible [65, 136]. Naclerio and Hawkes first performed low-speed vertical burrowing tests with a tip-extending robot body without aeration, controlling growth rate

and measuring reaction force at the base (see Materials and Methods). They found that resistive force does not vary substantially at low speed in 1 mm diameter PS (used because the robot cannot vertically penetrate sand without fluidization). Next, they performed a high-speed horizontal burrowing test in sand with speeds up to 480 cm/s, measuring reaction force and velocity. At these higher rates, the robot showed a relatively large (six times) increase in reaction force for an increase in speed of only two times (Figure 4.8B). Images of one of the tests are shown in Figure 4.8C, showing the robot covering 30 cm in 80 ms.

On the basis of the results shown in Figure 4.6 (D and E), we expect a horizontally burrowing robot to demonstrate different growth paths as the downward airflow rate is varied. We recorded the position of a vertical mast attached to the tip of the robot and protruding out of the sand as the robot grew horizontally with various aerating flow rates. Figure 4.8D shows that at low flow rates, lift causes the robot to travel at an angle substantially above horizontal; at intermediate flow rates, lift can be balanced near or below zero to enable diving; and at high flow rates, surfacing once again occurs, likely due to the reaction force of the airflow jet. The images in Figure 4.9 (A and B) show the cases of low and high tip flow, respectively.

The subterranean performance of the burrowing robot in the horizontal plane was demonstrated by Naclerio in traversing a sand bed in straight, curved, and serpentine paths (Figure 4.10). In the first demonstration, the robot successfully traversed 60 cm of sand at a depth of about 8 cm with a constant downward flow rate of 140 liters/min and a speed of 2 cm/s. In the second demonstration, the robot made a right turn under the same conditions by increasing tension on the right-side tendon. In the third demonstration, the robot turned right and then left to avoid a buried obstacle using tendon steering. The robot remained buried at a relatively constant depth, demonstrating depth control and horizontal planar steering.

The robot's performance in vertical burrowing was demonstrated with straight and "U"-shaped paths. In the first demonstration, the robot burrowed to a depth of 35 cm at 2 cm/s.

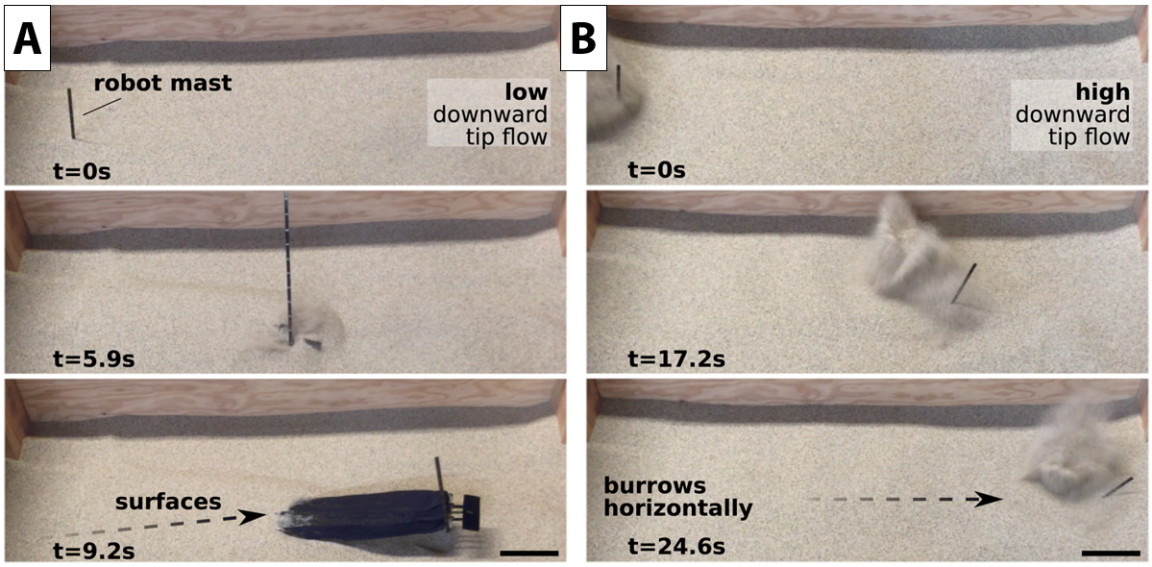

Figure 4.9: **Preventing Robot Breaching via Downward Tip Fluidization** (A) Effect of tip airflow on path of growth. Low downward airflow rates do not reduce lift sufficiently, and the robot surfaces. (B) However, with the increased downward flow, lift is reduced, and the robot is able to burrow horizontally. Scale bars each denote 10 cm. Experiments performed and figure prepared by Nicholas D. Naclerio [67].

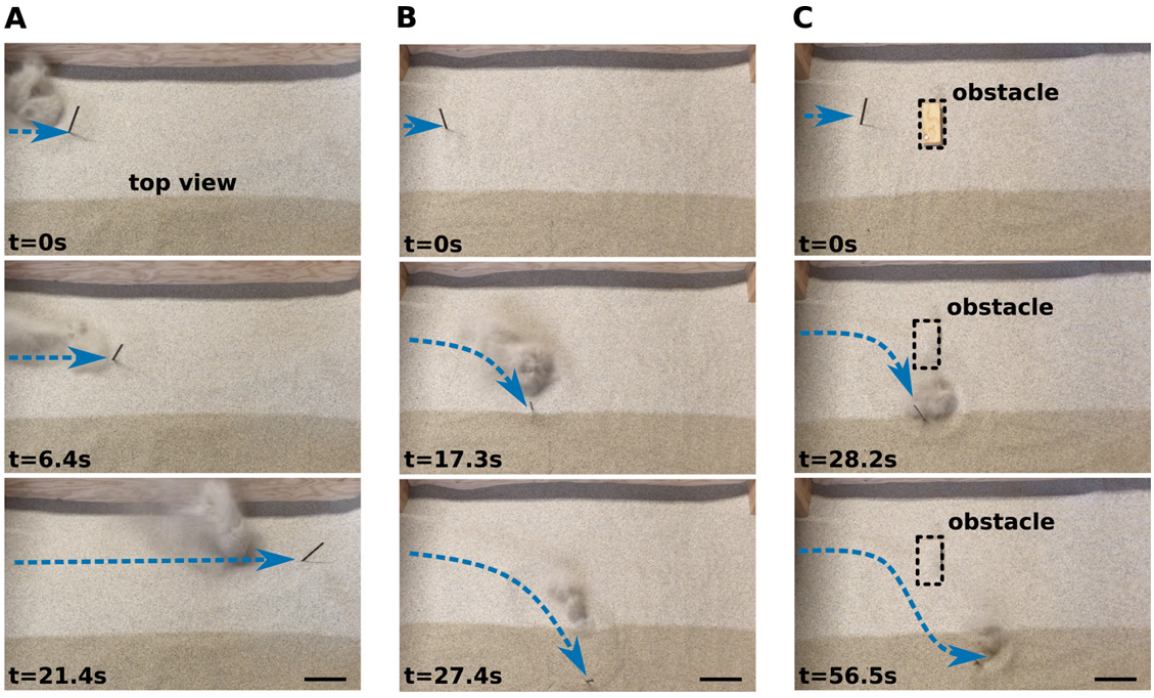

Figure 4.10: **Soft Robot Horizontal Steering Demonstrations** (A) Controlled horizontal burrowing to 60-cm length at a depth of 8 cm. (B) Right turn at a depth of 8 cm. (C) Right and then left turn to navigate around an obstacle. All scale bars denote 10 cm. Experiments performed and figure prepared by Nicholas D. Naclerio [67].

Next, it used tendons and a controlled aeration angle to burrow down, underneath, and then up to the far side of a buried obstacle. These demonstrations show the robot's ability to navigate vertical and horizontal obstacles while maintaining depth control.

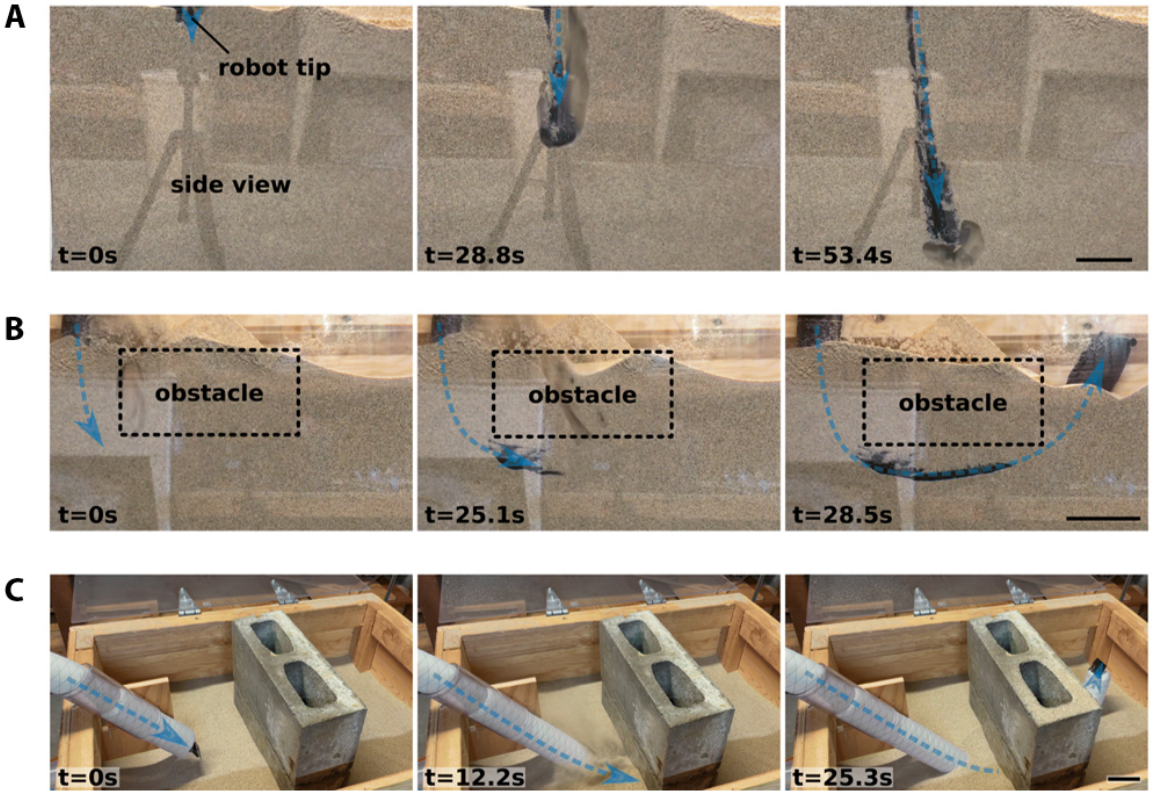

Figure 4.11: **Soft Robot Vertical Steering Demonstrations** (A) Vertical burrowing up to 35 cm deep. (B) Navigating down, under, and up on the other side of a buried obstacle. (C) Navigating down, under, and up on the other side of a cinder block wall. Arrows follow the robot's path and point to the tip of the robot. All scale bars denote 10 cm. Experiments performed and figure prepared by Nicholas D. Naclerio [67].

The tension in the steering tendon is largely independent of the surrounding medium for a given radius of curvature. Under a constant tendon displacement, body pressure, and radius of curvature, the tendon tension increased slightly with length as it grew in a bend with a 46-cm radius. As shown in Figure 4.12, the tension was roughly equivalent when turning in air, in loose, dry sand without airflow, and in sand with local airflow.

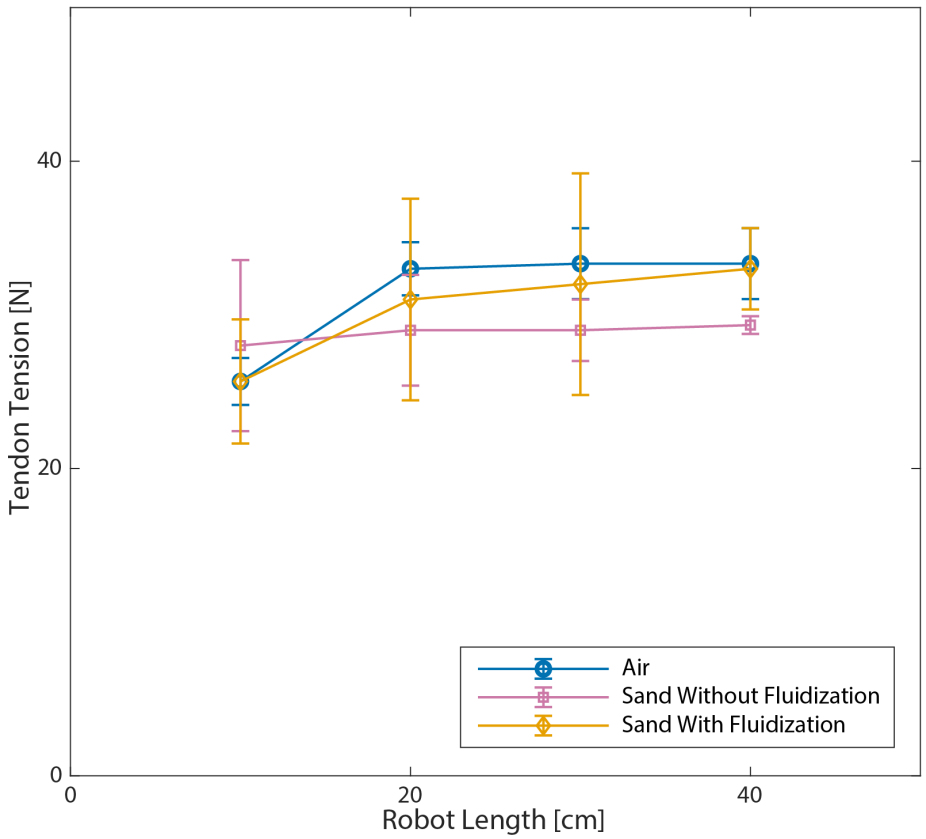

Figure 4.12: **Steering Tendon Tension vs. Length When Turning** Burrowing robot test conducted in air, sand without air flow, and sand with air flow. The robot lengthened under a constant tendon displacement, radius of curvature, and body pressure. N=3 trials. Error bars denote plus/minus one SD. Experiments performed and figure prepared by Nicholas D. Naclerio [67].

4.4 Materials & Methods

4.4.1 Robot Fabrication

Details of the burrowing robot are shown in Figure 4.2. It features three main components: the everting body, the tip-flow air supply line, and the steering mechanism.

The everting body is made of two layers of 50 μm thick silicone and urethane impregnated ripstop nylon (Seattle Fabrics; measured initial modulus of 74 MPa along fibers, 9.0 MPa at 45° bias), adhered together into a 60 mm diameter, 2 m long tube with room temperature vulcanizing silicone adhesive (Sil-Poxy, Smooth-On Inc.). One layer is oriented with its threads along the axial and circumferential axis of the robot and the other at a 45° angle for axial and torsional stiffness, respectively. A string is attached to the tail of the

robot that can be pulled to retract the robot. The end of the body is sealed around a solid, 60 mm diameter Delrin cylinder fixed to an air supply, with dynamic seals for the tail string and tip-flow air supply line to pass through.

The air supply line is made of two nested concentric nylon tubes (inner diameters of 2.4 and 6.4 mm) for separate forward and perpendicular (downward) airflow, wrapped in a carbon fiber braid and polytetrafluoroethylene sleeve with an outer diameter of 9.5 mm for increased torsional stiffness and reduced friction, respectively. The forward-facing nozzle is a simple hole, whereas the downward nozzle is "T" shaped, spreading the flow to the width of the robot. Attached to the airflow nozzle is a 55 mm by 25 mm fiberglass wedge, at a 10° angle of attack. It is positioned 15 mm in front of the downward nozzle so that the aeration does not negate its affects. The forward airflow supply line passes through the center of the wedge, negating its effects during vertical burrowing. Inside the body of the robot but around the airflow supply line is a constriction ring made of 6 mm thick neoprene foam that seals the inverted body material to the supply lines at the tip. Sealing at the distal end of the inverted body material allows the internal body pressure to equalize on either side of the material, reducing the pressure and friction that it exerts on the supply line. This helps prevent the air supply line from being spit out of the body as it everts and reduces tension on the supply line while increasing tension in the body wall, enabling the body to take a stable shape.

Four 1.6 mm diameter braided steel tendons control steering. They are equally spaced around the circumference of the body, running through 2.4 mm inner diameter, 2 cm long nylon guides adhered 2 cm apart along the length of the body with silicone adhesive, and covered in a ripstop nylon sheath. As the tendon is shortened, these nylon guides collide, setting a minimum radius of curvature of 19 cm that prevents kinking in any one section of the robot.

The robot weighs 780 g including the everting body, airflow supply line, and seals. It requires an additional 390 g of body and airflow tube per meter of length. The robot body

pressure is supplied by up to 150 kPa of compressed air or nitrogen, whereas the forward and downward airflow tubes can supply up to 30 and 300 liters/min of compressed gas from a 1 MPa source, respectively.

4.4.2 Experiments of Intrusion and Drag with Local Fluidization

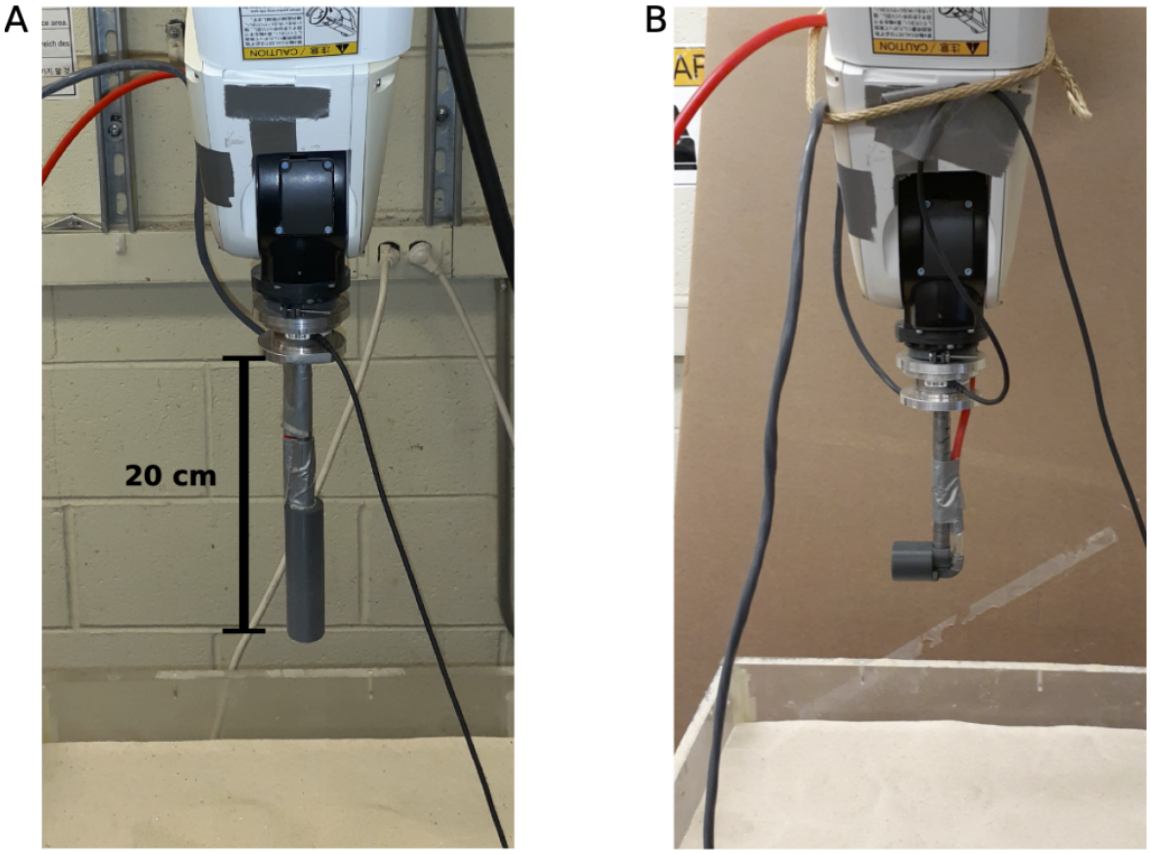

Figure 4.13: **Experimental Setup Used for Horizontal Lift and Drag Experiments** (A) The vertical intruder is mounted on a force torque sensor on a robot arm. It was plunged vertically 15 cm into the sand with varying levels of air flow rate. (B) The horizontal intruder is mounted on the same setup. It was dragged horizontally through the sand while measuring lift and drag forces with varying air flow rates and direction.

For the experiments of vertical intrusion with local fluidization in Figure 4.4, we intruded a 27 mm diameter, 100 mm tall cylinder with a 10 mm diameter circular opening at the bottom as an airflow outlet. All intruding bodies were 3D printed from ABS plastic using a Dimension Elite printer. Experiments were performed in a 42 cm x 28 cm x 15 cm bed (Figure 4.13) of dry silica sand (polydisperse particles ranging in diameter from 425 to

850 microns with a friction angle of 36° with a corresponding overall coefficient of friction of $\mu = 0.72$, Quikrete Pool Filter Sand). Between each trial, the bed was fluidized by blowing air from the bed's bottom inlet for 15 seconds to repeatably reset the sand to a loosely consolidated initial condition ($\varphi \approx 0.58$). Intrusions were performed by a DENSO VS087 robot arm connected to a 6-axis ATI Mini40 force/torque transducer controlled by a National Instruments DAQ (USB-6211) running NI LabView. A tool transformation was used to calculate the forces on the face of the intruder from the force and torque data recorded by the sensor. The air flow rates were recorded by an Omega FMA1845 mass flowmeter, and controlled by an ARO pressure regulator. The intruder was attached to the Mini40 forces transducer with a 13 mm thick, 100 mm long steel shaft (Figure 4.13A). Air flow was initialized as the intruder touched the surface of the sand, and was lowered at 10 mm/s for three trials per flow rate. Power was calculated as the airflow pressure at the base of the intruder multiplied by the measured volumetric flow rate (Figure 4.5).

For the horizontal drag tests shown in Figure 4.6, we used the identical setup as that of Figure 4.4 but with a different intruder attachment. The horizontal intruder was a 30 mm diameter, 30 mm long cylinder with its flat surface facing the direction of drag (Figure 4.13B). For each tested angle of tip air flow, we used a different 3D printed intruder with identical external dimension and an 8 mm diameter hole for airflow at 15 degree increments from the horizontal of the cylinder's center of geometry. The intruder was first lowered into the fluidized sand bed, then bed fluidization was turned off and the sand left to settle, then tip-based air flow was turned on and the intruder was dragged horizontally. Four trials were conducted for each flow and angle condition at a depth of 43 mm. We reported the average steady state resisitive force, which occurs after one or two body lengths of movement. Only one trial was conducted at 80 mm, so we report the average and standard deviation of the steady state force of that one trial. Raw data for that test is available in Figure 4.14 and Figure 4.15. The reaction force of the air flow jet without sand was minimal (order of 0.1 N) and was thus not subtracted from the results. The control lines

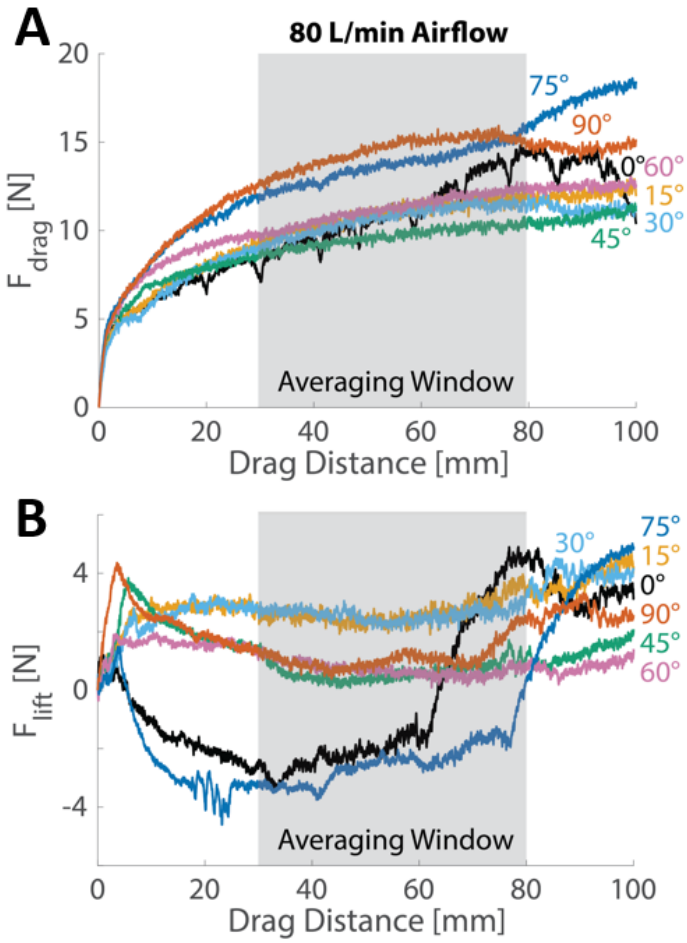

Figure 4.14: **Force Response for 80 mm Depth Horizontal Intrusion Tests at Low Airflows** See Figure 4.6C and E for steady state mean and SD taken from a drag domain of 30 mm to 80 mm. N=1 trial. (A) Drag force vs. intrusion distance as a function of tip flow angle with a flow rate of 80 L/min. (B) Lift force vs. intrusion distance as a function of tip flow angle with a flow rate of 80 L/min.

plotted in Figure 4.6 are the average force measured on an intruder without a hole for tip flow. The force on the steel rod moving horizontally through sand without a tip or air flow was subtracted from the results. Although the forces on the rod may be different with air flow, due to the increasing lithostatic pressure, the shallow rod has substantially less drag force than the deeper intruder tip.

4.4.3 Experiments Characterizing the Burrowing Robot

All burrowing robot experiments were performed by Naclerio in a 70 cm x 90 cm x 35 cm bed of Cemex Lapis Lustre 30 Mesh Sand (silica sand with polydisperse particles ranging

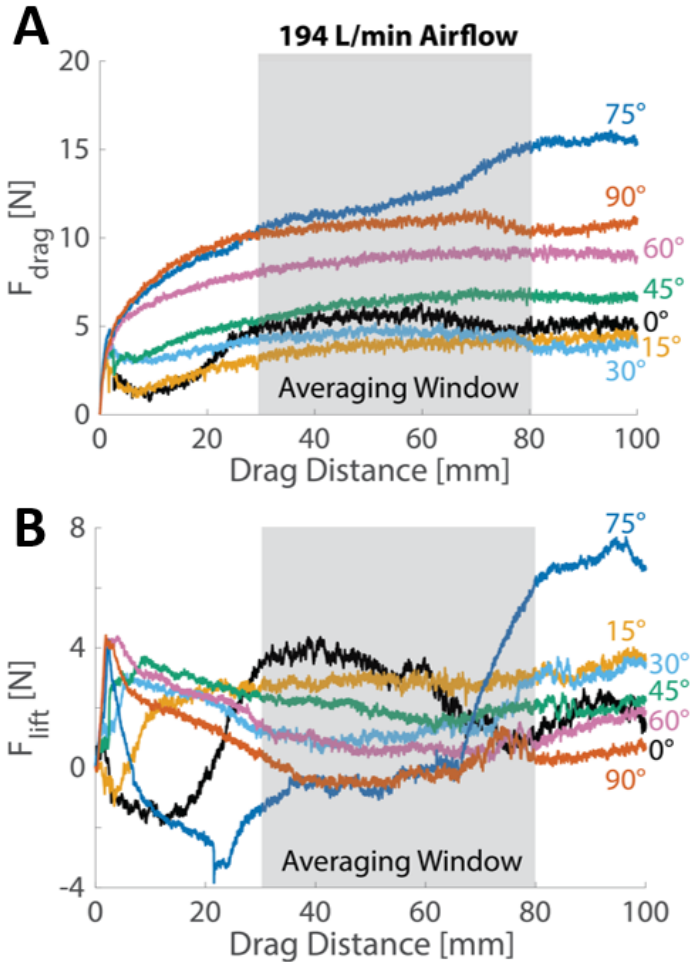

Figure 4.15: **Force Response for 80 mm Depth Horizontal Intrusion Tests at High Airflows** See Figure 4.6C and E for steady state mean and SD taken from a drag domain of 30 mm to 80 mm. N=1 trial. (A) Drag force vs. intrusion distance as a function of tip flow angle with a flow rate of 194 L/min. (B) Lift force vs. intrusion distance as a function of tip flow angle with a flow rate of 194 L/min.

in diameter from 300 to 850 microns), which was fluidized for 3 seconds between trials by blowing compressed nitrogen through an inlet at the bottom of the bed for a repeatable initial condition of loosely consolidated sand ($\varphi \approx 0.58$). For the results shown in Figure 4.3, an everting robot with a 22 mm diameter was positioned horizontally under a depth of 8 cm of sand, entering the bed through a tube in its side. The tip started 26 cm into the bed to reduce boundary affects from the bed inlet. The robot was grown 60 cm horizontally through the sand along a pre-tensioned steel wire that spanned the container to maintain a constant depth. The body pressure was recorded by an SSI Technologies digital pressure gauge and multiplied by its cross sectional area to approximate the growing force. The pressure of

the robot was slowly increased until it grew 4 cm. Growth was stopped and the pressure was manually recorded. This process was repeated until the robot grew approximately 60 cm for four trials. The test was repeated at the same depth with a rigid intruder of identical dimensions, built from a 21 mm diameter PVC tube sheathed in the skin of the everting robot, recording intrusion force with a Nextech DFS200 force gauge.

To characterize the self anchoring behavior of the robot in Figure 4.7, Naclerio performed tests with a similar setup and procedure as the experiment in Figure 4.3. To test pull out force, the 22 mm diameter robot with a constant pressure of 30 kPa was pulled out by its body 4 cm at a time, recording the maximum tension required for three trials. The retraction force test was similar, measuring the force to retract the robot by its tail with a constant pressure of 30 kPa for three trials. The force gauge was used to measure the rejection force of the robot as it grew horizontally into the sand, recording the maximum reaction force for every 4 cm increment for three trials. The force gauge was mounted one one end to the inlet tube of the sand bed, and attached at the other end to the robot body on the outside of the sand bed.

For the internal pressure vs. flow rate data in Figure 4.8A, Naclerio placed the full sized robot inside the sand box via the side entrance tube with a depth of 8 cm of sand above it. We measured various downward air flow rates with a Brooks Instruments 10 SCFM variable area flow meter and recorded the maximum pressure required to grow 1 cm via the pressure transducer. Five tests were recorded at each flow rate.

The growth rate experiment in Figure 4.8B was performed with the same robot setup as above. The body pressure was suddenly turned on for one second by manually opening a ball valve, allowing the robot to grow without constraint. The maximum reaction force was recorded by the force gauge. As the robot passed through the sand, it disturbed three rows of upright matchsticks spaced 20 cm apart on the surface of the sand (note that they are only spaced 15 cm apart in the demonstration in Figure 4.8C) The speed of the robot was calculated by recording the disturbance of surface sand and match sticks as the robot grew

(via an iPhone 7 camera at 240 FPS). One test was performed at six different pressures.

For the experiments in Figure 4.8D & Figure 4.9, the setup was identical to those in Figure 4.8 A & B, only with an 8 mm wide, 2 mm thick, 20 cm long carbon fiber mast with depth markings every 2 cm attached to the air flow tip to track the position of the robot. With a body pressure of 100 kPa, the robot burrowed at approximately 2 cm/s over 60 cm horizontally with various rates of downward air flow. The position of the mast was recorded by video (iPhone 7 camera), and the approximate linear trajectory of the robot was estimated by the initial and final mast depths. One trial at each of six flow rates was recorded.

For the steering demonstration experiments in Figure 4.10, the robot burrowed horizontally through the sand at a depth of 8 cm using a body pressure of approximately 100 kPa and a downward air flow rate of up to 300 L/min. The right hand turn in Figure 4.10B & C was initiated by applying a displacement of 65 mm to the right side steering tendon before growing the robot. As the robot grew, the tendon displacement remained fixed. To initiate the left turn in Figure 4.10, the growth of the robot was stopped, the tension on the right side tension was released, a displacement of 65 mm was added to the left side tendon, and the robot was allowed to resume growth around the wooden obstacle.

The vertical steering demonstrations in Figure 4.11A & B were preformed in a 70 cm x 8 cm x 35 cm sand bed with a clear glass and acrylic side panel. With a body pressure of approximately 100 kPa and a forward air flow rate of approximately 30 L/min, the robot was able to burrow vertically. To steer under the obstacle in Figure 4.11B, a downward air flow rate of approximately 100 L/min was added as the robot transitioned from a vertical to horizontal orientation. The turn was achieved by displacing the top steering tendon over 65 mm. The demonstration in Figure 4.11C was performed with a 6 cm diameter robot body, sewn from XPac TX07 fabric (Rockywoods) and sealed with 0.51DCF Dyneema composite fabric (Ripstop by the Roll) and a pressure sensitive adhesive (3M 9482PC). The robot had an identical tip-based flow device as described above, with a pre-shaped

turn sewn into its body. With a body pressure of approximately 200 kPa and a combined downward and forward air flow rate of approximately 300 L/min the robot burrowed down, under, and up on the other side of a 20 cm thick cinder block wall buried 15 cm deep.

For the data shown in Figure 4.12, tests were conducted with the full sized robot as described in the Robot Fabrication section in air, in sand without tip flow, and in sand with tip flow. For repeatable testing, the tendon housing was opened, inspected, and cleaned of any sand between trial sets. Trials in sand began at depth of 8 cm, although the trials without air flow surfaced. Three sets of trials were conducted, each one testing in each medium once. Each trial set began in a different medium. For each trial, one steering tendon was displaced 65 mm to create an average radius of curvature of 46 cm.

4.5 Discussion and Conclusions

We tested three hypotheses related to controlling subterranean interaction forces in GM and used the results of these tests to design, characterize, and demonstrate a fast, steerable, burrowing soft robot. In this section, we discuss the implications of our experimental findings and robot performance.

As shown in Hypothesis 1 testing, tip extension reduces overall drag by an amount equal to the skin drag, meaning that with only frontal drag remaining, the force-resisting motion of the tip of our tip-extending robot is independent of length and path at a fixed depth. This is especially important as robot length increases; without tip extension, the force-resisting motion would continue to rise and, eventually, the robot could no longer move forward. Furthermore, for curved paths in robots without tip extension, we expect that the body would experience even higher drag due to capstan friction, which increases exponentially with total path curvature [192].

Tip extension also decouples the magnitude of the external force required to move the body of the robot (e.g., pull it from the ground) and the magnitude of force required to move the tip (e.g., grow or retract). This means that the robot can modulate its anchoring force

by roughly seven times at a length of 90 cm (Figure 4.7A) and by even more for longer bodies, allowing it to control whether it remains firmly planted in the ground or slips out. Branching is also possible with this morphology of robot [193], potentially enabling multi-branched root-like structures to further increase these anchoring forces [194].

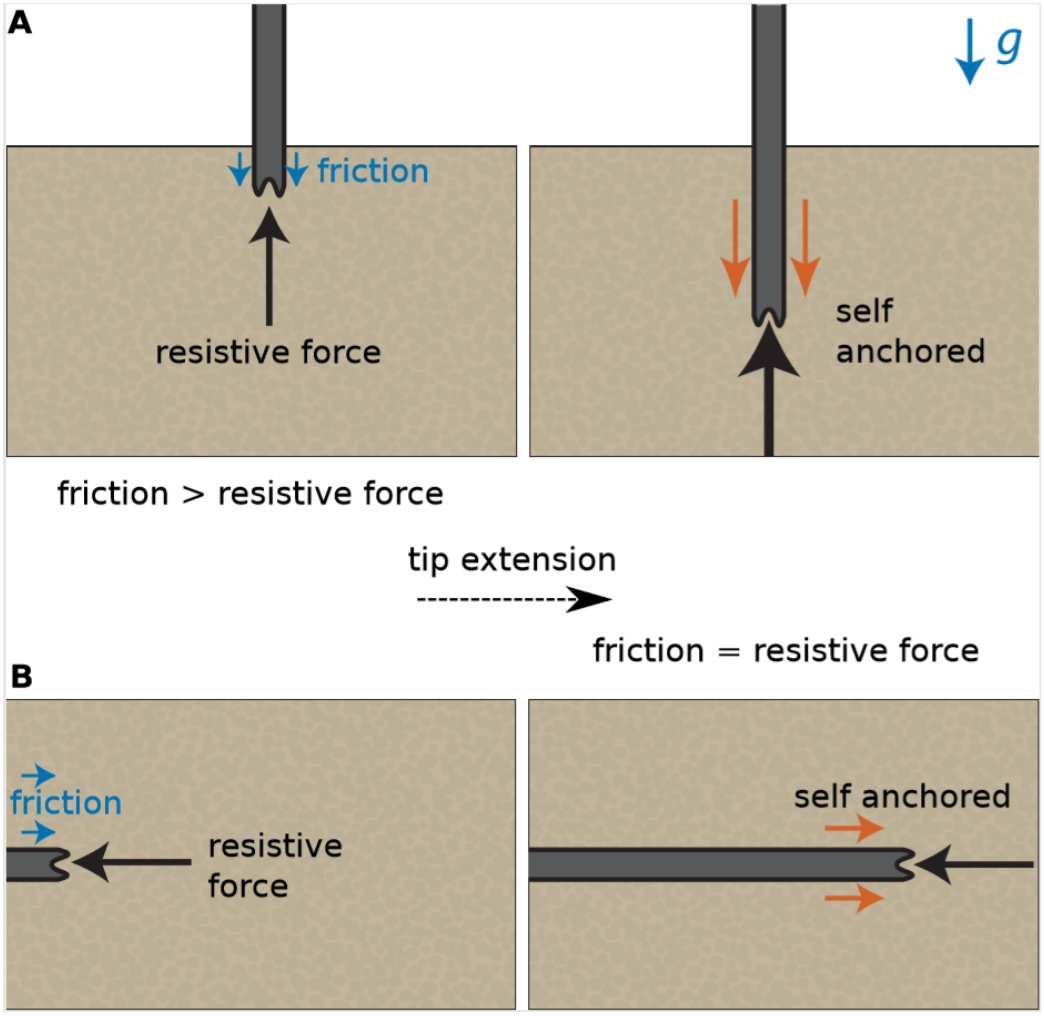

Figure 4.16: **Self Anchoring Force Balance Sketch** (A) When friction forces and reaction forces on a vertically-burrowing tip-extending robot balance each other the robot is self-anchored. (B) When the forces balance each other in horizontal burrowing, the robot is also self anchored.

At the same time, the decoupling of anchoring and growth forces results in a phenomenon we refer to as self-anchoring, wherein the friction along the length of the robot body becomes larger than the reaction force at the tip beyond a certain length (Figure 4.7B and Figure 4.16). Although tested in horizontal burrowing in this work, the effect should

occur for vertical burrowing as well. The minimum length at which the robot will self-anchor can be approximated as $r/2\mu$ in horizontal burrowing and r/μ in vertical burrowing, where r is the robot radius and μ is the effective coefficient of friction between the robot and the environment. Self-anchoring is especially important for cases where it is difficult to provide enough reaction force to prevent rejection from the soil. For instance, when burrowing in extraterrestrial settings with low gravity, self-anchoring in beneficial because it reduces the mass and cost of the robot base required. Critically, self-anchoring allows a robot to apply forces on the environment that exceed its own weight.

Self anchoring occurs when the tangential forces due to friction along the length of the robot body exceed the normal forces at its tip (Figure 4.16). This means that after a certain length, the robot requires no reaction force at the base prevent the robot from being ejected from the ground by reaction forces. The friction forces can be approximated as:

$$F_{friction} = \mu N = \mu P(h) A_{body} \tag{4.1}$$

where μ is the coefficient of friction between the robot and its environment, N is the normal force applied on the body, $P(h)$ is the external pressure as a function of depth h, and A_{body} is the body's surface area. Assuming that the shape of the robot is a cylinder with radius r and length L this becomes:

$$F_{friction} = \mu N = \mu P(h) 2\pi r L \tag{4.2}$$

Similarly, the normal force applied at the tip of the robot can be written as:

$$F_{normal} = P(h) A_{tip} = P(h) \pi r^2 \tag{4.3}$$

If we make the simplifying assumption that $P(h)$ is due only to lithostatic pressure, when the robot is moving horizontally, the $P(h)$ experienced on the tip and sides of the robot is

the same (in the limit of relatively small robot geometry). When the robot is burrowing vertically down, and we assume a linearly increasing lithostatic pressure, the average $P(h)$ on the sides is half that at the tip. In reality, the force on the tip of the robot is even higher than this assumption, because the tip must overcome some resistive strength that the sides do not. Further, cohesion may reduce the pressure exerted on the sides of the robot (as found by the HP^3 probe [147]). Thus, the robot self anchors at a length at least L_{anchor} when Equation 4.2 equals Equation 4.3. Therefore, only considering forces in the direction of motion in horizontal burrowing:

$$L_{anchor} > \frac{r}{2\mu} \qquad \text{(horizontal)} \tag{4.4}$$

and in vertical burrowing:

$$L_{anchor} > \frac{r}{\mu} \qquad \text{(vertical)} \tag{4.5}$$

Another advantage of steering with tip extension is the ability to create curved paths during subterranean navigation. A long continuum body without tip extension that is pushed through the soil is constrained to follow a path of constant curvature, because the whole body must move forward [195]. However, with tip extension and tip-localized steering, the robot is free to change curvature throughout its path because the more proximal body remains stationary while the tip can extend in a range of directions. Our steerable robot is also hollow, meaning that it can create hollow conduits for applications such as installing wire or irrigation lines. Such conduits could be placed without digging a trench and curve around and under obstacles as needed.

Finally, Naclerio and Hawkes' method of pneumatic tip extension enables the soft robot to burrow at high speeds. The speed (480 cm/s) achieved by the subsurface movement of the simple robot in Figure 4.8 nears its intrinsic limit in air. Higher speeds require more internal pressure, which is limited by the hoop stress of the fabric body. The full-sized

robot with tip flow and steering was operated at 2 cm/s. For comparison, previous steerable burrowing robots burrowed at 0.11 cm/s in glass beads [177], previous root-like robots that grew by additive manufacturing burrowed at 6.7×10^{-3} cm/s in plastic beads [158], and the InSIGHT HP^3 probe burrowed at 0.14 cm/s [147] in sand on Earth. None of these designs incorporated a mechanism like aeration to reduce the strength of the surrounding medium. In living examples, moles [196] and razor clams [197] can burrow at speeds up to 1 cm/s, and the sandfish lizard [45] can burrow up to 10 cm/s in short bursts.

As shown in the results of Hypothesis 2 testing, aeration reduces drag in GM, and although the relationship among depth, flow angle, and force is nonlinear, our characterization results show that tip flow is an effective method for reducing the force required to burrow in our robot. The first interesting nonlinearity we found is in the relationship between drag and depth in vertical burrowing while aerating. For a given flow rate, force is reduced to near zero until a critical depth, beyond which the effectiveness of aeration decreases, but is still present (Figure 4.4). Texier *et al.* [198] also observed a qualitatively similar behavior in an experiment that used a vibrating vertical intruder to fluidize GM. A possible explanation is that the lithostatic pressure and drag force increase with depth [98] to a point where the air can no longer mobilize the grains and fluidization is suppressed. Furthermore, with increasing depth, it likely becomes more difficult to fluidize the volume of sand above the aeration source. Because parameters are varied to increase the critical depth, the slope of the drag versus depth curve in the region beyond the critical depth increases. This could be caused by a higher lithostatic pressure or increased sand compactness due to the high-pressure airflow itself.

The second nonlinearity we found was in the relationship between flow direction and drag in horizontal burrowing. Although tip flow in line with the direction of movement is most effective at reducing drag, we also found that airflow perpendicular to the movement was still effective, even though none of the component of flow was in the direction of movement (Figure 4.6, B & C). One possible explanation is that air directed perpendicular

to the motion (here, downward flow for a horizontal motion) also fluidized the sand in front of the robot, as suggested by the visualization of particle flow in Figure 6 in Naclerio *et al.* [161] showing the movement of particles above and around the air injection source. This might also explain why the force reduction in vertical burrowing is much greater than in horizontal burrowing for a given flow rate: If the fluidized region tends to spread upward from the source, then it would be less effective at reducing drag around the tip of the robot when moving horizontally.

It is important to mention that the method of aeration and air fluidization used in our robot was only demonstrated in loose, dry, noncohesive sand. The effects observed should translate to other dry GM of a similar particle size and shape, such as other sands and extraterrestrial regolith, and to media with larger and more spherical particles, but with higher required flow rates [17, 199]. The effectiveness of aeration is likely limited in cohesive, damp, or saturated earth environments. However, water could be used for the fluidizing flow in these soils, as used by the southern sand octopus (*O. kaurna*) [167]. Similarly, vibration-induced liquefaction, such as in sonic drilling [174, 200], or an auger drill [201] could be implemented in the tip-based device on our robot.

Our method of aeration uses energy from a compressed gas to reduce the reaction force required to burrow. For a critical depth of 15 cm, a flow rate of 168 L/min at 130 kPa was used, with a corresponding power of 550 W. Intruding at 1 cm/s for 15 s required 42 liters of air and 8.3 kJ of energy, but less than 10 N of force. For comparison, the work done by the intruder without aeration was only 5.8 J but required more than 80 N of force. This suggests that aeration does not save energy in burrowing but reduces force by an order of magnitude, allowing the robot to be soft and, therefore, steerable. The reduced reaction force would be useful in low-gravity applications, such as planetary or asteroid exploration, where reaction forces are difficult to produce. Projects such as NASA's OSIRIS-REx's asteroid sample return mission already carry compressed gas for granular fluidization [202].

As shown in the results of Hypothesis 3 testing, asymmetric, downward-directed air-

flow can control lift, although the relationship between flow angle and lift reduction is nonmonotonic. The result is suspected to be unique to GM, because in a fluid, such downward airflow would increase lift rather than reduce it. Increasing the component of the downward airflow by varying the flow direction from horizontal to vertical does not monotonically decrease lift. Instead, at around 30° from the horizontal there is a range of angles that actually increases lift (Figure 4.6, D and E). At deeper depths and higher flow rates, this maximum is less pronounced. This increase does not appear without airflow, suggesting that it is not a product of nozzle geometry but could be an effect of airflow position and orientation. Although more study is needed to understand the granular physics of this behavior, we do note that the angle of repose of dry sand is approx. 30° [203]. Ding *et al.* [50] found that lift in GM was caused by sand being pushed up a slip plane, suggesting that aeration or fluidization along a slip direction could affect lift differently than at other angles. Last, we note that although lift increases with depth, it eventually saturates [98], suggesting that lift would still be an issue for a robot that burrows horizontally much deeper than ours, but would be smaller in comparison with the ever-increasing drag force.

Our work presents a terradynamic understanding of burrowing in GM and applies the key results to design a soft robot that controls subterranean interaction forces to achieve fast, steerable burrowing in three dimensions. Although our method of burrowing may not be ideal for soil penetration beyond a few meters, it offers improved performance in long, shallow, directional burrowing. Potential applications on Earth include soil sampling; minimally invasive irrigation, wire, or geothermal loop installation without trenches; erosion control; search and rescue; and granary inspection. Our method is also well suited for dry, low-gravity, extraterrestrial environments, where reactive forces may be difficult to produce. Example applications include thermal sensor placement on Mars, volcanic tunnel exploration on the moon, asteroid sampling or anchoring, and granular ice exploration on Enceladus, a moon of Saturn. More broadly, the mechanisms for controlling subterranean forces investigated in this paper are useful beyond the scope of a small burrowing

robot. Future work could examine integrating tip extension with conventional drilling and exploration technologies.

4.6 Contributions

Funding: This work is supported by the NSF (grant nos. 1637446, 1915445, 1915355, and 1935548), the Army Research Office (grant no. GR10005043), the Packard Foundation, and by an Early Career Faculty grant from NASA's Space Technology Research Grants Program. The work of N.D.N. is supported by a NASA Space Technology Research Fellowship. Author contributions: N.D.N. designed the robot, wrote the manuscript, prepared videos, and performed experiments. A.K. prepared figures and performed experiments. M.M.-C., Y.O.-A., and E.A. performed experiments. D.I.G. advised the paper and experiments. E.W.H. advised the design of robot, wrote the manuscript, and advised the paper and experiments. Competing interests: N.D.N. and E.W.H. are authors of international patent application WO2020060858A1, related to this work. All other authors declare that they have no competing interests.

CHAPTER 5

AERATION-INDUCED COMPLEX MULTIPHASE FLOWS

5.1 Preface and Summary

Recent studies of soft robot movement in sand have revealed that local high Reynolds number airflows can aid in intrusion (see Chapter 4), but the multiphase flow phenomena that emerge beneath the surface remain unexplored. We experimentally study the simplest version of such dynamics, the grain flow and structure formation created by a downward impinging buried air jet in a granular medium at different depths and flow rates. By bringing the probe to a clear sidewall, we observe rich phenomenology including pinned granular "bubbles" and breaching cavities. For certain parameters, bubbles can display a regular oscillation in their surface. We refer to these as "bubblators" and their dynamics are due to a creeping boundary flow that creates damped travelling vertical dunes along the bubblators length. A dimensional model based on self-similar turbulent jets captures the frequency scaling of these oscillations. We also find that pinned bubbles and bubblators can also be stably transported through space simply by moving the inlet source.

5.2 Introduction

Newtonian fluid flows interacting with solid granular media (GM) can transport and scour the solid phase by generating sufficient shear stresses [204, 205]. This coupling between fluid and solid phases is key in the field of sediment transport. However, the difficulty of the Navier-Stokes equations and the high number of grains in most physical systems often makes exact simulation infeasible in practice, and instead elaborate continuum modelling [206] or empirical methods [207] are required. Low density Newtonian fluids require high

This chapter's contents contain unpublished results by Andras Karsai and Daniel I. Goldman.

flow velocities to generate sufficient shear stresses to mobilize grains [204], which leads to high Reynolds numbers and thus turbulent flows, further complicating the system.

A common scenario of turbulent transport is impingement into GM by a turbulent jet [208, 209, 210]. Many previous studies have observed a system of GM immersed in dense fluids (often in water), with an incident flow from above pointing down in crater scour studies [211, 212], or from a source buried in the GM pointing upward in studying localized fluidization [213, 214]. Fluid injection from the bottom locally fluidizes and create bubbles within the GM that travel upwards to the surface with often unexpected dynamics [215, 216, 217]. However, such bubbles in both local and global fluidization have short lifespans as they escape to the free surface [218]. To study the long-term dynamics of such bubbles, one could create a situation where a bubble is 'pinned' via some mechanism. Zoueshtiagh [213] and Phillipe [214] both observed stationary bulges at their locally fluidizing inlets for certain flow rates. In a previous study, we also observed how a burrowing robot could create long-lived bubbles by impinging a buried air jet into GM with insufficient power for any solid to reach the surface [161, 67]. This strategy was also observed in wild razor clams that created transient fluidized cavities to assist in burial [219]. To further study the long-term dynamics of such phenomena, we aim to replicate these pinned bubbles in a controlled GM environment.

In this Chapter, we study a simple system of a high Reynolds number turbulent, non-wetting fluid jet that is initiated while buried in dry GM. We chose a dry fluid of compressed air to avoid changes in cohesion by wetting [220] of our chosen dry GM of 1 mm PS. The buried air jet creates a 'pinned' bubble in the GM, and we capture the dynamics of the bubble via high-speed side-wall imaging. Variation of the input volumetric airflow Q and the burial depth y_d creates bubbles which expand until reaching some equilibrium volume, after which . We observe a surprising class of bubble oscillators ("bubblators") that exhibit an emergent, long-term creeping mechanism in their boundaries. We describe this mechanism by examining oscillations of the cavity center over time, and show that a

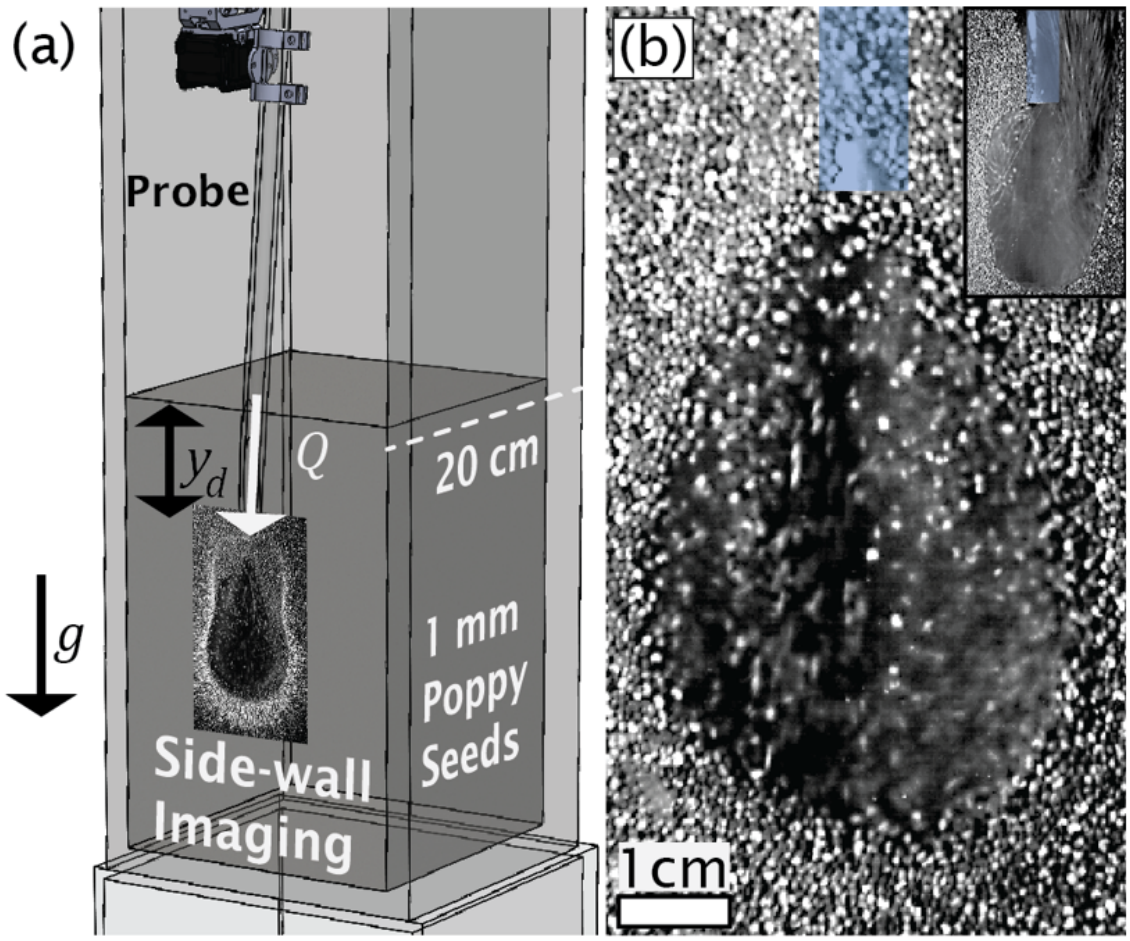

Figure 5.1: **Pinned Bubble Experiments** (a) Schematic diagram of locally fluidizing probe robot. (b) Side-wall image of a pinned bubble in poppy seeds with airflow injected by the blue-highlighted probe at top (Inset) Side-wall image of a breaching state where airflow carries grains to the surface.

simple geometric model can predict these oscillations' frequency scaling. We also show how pinned bubbles and bubblators can be stably transported through space by moving the inlet source.

5.3 Pinned Bubble Experiments

An automated robot maneuvers a cylindrical plastic probe of length 34 cm within a 18 cm x 18 cm x 25 cm volume of poppy seeds in a fluidizing bed (Figure 5.1(a)). The probe has an outlet diameter of $d = 8.7$ mm, which we can choke to $d = 6.35$ mm by inserting a 3D printed nozzle. A gantry of stepper motors driving a lead screw (OpenBuilds C-Beam

Linear Actuator) positions the probe along the y-coordinate, while a pair of Dynamixel AX-12 servomotors mounted perpendicular to each other control the angle of the probe. To achieve the desired probe position of the outlet touching the front wall, we angle the probe and thus at the outflowing jet 12° from the vertical for all trials.

For each test, we initiate airflow by opening a solenoid valve with a compressed air input regulated to 60 PSI flowing into plastic 1/4" tubing. Airflow starts once the probe is positioned within the bed at a set depth y_d in a range of $[0, 100]$ mm. We attached a stepper motor under PID control to a flow adjustment valve connecting the tubing to create an ad-hoc flow controller after the solenoid valve. An Omega Engineering FMA1700 mass flowmeter captures the output airflow signal (we tested a range for Q of $[40, 225]$ L/min), then the flow enters the GM. We estimate our Reynold's number ranges for the outlet pipe as $Re = [6.6 \times 10^3, 3.7 \times 10^4]$ for $d = 8.7$ mm and $Re = [4.8 \times 10^3, 2.7 \times 10^4]$ for $d = 6.35$ mm, well within the turbulent regime. We capture the bubble profiles at the side wall via a Phantom v210 camera running PCC 3.5, recording at 30 FPS for 120 sec for long duration trials, and at 4200 FPS for 2.1 sec for high-speed, short duration trials. We recorded a total of approximately 350 trials (full data and footage available on request). The experiment is run by an NI USB-DAQ 6341 executing a LabView program which coordinates the control signals and records the airflow feedback. Each video recording is synchronized with the opening of the solenoid valve via the DAQ. After each trial, the bed is globally fluidized from the bottom for 15 sec to reset the granular state.

5.4 Observing Oscillating Bubbles

Each trial run for 120 sec reaches some equilibrium state for a singular (Q, y_d) input, which we characterize in a phase diagram (Figure 5.2). A typical pinned bubble (Figure 5.1(b)) has grains near the nozzle blasted downwards by the turbulent jet and then recirculate upwards via boundary flow, while the rest of the granular volume remains stationary due to friction. These bubbles' boundaries are stationary over long periods. Breaches occur when

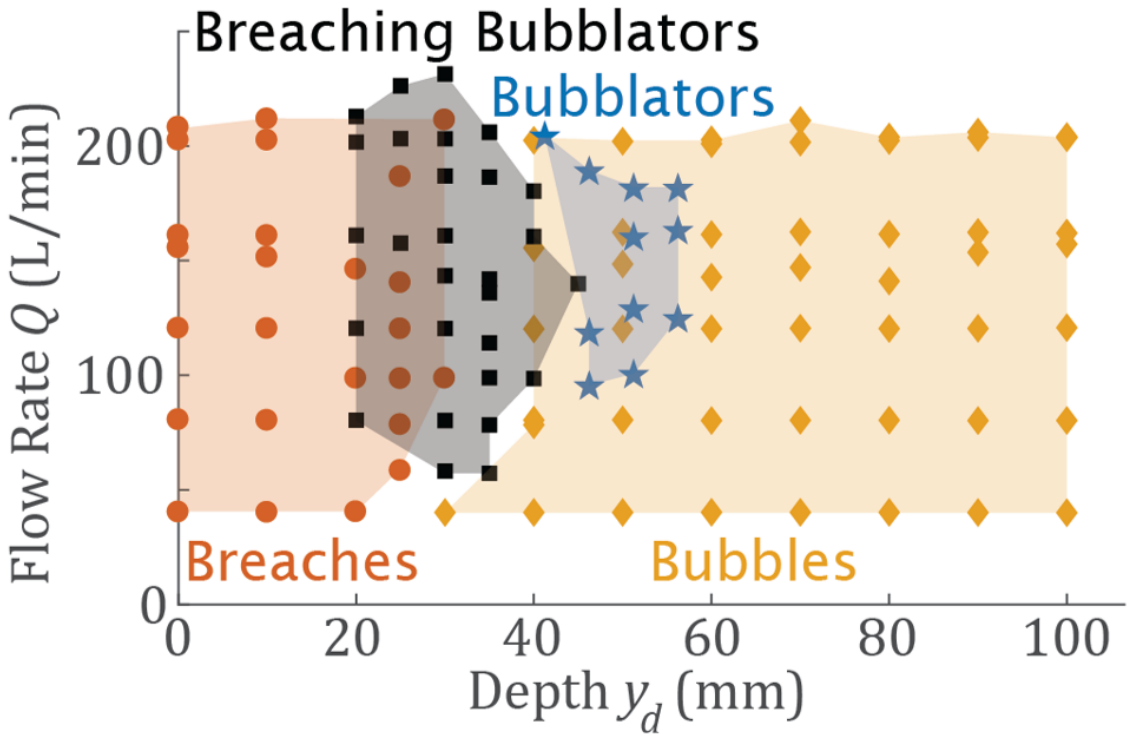

Figure 5.2: **Phase Diagram of Pinned Bubbles** Phase diagram of resultant steady states from experimental parameter sweeps of volumetric flow rate Q and burial depth y_d.

the air jet continuously carries grains to the surface (Figure 5.1(b,Inset)) in a chaotic and unpredictable state that modifies the GM surface via grain transport. Our newly observed 'bubblators' appear between these two extremes and look like elongated bubbles with oscillating boundaries (Figure 5.1(a)). Some bubblators begin life as transient breaches that re-collapse into the main cavity to form a bubblators. For certain (Q, y_d) combinations, we observed multiple possible end states (overlaps in the phase diagram), hinting at strong hysteresis from the GM agitation [221].

In both breaching and non-breaching bubblators, we observed macroscopic oscillations of the bubble boundaries (Figure 5.3). These boundary oscillations appeared to be caused by eddy-current induced grain jamming in the 'shadow' of the input turbulent jet. We examined videos of the grain motion and saw that the turbulent jet's outflow angle was about $\theta = 11.8°$, which matches established values for a jet impinging into an identical fluid [210, 209], and this creates a region where boundary flow upwards dominates. The

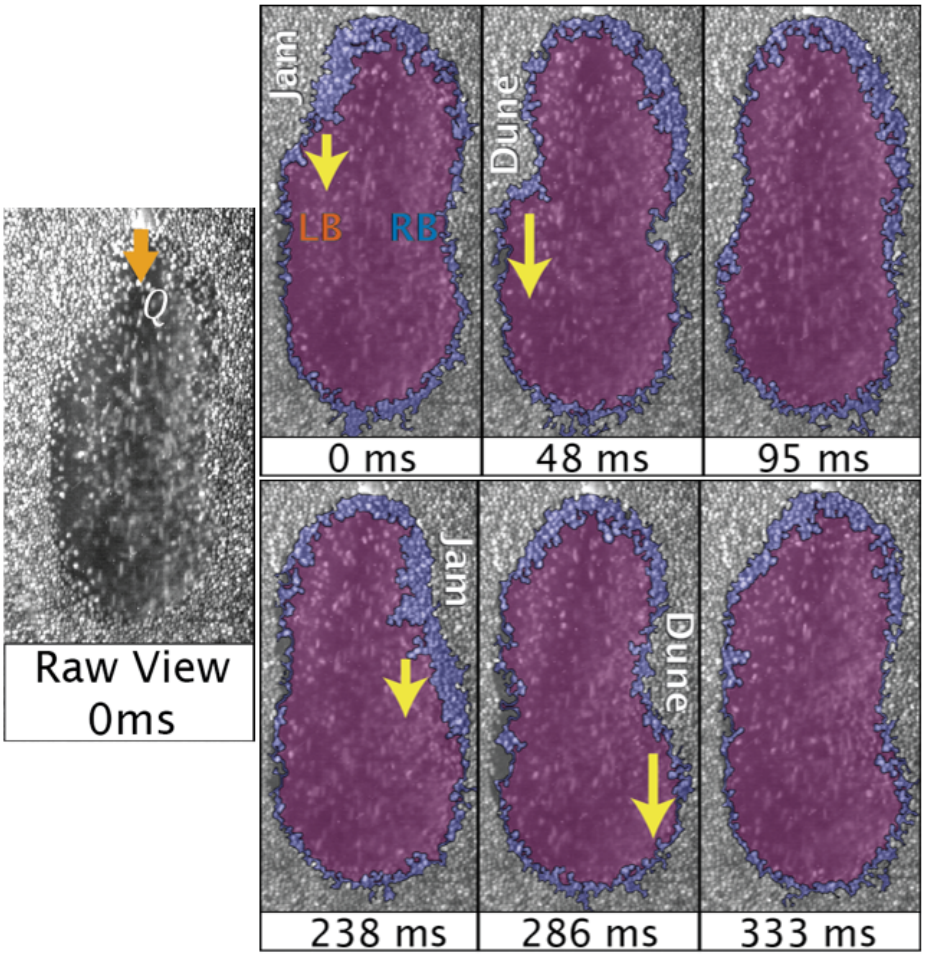

Figure 5.3: **Observing Bubblators and their Oscillating Boundaries** Time series of high-speed images for a bubble where $Q = 200$ L/min and $y_d = 50$ mm, highlighting the grain jamming formations that induces boundary oscillations, with moving sidewall grains colored in blue and void space in purple. The series shows a single cycle of boundary oscillation on the left boundary (LB) then the right boundary (RB) of the bubble.

jam grows as grains accumulate, then becomes large enough to intersect the outflowing jet, then becoming a 'dune' that saltates down the length of the bubbles. This process then repeats on the other side as the net grain mass recirculates away from the previous dune. To characterize the bubble boundaries, we binarize and simplify the recorded videos into a bubble boundary + centerline representation (Figure 5.4(a)), where we can take slices at each depth y to observe the relative position and phase of the left boundary (LB) and right boundary (RB) oscillation (Figure 5.4(b)). Looking at all of the slices in depth of the bubblator's centerline versus the probe's position, the rich dynamics of the bubblators long term creeping oscillations appear (Figure 5.4(c)).

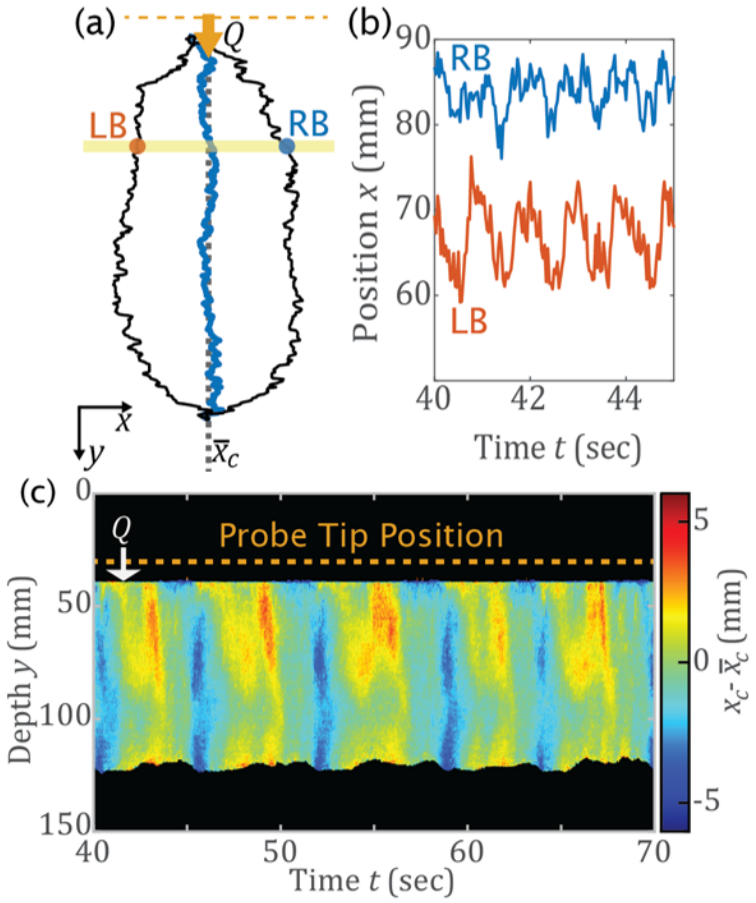

Figure 5.4: **Characterizing Bubblator Boundaries and Centerlines** (a) Snapshot of a bubblator's oscillating void space calculated from image processing. The black lines show the bubble bounds and the blue line shows the bubble centerline. Slices at a set y value give the x position of LB & RB and show their relative oscillations over a few cycles in (b). (c) Colorplot showing oscillation over time of the bubblator's centerline x_c relative to the probe position at $\bar{x}_c$ for a time interval of 30 sec for a trial of $Q = 200$ L/min, $y_d = 50$ mm.

On further examination of the bubblators' centerlines' (Figure 5.5(a)) signals x_c over y, we found strongly peaked power spectral densities, showing strong periodicity in the bubblators' oscillations. Of all the bubblators discovered for our $d = 8.7$ mm probe for tested (Q, y_d), x_c oscillated at one of two dominant frequencies, $f_1 = 0.98 \pm 0.14$ Hz and $f_2 = 2.06 \pm 0.32$ Hz. Bubblators with a smaller final length L oscillated at the more rapid f_2, while longer L bubblators oscillated at f_1. f_1 and f_2 are nearly a factor of 2 of each other, which may hint at an emergent period-halving bifurcation in this system if L increases further. Plotting all trials' mean + SD x_c amplitudes (Figure 5.5(b)), bubblators for our tested system exist when $0.25 < y_d/L < 1$ (recall L is the equilibrium result

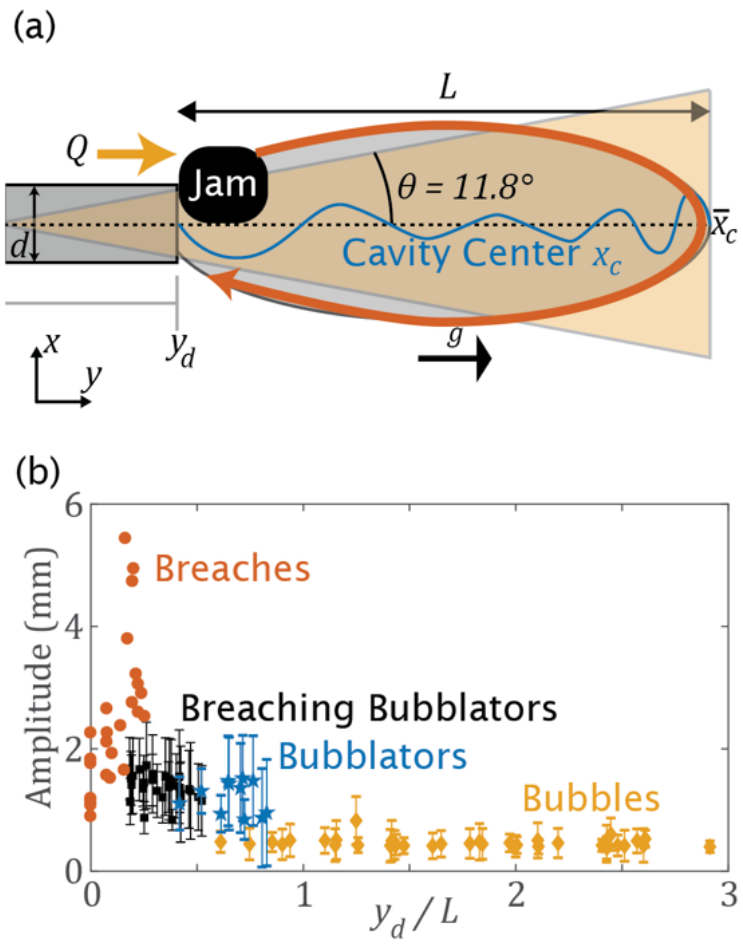

Figure 5.5: **Waves from the Bubblators' Creeping Action** (a) Diagram of the bubblator geometry, analyzing the oscillations of the cavity centerline x_c for various positions y. The jam's net grain flux must traverse an ellipse of length L created by an injected airflow Q through a nozzle diameter d. (b) Errorbar plot of mean + SD centerline oscillation amplitudes for all trials depicted in Figure 5.2 vs. starting depth y_d divided by the resultant bubble length L, also colored by resultant state. Errorbars are omitted for breaches as they are too chaotic.

of an input (Q, y_d)) and have distinctly higher oscillation amplitudes than bubbles, while breaches occur for $y_d/L < 0.25$ and oscillate severely. For the bubblators, we also observed x_c for each act as a damping travelling wave that travels downwards parallel to g for both f_1 and f_2 bubblators, with the f_1 group exhibiting more reversals (Figure 5.6(a)), as L was longer for this group. The oscillation amplitude of each bubblator along its length also varies (Figure 5.6(b)), with local amplitude minima corresponding to reversals in the damped travelling waves, as seen near $y_d/L = 0.7$.

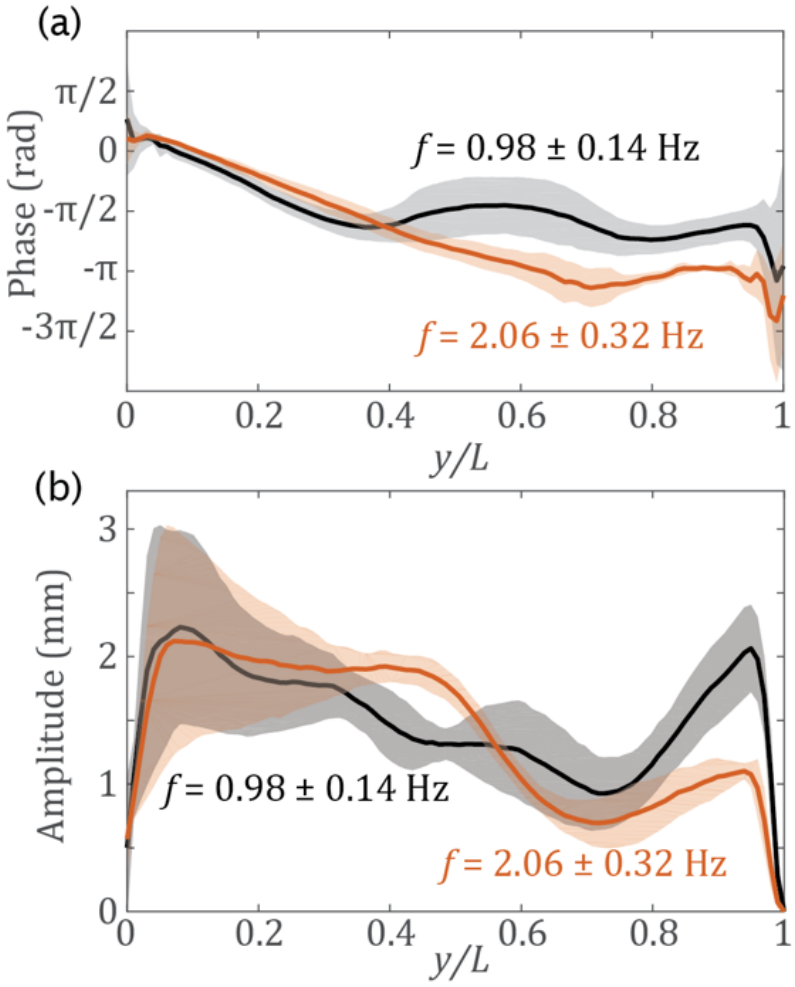

Figure 5.6: **Phases and Amplitudes of Single Bubblator Centerline Oscillations** (a) Mean + SD of the relative phases for the bubblator centerlines' traveling waves at mean dominant oscillations frequencies $f = 0.98$ Hz and $f = 2.06$ Hz, normalized to each bubblator's total length L. (b) Mean + SD of the oscillation amplitudes of the bubblator centerlines at mean dominant oscillations frequencies $f = 0.98$ Hz and $f = 2.06$ Hz, normalized to each bubblator's total length L.

5.5 Frequency Scaling of Bubblator Oscillations

For our measured Q's high Reynolds numbers, the fluid phase outflow from the probe is turbulent, yet strongly periodic boundary oscillations emerge from such a chaotic input flow. Based on observation, we attempt to create a simple relation predicting how the bubblators' dominant oscillation frequencies scale with the bubblators' properties.

Pope [209, 210] presents a model of self-similarity in turbulent jets where the an outlet into quiescent fluid creates a cone of angle θ symmetric about the horizontal with a

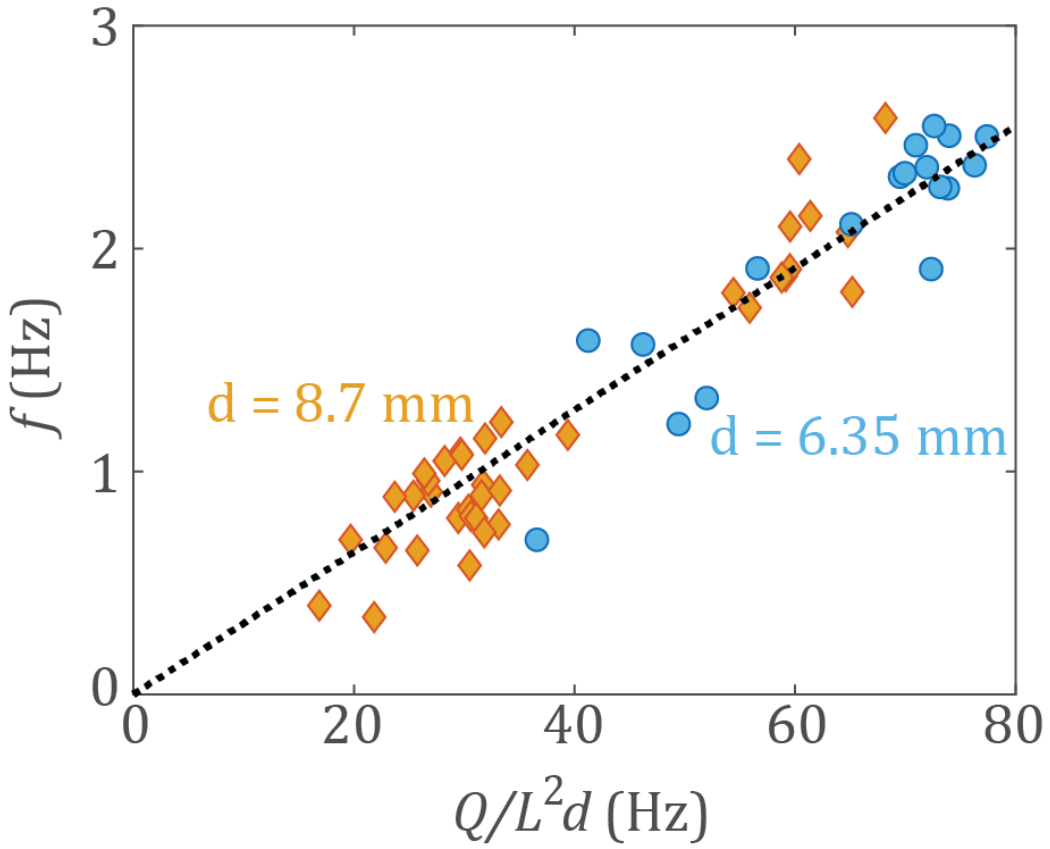

Figure 5.7: **Model of Bubblator Oscillation Frequencies** Using the boundary running model illustrated in Figure 5.5(a), plot of all observed dominant bubblator frequencies for two tested nozzle diameters d showing a linear relation between bubblator frequency and the parameter group $Q/(L^2 d)$ with dimension of t^{-1}.

Gaussian flow speed:

$$u(x, y) = u_{max} \exp\left(-\frac{2x^2}{y^2 \tan^2 \theta}\right) \tag{5.1}$$

following the diagram in Figure 5.5(a), and introducing the variable of $U = 4Q/\pi d^2$ is the outlet flow speed in a pipe. Taking the average of Equation 5.1 with an integral along x, and using the fact that $u_{max} = Ud/y \tan\theta$ gives a mean jet speed for each position y as:

$$\bar{u} = \frac{Ud}{2y \tan\theta} \tag{5.2}$$

Now we make an assumption in our model from observation: As grains are caught in the

jet they are entrained in the fluid flow and move at some proportion of the fluid velocity toward the bubble's bottom. By their end of travel they have some characteristic velocity v_{char} proportional to $\bar{u}$ at $y = L$:

$$v_{char} = k_1 \frac{Ud}{L} \tag{5.3}$$

Since we observed the angle θ to be near identical in all experiments of matching nozzle diameter d, and we absorb $\tan\theta$ and all constants into k_1. Now a second assumption: Once a jam forms and begins creeping down the bubble as in Figure 5.3, a net grain flux must flow via some path to form the observed jam on the opposite side of the inlet. Since upward grain movement is dominated by the recirculating boundary flow, consider the 'jam' as a particle that must flow along the circumference of the bubblator's ellipse of length L and eccentricity e (Figure 5.5(a)). The frequency of this oscillation would be some proportion of v_{char} divided by the ellipse circumference the jam travels:

$$f = k_2 \frac{v_{char}}{E(e)L} \tag{5.4}$$

$$f = k_1 k_2 \frac{1}{E(e)} \frac{Ud}{L^2} \tag{5.5}$$

where $E(e)$ is the elliptic integral of the second kind. Since $U = 4Q/\pi d^2$, and we observed near identical $e \approx 0.9$ for all bubblators, we can collect all constants in k and arrive at a scaling relation for the oscillation frequency:

$$f = k \frac{Q}{L^2 d} \tag{5.6}$$

Plotting this relation for inputs of Q and d and the resultant L and f for all trials with observed bubblators, Figure 5.7 shows a strong correlation, with $R^2 = 0.911$ and $k = 0.032$. This shows that the input fluid flow generates an oscillation that scales especially with bubble length, as it effects both the v_{char} at the bubble's terminus and the distance

the creeping mound must travel. Further studies may expand this relation by predicting or expanding L and k, as L remains an observed quantity of the bubble's equilibrium state not predicted in this Letter. Further dimensionless groups are expected to affect f in future studies.

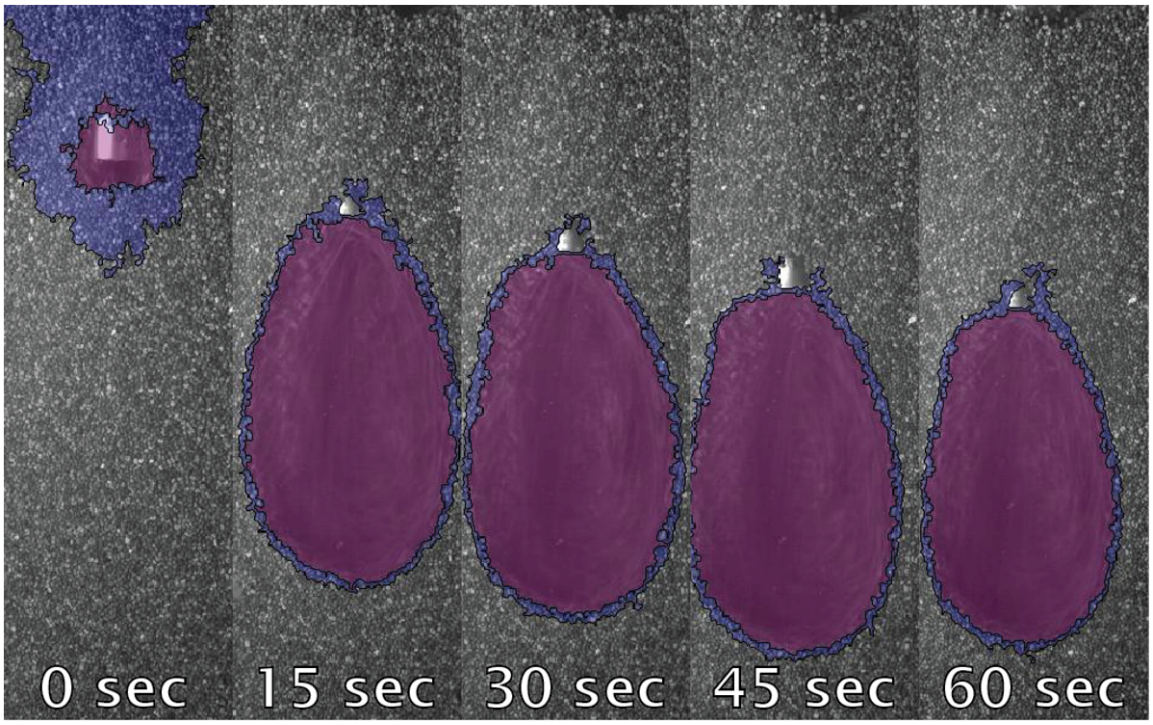

Figure 5.8: **Transporting Pinned Bubbles** Time series showing pinned bubble transport with a probe moving downward at $v_p = 0.5$ mm/sec from $y_d = 20$ mm to $y_d = 40$ mm at $Q = 160$ L/min, with coloring same as Figure 5.5(b).

5.6 Transporting Bubblators

Motivated by our previous study [67], we vary the input y_d over time for a subset of trials by slowly stepping the gantry motor (at 0.5 mm/sec) to drive the probe downward parallel to $\vec{g}$. We observed that the pinned bubbles and bubblators could be stably transported at a near constant bubble area through space, simply by moving the inlet source. The rapid boundary flow of the pinned bubble recirculated grains during intrusion such that grains near the intruding inlet would creep upwards toward the free surface after the probe passed through, while newly encountered grains at the bubble bottom were entrained in the fluid

flow. An intruding bubblator would also maintain its oscillating state during transport. Figure 5.8 shows one exemplary trial, where the figure shows the time series of a breaching bubblator's initiation and transport downwards while maintaining a near constant void area. Figure 5.9 shows the bubblator oscillation (as in Figure 5.4(c)) continuing as the probe moves from $y_d = 20$ mm to $y_d = 80$ mm. By collecting all stationary trials' bubbles volumes V normalized by the input Q, then dimensionally scaling by g, we can compare the normalized bubbles' volumes against y_d.

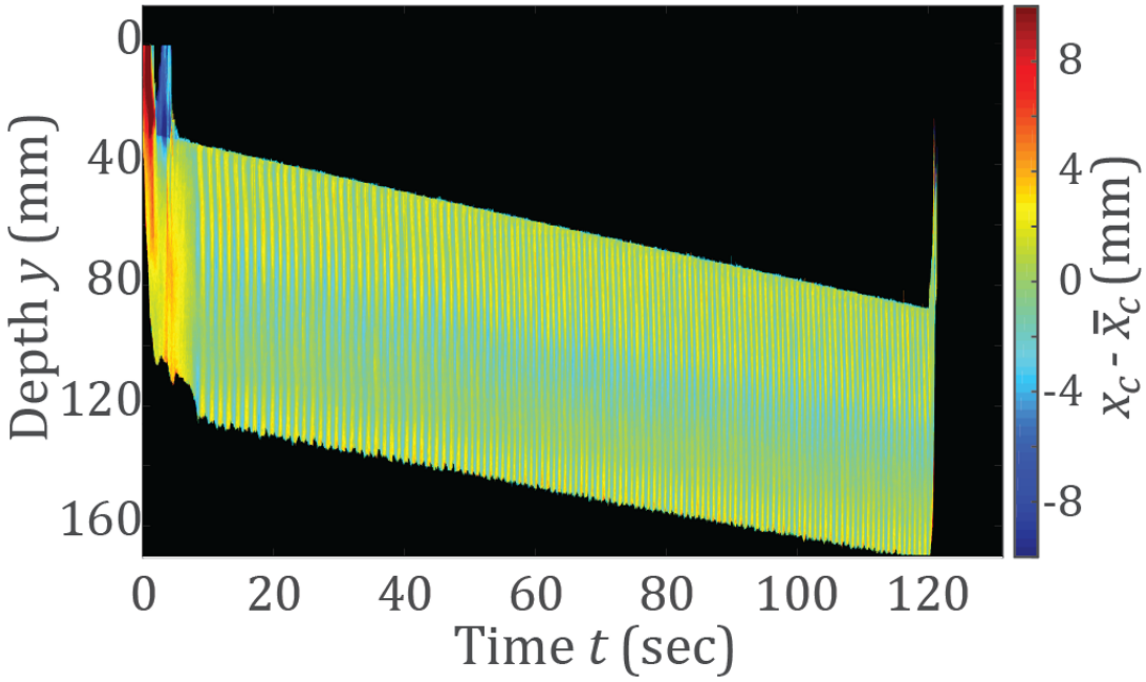

Figure 5.9: **Centerline Oscillations of a Bubblator Moving through GM** Colorplot showing oscillation over time of the transported bubblator's centerline x relative to the probe position at $\bar{x}$. Experimental data from a pinned bubble transport experiment with a probe moving downward at $v_p = 0.5$ mm/sec from $y_d = 20$ mm to $y_d = 40$ mm at $Q = 160$ L/min, same as Figure 5.8.

Figure 5.10 shows how a transported pinned bubble can maintain its volume during transport, where the moving pinned bubble enacts a net grain flow to reach depths at large volumes that the stationary trials could not generate. Due to this disparity in stationary vs. moving trials, these pinned bubbles appear to be highly history-dependent on the state of their GM substrate.

To ensure this was not only a near-boundary phenomenon, we also conducted experi-

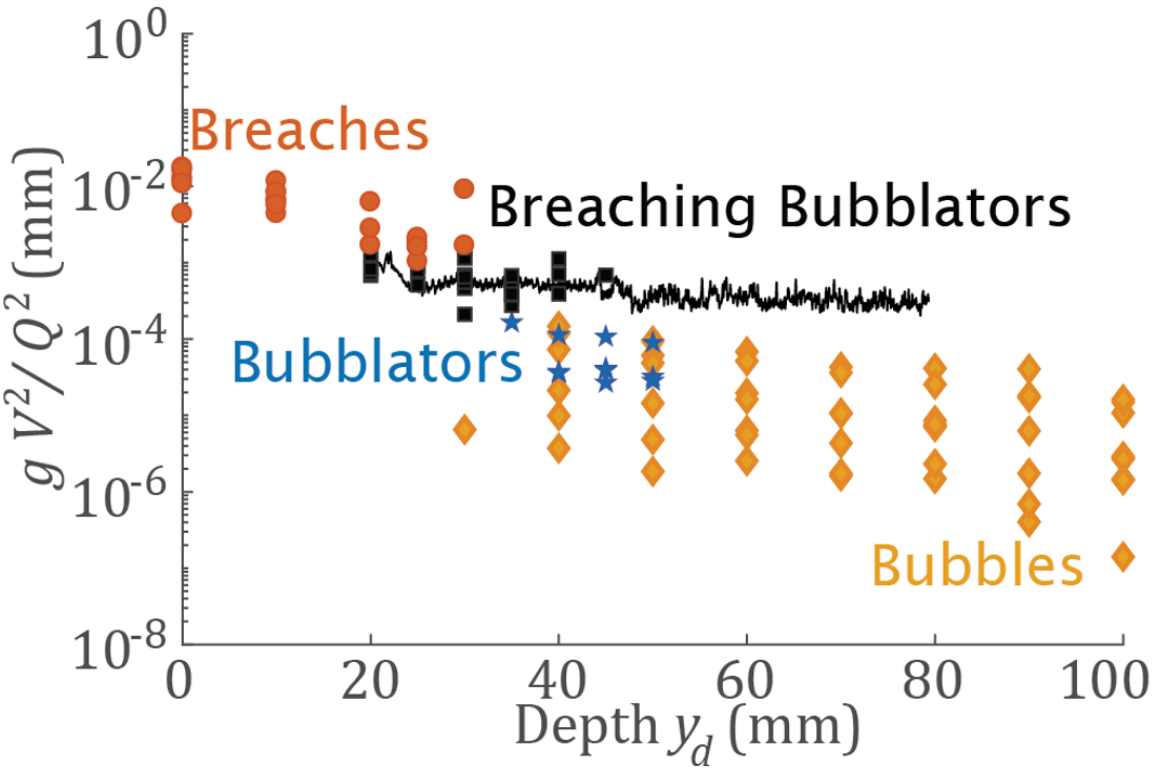

Figure 5.10: **Phase Diagram of Stationary vs. Transported Bubble States** Semi-log plot of gV^2/Q^2, a measure of bubble volume normalized by airflow, vs. input depth y_d. The points of various types represent all the stationary trials of Figure 5.2, while the line represents the trial of Figure 5.9.

ments in the mid-bed case, where the probe was kept completely vertical and positioned to intrude in the middle of the bed. These experiments were imaged via X-ray recordings with an Orthoscan Mobile DI with video output into an HDMI capture card. We conducted the experiment with all other parameters the same as the side-wall trials and again observed the phenomenon of pinned bubble transport in the mid-bed as well.

5.7 Conclusions and Future Work

Pinned bubbles in GM are multiphase flow phenomena that exhibits rich dynamics within a relatively simple system. By tuning the input fluid flow to a certain range, we an emergent creeping flow that creates long-period grain transport oscillations under high Reynolds number conditions. Future investigations can further characterize these dynamics with PIV and MRI techniques [222]. It will also be interesting to extend the predictive power of k for

oscillation frequency via experiments with granular media of varying cohesion, density, and grain size. Numerical and theoretical work could also *a priori* predict more dependencies of f via new insights. Finally, these bubbulators could allow for even more complex pinned granular structures when created in close proximity to each other. Preliminary experiments with two probes examining adjacency effects show cooperative phenomena in the multi-phase flow, with more elaborate equilibrium structures and instabilities like fingering [216] emerging where the flows interact.

5.8 Contributions

Andras Karsai conceived, performed, and interpreted this study and Daniel I. Goldman provided guidance and mentoring.

CHAPTER 6

UNUSUAL IMPACTS AND INTRUSIONS

6.1 Preface and Summary

In this chapter we present some ancillary studies on a more complex intrusion into GM featuring vertically intruding parallel plates, along with a study performed early in my PhD investigating the first and second laws of thermodynamics via the physics of inelastic impact. The study of twin parallel plate intrusions was partially motivated by a Swapnil et al.'s study on cylindrical parallel intruders creating emergent forces based on their horizontal spacing during vertical intrusion [223], with the continuum modeling performed by Shashank Agarwal, and experimental verification performed by myself. The thermodynamics of impact study was motivated as an experimental and pedagogical realization of textbook problems in Gerald Carrington's *Basic Thermodynamics* [224].

6.2 Twin Parallel Plate Intrusions

The intrusion of single passive intruders into GM has been studied in detail. However, the intrusion force produced by multiple intruders separated at a distance from one another, and hence the effect of their presence in close proximity to one another, is less explored [223]. Swapnil et al. discovered a force peak as a function of intruder separation W in GM at a gap spacing of ≈ 3 particle diameters d in vertical intrusion in a study published in 2021. This force peak was up to 25% greater in magnitude than force responses for spacings of $W > 11$, beyond which the force profile plateaued to a linear superposition of single intruders once again. The emergent force peak appears to violate the superposition assumption that characterizes RFT. Swapnil et al. hypothesized this was due to reduced

A portion of this chapter's contents are adapted from a co-authored paper published 2021 in *Soft Matter* [53], by Shashank Agarwal*, Andras Karsai, Daniel I. Goldman, and Ken Kamrin.

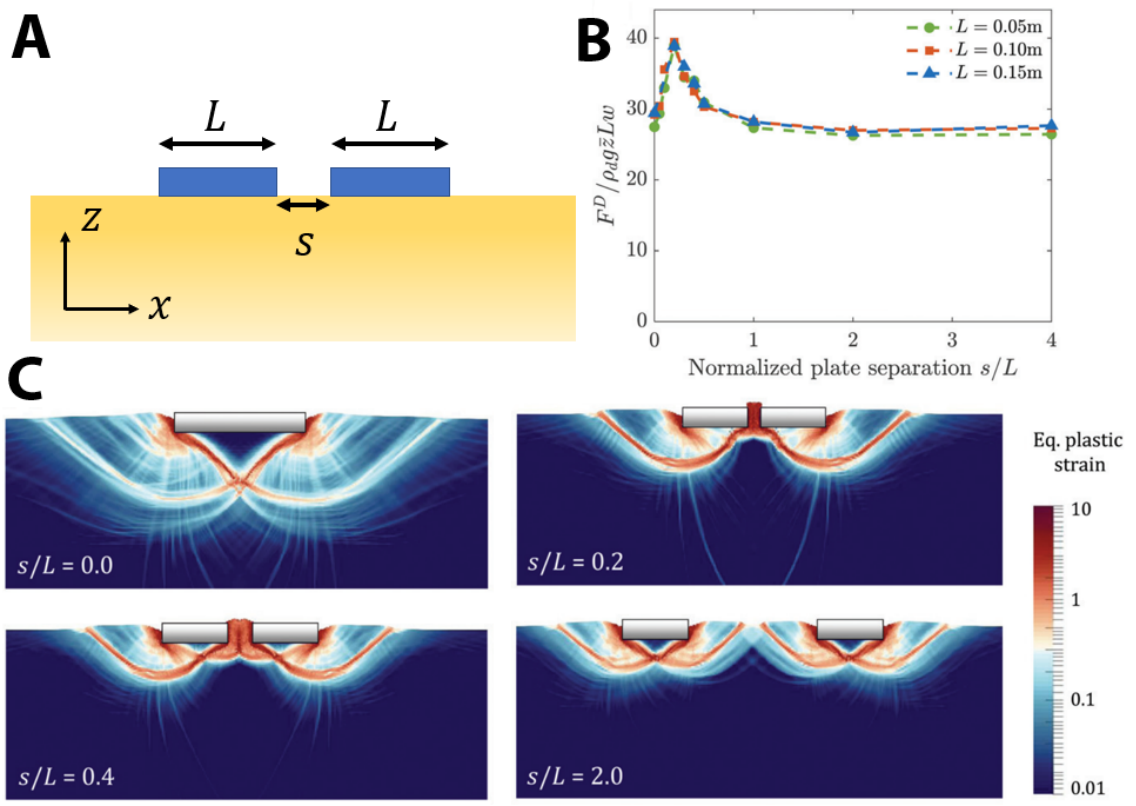

Figure 6.1: **GM Intrusion Experiment for Probing Adjacency Effects of Parallel Plates** Vertical intrusion of two parallel plates (using a non-dilatant plasticity model) (A) Diagram of intrusion scenario, with twin plates of width L and separation s moving in the $-z$ direction in GM. (B) Variation of vertical drag response (normalized) with plate separation s (normalised to plate width L) for equally sized plates ($L = 0.10$ m each). (C) The corresponding equivalent plastic strain fields at various separations. (Figures courtesy of Shashank Agarwal [65]).

particle flow between intruders and characterized this phenomenon as a granular effect, induced by increased force chains in the particle domain at $W \approx 3$. However, in a study published in *Soft Matter*, Agarwal showed that this same effect also emerges in a continuum description like the one used in Chapter 2 which is fundamentally grain-free [53]. Rather, this effect emerges from mutual inter-plate flow restriction during the plastic deformation of intrusion (Figure 6.1). The continuum plasticity model used was largely the same as detailed in Chapter 2, with additional details and modifications available in Agarwal & Karsai et al. [53].

To verify Agarwal's results from the continuum model, we also verified the drag force trend and the peak separation scaling relation with vertical intrusions experiments (Fig-

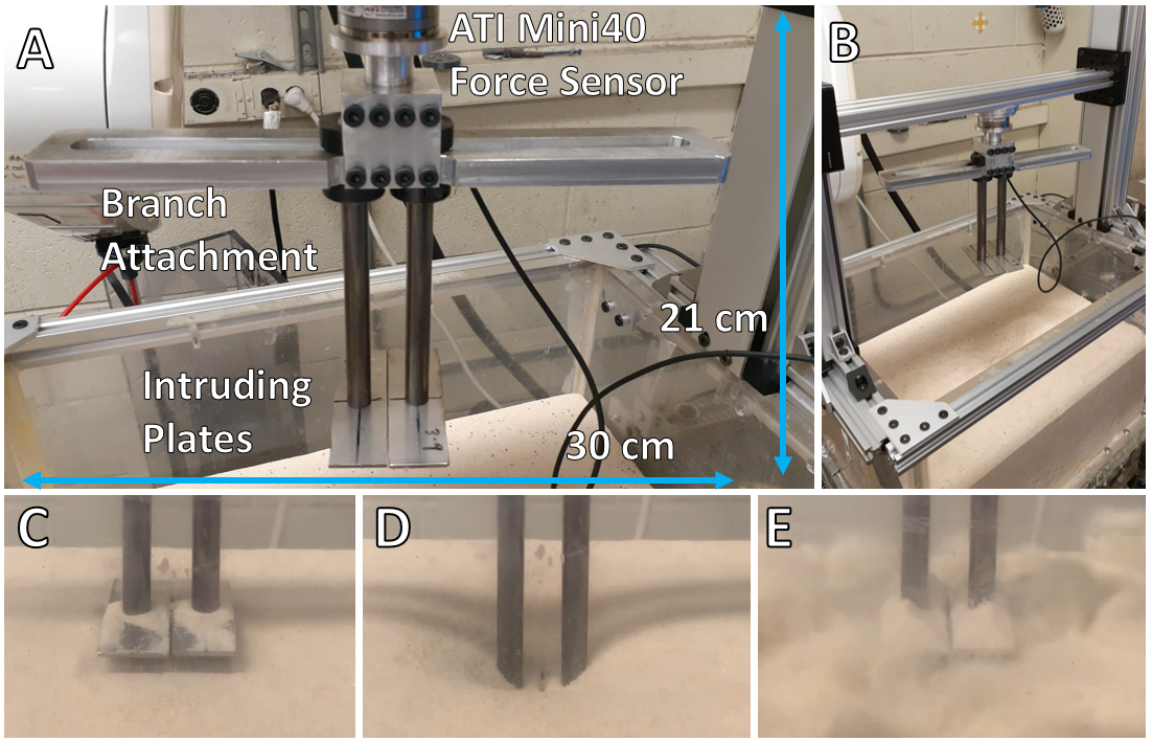

Figure 6.2: **GM Intrusion Experiment for Probing Adjacency Effects of Parallel Plates** (A) Photo of the double plate intrusion test apparatus. A pair of intruding plates are supported by 6.35 mm steel shafts clamped by shaft collars to an aluminium branch attachment, which is screwed to a tapped aluminum block connected to an ATI Mini40 force transducer. This transducer can be mounted to our Denso VS087 Robot Arm as in this figure, or (B) in an alternate configuration for vertical intrusion, mounting the branch attachment to a pair of NEMA 23 stepper motors and a pair of OpenBuilds® lead screw linear motion tracks to force the plates into the sand. (C) Double plates at a narrow spacing just before touching the sand surface. (D) Double plates fully intruded. (E) Fluidization of sand bed after double plate extrusion.

ure 6.2) and compared them to calibrated continuum simulations (Figure 6.3). A DENSO VS087 robot arm intruded an apparatus that held pairs of steel plates at various separations into a bed of loosely consolidated Quikrete Pool Filter Sand with grain density $\rho_g = 2520$ kg m^{-3} and effective close-packed density $\rho_d = 1512$ kg m^{-3}. The internal friction value of this medium was μ_s = 0.72 based on angle of repose measurements from experimental tilting tests, with the media globally fluidized for 15 seconds to an initial packing fraction of $\varphi \approx 0.58$ for all trials. All intrusions were performed at 11 mm s^{-3}, where speed dependence of the force response is negligible. Over 128 trials, the net resistive forces on the pair of intruding plates were measured using an ATI Mini40 force transducer. We observed a satisfactory match between the experiments and the simulations (Figure 6.3). The fact that

the experimental data for different values of L collapse onto a single dimensionless master curve supports the robustness of a scaling relation implied derived by Agarwal predicting the relevant dimensional values for the peak force magnitude (see y-axis of Figure 6.3) [53].

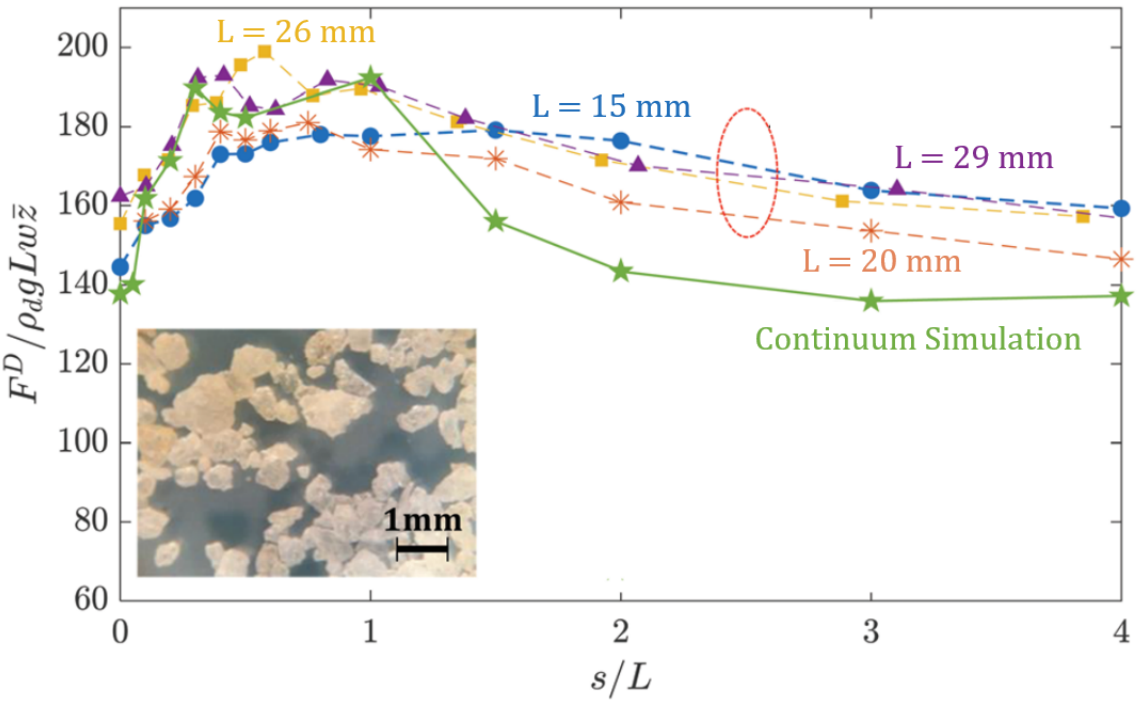

Figure 6.3: **Experimental Data of Emergent Forces from Adjacency Effects in Double Plate Intrusion** Comparison of experimental data (dotted lines) and calibrated continuum simulations (solid line) for two equal plate intrusion experiments. The experiments used plates of width $L = 15$ mm (blue dots), $L = 20$ mm (orange asterisks), $L = 26$ mm (yellow squares), $L = 29$ mm (violet triangles), and the continuum model result with plate width $L = 10$ mm (green stars). All paired plates have a $1 : 5$ horizontal aspect ratio for $L : w$. For the experiments, we used Quikrete Pool Filter sand with grain density $\rho_g = 2520kgm^{-3}$. Inset shows microscopic view of tested sand particles. The sand's effective critical density $\rho_d = 1500kgm^{-3}$ and a critical angle of $36° \pm 1°$. Continuum simulations provided by Shashank Agarwal [53] (calibrated to the Quikrete sand's properties) correspond to plane-strain two-plate intrusions with drag forces F^D averaged over a depth range of 6-8 cm with the y-axis normalized by $w = 1$ m, $g = 9.8ms^{-2}$, $\rho_d = 1500kgm^{-3} = \rho_g \times \varphi$.

Additionally, we observe that although both Figure 6.1(B) and Figure 6.3 show peaks in the normalised force responses of the media at low separations, the shapes of the graphs are not identical. A more comprehensive amalgamation of the macroscopic insight we develop in this study, combined with the microscopic observations made by Swapnil et al. [223] for grain-scale plate lengths may be helpful in future studies. Since these flow interference

effects appear to violate the linear superposition assumptions of RFT, further insight into the transient flow structures within GM that modulate force response is needed (discussed in Chapter 7) and may add further improvements the RFT's accuracy in modeling complex intrusions.

6.3 Thermodynamics of Inelastic Impact

Early in my PhD, I undertook a small project under Prof. Goldman as a way to familiarize myself with experimental methodology and independent scientific work. This project investigated a simple physical problem inspired by textbook problems Prof. Alberto Fernandez-Nieves and textbook problems in Gerald Carrington's *Basic Thermodynamics* [224]. The problem involved investigating the first two laws of thermodynamics by quantitatively examining conversions between various forms of energy.

To do this experimentally, we created an experimental setup (Figure 6.4) where we could convert tractable potential to kinetic to heat energy via a simple, hand-operated experiment. We raise a steel cylinder of $m_i = 1.21$ kg attached to a string (Figure 6.5A) to various initial heights h within an optically clear acrylic tube (Figure 6.5C). We then drop this mass onto a small lead sheet of $m_s = 0.15$ kg. Embedded inside the lead sheet is a thermistor: an electronic component that is sensitive to temperature, and lowers its resistance in response to a rise in temperature. We embedded the thermistor in the sheet by drilling out the sheet's narrow edge, inserting the thermistor, then filling the remaining space with a thermally conductive, electrically insulating epoxy. This thermistor is connected to a simple Op-Amp amplifying circuit (Figure 6.5B).

Since both the lead sheet and the epoxy are very thermally conductive, the energy from the impacting cylinder will transfer into the lead sheet as heat. Another thermistor element and amplifier was set in the ambient air nearby the impact to monitor any changes in the ambient temperature. To verify the final impacting speeds v for our experiments, we setup an AOS X-PRI high speed camera to monitor the terminus of our tube where the impact oc-

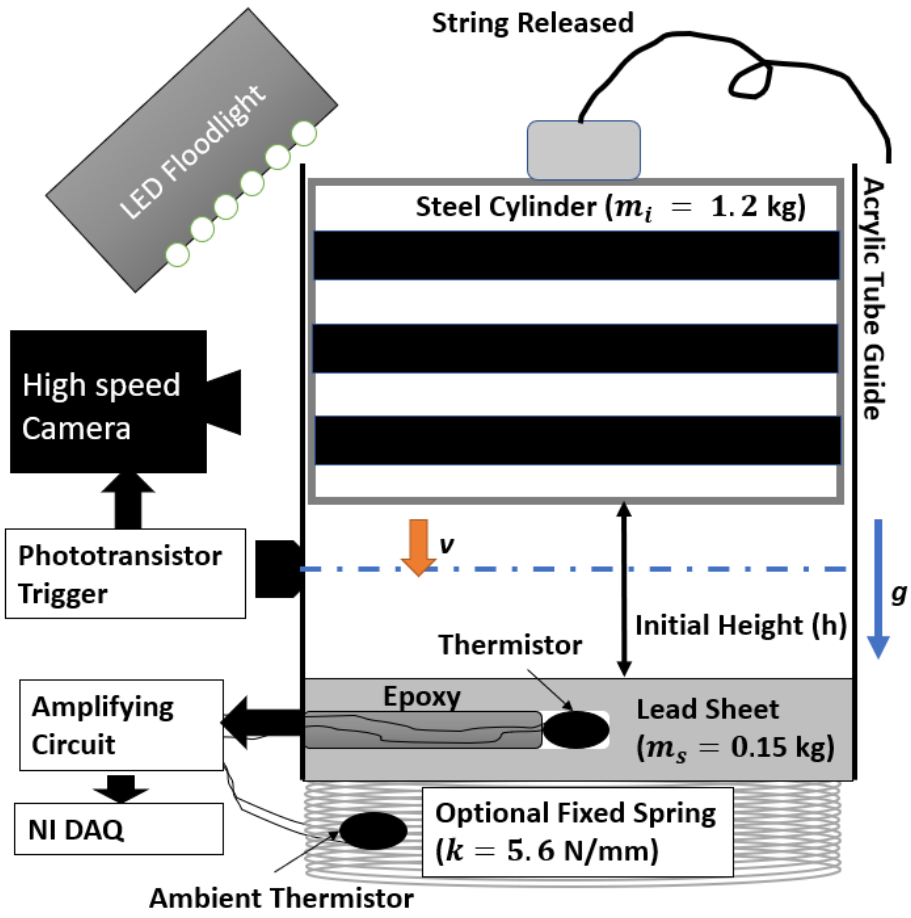

Figure 6.4: **Thermodynamics of Impact Experimental Diagram** Sketch showing experimental protocol for impact trials (not to scale). The steel cylinder of mass m_i is manually raised to a height h and dropped such that it impacts a lead sheet of mass m_s at a final velocity $v = \sqrt{2gh}$. A phototransistor detects when the impactor nears the end of travel and triggers a high speed camera to record. The temperature change on impact ΔT is recorded by an embedded thermistor and amplification circuit. A fixed spring can be optionally attached to the lead sheet to greatly increase the coefficient of restitution and cause a near-elastic impact.

curs. We wrapped the impacting cylinder in a piece of paper with a set striped black/white pattern (Figure 6.5D, right side), which allowed us to perform cross-correlation on the high-speed videos to extract the velocity at the point of impact (Figure 6.6A). To keep the lead sheet from bouncing upwards after impact, it was either mounted and screwed into a 3D printed cradle (Figure 6.5E) or glued to a piece of wood with cyanoacrylate. The impacts with the lead sheet appeared highly inelastic, and repeated impact experiments would eventually deform the lead sheet and sever the thin wires leading from the embedded thermistor. The coefficient of resistution for impacts seemed quite low, as we can observe from

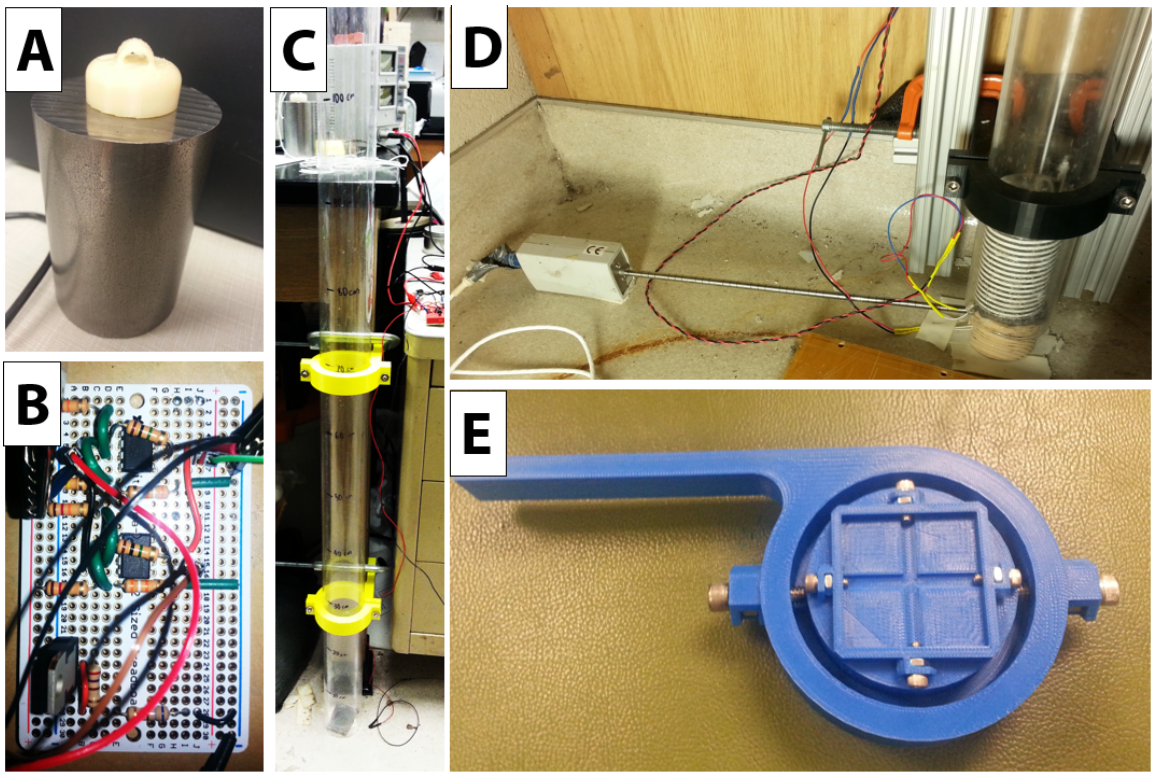

Figure 6.5: **Photographs of Impact Experiment Setup** (A) The impacting steel cylinder of mass $m_i = 1.21kg$. A 3D printed attachment is superglued to the top to attach a string. (B) The voltage amplifying circuit for the thermistors based on LM741 Op-Amps ICs. (C) Photo of the acrylic drop tube, with yellow clamps affixing it to a table leg. Initial drop heights are marked off in permanent marker. (D) Close-up of the drop tube's impacting site. See the striped impactor at the right. (E) 3D printed cradle with aligning screws used to hold lead sheet and drop tube in place.

Figure 6.6A, where the descending cylinder barely travels upward after impact.

With our thermistor circuit setup, we could detect temperature changes due to impacts quite well (Figure 6.6B). After a typical impact event, the voltage drop change across the thermistor element could be translated into a temperature change ΔT, which would rise rapidly after impact then plateau to a final value. We calibrated each thermistor component by immersing them in a heated water bath tested against an external thermometer for a range of temperatures.

To test the first law of thermodynamics with this experiment, we set up a simple energy balance equation, stating that the change in kinetic energy from impact must equal the

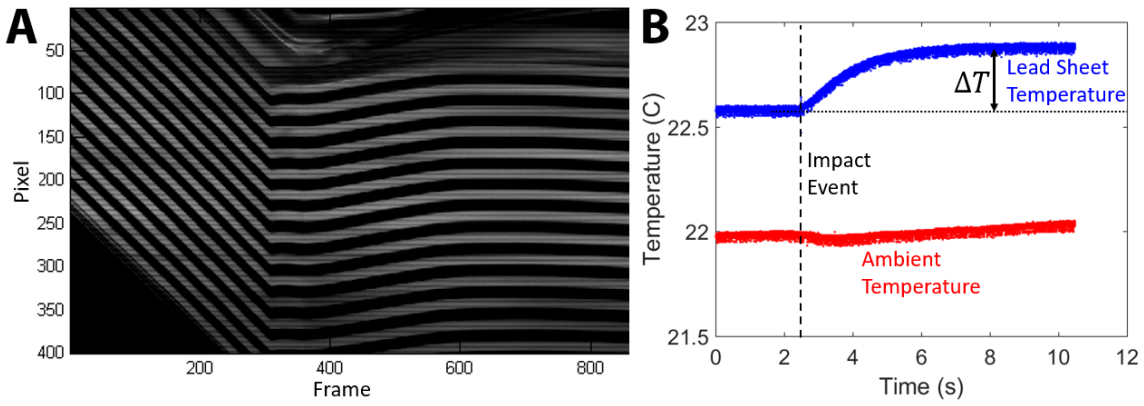

Figure 6.6: **Sample Raw Data Signals for Impact Experiments** (A) An AOS X-PRI high speed camera captured all impact trials, and was triggered by the cylinder passing a phototransistor pointing into the acrylic tube. This video capture is set to 16000 FPS, and the impact occurs at approx. frame 300. Cross-correlation on these videos verified our calculated values for $v = \sqrt{2gh}$. In this image, horizontally recorded pictures are averaged and compressed into a single vertical line, then plotted for each timestamp. Note that the impactor barely rebounds after frame 300. (B) Sample temperature vs. time signal for an inelastic impact event. The vertical dotted line indicated the timestamp of the impact.

change in the lead sheet's internal energy, characterized by temperature:

$$\Delta K_i = \Delta U_s \tag{6.1}$$

$$\frac{1}{2} m_i v_i^2 = m_s C \Delta T \tag{6.2}$$

$$\Delta T = \frac{m_i}{2 m_s C} v_i^2 \tag{6.3}$$

where T is change in temperature for the lead sheet, $C = 0.129$ [J/gK] is the heat capacity of lead, v_i is the impactor velocity at moment of impact, and m_i & m_s are the impactor and lead sheet masses, respectively. Now we recall that v_i was generated from free-fall from an initial height h, so we use the relation $v_i = \sqrt{2gh}$ to get:

$$\Delta T = \frac{ghm_i}{Cm_s} \tag{6.4}$$

One last consideration is that the above formula would imply that *all* of the kinetic energy would flow into the lead sheet, which is not physically feasible. Rather, the energy transfer would affect both the impactor and the sheet symmetrically, so we must divide by two to

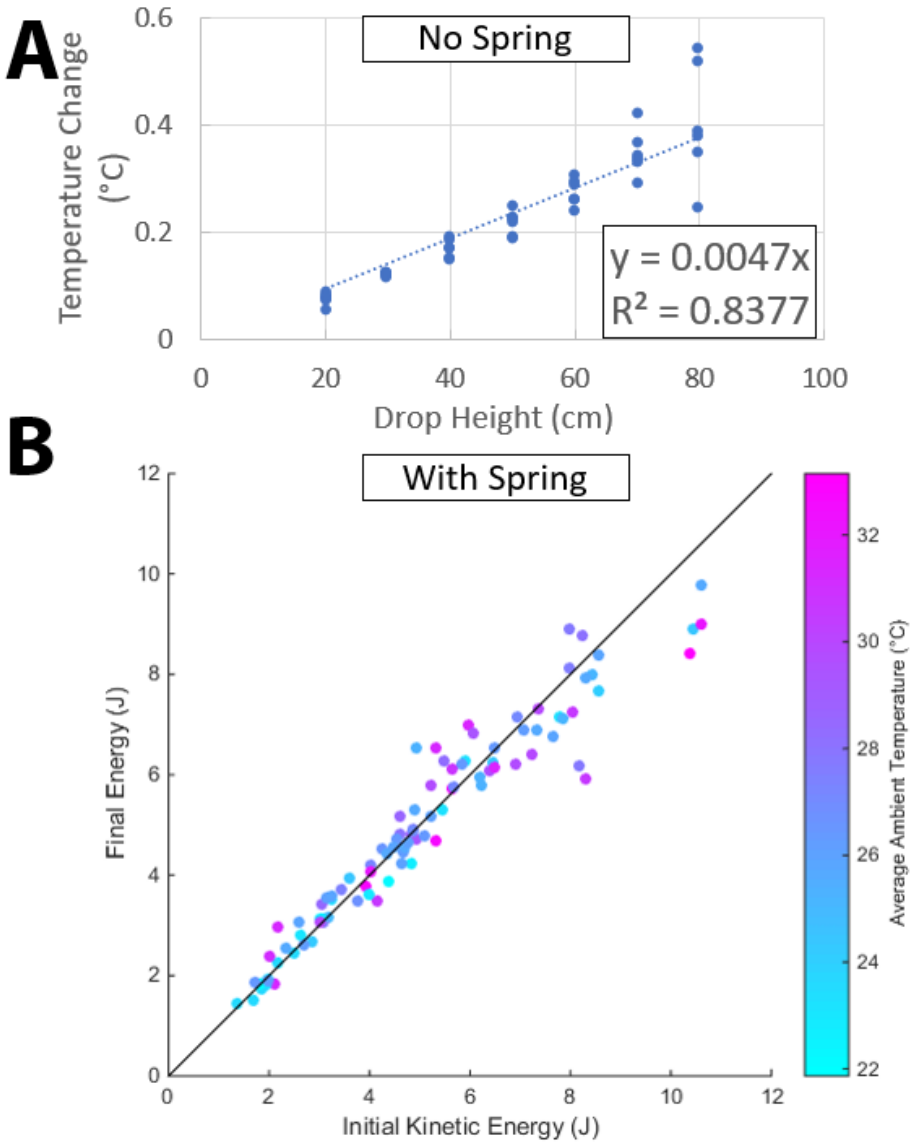

Figure 6.7: **Inelastic and Spring Impact Results** (A) For inelastic impact trials, the temperature change ΔT after impact rose linearly with drop height as predicted by Equation 6.6, with the linear coefficient matching very closely. The inset square shows the coefficients for a linear fit and the R-squared value of the fit. (B) For spring impact trials, we found the final energy when the spring was fully compressed $0.5k(\Delta x)^2$ to be near equal the input kinetic energy of $0.5m_i v_i^2$. The black line is set as $y = x$ to guide the eye.

get:

$$\Delta T = \frac{ghm_i}{2Cm_s} \tag{6.5}$$

Plugging in experimental values for this equation we obtain:

$$\Delta T = (0.0045)h \tag{6.6}$$

which matches very well with our observations for inelastic impact events in Figure 6.7A.

We also endeavored to capture the second law of thermodynamics by demonstrating some form of conversion of ambient heat into mechanical work during the impacting process. By inserting a spring under the lead sheet, the impact was made much more elastic, and energy could temporarily be stored in the spring, which would then launch the impactor back upwards. By heating the impact environment with a heat gun to a high ambient temperature, we wanted to see if the ambient thermal energy could be utilized by the spring, spontaneously extracted from the environment by the impact event. By examining the changes in both ambient temperature, the sheet temperature, the spring compression (via high speed video), and the outgoing impactor velocity, we wanted to characterize the thermodynamic efficiency and entropy of this elastic impact system.

However, this project was then shelved to begin work on the wheeled locomotion project presented in Chapter 2. Nevertheless, our preliminary data sets are plotted in Figure 6.7B, Figure 6.8, and Figure 6.9. Figure 6.7B and Figure 6.8 showed verification that we could capture an energy balance for this system, and Figure 6.9 showed an interesting trend where ambient temperature would drop during impact more and more for hotter initial temperatures, but it was never proven if this actually translated into mechanical work by the system.

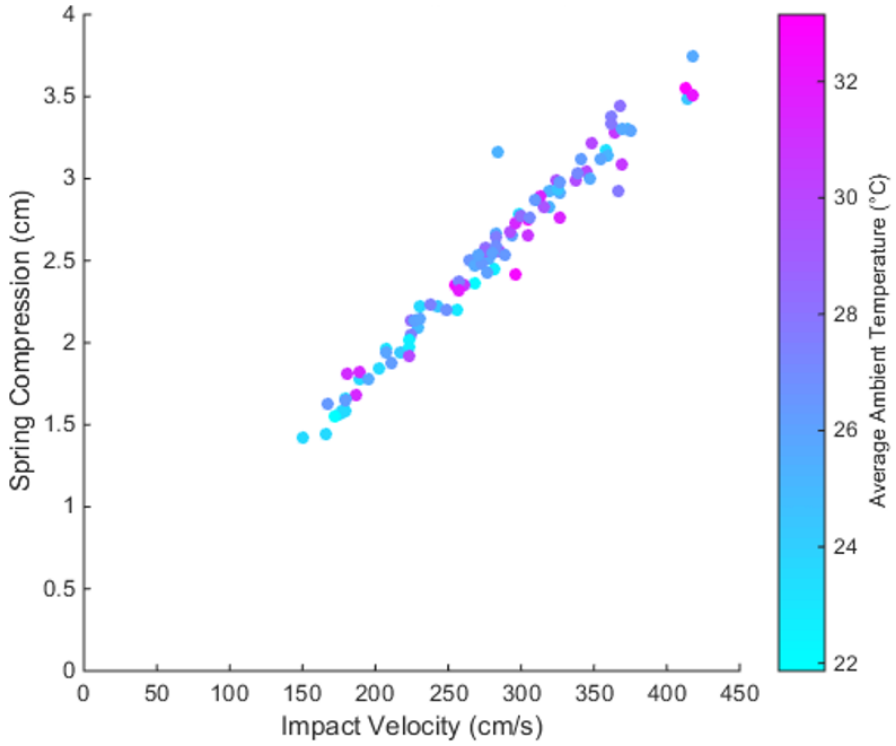

Figure 6.8: **Spring Compression vs. Impact Velocity in Spring Impacts** In spring impact trials, spring compression was linearly correlated with impact velocity, which is expected from an energy balance: $0.5kx^2 = 0.5mv^2$. There appeared to be no obvious correlation with the average ambient temperature.

6.4 Contributions

Shashank Agarwal performed the numerical analysis, continuum model simulations, and wrote the original manuscript for the publication in *Soft Matter* featuring the twin plate intrusion experiments [53]. Andras Karsai fabricated and performed the twin plate intrusion experiments. Shashank Agarwal, Andras Karsai, Daniel I. Goldman and Ken Kamrin all conceived the study, interpreted the data, and discussed the results. Ken Kamrin and Daniel I. Goldman supervised the project, provided comments on and modified the original manuscript [53]. Andras Karsai conceived, performed, and interpreted the thermodynamics study, and Daniel I. Goldman provided guidance and mentoring.

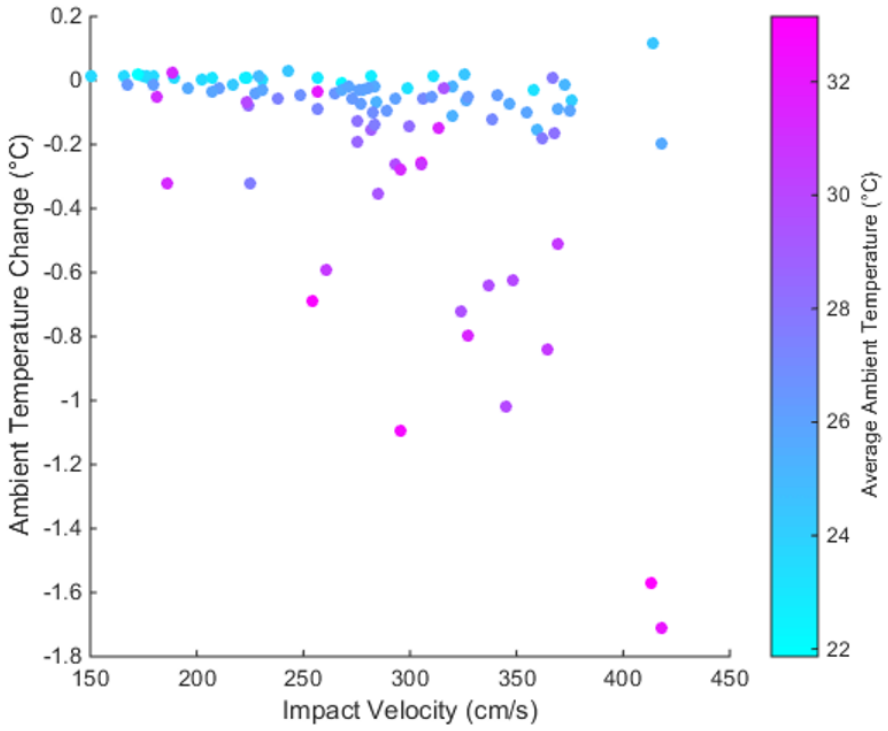

Figure 6.9: **Ambient Temperature Change vs. Impact Velocity in Spring Impacts** After heating the impact site with a heat gun, we observed temperature drops correlated with both impact velocity and the initial ambient temperature when the spring was attached. A hotter environment and faster impact both contributed to greater temperature drops.

CHAPTER 7
CONCLUSIONS AND FUTURE WORK

7.1 Summary of Accomplishments

In this dissertation, we have developed new insights into rate-dependent phenomena and multiphase flows in frictional substrates. Using a variety of experimental systems, we investigated wheeled locomotion, rover locomotion, directional fluidization during intrusion, and pinned fluid cavity oscillations within GM. We supplemented our experiments with extensive collaborations with colleagues in theoretical work, computational modeling, and engineering expertise to achieve understanding of these phenomena on multiple levels.

We discovered a great deal of non-intuitive phenomena during the course of this dissertation which were first observed in experiment. In Chapter 2, we developed an terramechanics testbed that autonomously and resets its granular terrain, allowing us to probe possible rate effects of rapid wheeled locomotion. The wheel system would experience increasing slipping at higher input ω in GM, which deviated from the expected reduced-order model description of RFT and from the expected scaling relations [97] for wheels. We found a structural rate-effect that would induce an effective traction loss as rapid centripetal shearing would weaken the GM. Continuum modeling by Agarwal showed that this rate-dependent shear would reduce the effective lithostatic pressure head that would otherwise provide strength to the GM under shear [65]. Understanding this structural effect would lead to a modification of RFT that accounts for such shear structures and captures the experimental kinematics in a reduced order model.

In Chapter 3, we demonstrated how long-term material remodeling of GM could facilitate locomotion on sloped GM terrain that would otherwise be difficult to traverse. Shrivastava constructed and tested a robophysical rover with variable gaits that could wheel

and ‘walk’ within another automated testbed called SCATTER [115, 66]. By using open-loop gaits that would induce avalanching in the GM to create a net flow towards the rover and along the gravity vector, the terrain could slowly deform into a traversable terrain even without any gait feedback or control. We also showed how localized agitation could reflow material near the wheels and maintain it in a frictional fluid state, reducing hysteretic effects and making the force responses tractable via granular RFT.

In Chapter 4, we investigated how directional fluidization of GM during intrusion could be used to modulate the drag and lift force responses of a frictional substrate. Our findings were used to inform local fluidization strategies in a soft burrowing robot created by Naclerio and Hawkes. As the robot everted its tip to grow, it would selectively fluidize the GM in orthogonal directions in order to reduce the resistive force, transport grains away, and grow rapidly within granular volumes. We further explored this local fluidization in Chapter 5 by pinning aerated cavities (bubbles) within GM with an automated air probe system. These bubbles were dynamically stable since frictional forces held the far-field grains in position, even as grains were chaotically tossed about within the cavity by the airflow. Upon overexpansion of the cavity, we found it would collapse into a strongly periodic structure with an emergent creeping boundary oscillation sustained by the input flow. We could predict the frequency scaling of these oscillations by using a simple model of turbulent fluid jets. These bubbles also displayed hysteretic qualities often found in GM, as they could be transported through the granular space with a volume dependent on their history of formation. These phenomena could have applications in robotics or geomechanics by creating controllable transient structures in granular volumes.

7.2 Future Investigations

Here we present projects and/or grant proposals currently in progress and possible directions for future study:

7.2.1 Dynamic Deformable Structures in Forced Granular Interactions

The physics of intruding solid bodies within yielding substrates is important for characterizing many natural phenomena, from the locomotion of lizards on flowable terrains to studying celestial bodies via impact collisions. Dry GM offer excellent examples of friction dominated yielding substrates that can self-organize and showcase unique multiphase physics, yet are unaffected by thermal fluctuations. The multibody physics of moving bodies within a granular substrate has traditionally focused on singular rigid bodies intruding into GM and characterizing the stress/shear responses of the substrate under various loads and global forcings. However, most GM interactions in the natural world consist of underexplored complex multibody deformable structures which interact via local stress, flow, and adjacency effects. Both a plant's root structure grown into soil and a lizard's foot intruding into GM during running create such structures, where compliance and adjacency in the intruding bodies generate emergent stresses.

Much like the multiphysics scenarios of fluid-structure coupling, allowing a moving body in GM to significantly bend can probe the local rheology of deformation via emergent mesoscopic structures. Unlike Newtonian fluids, GM can support stresses without flowing up to a failure criterion, allowing manipulation of local stress/flow fields to couple with deformable bodies. This allows for study of new phenomena where the medium becomes a dynamical entity, forming structures in both the moving body and the substrate (Figure 7.1). Granular substrates also exhibit strong memory effects in their stress fields and their spatial re-arrangements, allowing the system to explore new states under the correct forcing. Previous experiments have shown that adjacent rigid intruders in GM can interact purely through their local stress/flow fields (e.g. Chapter 6), changing their collective force response. As multiple deformable bodies move closer together, we expect additional multibody coupling through the GM as local jamming induces new non-local stress fields that vary from the far-field case. Such interactions may constitute the next generation of experiments and instrumentation in probing emergent physics in granular substrates.

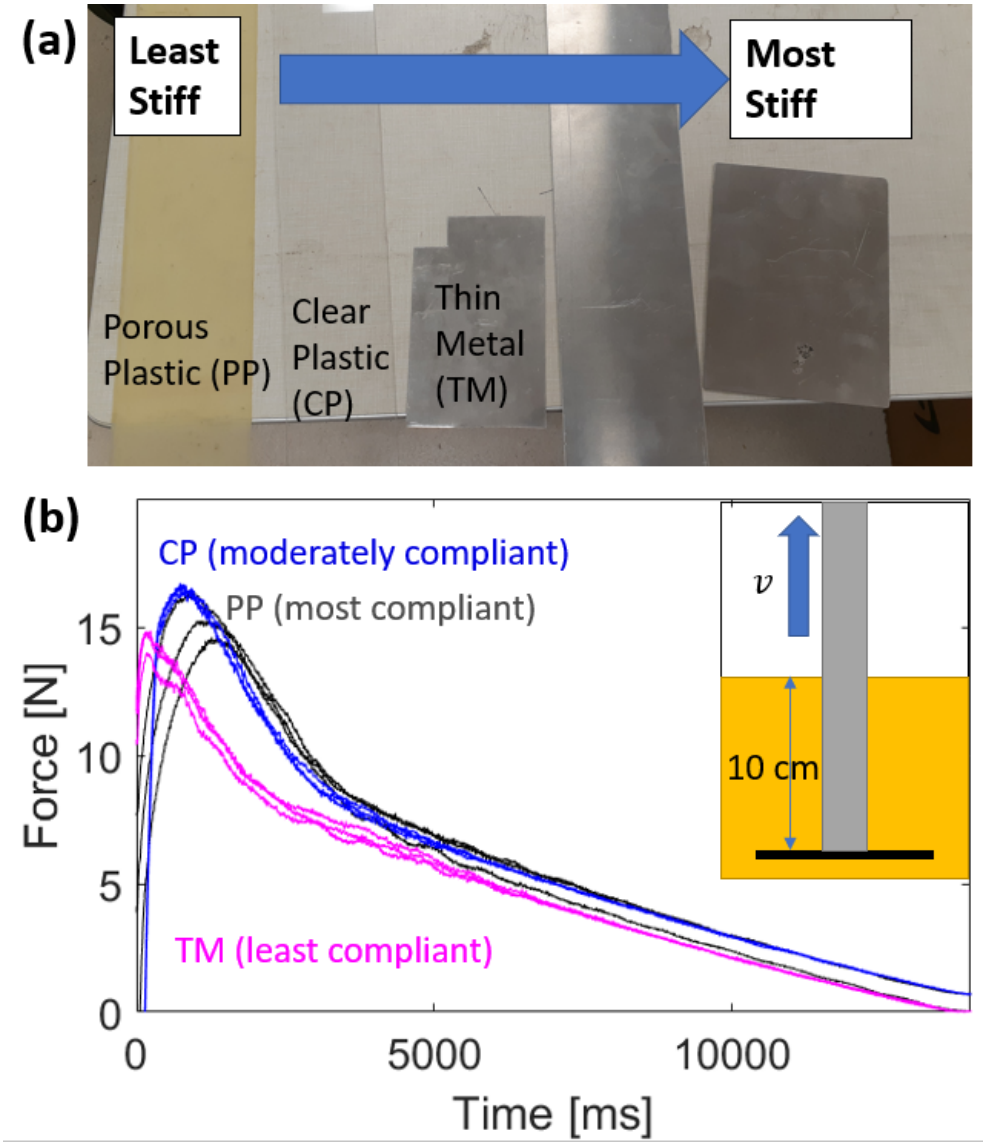

Figure 7.1: **Compliant Anchoring Plates in GM Pullout** Preliminary trials of lifting compliant intruders opposite to gravity. All trials were buried 10 cm in dry sand and pulled out at 7.4 mm/s. More compliant plates took longer (i.e. deformed under load) to reach higher peak pullout forces for the same geometry. This hints at coupling between the intruder's flexion and the stress fields generated in the granular volume, creating a transient structure.

Future work could focus on characterizing the GM response to various static and dynamic interactions with soft bodies on the macro, micro, and mesoscopic scale. Specifically, the interaction between compliant bodies of variable stiffness, soft growing probes, and dynamically shape-changing structures in GM such as poppy seeds, glass beads, and silica sand can be explored. Rather than subjecting the GM system to a global or point-like disturbance, we can focus on the evolution of the coupled body/substrate domain. GM response could be monitored via net force/torque sensing, sidewall and X-ray visualization, and force chain imaging using photoelastic particles in a laboratory setting. Insight into interactions between multiple soft structures of both membraned (balloon-like) and membraneless (cavity-like) void structures in GM would expand understanding of possible collective force and dynamics responses.

7.2.2 Machine Learning for Robot Locomotion in Frictional Fluids

Recent studies of robot movement in flowable granular media (inspired by difficulties faced by extraterrestrial rovers) reveal a coupled locomotor/substrate effect (Chapter 3) where the robot spontaneously remodels its environment. This strong coupling occurs in certain limb/wheel movement patterns and results in a localized granular flow allowing the robot to effectively "swim" up highly flowable slopes. However, these gaits were discovered via trial and error by human operators. To accelerate the discovery of effective gaits in flowable frictional media, we could use a neural net based machine learning (ML) scheme to characterize the gait and terrain interactions. We would capture the robot kinematics and its surrounding terrain deformation using external depth cameras and train a machine learning model to describe the coupling of the robot/terrain system. Preliminary tests by Daniel Soto have shown that a Bayesian optimization scheme modulating the RRP gait (Figure 7.2B) can improve performance even without knowledge of the terrain flow, showing that 'blind' learning can also be effective.

The ML method approach for the substrate flow can offer an approximate numerical

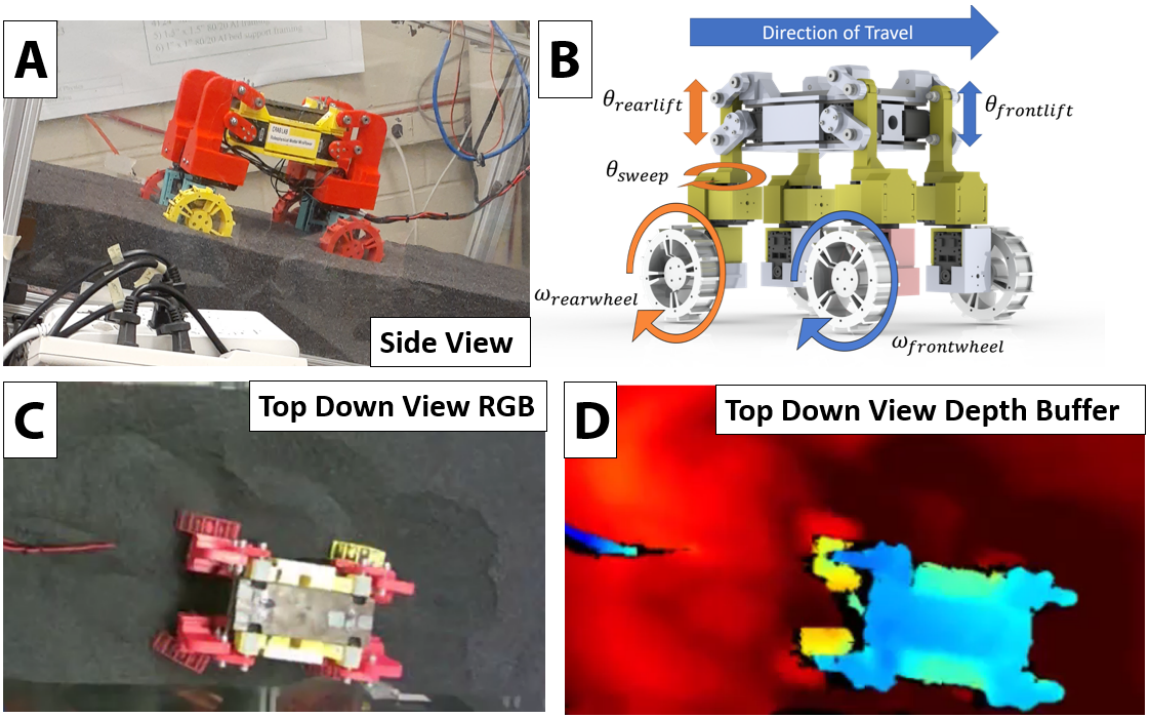

Figure 7.2: **Machine Learning for Robot Locomotion in Flowable Materials** (A) Side view of a new iteration (constructed by Daniel Soto) of the Mini Rover shown in Chapter 3 at rest in the SCATTER system. (B) Diagram of possible gait angle modulations in learning more effect RRP gaits. (C) Top down views of the new Mini Rover in SCATTER (D) Top down view of the depth buffer for subfigure C (blue is closer to the camera, red is farther). An Intel D435 depth camera can generate depth buffers of the terrain at 30 FPS via stereoscopic visualization, allowing us to create a learning data set for terrain deformation. Subfigures (C) and (D) are courtesy of Daniel Soto.

model of the environment that learns from terrain data, circumventing the need for approximate numerical models or computationally costly and potentially inaccurate continuum models for frictional material and offers an approximate numerical model that learns from terrain data. This scheme may offer insights into the physics of locomotion within such media, and also lead to insights into effective substrate remodeling schemes that improve robot mobility *in situ* for real-world environments by offering adaptability to flowable terrain via rapid learning.

7.2.3 RFT Applications for Extraterrestrial Granular Ices

Enceladus and possibly Europa spew materials from their internal ocean into their exosphere as ice plumes, some of which are deposited back onto the surface of those ocean

worlds. This setting provides a unique opportunity to seek traces of past or extant life in ice plume deposits on their surfaces. Studies at NASA JPL by Choukroun et al. [225] created ice plume deposit analogs deposits in the laboratory to obtain first-order estimates of deposit strength under geologic timescales, and found that such deposits are likely weak and poorly consolidated on Enceladus. The design of future landers and sampling missions will be heavily influenced by the expected ice strength.

Since the ice is expected to granular, weak, and poorly consolidated, we can attempt to extend reduced-order models like RFT to such materials. If granular ices behave like frictional fluids, with hyperbolic constitutive equations, then RFT-like superposition may be valid and can inform future lander designs for stability. Enceladus ices are expected to be very fine (approx 12 microns) and polydisperse, and will experience particle sintering over time. These properties may make such ices out of reach of RFT's descriptive power, which is used to characterizing monodisperse, larger grained, cohesionless particles. Future studies could perform careful intrusion experiments of various geometries on granular ice samples specifically to test if superposition would be valid, and to gain insight to what kind of lander configurations would be ideal for future missions.

Appendices

APPENDIX A

JOURNAL COVERS

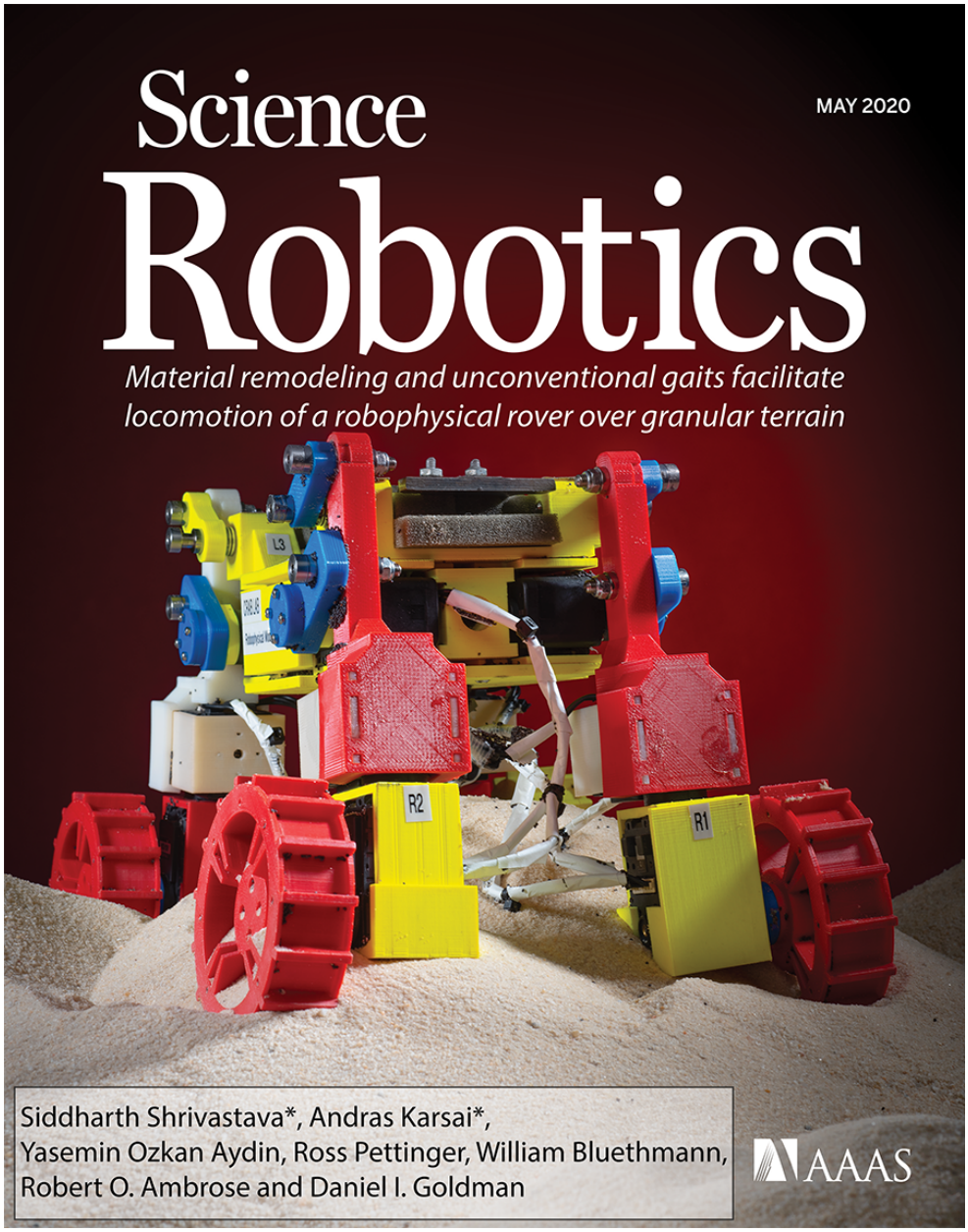

Figure A.1: **Robophysical Rover Locomotion Journal Cover** Cover for the May 2020 issue of Science Robotics by AAAS (Volume 5, Issue 42). The paper title and author lists have been added in by Andras Karsai for printing as a poster. Photo Credit: Christopher Moore / Institute Communications, Georgia Institute of Technology, Georgia Tech Research Corporation.

Figure A.2: **Burrowing Soft Robot Journal Cover** Cover for the June 2021 issue of Science Robotics by AAAS (Volume 6, Issue 55). The paper title and author lists have been added in by Andras Karsai for printing as a poster. Photo Credit: Sicheng Wang

REFERENCES

[1] M. C. Peel, B. L. Finlayson, and T. A. McMahon, "Updated world map of the köppen-geiger climate classification," *Hydrology and Earth System Sciences*, vol. 11, no. 5, pp. 1633–1644, Oct. 2007.

[2] M. J. Rodwell and B. J. Hoskins, "Subtropical anticyclones and summer monsoons," *Journal of Climate*, vol. 14, no. 15, pp. 3192–3211, Aug. 2001.

[3] J. T. Abatzoglou, S. Z. Dobrowski, S. A. Parks, and K. C. Hegewisch, "TerraClimate, a high-resolution global dataset of monthly climate and climatic water balance from 1958–2015," *Scientific Data*, vol. 5, no. 1, Jan. 2018.

[4] A. Mirzabaev, J. Wu, J. Evans, F. Garcia-Oliva, I. A. G. Hussein, M. H. Iqbal, J. Kimutai, T. Knowles, F. Meza, D. Nedjroaoui, F. Tena, M. Türke, R. J. Vázquez, and M. Weltz, "Desertification," in *Climate Change and Land: an IPCC special report on climate change, desertification, land degradation, sustainable land management, food security, and greenhouse gas fluxes in terrestrial ecosystems*, P. R. Shukla, J. Skeg, E. C. Buendia, V. Masson-Delmotte, H.-O. Pörtner, D. C. Roberts, P. Zhai, R. Slade, S. Connors, S. van Diemen, M. Ferrat, E. Haughey, S. Luz, M. Pathak, J. Petzold, J. P. Pereira, P. Vyas, E. Huntley, K. Kissick, M. Belkacemi, and J. Malley, Eds., 2019.

[5] K. Briggs, *Physical geography : process and system*. London: Hodder and Stoughton, 1985, ISBN: 9780340359518.

[6] R. A. Bagnold, *The Physics of Blown Sand and Desert Dunes (Dover Earth Science)*. Dover Publications, 2005, ISBN: 0-486-43931-3.

[7] Z. T. Aanderud, J. Bahr, D. M. Robinson, J. Belnap, T. P. Campbell, R. A. Gill, B. McMillian, and S. S. Clair, "The burning of biocrusts facilitates the emergence of a bare soil community of poorly-connected chemoheterotrophic bacteria with depressed ecosystem services," *Frontiers in Ecology and Evolution*, vol. 7, Dec. 2019.

[8] J. F. Reynolds, D. M. S. Smith, E. F. Lambin, B. L. Turner, M. Mortimore, S. P. J. Batterbury, T. E. Downing, H. Dowlatabadi, R. J. Ferna
ndez, J. E. Herrick, E. Huber-Sannwald, H. Jiang, R. Leemans, T. Lynam, F. T. Maestre, M. Ayarza, and B. Walker, "Global desertification: Building a science for dryland development," *Science*, vol. 316, no. 5826, pp. 847–851, May 2007.

[9] R. A. McLeman, J. Dupre, L. B. Ford, J. Ford, K. Gajewski, and G. Marchildon, "What we learned from the dust bowl: Lessons in science, policy, and adaptation," *Population and Environment*, vol. 35, no. 4, pp. 417–440, Aug. 2013.

[10] R. Gardner, "Trees as technology: Planting shelterbelts on the great plains," *History and Technology*, vol. 25, no. 4, pp. 325–341, Dec. 2009.

[11] Y. Dai, Z. Dong, H. Li, Y. He, J. Li, and J. Guo, "Effects of checkerboard barriers on the distribution of aeolian sandy soil particles and soil organic carbon," *Geomorphology*, vol. 338, pp. 79–87, Aug. 2019.

[12] Z. Yi and C. Zhao, "Desert "soilization": An eco-mechanical solution to desertification," *Engineering*, vol. 2, no. 3, pp. 270–273, Sep. 2016.

[13] F. Herbert, *Dune*. Penguin Group, 1965, ISBN: 0-399-12896-4.

[14] M. Welland, *Sand : the never-ending story*. Berkeley: University of California Press, 2009, ISBN: 9780520254374.

[15] R. M. Nedderman, *Statics and Kinematics of Granular Materials*. Cambridge University Press, Jun. 2005, 372 pp., ISBN: 0521019079.

[16] B. Andreotti, Y. Forterre, and O. Pouliquen, *Granular Media*. Cambridge University Press, 2009.

[17] C. Li, T. Zhang, and D. I. Goldman, "A Terradynamics of Legged Locomotion on Granular Media," *Science*, vol. 339, pp. 1408–1412, Mar. 2013. arXiv: 1303.7065 [physics.bio-ph].

[18] H. M. Jaeger, S. R. Nagel, and R. P. Behringer, "Granular solids, liquids, and gases," *Reviews of Modern Physics*, vol. 68, no. 4, pp. 1259–1273, Oct. 1996.

[19] L. Zhang, N. G. H. Nguyen, S. Lambert, F. Nicot, F. Prunier, and I. Djeran-Maigre, "The role of force chains in granular materials: From statics to dynamics," *European Journal of Environmental and Civil Engineering*, vol. 21, no. 7-8, pp. 874–895, Jun. 2016.

[20] K. L. Johnson and K. L. Johnson, *Contact mechanics*. Cambridge university press, 1987.

[21] R. D. Maladen, Y. Ding, P. B. Umbanhowar, A. Kamor, and D. I. Goldman, "Mechanical models of sandfish locomotion reveal principles of high performance subsurface sand-swimming," *Journal of The Royal Society Interface*, vol. 8, no. 62, pp. 1332–1345, Mar. 2011.

[22] R. A. Vásquez, L. A. Ebensperger, and F. Bozinovic, "The influence of habitat on travel speed, intermittent locomotion, and vigilance in a diurnal rodent," *Behavioral Ecology*, vol. 13, no. 2, pp. 182–187, 2002.

[23] J. Aguilar, "Probing the dynamics of a simple jumping robot on hard and soft ground," Ph.D. dissertation, Georgia Institute of Technology, 2016.

[24] C. P. McGowan and C. E. Collins, "Why do mammals hop? Understanding the ecology, biomechanics and evolution of bipedal hopping," *Journal of Experimental Biology*, vol. 221, no. 12, Jun. 2018, jeb161661. eprint: https://journals.biologists.com/jeb/article-pdf/221/12/jeb161661/1901390/jeb161661.pdf.

[25] T. M. Lejeune, P. A. Willems, and N. C. Heglund, "Mechanics and energetics of human locomotion on sand.," *Journal of Experimental Biology*, vol. 201, no. 13, pp. 2071–2080, Jul. 1998. eprint: https://journals.biologists.com/jeb/article-pdf/201/13/2071/1234121/2071.pdf.

[26] J. Aguilar and D. I. Goldman, "Robophysical study of jumping dynamics on granular media," *Nature Physics*, vol. 12, no. 3, pp. 278–283, Nov. 2015.

[27] Y. Ding, S. S. Sharpe, A. Masse, and D. I. Goldman, "Mechanics of undulatory swimming in a frictional fluid," *PLOS Computational Biology*, vol. 8, no. 12, pp. 1–13, Dec. 2012.

[28] M. G. Bekker, *Off-the-road locomotion : research and development in terramechanics*. Ann Arbor: University of Michigan Press, 1960.

[29] J.-Y. Wong and A. Reece, "Prediction of rigid wheel performance based on the analysis of soil-wheel stresses part i. performance of driven rigid wheels," *Journal of Terramechanics*, vol. 4, no. 1, pp. 81–98, Jan. 1967.

[30] J. Wong and W. Huang, "
wheels vs. tracks"–a fundamental evaluation from the traction perspective," *Journal of terramechanics*, vol. 43, no. 1, pp. 27–42, 2006.

[31] K. Iagnemma and S. Dubowsky, "Traction control of wheeled robotic vehicles in rough terrain with application to planetary rovers," *The International Journal of Robotics Research*, vol. 23, no. 10-11, pp. 1029–1040, 2004. eprint: http://dx.doi.org/10.1177/0278364904047392.

[32] J. Wong, "Chapter 2 - modelling of terrain behaviour," in *Terramechanics and Off-Road Vehicle Engineering (Second Edition)*, J. Wong, Ed., Second Edition, Oxford: Butterworth-Heinemann, 2010, pp. 21–63, ISBN: 978-0-7506-8561-0.

[33] J. Wong, C. Senatore, P. Jayakumar, and K. Iagnemma, "Predicting mobility performance of a small, lightweight track system using the computer-aided method ntvpm," *Journal of Terramechanics*, vol. 61, pp. 23–32, 2015.

[34] H. Marvi, C. Gong, N. Gravish, H. Astley, M. Travers, R. L. Hatton, 3. Mendelson J. R., H. Choset, D. L. Hu, and D. I. Goldman, "Sidewinding with minimal slip: Snake and robot ascent of sandy slopes," *Science*, vol. 346, no. 6206, pp. 224–9, 2014, 1095-9203 Marvi, Hamidreza Gong, Chaohui Gravish, Nick Astley, Henry Travers, Matthew Hatton, Ross L Mendelson, Joseph R 3rd Choset, Howie Hu, David L Goldman, Daniel I Journal Article Research Support, Non-U.S. Gov't Research Support, U.S. Gov't, Non-P.H.S. United States Science. 2014 Oct 10;346(6206):224-9. doi: 10.1126/science.1255718.

[35] Y. Ding, C. Li, and D. I. Goldman, "Swimming in the desert," *Physics Today*, vol. 66, no. 11, p. 68, Nov. 2013.

[36] K. Terzaghi, R. B. Peck, and G. Mesri, *Soil mechanics in engineering practice*. John Wiley & Sons, 1996.

[37] F. Radjai and F. Dubois, *Discrete-Element Modeling of Granular Materials*. ISTE LTD, May 2011, 496 pp., ISBN: 1848212607.

[38] M. Kobayakawa, S. Miyai, T. Tsuji, and T. Tanaka, "Local dilation and compaction of granular materials induced by plate drag," *Physical Review E*, vol. 98, no. 5, p. 052 907, Nov. 2018.

[39] Z. Yan, S. K. Wilkinson, E. H. Stitt, and M. Marigo, "Discrete element modelling (DEM) input parameters: Understanding their impact on model predictions using statistical analysis," *Computational Particle Mechanics*, vol. 2, no. 3, pp. 283–299, Jul. 2015.

[40] Y. Xia, J. J. Stickel, W. Jin, and J. Klinger, "A review of computational models for the flow of milled biomass part i: Discrete-particle models," *ACS Sustainable Chemistry & Engineering*, vol. 8, no. 16, pp. 6142–6156, Apr. 2020.

[41] N. Gravish, P. B. Umbanhowar, and D. I. Goldman, "Force and flow transition in plowed granular media," *Phys. Rev. Lett.*, vol. 105, p. 128 301, 12 Sep. 2010.

[42] H. Suzuki, K. Katsushima, and S. Ozaki, "Study on applicability of RFT to traveling analysis of wheel with grousers: Comparison with DEM analysis as a virtual test," *Journal of Terramechanics*, vol. 83, pp. 15–24, Jun. 2019.

[43] P. A. Cundall and O. D. L. Strack, "A discrete numerical model for granular assemblies," *Géotechnique*, vol. 29, no. 1, pp. 47–65, Mar. 1979.

[44] S. J. Burns, P. T. Piiroinen, and K. J. Hanley, "Critical time step for DEM simulations of dynamic systems using a hertzian contact model," *International Journal for Numerical Methods in Engineering*, vol. 119, no. 5, pp. 432–451, Mar. 2019.

[45] R. D. Maladen, Y. Ding, C. Li, and D. I. Goldman, "Undulatory swimming in sand: Subsurface locomotion of the sandfish lizard," *Science*, vol. 325, no. 5938, pp. 314–318, Jul. 2009.

[46] S. Agarwal, C. Senatore, T. Zhang, M. Kingsbury, K. Iagnemma, D. I. Goldman, and K. Kamrin, "Modeling of the interaction of rigid wheels with dry granular media," *Journal of Terramechanics*, vol. 85, pp. 1–14, Oct. 2019.

[47] J. Slonaker, D. C. Motley, Q. Zhang, S. Townsend, C. Senatore, K. Iagnemma, and K. Kamrin, "General scaling relations for locomotion in granular media," *Physical Review E*, vol. 95, no. 5, p. 052 901, May 2017.

[48] J. Aguilar, T. Zhang, F. Qian, M. Kingsbury, B. McInroe, N. Mazouchova, C. Li, R. Maladen, C. Gong, M. Travers, R. L. Hatton, H. Choset, P. B. Umbanhowar, and D. I. Goldman, "A review on locomotion robophysics: The study of movement at the intersection of robotics, soft matter and dynamical systems," *Reports on Progress in Physics*, vol. 79, no. 11, p. 110 001, 2016.

[49] T. Zhang and D. I. Goldman, "The effectiveness of resistive force theory in granular locomotion," *Physics of Fluids*, vol. 26, no. 10, p. 101 308, 2014. eprint: http://dx.doi.org/10.1063/1.4898629.

[50] Y. Ding, N. Gravish, and D. I. Goldman, "Drag induced lift in granular media," *Phys. Rev. Lett.*, vol. 106, p. 028 001, 2 Jan. 2011.

[51] Y. Ding, S. S. Sharpe, A. Masse, and D. I. Goldman, "Mechanics of undulatory swimming in a frictional fluid," *PLOS Computational Biology*, vol. 8, no. 12, pp. 1–13, Dec. 2012.

[52] A. M. Spencer, *Continuum Mechanics*. DOVER PUBN INC, Apr. 2004, 183 pp., ISBN: 0486435946.

[53] S. Agarwal, A. Karsai, D. I. Goldman, and K. Kamrin, "Efficacy of simple continuum models for diverse granular intrusions," *Soft Matter*, 2021.

[54] N. V. Brilliantov and T. Pöschel, *Kinetic theory of granular gases*. Oxford University Press on Demand, 2004.

[55] A. N. Schofield and P. Wroth, *Critical state soil mechanics*. McGraw-hill London, 1968, vol. 310.

[56] P. Jop, Y. Forterre, and O. Pouliquen, "A constitutive law for dense granular flows," *Nature*, vol. 441, no. 7094, p. 727, 2006.

[57] D. L. Henann and K. Kamrin, "A predictive, size-dependent continuum model for dense granular flows," *Proceedings of the National Academy of Sciences*, vol. 110, no. 17, pp. 6730–6735, Mar. 2013.

[58] Y. Zhang, M. Bernhardt, G. Biscontin, R. Luo, and R. L. Lytton, "A generalized drucker–prager viscoplastic yield surface model for asphalt concrete," *Materials and Structures*, vol. 48, no. 11, pp. 3585–3601, Oct. 2014.

[59] M. Kuznecova and A. Guskov, "Finite element simulation of behaviour of granular materials under low-cyclic loading," *Science and Education of the Bauman MSTU*, vol. 14, no. 11, Nov. 2014.

[60] W. Kang, Y. Feng, C. Liu, and R. Blumenfeld, "Archimedes' law explains penetration of solids into granular media," *Nature Communications*, vol. 9, no. 1, Mar. 2018.

[61] M.-h. Yu, "Advances in strength theories for materials under complex stress state in the 20th century," *Appl. Mech. Rev.*, vol. 55, no. 3, pp. 169–218, 2002.

[62] D. C. Drucker and W. Prager, "Soil mechanics and plastic analysis or limit design," *Quarterly of applied mathematics*, vol. 10, no. 2, pp. 157–165, 1952.

[63] H. Askari and K. Kamrin, "Intrusion rheology in grains and other flowable materials," *Nature Materials*, vol. 15, no. 12, pp. 1274–1279, Aug. 2016.

[64] Y. Ding, N. Gravish, and D. I. Goldman, "Drag induced lift in granular media," *Phys. Rev. Lett.*, vol. 106, p. 028 001, 2 Jan. 2011.

[65] S. Agarwal, A. Karsai, D. I. Goldman, and K. Kamrin, "Surprising simplicity in the modeling of dynamic granular intrusion," *Science Advances*, vol. 7, no. 17, eabe0631, Apr. 2021.

[66] S. Shrivastava, A. Karsai, Y. O. Aydin, R. Pettinger, W. Bluethmann, R. O. Ambrose, and D. I. Goldman, "Material remodeling and unconventional gaits facilitate locomotion of a robophysical rover over granular terrain," *Science Robotics*, vol. 5, no. 42, eaba3499, May 2020.

[67] N. D. Naclerio, A. Karsai, M. Murray-Cooper, Y. Ozkan-Aydin, E. Aydin, D. I. Goldman, and E. W. Hawkes, "Controlling subterranean forces enables a fast, steerable, burrowing soft robot," *Science Robotics*, vol. 6, no. 55, eabe2922, Jun. 2021.

[68] D. van der Meer, "Impact on granular beds," *Annual Review of Fluid Mechanics*, vol. 49, no. 1, pp. 463–484, Jan. 2017.

[69] D. Lohse, R. Bergmann, R. Mikkelsen, C. Zeilstra, D. van der Meer, M. Versluis, K. van der Weele, M. van der Hoef, and H. Kuipers, "Impact on soft sand: Void collapse and jet formation," *Physical Review Letters*, vol. 93, no. 19, p. 198 003, Nov. 2004.

[70] N. Mazouchova, P. B. Umbanhowar, and D. I. Goldman, "Flipper-driven terrestrial locomotion of a sea turtle-inspired robot," *Bioinspiration & Biomimetics*, vol. 8, no. 2, p. 026 007, Apr. 2013.

[71] P. E. Schiebel, H. C. Astley, J. M. Rieser, S. Agarwal, C. Hubicki, A. M. Hubbard, K. Diaz, J. R. M. III, K. Kamrin, and D. I. Goldman, "Mitigating memory effects during undulatory locomotion on hysteretic materials," *eLife*, vol. 9, Jun. 2020.

[72] R. Arvidson, P. DeGrosse Jr, J. Grotzinger, M. Heverly, J. Shechet, S. Moreland, M. Newby, N. Stein, A. Steffy, F. Zhou, *et al.*, "Relating geologic units and mobility system kinematics contributing to curiosity wheel damage at gale crater, mars," *Journal of Terramechanics*, vol. 73, pp. 73–93, 2017.

[73] A. Singh, *Man running on sand*, Pexels.com, Sep. 2018.

[74] A. M. Johnson, M. T. Hale, G. C. Haynes, and D. E. Koditschek, "Autonomous legged hill and stairwell ascent," in *2011 IEEE International Symposium on Safety, Security, and Rescue Robotics*, IEEE, 2011, pp. 134–142.

[75] Daniel, *Rider riding green motocross dirt bike*, Pexels.com, Feb. 2011.

[76] G. MiDi, "On dense granular flows," *The European Physical Journal E*, vol. 14, no. 4, pp. 341–365, 2004.

[77] N. Gravish, P. B. Umbanhowar, and D. I. Goldman, "Force and flow at the onset of drag in plowed granular media," *Physical Review E*, vol. 89, no. 4, Apr. 2014.

[78] J. Uehara, M. Ambroso, R. Ojha, and D. J. Durian, "Low-speed impact craters in loose granular media," *Physical review letters*, vol. 90, no. 19, p. 194 301, 2003.

[79] H. J. Melosh, "Impact cratering: A geologic process," *Research supported by NASA. New York, Oxford University Press (Oxford Monographs on Geology and Geophysics, No. 11), 1989, 253 p.*, vol. 11, 1989.

[80] R. Zhao, Q. Zhang, H. Tjugito, and X. Cheng, "Granular impact cratering by liquid drops: Understanding raindrop imprints through an analogy to asteroid strikes," *Proceedings of the National Academy of Sciences*, vol. 112, no. 2, pp. 342–347, 2015.

[81] D. Van Der Meer, "Impact on granular beds," *Annual review of fluid mechanics*, vol. 49, pp. 463–484, 2017.

[82] S. Joubaud, T. Homan, Y. Gasteuil, D. Lohse, and D. van der Meer, "Forces encountered by a sphere during impact into sand," *Physical Review E*, vol. 90, no. 6, p. 060 201, 2014.

[83] C. Li, P. Umbanhowar, H. Komsuoglu, D. Koditschek, and D. I. Goldman, "Sensitive dependence of the motion of a legged robot on granular media," *PNAS*, vol. 106, pp. 3029–3034, Mar. 2009.

[84] W. Thielicke and R. Sonntag, "Particle image velocimetry for MATLAB: Accuracy and enhanced algorithms in PIVlab," *Journal of Open Research Software*, vol. 9, 2021.

[85] S. Dunatunga and K. Kamrin, "Continuum modelling and simulation of granular flows through their many phases," *Journal of Fluid Mechanics*, vol. 779, pp. 483–513, 2015.

[86] ——, "Continuum modeling of projectile impact and penetration in dry granular media," *Journal of the Mechanics and Physics of Solids*, vol. 100, pp. 45–60, 2017.

[87] D. Rubin, N. Goldenson, and G. A. Voth, "Failure and strengthening of granular slopes under horizontal vibration," *Physical Review E*, vol. 74, no. 5, p. 051 307, 2006.

[88] GDrMiDi, "On dense granular flows," *The European Physical Journal E*, vol. 14, no. 4, pp. 341–365, Aug. 2004.

[89] H. Katsuragi and D. J. Durian, "Unified force law for granular impact cratering," *Nat Phys*, vol. 3, no. 6, pp. 420–423, Jun. 2007.

[90] A. H. Clark, A. J. Petersen, and R. P. Behringer, "Collisional model for granular impact dynamics," *Physical Review E*, vol. 89, no. 1, p. 012 201, 2014.

[91] P. Umbanhowar and D. I. Goldman, "Granular impact and the critical packing state," *Phys. Rev. E*, vol. 82, p. 010 301, 1 Jul. 2010.

[92] A. H. Clark, L. Kondic, and R. P. Behringer, "Steady flow dynamics during granular impact," *Physical Review E*, vol. 93, no. 5, p. 050 901, May 2016.

[93] ——, "Particle scale dynamics in granular impact," *Physical Review Letters*, vol. 109, no. 23, p. 238 302, Dec. 2012.

[94] C. S. Bester and R. P. Behringer, "Collisional model of energy dissipation in three-dimensional granular impact," *Physical Review E*, vol. 95, no. 3, p. 032 906, 2017.

[95] J. Hambleton and A. Drescher, "On modeling a rolling wheel in the presence of plastic deformation as a three- or two-dimensional process," *International Journal of Mechanical Sciences*, vol. 51, no. 11-12, pp. 846–855, Nov. 2009.

[96] M. G. Bekker, "Introduction to terrain-vehicle systems," *The University of Michigan Press*, 1969.

[97] J. Slonaker, D. Carrington Motley, C. Senatore, K. Iagnemma, and K. Kamrin, "Geometrically general scaling relations for locomotion on granular beds," *ArXiv e-prints*, Apr. 2016. arXiv: 1604.02490 [cond-mat.soft].

[98] F. Guillard, Y. Forterre, and O. Pouliquen, "Lift forces in granular media," *Physics of Fluids*, vol. 26, no. 4, p. 043 301, Apr. 2014.

[99] T. Zhang, F. Qian, C. Li, P. Masarati, A. M. Hoover, P. Birkmeyer, A. Pullin, R. S. Fearing, and D. I. Goldman, "Ground fluidization promotes rapid running of a lightweight robot," *The International Journal of Robotics Research*, vol. 32, no. 7, pp. 859–869, 2013. eprint: https://doi.org/10.1177/0278364913481690.

[100] B. Schäfer, A. Gibbesch, R. Krenn, and B. Rebele, "Planetary rover mobility simulation on soft and uneven terrain," *Vehicle System Dynamics*, vol. 48, no. 1, pp. 149–169, Jan. 2010.

[101] R. E. Arvidson, J. F. Bell, P. Bellutta, N. A. Cabrol, J. G. Catalano, J. Cohen, L. S. Crumpler, D. J. D. Marais, T. A. Estlin, W. H. Farrand, R. Gellert, J. A. Grant, R. N. Greenberger, E. A. Guinness, K. E. Herkenhoff, J. A. Herman, K. D. Iagnemma, J. R. Johnson, G. Klingelhöfer, R. Li, K. A. Lichtenberg, S. A. Maxwell, D. W. Ming, R. V. Morris, M. S. Rice, S. W. Ruff, A. Shaw, K. L. Siebach, P. A. de Souza, A. W. Stroupe, S. W. Squyres, R. J. Sullivan, K. P. Talley, J. A. Townsend, A. Wang, J. R. Wright, and A. S. Yen, "Spirit mars rover mission: Overview and selected results from the northern home plate winter haven to the side of scamander crater," *Journal of Geophysical Research*, vol. 115, Sep. 2010.

[102] J. L. Callas, "Mars exploration rover spirit end of mission report," California Institute of Technology, Jet Propulsion Laboratory, Tech. Rep., Dec. 2015.

[103] D. B. Bickler, "The new family of jpl planetary surface vehicles," in *In CNES, Missions, Technologies, and Design of Planetary Mobile Vehicles p 301-306 (SEE N94-23373 06-91)*. Missions, Technologies, and Design of Planetary Mobile Vehicles, 1993, ch. 19, pp. 301–306.

[104] K. Yoshida and H. Hamano, "Motion dynamics of a rover with slip-based traction model," in *Proceedings 2002 IEEE International Conference on Robotics and Automation (Cat. No.02CH37292)*, IEEE, 2002.

[105] R. Lindemann and C. Voorhees, "Mars exploration rover mobility assembly design, test and performance," in *2005 IEEE International Conference on Systems, Man and Cybernetics*, IEEE, 2005.

[106] Y. Ozkan-Aydin, J. M. Rieser, C. M. Hubicki, W. Savoie, and D. I. Goldman, "6 - physics approaches to natural locomotion: Every robot is an experiment," in *Robotic Systems and Autonomous Platforms*, ser. Woodhead Publishing in Materials, S. M. Walsh and M. S. Strano, Eds., Woodhead Publishing, 2019, pp. 109–127, ISBN: 978-0-08-102260-3.

[107] G. Ishigami, A. Miwa, K. Nagatani, and K. Yoshida, "Terramechanics-based model for steering maneuver of planetary exploration rovers on loose soil," *Journal of Field Robotics*, vol. 24, no. 3, pp. 233–250, 2007.

[108] P. Tompkins, R. Hunt, M. D'Ortenzio, K. Galal, D. Foreman, J. Munger, M. Shirley, J. Strong, R. Barber, and E. Drucker, "Flight operations for the LCROSS lunar impactor mission," in *SpaceOps 2010 Conference*, American Institute of Aeronautics and Astronautics, Apr. 2010.

[109] P. H. Schultz, B. Hermalyn, A. Colaprete, K. Ennico, M. Shirley, and W. S. Marshall, "The LCROSS cratering experiment," *Science*, vol. 330, no. 6003, pp. 468–472, Oct. 2010.

[110] M. A. Rosenburg, O. Aharonson, J. W. Head, M. A. Kreslavsky, E. Mazarico, G. A. Neumann, D. E. Smith, M. H. Torrence, and M. T. Zuber, "Global surface slopes and roughness of the moon from the lunar orbiter laser altimeter," *Journal of Geophysical Research*, vol. 116, no. E2, Feb. 2011.

[111] M. A. Kreslavsky and J. W. Head, "The steepest slopes on the moon from lunar orbiter laser altimeter (LOLA) data: Spatial distribution and correlation with geologic features," *Icarus*, vol. 273, pp. 329–336, Jul. 2016.

[112] H. M. Jaeger, C.-h. Liu, and S. R. Nagel, "Relaxation at the angle of repose," *Physical Review Letters*, vol. 62, no. 1, pp. 40–43, Jan. 1989.

[113] N. Gravish and D. I. Goldman, "Effect of volume fraction on granular avalanche dynamics," *Physical Review E*, vol. 90, no. 3, Sep. 2014.

[114] P. Tegzes, T. Vicsek, and P. Schiffer, "Development of correlations in the dynamics of wet granular avalanches," *Phys. Rev. E*, vol. 67, p. 051 303, 5 May 2003.

[115] F. Qian, T. Zhang, W. Korff, P. B. Umbanhowar, R. J. Full, and D. I. Goldman, "Principles of appendage design in robots and animals determining terradynamic performance on flowable ground," *Bioinspiration & Biomimetics*, vol. 10, no. 5, p. 056 014, Oct. 2015.

[116] D. Andrews, A. Colaprete, J. Quinn, B. Bluethmann, and J. Trimble, "Resource prospector (rp) - early prototyping and development," in *Space 2015*, NASA Ames Research Center, American Inst. of Aeronautics and Astronautics; Reston, VA, United States, Aug. 2015.

[117] F. Qian, K. Daffon, T. Zhang, and D. I. Goldman, "An automated system for systematic testing of locomotion on heterogeneous granular media," in *Nature-Inspired Mobile Robotics*, World Scientific, Jul. 2013, pp. 547–554 (2013).

[118] B. McInroe, H. C. Astley, C. Gong, S. M. Kawano, P. E. Schiebel, J. M. Rieser, H. Choset, R. W. Blob, and D. I. Goldman, "Tail use improves performance on soft substrates in models of early vertebrate land locomotors," *Science*, vol. 353, no. 6295, pp. 154–158, 2016. eprint: http://science.sciencemag.org/content/353/6295/154.full.pdf.

[119] B. Chong, Y. O. Aydin, C. Gong, G. Sartoretti, Y. Wu, J. Rieser, H. Xing, J. Rankin, K. Michel, A. Nicieza, J. Hutchinson, D. Goldman, and H. Choset, "Coordination of back bending and leg movements for quadrupedal locomotion," in *Proceedings of Robotics: Science and Systems*, Pittsburgh, Pennsylvania, Jun. 2018.

[120] J.-Y. Wong and A. Reece, "Prediction of rigid wheel performance based on the analysis of soil-wheel stresses: Part ii. performance of towed rigid wheels," *Journal of Terramechanics*, vol. 4, no. 2, pp. 7–25, 1967.

[121] L. E. Silbert, D. Erta ş, G. S. Grest, T. C. Halsey, D. Levine, and S. J. Plimpton, "Granular flow down an inclined plane: Bagnold scaling and rheology," *Phys. Rev. E*, vol. 64, p. 051 302, 5 Oct. 2001.

[122] J. Wong, "Chapter 2 - modelling of terrain behaviour," in *Terramechanics and Off-Road Vehicle Engineering (Second Edition)*, J. Wong, Ed., Second Edition, Oxford: Butterworth-Heinemann, 2010, pp. 21–63, ISBN: 978-0-7506-8561-0.

[123] C. Creager, S. Moreland, K. Skonieczny, K. Johnson, V. Asnani, and R. Gilligan, "Benefit of "push-pull" locomotion for planetary rover mobility," in *Earth and Space 2012*, American Society of Civil Engineers, Apr. 2012.

[124] S. S. Sharpe, R. Kuckuk, and D. I. Goldman, "Controlled preparation of wet granular media reveals limits to lizard burial ability," *Physical Biology*, vol. 12, no. 4, p. 046 009, 2015.

[125] N. Patel, R. Slade, and J. Clemmet, "The ExoMars rover locomotion subsystem," *Journal of Terramechanics*, vol. 47, no. 4, pp. 227–242, Aug. 2010.

[126] C. C. Ward and K. Iagnemma, "A dynamic-model-based wheel slip detector for mobile robots on outdoor terrain," *IEEE Transactions on Robotics*, vol. 24, no. 4, pp. 821–831, Aug. 2008.

[127] M. Sutoh, K. Nagaoka, K. Nagatani, and K. Yoshida, "Design of wheels with grousers for planetary rovers traveling over loose soil," *Journal of Terramechanics*, vol. 50, no. 5-6, pp. 345–353, Oct. 2013.

[128] L. Crumpler, R. Arvidson, M. Golombek, J. Grant, B. Jolliff, and D. Mittlefehldt, "Rim structure, stratigraphy, and aqueous alteration exposures along opportunity rover's traverse of the noachian endeavour crater," in *48th Lunar and Planetary Science Conference*, NASA Johnson Space Center, The Woodlands, TX; United States, Mar. 2017.

[129] A. Colaprete, D. Andrews, W. Bluethmann, R. C. Elphic, B. Bussey, J. Trimble, K. Zacny, and J. E. Captain, "An Overview of the Volatiles Investigating Polar Exploration Rover (VIPER) Mission," in *AGU Fall Meeting Abstracts*, vol. 2019, Dec. 2019, P34B–03.

[130] A. Colaprete, R. C. Elphic, M. Shirley, K. Ennico-Smith, J. Heldmann, D. S. S. Lim, L. Falcone, M. Siegler, and J. Coyan, "The Volatiles Investigating Polar Exploration Rover (VIPER) Mission: Measurement Goals and Traverse Planning," in *Lunar and Planetary Science Conference*, ser. Lunar and Planetary Science Conference, Mar. 2020, p. 2241.

[131] R. E. Arvidson, K. D. Iagnemma, M. Maimone, A. A. Fraeman, F. Zhou, M. C. Heverly, P. Bellutta, D. Rubin, N. T. Stein, J. P. Grotzinger, and A. R. Vasavada, "Mars science laboratory curiosity rover megaripple crossings up to sol 710 in gale crater," *Journal of Field Robotics*, vol. 34, no. 3, pp. 495–518, 2017.

[132] E. Uchupi, M. T. Muck, and R. D. Ballard, "The geology of the titanic site and vicinity," *Deep Sea Research Part A. Oceanographic Research Papers*, vol. 35, no. 7, pp. 1093–1110, Jul. 1988.

[133] S. Kawatsuma, M. Fukushima, and T. Okada, "Emergency response by robots to fukushima-daiichi accident: Summary and lessons learned," *Industrial Robot: An International Journal*, vol. 39, no. 5, pp. 428–435, Aug. 2012.

[134] J. Duran, *Sands, powders, and grains: an introduction to the physics of granular materials*, E. Guyon, L. Lam, D. Langevin, and H. Stanley, Eds. Springer Science & Business Media, 2012.

[135] K. Wieghardt, "Experiments in granular flow," *Annual Review of Fluid Mechanics*, vol. 7, no. 1, pp. 89–114, 1975.

[136] F. Q. Potiguar and Y. Ding, "Lift and drag in intruders moving through hydrostatic granular media at high speeds," *Physical Review E*, vol. 88, no. 1, p. 012 204, Jul. 2013.

[137] D. F. Youch, "Efficient calculation of earth penetrating projectile trajectories," NAVAL POSTGRADUATE SCHOOL MONTEREY CA DEPT OF MECHANICAL and ASTRONAUTICAL . . ., Tech. Rep., 2006.

[138] R. D. Maladen, P. B. Umbanhowar, Y. Ding, A. Masse, and D. I. Goldman, "Granular lift forces predict vertical motion of a sand-swimming robot," in *2011 IEEE International Conference on Robotics and Automation*, IEEE, May 2011.

[139] E. Shuter and W. E. Teasdale, *Application of drilling, coring, and sampling techniques to test holes and wells*. Department of the Interior, US Geological Survey, 1989, vol. 2.

[140] G. Girmscheid and C. Schexnayder, "Tunnel boring machines," *Practice Periodical on Structural Design and Construction*, vol. 8, no. 3, pp. 150–163, Aug. 2003.

[141] A. T. Bourgoyne, K. K. Millheim, M. E. Chenevert, F. S. Young, *et al.*, *Applied drilling engineering*. Society of Petroleum Engineers Richardson, TX, 1986, vol. 2.

[142] E. N. Allouche, S. T. Ariaratnam, and J. S. Lueke, "Horizontal directional drilling: Profile of an emerging industry," *Journal of Construction Engineering and Management*, vol. 126, no. 1, pp. 68–76, Jan. 2000.

[143] K. Nagaoka, T. Kubota, M. Otsuki, and S. Tanaka, "Experimental study on autonomous burrowing screw robot for subsurface exploration on the moon," in *2008 IEEE/RSJ International Conference on Intelligent Robots and Systems*, IEEE, Sep. 2008.

[144] C. Pitcher and Y. Gao, "Analysis of drill head designs for dual-reciprocating drilling technique in planetary regoliths," *Advances in Space Research*, vol. 56, no. 8, pp. 1765–1776, Oct. 2015.

[145] Y. Gao, A. Ellery, M. Jaddou, J. Vincent, and S. Eckersley, "Planetary micropenetrator concept study with biomimetric drill and sampler design," *IEEE Transactions on Aerospace and Electronic Systems*, vol. 43, no. 3, pp. 875–885, Jul. 2007.

[146] J. Grygorczuk, L. Wisniewski, B. Kedziora, M. Borys, R. Przybyla, T. Kucinski, M. Ossowski, W. Konior, O. Kromer, T. Spohn, *et al.*, "Hammering mechanism

for hp3 experiment (insight)," in *Proceedings of the 43rd Aerospace Mechanisms Symposium*, NASA Ames Research Center, 2016, pp. 415–428.

[147] T. Wippermann, T. Hudson, T. Spohn, L. Witte, M. Scharringhausen, G. Tsakyridis, M. Fittock, O. Krömer, S. Hense, M. Grott, J. Knollenberg, and R. Lichtenheldt, "Penetration and performance testing of the hp3 mole for the insight mars mission," *Planetary and Space Science*, vol. 181, p. 104 780, Feb. 2020.

[148] T. Spohn, T. L. Hudson, L. Witte, T. Wippermann, L. Wisniewski, B. Kediziora, C. Vrettos, R. D. Lorenz, M. Golombek, R. Lichtenfeld, M. Grott, J. Knollenberg, C. Krause, C. Fantinati, S. Nagihara, and J. Grygorczuk, *The insight hp*^{3}$moleonmars$: $Lessonslearnedfromattemptstopenetratetodepthinthemartiansoil$, 2021. arXiv: 2112.03234 [astro-ph.IM].

[149] A. R. Dexter, "Mechanics of root growth," *Plant and Soil*, vol. 98, no. 3, pp. 303–312, Oct. 1987.

[150] A. G. BENGOUGH and C. E. MULLINS, "Mechanical impedance to root growth: A review of experimental techniques and root growth responses," *Journal of Soil Science*, vol. 41, no. 3, pp. 341–358, Sep. 1990.

[151] L. J. Clark, W. R. Whalley, and P. B. Barraclough, "How do roots penetrate strong soil?" In *Roots: The Dynamic Interface between Plants and the Earth*, Springer Netherlands, 2003, pp. 93–104.

[152] A. Bengough and B. McKenzie, "Sloughing of root cap cells decreases the frictional resistance to maize (zea maysL.) root growth," *Journal of Experimental Botany*, vol. 48, no. 4, pp. 885–893, 1997.

[153] M. IIJIMA and Y. KONO, "Development of golgi apparatus in the root cap cells of maize (zea mays l.) as affected by compacted soil," *Annals of Botany*, vol. 70, no. 3, pp. 207–212, Sep. 1992.

[154] M. Iijima, T. Higuchi, P. W. Barlow, and A. G. Bengough, "Root cap removal increases root penetration resistance in maize (zea mays l.)," *Journal of Experimental Botany*, vol. 54, no. 390, pp. 2105–2109, Sep. 2003.

[155] C. Glenday, *Guinness world records 2008*. Bantam, 2008.

[156] J. A. Kemperman and B. V. Barnes, "Clone size in american aspens," *Canadian Journal of Botany*, vol. 54, no. 22, pp. 2603–2607, Nov. 1976.

[157] A. Sadeghi, A. Tonazzini, L. Popova, and B. Mazzolai, "A novel growing device inspired by plant root soil penetration behaviors," *PLoS ONE*, vol. 9, no. 2, J. Bongard, Ed., e90139, Feb. 2014.

[158] A. Sadeghi, A. Mondini, and B. Mazzolai, "Toward self-growing soft robots inspired by plant roots and based on additive manufacturing technologies," in *Soft robotics*, 2017.

[159] A. Sadeghi, E. D. Dottore, A. Mondini, and B. Mazzolai, "Passive morphological adaptation for obstacle avoidance in a self-growing robot produced by additive manufacturing," *Soft Robotics*, vol. 7, no. 1, pp. 85–94, Feb. 2020.

[160] A. Sadeghi, A. Tonazzini, L. Popova, and B. Mazzolai, "Robotic mechanism for soil penetration inspired by plant root," in *2013 IEEE International Conference on Robotics and Automation*, IEEE, May 2013.

[161] N. D. Naclerio, C. M. Hubicki, Y. O. Aydin, D. I. Goldman, and E. W. Hawkes, "Soft robotic burrowing device with tip-extension and granular fluidization," in *2018 IEEE/RSJ International Conference on Intelligent Robots and Systems (IROS)*, IEEE, Oct. 2018.

[162] Y. Ozkan-Aydin, M. Murray-Cooper, E. Aydin, E. N. McCaskey, N. Naclerio, E. W. Hawkes, and D. I. Goldman, "Nutation aids heterogeneous substrate exploration in a robophysical root," in *2019 2nd IEEE International Conference on Soft Robotics (RoboSoft)*, IEEE, Apr. 2019.

[163] K. M. Dorgan, "The biomechanics of burrowing and boring," *Journal of Experimental Biology*, vol. 218, no. 2, pp. 176–183, Jan. 2015.

[164] O. Zik, J. Stavans, and Y. Rabin, "Mobility of a sphere in vibrated granular media," *Europhysics Letters (EPL)*, vol. 17, no. 4, pp. 315–319, Jan. 1992.

[165] I. MacDonald, "Burial mechanics of the pacific sandfish: The role of the ventilatory pump and physical constraints on the behavior," Copyright - Database copyright ProQuest LLC; ProQuest does not claim copyright in the individual underlying works; Last updated - 2021-08-05, Ph.D. dissertation, 2015, p. 57, ISBN: 978-1-339-43051-5.

[166] E. Trueman, "The mechanism of burrowing of the mole crab, emerita," *Journal of Experimental Biology*, vol. 53, no. 3, pp. 701–710, 1970.

[167] J. Montana, J. K. Finn, and M. D. Norman, "Liquid sand burrowing and mucus utilisation as novel adaptations to a structurally-simple environment in octopus kaurna stranks, 1990," *Behaviour*, vol. 152, no. 14, pp. 1871–1881, 2015.

[168] E. R. Trueman, "Bivalve mollusks: Fluid dynamics of burrowing," *Science*, vol. 152, no. 3721, pp. 523–525, Apr. 1966.

[169] A. G. Winter, R. L. H. Deits, and A. E. Hosoi, "Localized fluidization burrowing mechanics of ensis directus," *Journal of Experimental Biology*, vol. 215, no. 12, pp. 2072–2080, Jun. 2012.

[170] A. G. Winter, V, R. L. H. Deits, D. S. Dorsch, A. H. Slocum, and A. E. Hosoi, "Razor clam to RoboClam: Burrowing drag reduction mechanisms and their robotic adaptation," *Bioinspiration & Biomimetics*, vol. 9, no. 3, p. 036 009, Apr. 2014.

[171] J. (Tao, S. Huang, and Y. Tang, "SBOR: A minimalistic soft self-burrowing-out robot inspired by razor clams," *Bioinspiration & Biomimetics*, vol. 15, no. 5, p. 055 003, Jul. 2020.

[172] K. Zacny, D. Currie, G. Paulsen, T. Szwarc, and P. Chu, "Development and testing of the pneumatic lunar drill for the emplacement of the corner cube reflector on the moon," *Planetary and Space Science*, vol. 71, no. 1, pp. 131–141, Oct. 2012.

[173] B. M. Das and N. Sivakugan, *Principles of foundation engineering*, R. P. Kernan, Ed. Cengage learning, 2018.

[174] J. C. Barrow, "The resonant sonic drilling method: An innovative technology for environmental restoration programs," *Groundwater Monitoring & Remediation*, vol. 14, no. 2, pp. 153–160, May 1994.

[175] E. N. Arnold, "Identifying the effects of history on adaptation: Origins of different sand-diving techniques in lizards," *Journal of Zoology*, vol. 235, no. 3, pp. 351–388, Mar. 1995.

[176] K. S. Norris and J. L. Kavanau, "The burrowing of the western shovel-nosed snake, chionactis occipitalis hallowell, and the undersand environment," *Copeia*, vol. 1966, no. 4, p. 650, Dec. 1966.

[177] M. Barenboim and A. Degani, "Steerable burrowing robot: Design, modeling and experiments," in *2020 IEEE International Conference on Robotics and Automation (ICRA)*, IEEE, May 2020.

[178] R. A. Russell, "CRABOT: A biomimetic burrowing robot designed for underground chemical source location," *Advanced Robotics*, vol. 25, no. 1-2, pp. 119–134, Jan. 2011.

[179] B. Liu, Y. Ozkan-Aydin, D. I. Goldman, and F. L. Hammond, "Kirigami skin improves soft earthworm robot anchoring and locomotion under cohesive soil," in *2019 2nd IEEE International Conference on Soft Robotics (RoboSoft)*, IEEE, Apr. 2019.

[180] K. Isaka, K. Tsumura, T. Watanabe, W. Toyama, M. Sugesawa, Y. Yamada, H. Yoshida, and T. Nakamura, "Development of underwater drilling robot based on earthworm locomotion," *IEEE Access*, vol. 7, pp. 103 127–103 141, 2019.

[181] D. Ortiz, N. Gravish, and M. T. Tolley, "Soft robot actuation strategies for locomotion in granular substrates," *IEEE Robotics and Automation Letters*, vol. 4, no. 3, pp. 2630–2636, Jul. 2019.

[182] X. Yan, S. T. Ariaratnam, S. Dong, and C. Zeng, "Horizontal directional drilling: State-of-the-art review of theory and applications," *Tunnelling and Underground Space Technology*, vol. 72, pp. 162–173, Feb. 2018.

[183] E. W. Hawkes, L. H. Blumenschein, J. D. Greer, and A. M. Okamura, "A soft robot that navigates its environment through growth," *Science Robotics*, vol. 2, no. 8, Jul. 2017.

[184] L. H. Blumenschein, A. M. Okamura, and E. W. Hawkes, "Modeling of bioinspired apical extension in a soft robot," in *Biomimetic and Biohybrid Systems*, Springer International Publishing, 2017, pp. 522–531.

[185] C. Watson and T. K. Morimoto, "Permanent magnet-based localization for growing robots in medical applications," *IEEE Robotics and Automation Letters*, vol. 5, no. 2, pp. 2666–2673, Apr. 2020.

[186] B. Park and H. Myung, "Underground localization using dual magnetic field sequence measurement and pose graph SLAM for directional drilling," *Measurement Science and Technology*, vol. 25, no. 12, p. 125 101, Oct. 2014.

[187] Z. Yanshun, W. Shuwei, and F. Jiancheng, "Measurement-while-drilling instrument based on predigested inertial measurement unit," *IEEE Transactions on Instrumentation and Measurement*, vol. 61, no. 12, pp. 3295–3302, Dec. 2012.

[188] R. Xu, A. Yurkewich, and R. V. Patel, "Curvature, torsion, and force sensing in continuum robots using helically wrapped FBG sensors," *IEEE Robotics and Automation Letters*, vol. 1, no. 2, pp. 1052–1059, Jul. 2016.

[189] M. M. Coad, R. P. Thomasson, L. H. Blumenschein, N. S. Usevitch, E. W. Hawkes, and A. M. Okamura, "Retraction of soft growing robots without buckling," *IEEE Robotics and Automation Letters*, vol. 5, no. 2, pp. 2115–2122, Apr. 2020.

[190] R. Albert, M. A. Pfeifer, A.-L. Barabási, and P. Schiffer, "Slow drag in a granular medium," *Physical Review Letters*, vol. 82, no. 1, pp. 205–208, Jan. 1999.

[191] B. Percier, S. Manneville, J. N. McElwaine, S. W. Morris, and N. Taberlet, "Lift and drag forces on an inclined plow moving over a granular surface," *Physical Review E*, vol. 84, no. 5, p. 051 302, Nov. 2011.

[192] J. H. Jung, N. Pan, and T. J. Kang, "Capstan equation including bending rigidity and non-linear frictional behavior," *Mechanism and Machine Theory*, vol. 43, no. 6, pp. 661–675, Jun. 2008.

[193] L. H. Blumenschein, L. T. Gan, J. A. Fan, A. M. Okamura, and E. W. Hawkes, "A tip-extending soft robot enables reconfigurable and deployable antennas," *IEEE Robotics and Automation Letters*, vol. 3, no. 2, pp. 949–956, Apr. 2018.

[194] S. B. Mickovski, A. G. Bengough, M. F. Bransby, M. C. R. Davies, P. D. Hallett, and R. Sonnenberg, "Material stiffness, branching pattern and soil matric potential affect the pullout resistance of model root systems," *European Journal of Soil Science*, vol. 58, no. 6, pp. 1471–1481, Dec. 2007.

[195] R. J. Webster, J. S. Kim, N. J. Cowan, G. S. Chirikjian, and A. M. Okamura, "Nonholonomic modeling of needle steering," *The International Journal of Robotics Research*, vol. 25, no. 5-6, pp. 509–525, May 2006.

[196] R. S. Seymour, P. C. Withers, and W. W. Weathers, "Energetics of burrowing, running, and free-living in the namib desert golden mole (eremitalpa namibensis)," *Journal of Zoology*, vol. 244, no. 1, pp. 107–117, Jan. 1998.

[197] E. Trueman, "The dynamics of burrowing inEnsis(bivalvia)," *Proceedings of the Royal Society of London. Series B. Biological Sciences*, vol. 166, no. 1005, pp. 459–476, Jan. 1967.

[198] B. D. Texier, A. Ibarra, and F. Melo, "Low-resistive vibratory penetration in granular media," *PLOS ONE*, vol. 12, no. 4, K. Garikipati, Ed., e0175412, Apr. 2017.

[199] M. O. A. Alsaydalani and C. R. I. Clayton, "Internal fluidization in granular soils," *Journal of Geotechnical and Geoenvironmental Engineering*, vol. 140, no. 3, p. 04 013 024, Mar. 2014.

[200] D. Firstbrook, K. Worrall, R. Timoney, F. Suñol, Y. Gao, and P. Harkness, "An experimental study of ultrasonic vibration and the penetration of granular material," *Proceedings of the Royal Society A: Mathematical, Physical and Engineering Sciences*, vol. 473, no. 2198, p. 20 160 673, Feb. 2017.

[201] D. Pachisia, E. Quinn, B. Shitaye, and J. Wang, "Soft eversion robots in application of minimally invasive subsurface drip irrigation," *Princeton University Senior Theses*, 2020.

[202] E. B. Bierhaus, B. C. Clark, J. W. Harris, K. S. Payne, R. D. Dubisher, D. W. Wurts, R. A. Hund, R. M. Kuhns, T. M. Linn, J. L. Wood, A. J. May, J. P. Dworkin, E. Beshore, and D. S. Lauretta, "The osiris-rex spacecraft and the touch-and-go sample acquisition mechanism (tagsam)," *Space Science Reviews*, vol. 214, no. 7, Sep. 2018.

[203] A. V. BURKALOW, "ANGLE OF REPOSE AND ANGLE OF SLIDING FRICTION: AN EXPERIMENTAL STUDY," *Geological Society of America Bulletin*, vol. 56, no. 6, p. 669, 1945.

[204] A. Shields, "Application of similarity principles and turbulence research to bed-load movement," Ph.D. dissertation, Technical University Berlin, 1936.

[205] H. Rouse, "Criteria for similarity in the transportation of sediment," *University of Iowa Studies in Engineering*, vol. 20, pp. 33–49, 1940.

[206] A. S. Baumgarten, B. L. Couchman, and K. Kamrin, "A coupled finite volume and material point method for two-phase simulation of liquid–sediment and gas–sediment flows," *Computer Methods in Applied Mechanics and Engineering*, vol. 384, p. 113 940, 2021.

[207] R. M. Turian and T.-F. Yuan, "Flow of slurries in pipelines," *AIChE Journal*, vol. 23, no. 3, pp. 232–243, May 1977.

[208] B. R. Morton, G. I. Taylor, and J. S. Turner, "Turbulent gravitational convection from maintained and instantaneous sources," *Proceedings of the Royal Society of London. Series A. Mathematical and Physical Sciences*, vol. 234, no. 1196, pp. 1–23, Jan. 1956.

[209] S. B. Pope, *Turbulent Flows*. Cambridge University Press, Aug. 2000.

[210] B. Cushman-Roisin, *Environmental Fluid Mechanics*. John Wiley & Sons, Inc., Jan. 2019.

[211] B. R. Sutherland and S. Dalziel, "Bedload transport by a vertical jet impinging upon sediments," *Physics of Fluids*, vol. 26, no. 3, p. 035 103, Mar. 2014.

[212] S. Badr, G. Gauthier, and P. Gondret, "Crater jet morphology," *Physics of Fluids*, vol. 28, no. 3, p. 033 305, Mar. 2016.

[213] F. Zoueshtiagh and A. Merlen, "Effect of a vertically flowing water jet underneath a granular bed," *Physical Review E*, vol. 75, no. 5, May 2007.

[214] P. Philippe and M. Badiane, "Localized fluidization in a granular medium," *Physical Review E*, vol. 87, no. 4, Apr. 2013.

[215] T. Homan, V. Vidal, C. Picard, and S. Joubaud, "Fluid-particle suspension by gas release from a granular bed," *Physical Review Fluids*, vol. 5, no. 10, Oct. 2020.

[216] C. P. McLaren, T. M. Kovar, A. Penn, C. R. Müller, and C. M. Boyce, "Gravitational instabilities in binary granular materials," *Proceedings of the National Academy of Sciences*, vol. 116, no. 19, pp. 9263–9268, Apr. 2019.

[217] Q. Guo, A. Padash, and C. M. Boyce, "A two fluid modeling study of bubble collapse due to bubble interaction in a fluidized bed," *Chemical Engineering Science*, vol. 232, p. 116 377, Mar. 2021.

[218] J. Ding and D. Gidaspow, "A bubbling fluidization model using kinetic theory of granular flow," *AIChE Journal*, vol. 36, no. 4, pp. 523–538, 1990. eprint: https://aiche.onlinelibrary.wiley.com/doi/pdf/10.1002/aic.690360404.

[219] A. G. Winter and A. E. Hosoi, "Identification and evaluation of the atlantic razor clam (ensis directus) for biologically inspired subsea burrowing systems," *Integrative and Comparative Biology*, vol. 51, no. 1, pp. 151–157, Jun. 2011.

[220] N. Mitarai and F. Nori, "Wet granular materials," *Advances in Physics*, vol. 55, no. 1-2, pp. 1–45, Jan. 2006.

[221] J. A. Dijksman, G. H. Wortel, L. T. H. van Dellen, O. Dauchot, and M. van Hecke, "Jamming, yielding, and rheology of weakly vibrated granular media," *Physical Review Letters*, vol. 107, no. 10, Sep. 2011.

[222] A. Penn, T. Tsuji, D. O. Brunner, C. M. Boyce, K. P. Pruessmann, and C. R. Müller, "Real-time probing of granular dynamics with magnetic resonance," *Science Advances*, vol. 3, no. 9, Sep. 2017.

[223] S. Pravin, B. Chang, E. Han, L. London, D. I. Goldman, H. M. Jaeger, and S. T. Hsieh, "Effect of two parallel intruders on total work during granular penetrations," *Phys. Rev. E*, vol. 104, p. 024 902, 2 Aug. 2021.

[224] G. Carrington, *Basic thermodynamics*. Oxford University Press on Demand, 1994.

[225] M. Choukroun, J. L. Molaro, R. Hodyss, E. Marteau, P. Backes, E. M. Carey, W. Dhaouadi, S. Moreland, and E. M. Schulson, "Strength evolution of ice plume deposit analogs of enceladus and europa," *Geophysical Research Letters*, vol. 47, no. 15, e2020GL088953, 2020, e2020GL088953 2020GL088953. eprint: https://agupubs.onlinelibrary.wiley.com/doi/pdf/10.1029/2020GL088953.

VITA

Andras 'Andy' Karsai was born on a dark and stormy night on June 14, 1993 in Szeged, Hungary to Istvan Karsai and Johanna Preiszner. He immigrated to the United States in 1996 and grew up in Johnson City, Tennessee before attending Georgia Institute of Technology in 2011. He graduated a Bachelor's of Science in Physics with Highest Honors in May 2015 and as a Masters of Science in Physics in 2018. He resides in Atlanta, Georgia, and can be often be found writing, tinkering, or lifting heavy objects.